FORMULATION OF FINAL RESISTANCE OF THE AIR FILTERS

YIT JING EE

FACULTY OF ENGINEERING
UNIVERSITI MALAYA
KUALA LUMPUR

2023

FORMULATION OF FINAL RESISTANCE OF THE AIR FILTERS

YIT JING EE

THESIS SUBMITTED IN FULFILMENT OF THE REQUIREMENTS FOR THE DEGREE OF DOCTOR OF PHILOSOPHY

FACULTY OF ENGINEERING
UNIVERSITI MALAYA
KUALA LUMPUR

2023

UNIVERSITI MALAYA

ORIGINAL LITERARY WORK DECLARATION

Name of Candidate: YIT JING EE

Matric No: 17116153/2

Name of Degree: DOCTOR OF PHILOSOPHY

Title of Project Paper/Research Report/Dissertation/Thesis ("this Work"):

FORMULATION OF FINAL RESISTANCE OF THE AIR FILTERS

Field of Study: ELECTRICITY AND ENERGY

I do solemnly and sincerely declare that:

(1) I am the sole author/writer of this Work;
(2) This Work is original;
(3) Any use of any work in which copyright exists was done by way of fair dealing and for permitted purposes and any excerpt or extract from, or reference to or reproduction of any copyright work has been disclosed expressly and sufficiently and the title of the Work and its authorship have been acknowledged in this Work;
(4) I do not have any actual knowledge nor do I ought reasonably to know that the making of this work constitutes an infringement of any copyright work;
(5) I hereby assign all and every rights in the copyright to this Work to the Universiti Malaya ("UM"), who henceforth shall be owner of the copyright in this Work and that any reproduction or use in any form or by any means whatsoever is prohibited without the written consent of UM having been first had and obtained;
(6) I am fully aware that if in the course of making this Work I have infringed any copyright whether intentionally or otherwise, I may be subject to legal action or any other action as may be determined by UM.

Candidate's Signature Date: 16 January 2023

Subscribed and solemnly declared before,

Witness's Signature Date: 16/01/2023

Name:

Designation:

FORMULATION OF FINAL RESISTANCE OF THE AIR FILTERS

ABSTRACT

Air filters play an indispensable role in maintaining a good indoor air quality (IAQ) for the occupants in a building. However, a significant drawback of the air filter applications is the high pressure drop across it, causing a high energy consumption of the HVAC system. The dust cake formation on the filter media after a certain period of usage can even further increase the high energy consumption. Therefore, an accurate setpoint of the final resistance can ensure energy-saving of the system while the indoor air quality is not compromised. In the industrial practice, the final resistance is set twice the initial resistance according to ASHRAE 52.2-2020 recommendation or set using Rule of Thumbs as there is a lack of final resistance study in the literature. In this research, a pleated fibreglass air filter is studied to identify the factors affecting filtration performance and formulate the final resistance relationship. The filtration performance parameters, including the initial pressure drop, filtration efficiency, pressure drop across dust cake and the dust holding capacity of the filter, are studied experimentally and via CFD. A triangular pleat is found to have the lowest initial pressure drop, and it is found that the fibre diameter, filtration velocity, pleat density and pleat depth are the contributing factors affecting filtration performance. The empirical models of filtration performance parameters are expressed in terms of the contributing factors. The models are validated that the predicted models are acceptable as the difference between predicted and validated R^2 values are only less than 1.5 %. The validated empirical models are used for the prediction in the final resistance model in consideration of the filter lifespan and the energy cost. The findings of this study can effectively provide a guideline to the filter manufacturers in the filter design stage or the filter selection stage. The filtration performance can be easily predicted by inserting the design parameters into the empirical models. The final resistance can also be determined analytically with the proposed model

in consideration of the predicted filter lifespan and energy cost. The proposed filtration performance parameter models and final resistance model can provide a better filter selection for the end-users, giving a better solution in maintaining the building's IAQ and, at the same time, minimizing the operation cost.

Keywords: final efficiency; initial pressure drop; dust holding capacity; energy consumption; filter lifespan

FORMULASI RINTANGAN AKHIR PENAPIS UDARA

ABSTRAK

Penapis udara memainkan peranan yang amat penting dalam mengekalkan kualiti udara dalaman (IAQ) yang baik untuk penghuni dalam sesebuah bangunan. Namum, kelemahan ketara bagi aplikasi penapis udara ialah penurunan tekanan yang tinggi menyebabkan penggunaan tenaga tinggi dalam sistem HVAC. Pembentukan kek habuk pada media penapis selepas tempoh penggunaan tertentu meningkatkan lagi penggunaan tenaga. Oleh itu, titik tetapan yang tepat bagi rintangan akhir, yang boleh memastikan penjimatan tenaga sistem, dan kualiti udara dalaman tidak terjejas. Dalam amalan perindustrian, rintangan akhir ditetapkan dua kali rintangan awal mengikut pengesyoran ASHRAE 52.2-2020 atau ditetapkan menggunakan Peraturan Amalan disebabkan kekurangan kajian rintangan akhir dalam literatur. Dalam penyelidikan ini, penapis udara gentian kaca berlipat dikaji untuk mengenal pasti faktor yang mempengaruhi prestasi penapisan dan untuk merumuskan formulasi rintangan akhir. Parameter prestasi penapisan termasuk penurunan tekanan awal, kecekapan penapisan, penurunan tekanan merentas kek habuk dan kapasiti pegangan habuk penapis dikaji secara eksperimen dan melalui CFD. Lipatan segi tiga didapati mempunyai penurunan tekanan awal yang paling rendah dan didapati diameter gentian, halaju penapisan, ketumpatan lipatan dan kedalaman lipatan adalah faktor penyumbang yang mempengaruhi prestasi penapisan. Model empirikal parameter prestasi penapisan dinyatakan dari segi faktor sumbangan. Model tersebut telah disahkan bahawa model yang diramalkan boleh diterima kerana perbezaan antara nilai R2 hanya kurang daripada 1.5%. Model empirikal ini digunakan untuk ramalan dalam model rintangan akhir dengan mengambil kira jangka hayat penapis dan kos tenaga. Dapatan kajian ini dapat memberi garis panduan secara berkesan kepada pengilang penapis dalam peringkat reka bentuk penapis atau peringkat pemilihan penapis. Prestasi penapisan boleh diramalkan dengan mudah dengan memasukkan parameter reka bentuk ke dalam model

empirikal. Rintangan akhir juga boleh ditentukan secara analitikal dengan model yang dicadangkan dengan mengambil kira jangka hayat penapis dan kos tenaga yang diramalkan. Model parameter prestasi penapisan yang dicadangkan dan model rintangan akhir boleh memberi pemilihan penapis yang lebih baik untuk pengguna, dengan memberikan penyelesaian yang lebih baik dalam mengekalkan IAQ bangunan dan pada masa yang sama meminimumkan kos operasi.

Kata kunci: kecekapan akhir; penurunan tekanan awal; kapasiti memegang habuk; penggunaan tenaga; jangka hayat penapis

ACKNOWLEDGEMENTS

Firstly, I would like to express my most profound appreciation to my supervisors, Professor Ir. Dr. Yau Yat Huang and Dr. Chew Bee Teng, for guiding me throughout the research journey. They were very supportive and helpful by sacrificing their valuable time to provide comprehensive guidance, inspiration and practical advices to me all the time.

Secondly, I extend my gratitude to the management team and colleagues from Japan Air Filter Malaysia Sdn. Bhd. for their continuous support in this project. Special thanks are extended to Mr. Ng KH and Mr. Lee BH for their generous sponsorship of the construction of the test rigs and materials used in this study.

Thirdly, I would like to acknowledge Yayasan Khazanah for sponsoring me in this PhD study and giving me strong mental support throughout the journey. I have gained invaluable knowledge and experiences from this journey with all the support I received from different parties. I would like to thank numerous people whose names are not mentioned for their assistance in this study.

Last but not least, I would like to express my deepest gratitude to my beloved parents and family members for their understanding, moral support and love. Special thanks are extended to Mr. Ng BL for providing me with unfailing support and continuous encouragement.

TABLE OF CONTENTS

LIST OF FIGURES

LIST OF TABLES

LIST OF SYMBOLS AND ABBREVIATIONS

σ	:	Surface charge density ($C \cdot m^{-2}$)
ρ_p	:	Density of particle (kg/m^3)
ρ_f	:	Density of fibreglass (kg/m^3)
$\propto$	:	Pleat ratio
$\propto_f$	:	Fibre solidity
φ	:	Collision efficiency (%)
ε	:	Porosity
μ	:	Fluid dynamic viscosity (Pa·s)
$\%OA$	:	Percentage of fresh air or outdoor air (%)
$\%RA$	:	Percentage of return air (%)
A_{avg}	:	Average arrestance (%)
A_j	:	Arrestance after each dust loading step (%)
B	:	Media permeability ($cm^3/s/cm^2$)
C	:	Media inertial resistance (Pa)
C_E	:	Filter energy cost ($)
C_F	:	Filter cost ($)
C_I	:	Filter installation cost ($)
C_{indoor}	:	Indoor particle concentration (kg/m^3)
C_n	:	Cunningham slip correction coefficient
$C_{outdoor}$	:	Outdoor particle concentration (kg/m^3)
C_{up}	:	Upstream dust concentration (kg/m^3)
D	:	Diffusion coefficient of particle (m^2/s)
d_f	:	Diameter of the filter fibre (μm)
d_{fg}	:	Geometric diameter of the filter fibre (μm)

d_p	:	Diameter of particle (μm)
d_{vg}	:	Geometric mean diameter of d_v (μm)
d_v	:	Volume equivalent diameter (μm)
d_{ps}	:	Lower limit of the particle size channel (μm)
d_{ps+1}	:	Upper limit of the particle size channel (μm)
ePM_1	:	Efficiency of an air cleaning device to particles with an optical diameter between 0.3 μm and 1 μm (%)
$ePM_{2.5}$	:	Efficiency of an air cleaning device to particles with an optical diameter between 0.3 μm and 2.5 μm (%)
ePM_{10}	:	Efficiency of an air cleaning device to particles with an optical diameter between 0.3 μm and 10 μm (%)
E	:	Energy consumption (J)
$\overline{FE}$	:	Average filtration efficiency at a particle size of 0.4μm at 0.944m^3/s (%)
J	:	Pre-occupant cost function ($)
J_E	:	Cost due to energy consumption ($)
J_{IAQ}	:	Cost due to indoor exposure due to PM2.5 and ozone of outdoor origin ($)
J_{filter}	:	Cost for filter purchase and replacement ($)
k_n	:	Variable of number of cake layers
K_S	:	Dynamic shape factor
K_1	:	Clean media specific viscous resistance coefficient (Pa·s/m)
K_i	:	Inertial resistance coefficient to air flow for clean filter (Pa·s^2/m^2)
K_c	:	Specific dust cake resistance coefficient (m/g)
Ku	:	Kuwabara's hydrodynamic factor
L	:	Filter thickness (mm)

L_H	:	Lamb's hydrodynamic factor
M	:	Total mass of dust loading (g)
m	:	Variable of loaded dust (g)
Δm_s	:	Particle mass in each cake layer (g)
m_A	:	Mass of dust passing through filter (g)
M_A	:	Mass of dust fed (g)
M_j	:	Mass of loaded dust at the dust loading stage j (g)
m_j	:	Mass of dust passing through filter at the dust loading stage j (g)
N	:	Number of cake layers
n	:	Number of samples
η	:	System energy efficiency (%)
η_T	:	Overall efficiency (%)
η_F	:	Single fibre efficiency (%)
η_R	:	Single fibre efficiency due to interception (%)
η_I	:	Single fibre efficiency due to impaction (%)
η_D	:	Single fibre efficiency due to diffusion (%)
η_G	:	Gravitational settling efficiency (%)
η_{ps}	:	Fractional efficiency for each particle size (%)
P_w	:	Distance between two pleats / pleat width (mm)
P_d	:	Pleat depth (mm)
P_ρ	:	Pleat density (pleats per inch)
P	:	Penetration (%)
P_ρ	:	Pleat density
$P(m)$	:	Instantaneous pressure drop across filter (Pa)
$\overline{\Delta P}$	:	Average pressure drop of air filter (Pa)
ΔP	:	Pressure drop across the filter (Pa)

ΔP_0	:	Resistance to airflow or pressure drop across the clean filter medium (Pa)
ΔP_c	:	Pressure drop across dust cake (Pa)
ΔP_f	:	Final pressure drop (Pa)
Q	:	Airflow rate (m^3/s)
QF	:	Quality factor (Pa^{-1})
R	:	Fibre radius (μm)
r	:	Radial distance from fibre axis (μm)
r_p	:	Radius of particle (μm)
r_f	:	Radius of fibre (μm)
Re	:	Reynolds number
S	:	Dust cake drag coefficient (Pa·s/m)
s	:	Sticking probability
S_f	:	Filtration surface area (mm^2)
Stk	:	Stokes number
t	:	Operation time (year)
t_{cost}	:	Filter operation time when energy cost is same as replacement cost (year)
t_f	:	Total filtration time (year)
t_{FR}	:	Recommended filter operational time (year)
Δt	:	Time required for the cake formation of each layer (days)
U_0	:	Air velocity (m/s)
u_S	:	Superficial velocity (m/s)
u_i	:	Interstitial velocity (m/s)
V_{inlet}	:	Duct air velocity (m/s)
V_S	:	Terminal settling velocity (m/s)

V_f	:	Filtration velocity (m/s)
W	:	Dust mass deposited per unit filter area (g/m^2)
W_{avg}	:	Average power consumption of filter (W)
W_f	:	Basis weight of fibre media (g/m^2)
W_{t_f}	:	Total power consumption throughout filter lifespan (W)
Y	:	Distance between particles and the center of fibre center (μm)
Z	:	Filter media thickness (mm)
ASHRAE	:	American Society of Heating, Refrigerating and Air-Conditioning Engineers
DEHS	:	DiEthylHexylSebacate
EPA	:	Environmental Protection Agency
HVAC	:	Heating, ventilation, and air conditioning
IPA	:	Isopropanol
KCl	:	Potassium chloride
kep	:	Key energy performance
LES	:	Large eddy simulation
MERV	:	Minimum efficiency reporting value
MPPS	:	Most penetrating particle size
PIV	:	Particle Image Velocimetry
PPI	:	Pleats per inch
PM	:	Particulate matter
PSE	:	Particle size efficiency
RANS	:	Reynolds-averaged navier-stokes
RNG	:	Renormalization group theory
RSM	:	Reynolds stress models
SST	:	Shear-stress transport

SVF	:	Solid volume fraction
ULPA	:	Ultra low particulate air
URANS	:	Unsteady reynolds-averaged navier-stokes
VIF	:	Variance inflation factor

LIST OF APPENDICES

CHAPTER 1: INTRODUCTION

1.1 Background

Nowadays, the emission of particulate matter (PM) or particle pollution is becoming more severe due to urbanization and industrialization. This has raised the alarm as the breathing in of microscopic particles will bring serious health problems to humans. Breathing in air pollution particles can cause cardiac-respiratory problems in the human body and the long-term damage can even cause reduced life expectancy (Khomenko et al., 2021; Tainio et al., 2021). Therefore, indoor air quality has always been a concern and the fibrous filtration is necessary for the heating, ventilation and air conditioning (HVAC) system of a building to reduce fine particles like $PM_{2.5}$ or nanoparticle emissions to the environment (Vijayan et al., 2015).

The primary filtration mechanisms in trapping the particles are interception, inertial impaction, diffusion and gravitational settling (Billings, 1966), while the particle size is the critical factor in affecting the domination of the filtration mechanism. The fibrous filter performance is evaluated by the initial resistance to airflow, filtration efficiency, as well as the pressure differential and collection efficiency changes when the filter is loaded with dust (Billings, 1966; National Air Filtration Association, 1993). The filtration performance depends on various factors such as the physical properties of the media such as media porosity, fibre diameter, media thickness, solidity etc. (Bian et al., 2020; Kim et al., 2021; Payen et al., 2012), the construction of the filter (pleat geometry) (Li et al., 2019; Park et al., 2012), dust particle properties (particle diameter, size, dust loading rate etc.)(Endo et al., 1998; Shihang et al., 2019; Wang et al., 2016) or the environmental properties such as filtration velocity, humidity and temperature (Alderman et al., 2008; Leung et al., 2010; Xia et al., 2018). These factors can significantly affect the filtration performance.

However, one major drawback of the filtration system in the HVAC system of a building is the high pressure differential across the several filter layers, which subsequently leads to a higher energy consumption. The challenge in filtration system design is to reduce the pressure differential across the filter, at the same time maintaining the filtration efficiency and prolonging the filter service lifespan in order to achieve a more energy and cost-efficient system for a building operation. Much research has been carried out to investigate the energy and operational cost of air filters in optimizing the energy consumed by the filtration system.

In addition to that, a filter parameter which is the final resistance can significantly affect the total operational cost of the air filters. The final resistance of the air filter is defined as the resistance to airflow up to which the filtration performance is measured to determine the average arrestance and test dust capacity. In other words, the final resistance acts as a reference point to replace the air filters. If the air filter is overloaded with dust without regular filter replacement, the filter operational cost could be increased due to the high pressure drop across the dust cake. In actual application, the final resistance or the maximum operating resistance to airflow of air filter is normally recommended by the manufacturers (ISO, 2016b). The final resistance is recommended to be two times the initial resistance or the pressure drop of a clean filter as recommended in ASHRAE 52.2:2017 (ASHRAE, 2017; Nassif, 2012) and most of the time is recommended using the Rule of Thumbs. The recommendation of the final resistance is required to be investigated in consideration of the energy cost and different contributing factors to the filtration performance. Hence, in this study, a formulation of the final resistance is determined by studying various parameters contributing to the filtration performance and the energy cost.

1.2 Problem Statement

In the current air filtration industry, the final resistance of the air filters, which corresponds to the filter replacement time, is recommended by the manufacturers based on the Rules of Thumbs or by predefining the values to be two times of the initial pressure drop of the air filters. This might bring to a high energy consumption when the filter is overloaded with thick dust cake, before reaching the recommended final resistance. In addition to that, the filter might rupture with the overloaded dust cake and this can severely affect the building's indoor air quality. Thus, the formulation of the final resistance is required in consideration of various contributing factors of filtration performance and the energy cost of the air filters. The final resistance model could act as an important guideline for the manufacturers to determine the filter lifespan at the optimal filtration performance and energy cost.

1.3 Research Questions

The research questions of the present project are as follows:

1. What are the factors affecting the filtration performance of the air filter?
2. How does the filter energy consumption and lifespan affect the final resistance of an air filter?
3. What is the mathematical relationship of the final resistance to achieve the optimum filtration performance?

1.4 Research Objectives

The aim of this research study is to develop a final resistance relationship with empirical formulae of the filtration performance parameters in consideration of the energy factors. The objectives of this research study are as below:

1. To determine the effect of the pleat shape on the initial pressure drop using CFD simulation.

2. To analyse the effect of filter media, filtration velocity and pleat geometry on the filtration performance of the air filters.
3. To develop empirical models of filtration performance parameters based on different contributing or filter design factors investigated.
4. To develop a mathematical model for determining the final resistance of air filters based on the energy and design factors.

1.5 Scopes and Limitations

The present work focuses on experimental studies and CFD simulation of the air filtration performance under different contributing factors of the fibreglass media. Therefore, the research work conducted in this project is restricted to fibreglass media filters with the holt-melt separators.

1.6 Outline of Thesis

Chapter 1 outlines the background of this research work and defines the research questions and objectives of the study. In Chapter 2, a detailed literature review is conducted on the filtration mechanisms, factors affecting the filtration performance, CFD techniques in evaluating the pressure drop and lifespan cost of the filters. Next, a detailed comparison of air filter test standards available in the market is performed in Chapter 3. Chapter 4 describes the methodology adopted in this study. Chapter 5 studies the effect of the pleat shape on the initial pressure drop using CFD simulation. Chapters 6 to 8 explain the effect of media types, filtration velocity and pleat geometry, respectively, on the filtration performance experimentally. Then, in Chapter 9, the empirical models of each filtration performance parameter and the formulation of the final resistance are done. Lastly, the main findings of this study and the recommendations for future works are described in Chapter 10.

CHAPTER 2: LITERATURE REVIEW

2.1 Background Study

2.1.1 Indoor Air Quality

It is essential to maintain good indoor air quality (IAQ) as prolonged taking in indoor pollutants such as biological contaminants (allergens, endoxins, building-related dampness, and mould), chemicals (combustion products, off-gassing emissions, carcinogens) can drastically increase the health risk (Dales et al., 2008). Increasing ventilation rate in the HVAC system according to ASHRAE Standard 62 (ASHRAE Standard, 2019) can reduce sick building syndrome, hence reducing IAQ problems in Malaysia (Syazwan Aizat et al., 2009). Urbanization and industrialization have severely increased the toxic emissions such as particulate matter ($PM_{2.5}$) and greenhouse gases to the environment which can cause cardio-respiratory diseases to human (Vijayan et al., 2015; Wang et al., 2019; Yang et al., 2018). The air filtration plays an important role in maintaining indoor air quality by effectively removing fine particles and allergens, consequently improving human cardiorespiratory health (Vijayan et al., 2015; Xu et al., 2010).

2.1.2 Energy Consumption of HVAC System

One of the major global concerns is the high building energy consumption which gives rise to environmental impacts such as climate change and global warming. According to Pérez-Lombard et al. (2008), the buildings in developed countries use up to 20 - 40% of total energy usage, and the HVAC system has consumed almost half of the building energy. HVAC system plays an essential role in maintaining thermal comfort for occupants in a building (Guo & Zhou, 2009). In Malaysia, the building energy consumption is at 48% of the total energy generated with half of the energy consumed at the HVAC system (Hassan et al., 2014).

High fan power is used to overcome the airflow resistance across the distribution duct in the HVAC system. The air filter is able to protect the HVAC equipment by preventing airborne debris into the system which can cause fouling and clogging of the HVAC components (Betts, 2013), at the same time effectively reduce $PM_{2.5}$ level (Zhang et al., 2016; Zhao et al., 2017). However, one significant drawback of using air filters in the HVAC system is the high energy consumption as a consequence of the pressure drop across several layers of air filter applications (pre-filter, secondary filter, HEPA and ULPA grade filter) (Zaatari et al., 2014). The high flow resistance of air filters contributes 25-40% to the overall fan energy consumption of the HVAC system (Montgomery, 2015).

Therefore, the specification of the air filters should be designed in order to reduce energy consumption, at the same time maintaining good filtration properties.

2.2 Filtration Performance and Mechanisms of a Clean Air Filter

2.2.1 Filtration Performance Parameters

The air filter performance is evaluated at the filtration efficiency, pressure drop, and dust holding capacity (National Air Filtration Association, 1993). The performance of air filters is evaluated at the factors (Billings, 1966):

1. The initial pressure drop of a clean filter
2. The filtration efficiency at the beginning of the filtration process
3. Changes in the efficiency and pressure drop of air filter caused by the dust loading process

A high-performance air filter is expected to achieve high efficiency, low pressure drop, and high dust holding capacity. The challenge in air filtration is to obtain high efficiency and high dust holding capacity at a low pressure drop of air filters. A

quantitative criterion, which is called filter quality, q_f is used to compare filter performance (Zhang, 2004)

$$q_f = \frac{-\ln(1-\eta_T)}{\Delta P} = \frac{4 \propto_f \eta_F L}{\pi d_f \Delta P} \quad \textbf{(2.1)}$$

where η_T is the overall efficiency, ΔP is the pressure drop across the filter, $\propto_f$ is the fibre solidity, η_F is the total single fibre efficiency, L is the filter thickness and d_f is the diameter of the filter fibre.

2.2.1.1 Pressure Drop

A fibrous filter is made up of loosely-packed fibres with a preferred orientation across the airflow direction. A packing density or filter solidity, $\propto_f$ which is the ratio of the total volume of the filter fibres to the volume of the air filter, is within a range of 1 – 15 %. The lower the packing density, the lower the pressure drop of the air filter (Wang, 2001).

For flow in a fibre filter, Darcy's Law is expressed as (Billings, 1966)

$$\frac{\Delta P_0}{L} \cdot \frac{R^2}{\mu U_0} = K_0(\propto_f) \quad \textbf{(2.2)}$$

An empirical formula given for pressure drop across the filter is defined by Davies (1953) as

$$\Delta P_0 = \frac{64 \mu L U_0 \propto_f^{1.5} (1 + 56 \propto_f^3)}{d_f^2}, 0.006 < \propto_f < 0.3 \quad \textbf{(2.3)}$$

where ΔP_0 is the resistance to airflow or pressure drop across the filter medium, $K_0(\propto_f)$ is the theoretical resistivity of the medium, $\propto_f$ is the solidity, μ is the fluid viscosity, R is the fibre radius, d_f is the fibre diameter, U_0 is the air velocity and L is the filter thickness.

Del Fabbro et al. (2002) developed a semi-empirical model using dimensionless approach principles in defining the pressure drop of a clean pleated filter over different parameters:

$$\frac{\Delta P_0}{Z \cdot K_1 \cdot v_f} = \left(1 + \frac{h \cdot Z}{{P_w}^2}\right)^{460 \cdot \left(\frac{\mu}{Z^2 \cdot K_1}\right)^{0.7}} \cdot 10^{\frac{0.7 \cdot \left(\frac{\mu}{Z^2 \cdot K_1}\right)^{0.7} \cdot \left(\frac{h}{P_w}\right)^2}{log\left(1+\frac{h}{Z}\frac{1}{Re}\right)}} \quad \textbf{(2.4)}$$

where ΔP_0 is the filter pressure drop; Z is the filter media thickness; K_1 is the media airflow resistance; v_f is the filtration velocity; h is the pleat height; P_w is the distance between two pleats; μ is the air dynamic viscosity and Re is the Reynolds number.

There are a lot of researches done to reduce and optimize initial pressure drop across air filters by studying the effect of the type of filter media (Bao et al., 2016), fibre separation factor (Liu & Wang, 1997), the spacing between filter web (Roh et al., 2019), face velocity at filter media (Xia et al., 2018), dust loading rate (Hinds & Kadrichu, 1997), etc. The energy consumption across the air filters can be reduced with a lower initial resistance of air filters.

2.2.1.2 Filter Efficiency

(a) ***Single Fibre Efficiency***

For a particle-free and clean filter, the analytical expressions for overall efficiency and pressure drop are formed based on the individual fibre contribution (Kasper et al., 2009). According to Löffler (1968), the single fibre efficiency, η_F is defined as

$$\eta_F = \varphi \cdot s \quad \textbf{(2.5)}$$

where φ is the collision efficiency and s is the sticking probability.

As shown in Figure 2.1, if a fibre with a radius of R removes all the particles at a distance of Y from fibre center, the single fibre efficiency is defined as (Chae, 2000)

$$\eta_F = \frac{Y}{R} \tag{2.6}$$

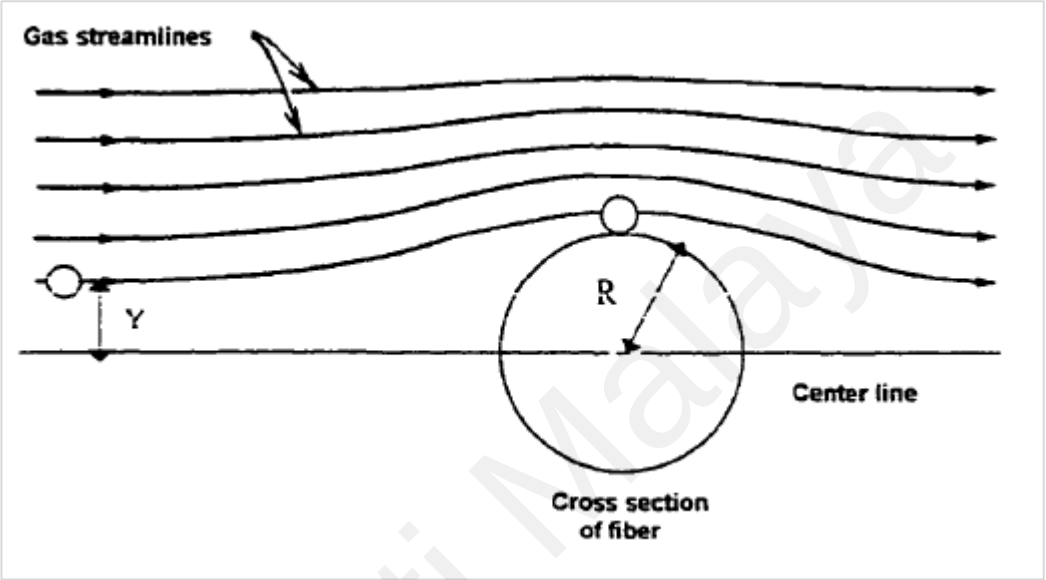

Figure 2.1: Definition of Single Fibre Efficiency (Chae, 2000)

It can be seen from the definitions of single fibre efficiency above that the efficiency is independent of the filter thickness, L (Chae, 2000). An air filter with a lower single fibre efficiency can be improved to a higher overall efficiency using thicker filter media. Therefore, it would be fair to evaluate an air filter performance using single fibre efficiency.

The single fibre efficiency can be calculated by taking the sum of efficiencies for each filtration mechanism. With single fibre efficiency due to interception η_R, impaction η_I, diffusion η_D and gravitational settling efficiency η_G respectively, the total single fibre efficiency is calculated by

$$\eta_F = \eta_R + \eta_I + \eta_D + \eta_G \tag{2.7}$$

The single fibre efficiency for different filtration mechanism (interception η_R, impaction η_I, diffusion η_D and gravitational settling efficiency η_G) will be discussed in sections later.

(b) ***Overall Efficiency***

The overall efficiency, η_T of an air filter with circular fibres can be obtained using the single fibre efficiency using equation (2.8)(Regan & Raynor, 2009).

$$\eta_T = 1 - exp\left[\frac{-4 \propto_f \eta_F L}{\pi d_f}\right] \quad \textbf{(2.8)}$$

where $\propto_f$ is the filter solidity or the fraction of the bulk volume of a filter occupied by fibres, L is the filter thickness and d_f is the fibre diameter.

2.2.2 Filtration Mechanism

There are two types of air filters: mechanical air filters and electronic air cleaners. The main difference of electronic air cleaners is that they function with the electrostatic effect which requires external power source whereas a mechanical air filter can function passively (National Air Filtration Association, 1993). Figure 2.2 shows a summary of different types of filtration mechanisms.

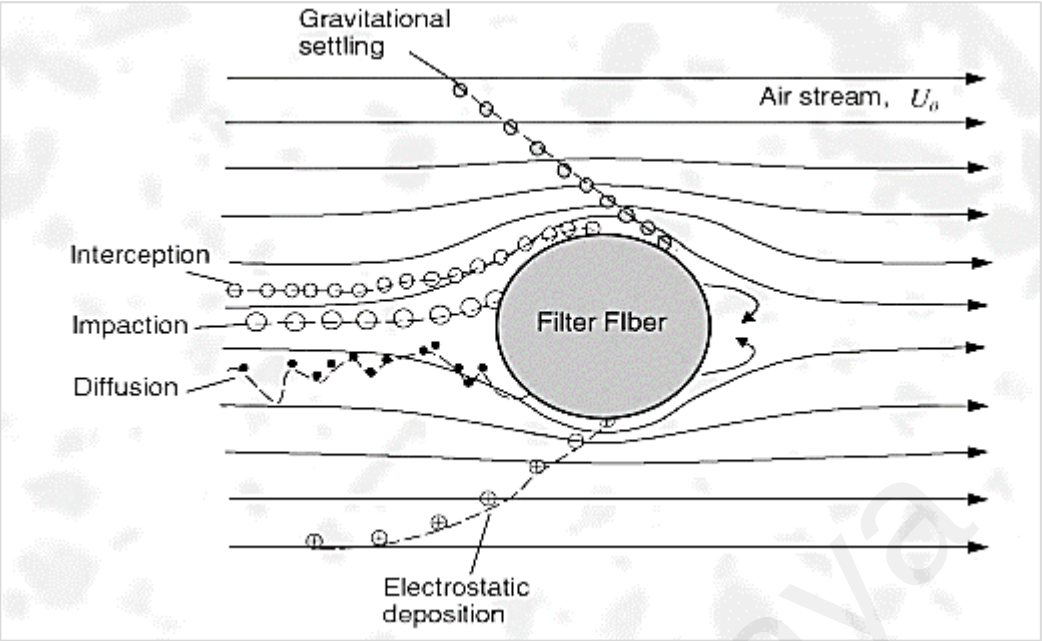

Figure 2.2: Filtration Mechanism (Zhang, 2004)

2.2.2.1 Mechanical Air Filters

The working principle of mechanical filtration is that the filter medium acts as a porous screen barrier of airflow to retain particles from the air stream. In mechanical filtration, one important note is that the electrical charges are absent between air particles and filter fibres and the particle collection happens purely because of the Van der Waal's force of attraction between them (Sutherland & Chase, 2011).

The assumptions used in deriving the single fibre model of the primary filtration mechanisms (interception, impaction, diffusion, and gravitational settling) are (Billings, 1966):

1. The filter fibres are adequately far apart so that the airflow in the vicinity of a given filter fibre can be taken as the airflow around an isolated fibre. The fibre crossing effect and inter-fibre interference can be neglected.
2. There is no additional hydrodynamic lift or drag caused when the particles are approaching a surface and do not distort the airflow.
3. The surface migration, re-entrainment, and effective contacts are neglected.

The particle size is an important factor in the filtration mechanism and its efficiency. Inertial impaction dominates in larger particles while diffusion happens at fine particles. There is a region where the penetration of particles is maximum, and the filtration efficiency is the lowest. This happens at the most penetrating particle size, MPPS at the diffusion and interception regime as shown in Figure 2.3 and it is the most difficult to be captured by the filters (Chae, 2000; Lee & Liu, 1980).

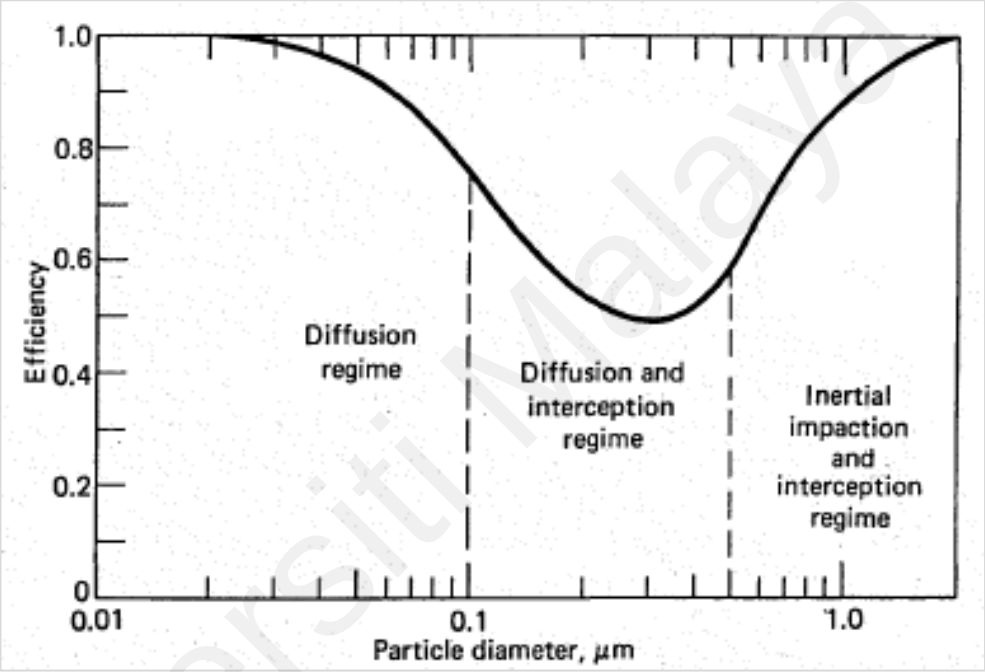

Figure 2.3: Filtration Mechanism at Different Particle Size (Lee & Liu, 1980)

(a) ***Interception***

Interception is a mechanism of filtration that occurs when a particle follows the airstream around a fibre and is intercepted by the fibre if the force of attraction between the fibre and dust particles is strong enough (National Air Filtration Association, 1993). The key factor for interception for single fibre efficiency is the ratio of particle to fibre diameter and the airstream velocity (Brown, 1993). An interception occurs if a particle is at a distance of less than its radius from the fibre surface (Sutherland & Chase, 2011). The limitation of interception efficiency is that the maximum efficiency is achieved when the ratio of particle to fibre diameter is equal to one, with the efficiency increasing with this

ratio up to one (Zhang, 2004). Based on this relationship, interception is an important mechanism for large diameter particles and particles with odd shapes resulting in large aerodynamic diameters.

$$I = \frac{r_p}{R} \tag{2.9}$$

where I is the interception parameter, r_p and R are the radius of particle and fibre respectively (Lee & Gieseke, 1980),

For a filter fibre in sphere, the interception efficiency, η_R around Stokes flow is defined as (Lee & Gieseke, 1980)

$$\eta_R = (1+I)^2\left[1 - \frac{3}{2(1+I)} + \frac{1}{2(1+I)^3}\right] \tag{2.10}$$

For a cylindrical fibre, the interception efficiency, η_R designated by Lamb's flow is given by (Chen, 1955; Langmuir, 1942; Lee & Gieseke, 1980)

$$\eta_R = \frac{(1+I)}{2L_H}\left[2\ln(1+I) - 1 + \frac{1}{(1+I)^2}\right] \tag{2.11}$$

where $L_H = 1 - \ln Re$ is the Lamb's hydrodynamic factor and Re is the Reynolds number.

(b) ***Impaction***

Inertial impingement or impaction usually happens on large and high density dust particles, where they travel in a straight line and hit at the filter media, despite following the air streamlines around the filter fibres (National Air Filtration Association, 1993). Impaction is driven by the inertia of the particle in the air stream and can be predicted based on the Stokes number, Stk, which is the ratio of the particle's stopping distance and the fibre's diameter (Brown, 1993).

$$Stk = \frac{d_p^2 \rho_p U_o C_n}{18 \mu d_f} \quad \textbf{(2.12)}$$

where d_p and ρ_p are the diameter and density of particle respectively, U_o is the free stream velocity, C_n is the Cunningham slip correction coefficient, μ is the fluid dynamic viscosity and d_f is the diameter of filter fibre.

As the Stokes number increases and so does the fibre efficiency, except when the ratio of particle to fibre diameter increase for small particles and thicker fibres where the efficiency will decrease (Zhang, 2004). Inertial impingement or impaction is a key mechanism of filtration for capturing dense particles.

Kuwabara's hydrodynamic factor for cylinder is used at the flow around the fibre, depending on the filter solidity,$\propto_f$ (Kuwabara, 1959).

$$Ku = -0.5 \ln \propto_f - 0.75 + \propto_f - 0.25 \propto_f{}^2 \quad \textbf{(2.13)}$$

The collection efficiency due to impaction, η_I is expressed as (Zhu et al., 2000)

$$\eta_I = \frac{2(1-\propto_f)\sqrt{\propto_f}}{Ku} Stk \left(\frac{d_p}{d_f}\right) + \frac{(1-\propto_f) \propto_f}{Ku} Stk^2 \quad \textbf{(2.14)}$$

(c) ***Diffusion***

Diffusion occurs at fine particles that are bombarded by air molecules in the Brownian movement. The erratic Brownian movement increases the probability of dust particles to collide at filter media and stay attached to them (National Air Filtration Association, 1993). Diffusional single fibre efficiency depends on the ratio of particle to fibre diameter and the Peclet and Kuwabara hydrodynamic factor dimensionless numbers (Zhang, 2004).

From the equation of convective diffusion, as the Brownian movement and diffusive deposition of particles increase with decreasing particle size, Peclet number,Pe is defined as

$$Pe = \frac{d_f U_o}{D} \tag{2.15}$$

where d_f is the diameter of filter fibre, U_o is the average air velocity inside the filter media whereas D is defined as the diffusion coefficient of particle. The Peclet number is used to determine the effect of convection and diffusion in particle transport (Billings, 1966; Chae, 2000).

Diffusion efficiency is the driving mechanism that allows a filter to capture particles with a diameter less than the porosity of the filter at a low air velocity, which can be a large component of a filter's overall efficiency. Hence, the diffusion efficiency is expressed by Brown (1993).

$$\eta_D = 2.9 Ku^{-1/3} Pe^{-2/3} \tag{2.16}$$

(d) ***Gravitational Settling***

Gravitational settling occurs when particles are removed from airstream because of gravitational force. Gravitational settling is proportional to the terminal settling velocity, V_S and inversely proportional to airstream velocity, U_O as described as a "settling parameter", G (Chen, 1955; Pich, 1973). The gravitational settling efficiency, η_G is equal to settling parameter, G as concluded by Ranz (1951) for a random cylinder transverse to the flow.

$$\eta_G = G = \frac{V_S}{U_O} = \frac{d_p^2 \rho_p g}{18 \mu U_O} \tag{2.17}$$

where d_p is the particle diameter, $\rho_p$is the density of the particle, g is the gravitational acceleration, and μ is the fluid viscosity.

Another important factor for gravitational settling is the direction of the airflow Upward airflow results in an efficiency of zero while downward airflow would result in a non-zero efficiency. With horizontal airflows with a velocity greater than 0.01 ms^{-1}, the efficiency of gravitational settling for moderate to small particles is negligible, except for very large particles in airflows with low velocity (Zhang, 2004). Gravitational settling can be an efficient mode of filtration, though the requirements in velocity are unrealistic for many filters leading to gravitational settling commonly being neglected for single fibre and overall filter efficiency predictions.

(e) ***Straining***

Straining is the simplest air filter particle capture mechanism, typically happening when a dust particle is smaller than the distance between filter media fibres (National Air Filtration Association, 1993). Straining is not an efficient way to remove fine particles and mainly occurs on the filter media surface. Figure 2.4 depicts the straining mechanism.

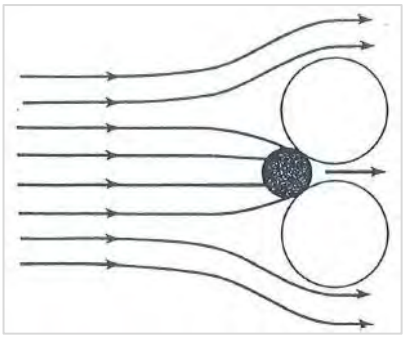

Figure 2.4: Straining (National Air Filtration Association, 1993)

2.2.2.2 Electrostatic Mechanism

The electrostatic mechanism of filtration is a simple mechanism, although sometimes it is difficult to predict performance. Electrostatic mechanism occurs when the filter fibre

is charged or is placed under an electric field and attracts the charged or neutral particles (Brown, 1993; Wang, 2001). Table 2.1 summarizes different electrostatic expression based on various situations (Liu et al., 2017; Wang, 2001).

Table 2.1: Electrostatic Expressions

Particle	Source of Electric Field around the fibre	Electrostatic Expression
Net charge	By external electric field	$N_E = q\bar{E}$
Induced Dipole	By external electric field	$N_E = \frac{\pi\varepsilon_0 d_p^3}{4}\left(\frac{\varepsilon_p - 1}{\varepsilon_p + 2}\right)\nabla\lvert\bar{E}\rvert^2$
Net charge	By the charge on particle	$N_E = \frac{1}{16\pi\varepsilon_0}\left(\frac{\varepsilon_f - 1}{\varepsilon_f + 1}\right)\frac{q^2}{(r - r_f)^2}$
Net charge	By the charged fibre	$N_E = \frac{qQ_c}{2\pi\varepsilon_0 r}$
Induced Dipole	By the charged fibre	$N_E = \frac{d_p^3}{8\pi\varepsilon_0}\left(\frac{\varepsilon_p - 1}{\varepsilon_p + 2}\right)\frac{{Q_c}^2}{r^3}$
Net Charge	By line-dipole induced in fibre with surface charge distribution $\sigma(\theta) = \sigma\cos\theta$	$N_E = \frac{q\sigma d_f^2}{4\varepsilon_0(1 + \varepsilon_f)r^2}$
Induced Dipole	By line-dipole induced in fibre with surface charge distribution $\sigma(\theta) = \sigma\cos\theta$	$N_E = \frac{\pi d_p^3}{16\varepsilon_0}\left(\frac{\varepsilon_p - 1}{\varepsilon_p + 2}\right)\frac{\sigma^2 d_f^4}{(1 + \varepsilon_f)^2 r^5}$

Legends:

$\boldsymbol{\varepsilon_0}$	Permittivity of free space	ε_p	Dielectric constant of particle	ε_f	Dielectric constant of fibre
$\boldsymbol{d_p}$	Diameter of particle	d_f	Diameter of fibre	r_f	Radius of fibre
$\boldsymbol{q}$	Net charge on particle	Q_c	Net charge on unit length of fibre	σ	Surface charge density
$\boldsymbol{r}$	Radial distance from fibre axis	θ	Polar angular coordinate	E_0	Externally applied electric field
$\bar{\boldsymbol{E}}$	Electric field with components of E_r and E_θ	$E_r = \left[1 + \left(\frac{\varepsilon_f - 1}{\varepsilon_f + 1}\right)\frac{r_f^2}{r^2}\right]E_0\cos\theta$		$E_\theta = \left[1 + \left(\frac{\varepsilon_f - 1}{\varepsilon_f + 1}\right)\frac{r_f^2}{r^2}\right]E_0\sin\theta$	

Due to the lack of knowledge of the charge of particles, this mechanism is typically negligible for prediction purposes, although it is known to increase filter efficiency (Zhang, 2004). The common downside to electrostatic mechanisms of charged filters is that the media is known to lose its charge with time and must be periodically charged to

maintain filtration efficiency levels and that particles with the same charge as the filter media will decrease the overall efficiency (Zhang, 2004).

2.2.3 Factors affecting Air Filter Performance

2.2.3.1 Air Velocity

If the velocity approaching the filter is not uniform, this non-uniformity can bring significant effects on clean filter performance on the efficiency. The air velocity distribution can be affected by filter housing geometry (Chambers et al., 2001). The velocity distribution has also been studied by Kang et al. (2020) using a particle image velocimetry (PIV). The experimental results obtained using PIV are similar to the CFD simulated results. They found that the pleat geometry and the pleat stabilizing technique are affecting the air velocity distributions and should be taken into consideration in flow effect estimation. As discussed earlier in Equation (2.4), Del Fabbro et al. (2002) had also developed a model in relating filtration velocity and other parameters with the initial pressure drop, ΔP_0.

2.2.3.2 Filter Media Geometry

The pressure drop across an air filter can be affected by the filter geometrical properties. Théron et al. (2017) studied the geometrical configuration of down-sized pleated filters (120×120 mm^2) according to standard EN 779-2012 and concluded that the pressure drop can be lowered by reducing the pleat height and increasing pleat width, which is toward a flat geometry. This happens because of the narrowness of the airflow inlet across the filter media. With a smaller pleat width, the air is forced to pass through the smaller filter inlet, causing a large differential pressure across the filter (Wiegmann et al., 2007).

Park et al. (2012) studied the effect of pleat geometry on a pleated cartridge filter and found that the pleat ratio is 1.48 to obtain an optimum pressure drop and the highest efficiency while Li et al. (2019) found that the pleat ratio should be kept below 1.59 for

an effective filtration. Lo et al. (2010) concluded that the pleat ratio is affected by the cleaning mode for filter cartridges with pulse-jet cleaning. Kim and Lee (2019) found that the pleat ratio of 2.21 causes the maximum effective filtration area and filter cleaning efficiency.

2.3 Dust Loading Behaviour of an Air Filter

Besides the initial performance of the clean filter, it is important to consider the behavior of an air filter with dust accumulation. Generally, the pressure drop across the filter will increase with loaded dust while the collection efficiency of loaded filter media will improve (Wang et al., 2016). The amount of dust that an air filter is able to hold is important to determine the lifespan of the air filter application.

As shown in Figure 2.5, there are three different phases of dust loading process (Brown, 1993):

1. Depth filtration regime. The particles are accumulated inside the filter media. The pressure drop increases gradually with increasing dust collected. The particles are retained within the filter media by Van-der-Waals forces (Huurdeman & Banzhaf, 2006).
2. Transitional regime. Most of the void space in the media is filled with dust. Apparent fibre shape changes due to loaded dust (Kanaoka, 2019), causing the pressure drop increases at a higher rate than that of depth filtration regime.
3. Dust cake region / Surface filtration regime. The dust cake starts to build on the filter surface and the pressure drop increases significantly in this region.

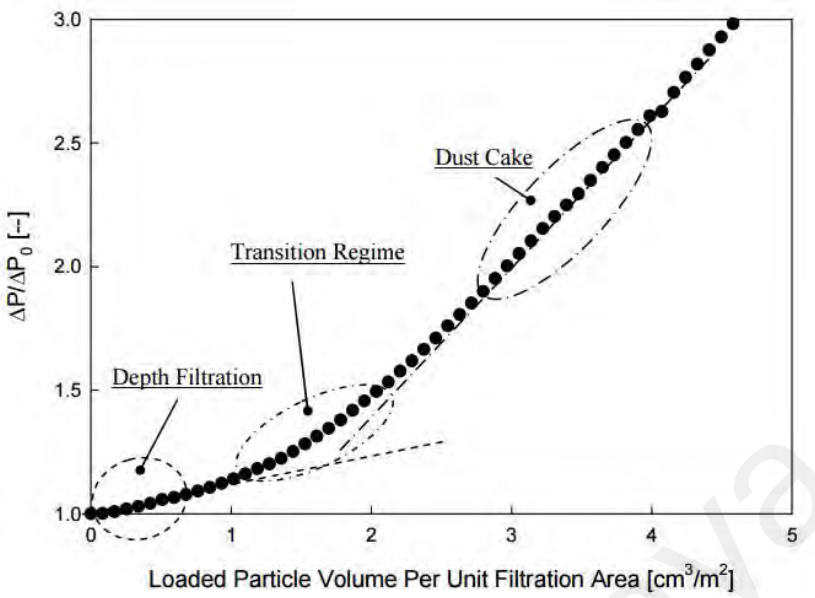

Figure 2.5: Dust Loading Phases (Zhang, 2004)

2.3.1 Filtration Performance Parameters

2.3.1.1 Pressure Drop across Dust Cake

From Darcy's Law, the total pressure drop, ΔP across filter can be described as:

$$\Delta P = \Delta P_0 + \Delta P_c \quad \textbf{(2.18)}$$

$$\Delta P_0 = K_1 V_f \quad \textbf{(2.19)}$$

$$\Delta P_c = K_c V_f W \quad \textbf{(2.20)}$$

$$S = \frac{\Delta P_c}{V_f} = K_c W \quad \textbf{(2.21)}$$

where ΔP_0 is the pressure drop across a clean filter as discussed in Section 2.2.1.1; K_1 depends on the physical characteristics of filter media such as media porosity; ΔP_c is the pressure drop across dust cake; K_c is the dust cake resistance coefficient; V_f is the filtration velocity; W is the dust mass deposited per unit filter area and S is the dust cake drag coefficient.

2.3.1.2 Dust Holding Capacity

Dust holding capacity, which is also known a test dust capacity, is defined as the total weight of dust a filter can capture, at the same time maintaining the filtration efficiency until reaching the rated final pressure drop (Legg, 2017). Dust holding capacity is also used to predict the lifespan of a filter. The dust holding capacity is calculated by deducting the amount of dust left uncaptured by the test filter and increment of mass of the final filter downstream from the total dust fed into the filter. The capability of the collection of the test dust is called arrestance.

2.3.1.3 Arrestance

Arrestance is defined as the ability of a test filer to capture synthetic dust and usually used to represent the filtration efficiency of a coarse filter (Zhang, 2004). The filtration efficiency is the ability of a filter to remove microscopic particles. As for the coarse filter where is the efficiency is low, the arrestance is used to measure the ability of the coarse filter to remove relatively larger particles. In the air filter test standards, synthetic dust, which is relatively bigger in particle size compared to fine particles generated from aerosol, is used to determine the test filter arrestance. The arrestance, A is defined as

$$A = \left(1 - \frac{m_A}{M_A}\right) \times 100\% \tag{2.22}$$

where m_A is the mass of dust which passes through the test filter and M_A is the mass of dust loaded to the test filter.

2.3.2 Factors Affecting Filtration Performance of Dust-loaded Filters

This section discusses on the different factors affecting the filtration performance when a filter is loaded with dust.

2.3.2.1 Fibre Media Characteristics

The filtration performance is strongly dependent on the fibre media characteristics such as media porosity, the thickness of the filter media, and the fibre media arrangement. The purpose is to prolong the clogging time of the filter media with slow increase in pressure drop (Huurdeman & Banzhaf, 2006).

2.3.2.2 Particle Characteristics

Chen et al. (2014) studied the effect of different test dust which are 325 mesh talcum powder, ASHRAE dust, and ISO A2 dust on the dust holding capacity and cleaning effectiveness using experimental set-up according to EN 779:2012 with pulse-jet cleaning system. The results recommended ASHRAE dust in filter testing due to its size distribution and it can simulate the actual effects of atmospheric aerosol.

Lee et al. (2020) found that the pressure drop is higher at a same amount of loaded mass for bigger geometric volume particles due to particle deposition via inertial impaction. This can be explained by Stokes number in Equation (2.12). As the Stokes number is proportional to the square of particle size, the dust cake of larger A2 fine dust particles is more compressed than that of A1 ultrafine dust. This causes the A2 dust cake, which is made up of larger dust particle size, to be less permeable, causing a higher pressure drop.

Cheng and Tsai (1998) investigated the effect of dust particle shape on the dust cake resistance. Irregular particles which are irregular limestone and SAE fine dust have larger dust cake porosity compared to spherical fly ash particles. The more random arrangement causes a lower pressure drop across dust cake.

Saleh et al. (2014) found out that the filter service life is longer when monodispersed particles are used compared to the polydisperse aerosols with the same mass flux. An

analytical equation was introduced by Endo et al. (1998) to study the effect of polydispersity and shape factor on dust cake formation:

$$\frac{\Delta P_c}{\mu u_S H}\frac{d_{vg}^2 \exp\left(4\ln^2\sigma_g\right)}{K_S} = \frac{18(1-\varepsilon)\, v(\varepsilon)}{\varepsilon^2} \tag{2.23}$$

The equation is simplified for monodisperse and spherical particles:

$$\frac{\Delta P_c d_p^2}{\mu u_S H} = \frac{18(1-\varepsilon)\, v(\varepsilon)}{\varepsilon^2} \tag{2.24}$$

where ΔP_c is the dust cake layer pressure drop; μ is the air viscosity; $u_S = u_i\varepsilon$ is the superficial velocity; u_i is the interstitial velocity; ε is the porosity; d_{vg} is the geometric mean diameter of d_v; d_v is the volume equivalent diameter; σ_g is the geometric standard deviation; K_S is the dynamic shape factor and $v(\varepsilon)$ is the void function.

2.3.2.3 Presence of External Electric Field

A simulation of particle deposition is carried out by Park and Park (2005) on filter fibre in studying the effect of external electric field. Particles deposit in a linear dendritic form on a fibre with an external electric field, causing more porous structure due to electrostatic forces and therefore a lower pressure drop.

Lee et al. (2020) has proven experimentally that the dust holding capacity increases with the presence of the external electric field. The cake porosities of the filter are higher with an external electric field, which eventually increases the filter lifespan.

2.3.2.4 Dust Loading Rate

At increasing dust loading rate, the pressure drop across filter media decreases with a same mass of dust loaded at unit filter area. At low dust loading rate, the particles move with more intra-particles spaces and this allows more time for the particles to arrange themselves on the media surface without the interference of incoming particles, forming

a denser cake micro-structure and higher pressure drop across the dust cake (Wang et al., 2016).

2.3.2.5 Air Velocity

The filtration velocity contributes to the dust cake resistance. The relationship between the two factors can be described as (Dennis & JA, 1981):

$$K_c = fV_f^n \tag{2.25}$$

where K_c is the dust cake resistance coefficient; V_f is the filtration velocity; f and n are constants. K_c increases when the particle size increases or when the filtration velocity increases. This happens due to the irreversible compaction on the dust cake and smaller dust cake porosity at a higher filtration velocity, causing a larger K_c value and hence higher airflow resistance (Cheng & Tsai, 1998).

The relationship between the dust cake porosity and the filtration superficial velocity is represented by

$$1 - \varepsilon = fV_f^n \tag{2.26}$$

where ε is the dust cake porosity (Choi et al., 2002).

Théron et al. (2017) studied the effect of the velocity profiles on the pleat geometry influencing the initial local collection efficiencies. Schousboe (2017) also investigated the maximum local velocity numerically to determine the filter pleat geometry. Alderman et al. (2008) has studied the influence of media on the filter efficiency of the HEPA filters. The efficiency decreases with increasing face velocity due to the reduced retention time of particles in the nanofibre.(Leung et al., 2010) Saleem and Krammer (2007) found that the specific resistance and density of dust cake are higher at a higher filtration velocity when the dust concentration is constant for bag filters.

2.3.3 Pleat Geometry

Li et al. (2019) studied the effect of pleat geometry on small-scale pleats experimentally and concluded that the pleat ratio should be below 1.59 to achieve a good filtration effect. The influence of the pleat ratio is more pronounced on the pressure drop as the superficial velocity increases. Teng et al. (2022) found that the effective filtration area increases with a pleat ratio of 2.22 to 3.70. A larger pleat ratio can allow the larger dust particles to deposit at the pleat corners more easily. Park et al. (2012) also found that the pleat configuration at a pleat ratio of 1.48 can result in the highest cleaning efficiency. The aging of the filter can be decelerated by increasing the pleat count, which is concluded by Fotovati et al. (2012) using numerical simulation on V-shaped pleats.

Théron et al. (2017) investigated a lab-scale pleated fibrous filter and summarised that the pressure drop could be reduced with a pleated shape toward a flat geometry. Persaud et al. (2021) concluded that the two pleat conditions to obtain optimum filtration performance on a cartridge filter are using a longer pleat depth to increase filtration area and using an optimal number of pleats, which is consistent with the findings of Maddineni et al. (2019).

2.3.3.1 Humidity

The pressure drop across the air filter can be reduced at humid airflow. This is due to the adsorption of water contained in the air on the dust cake surface. The deposition of dust is restructured which leads to a more organized dust cake with lower pressure drop; thus the time required to reach the final resistance is longer. A pressure drop across the dust cake of a clogged filter, ΔP_c in term of air humidity is described as (Joubert et al., 2011):

$$\Delta P_c = \mu \frac{\Delta m_s v_f}{s_f} \sum_{k_n=1}^{N} K_c\left(t_f - k\Delta t\right) \tag{2.27}$$

where μ is the air dynamic viscosity; Δm_s is the particle mass in each cake layer; v_f is the filtration velocity; s_f is the filtration surface area; k_n is the variable of number of cake layers; N is the number of cake layers; K_c is the specific cake resistance; t_f is the total filtration time and Δt is the time required for the cake formation of each layer.

2.4 Energy and Operational Costs of Air Filters

2.4.1 Energy Calculation Method

It is important to consider the energy consumption calculation of the air filters. All three standards have no specification on the calculation method on energy an air filter will consume until the final resistance is reached. There are two energy efficiency classification methods have been introduced.

2.4.1.1 Key Energy Performance

The first method is the "key energy performance" (kep) in Europe (Mayer et al., 2008) and is expressed as

$$kep = \frac{-100 \log (1 - \overline{FE})}{\overline{\Delta P} - C} \tag{2.28}$$

$$\overline{\Delta P} = \frac{1}{M} \int_0^M P(m) dm \tag{2.29}$$

where $\overline{FE}$ is the average filtration efficiency at a particle size of 0.4μm at 0.944m^3/s which is obtained from EN 779 test; $\overline{\Delta P}$ is the average pressure drop of air filter in Pa; $P(m)$ is the instantaneous pressure drop across filter; M is the total mass of dust loading in g, m is the variable of loaded dust, and C is an empirical constant. For energy efficiency classification of the air filters with ASHRAE 52.2 test, a similar method can be used by defining $\overline{FE}$ as the average efficiency according to minimum efficiency reporting value (MERV) (Sun & Woodman, 2009).

2.4.1.2 Wattage Method

The Wattage method determines the power of energy needed to overcome the airflow resistance across the air filter. This method does not take into account of filtration efficiency and the energy consumption is defined as

$$E = \frac{Q \cdot \overline{\Delta P} \cdot t}{\eta \cdot 1000} \tag{2.30}$$

where E is the energy consumption in kWh; Q is the airflow rate in m^3/s; t is the operation time in hour; η is the system energy efficiency, which is a product of motor, fan and transmission efficiencies and $\overline{\Delta P}$ is the average pressure drop of air filter in Pa. $\overline{\Delta P}$ is determined as shown in the first method(Sun & Woodman, 2009).

The Wattage method using the results obtained from EN 779 is published in Eurovent 4/21-2014 (Eurovent, 2014). Eurovent 4/21-2014 was the guideline published in Europe to define a method of air filter classification in consideration of energy efficiency. This guideline makes use of the test result from EN 779 to further analyse the energy consumption of air filters. After EN 779 is replaced by ISO 16890 in Europe since 2016(Courtey, 2017), the calculation method is amended according to ISO 16890 classification and the latest version is Eurovent 4/21-2018 (Eurovent, 2018).

2.4.2 Filter Life Cycle and Operational Cost Functions

The life cycle cost and operational cost of air filters are the important factors in selecting suitable air filters in different applications. Some manufactures have compared the effect of total filtration area such as the number of pockets of air filters on the annual energy consumption by developing calculation software. Energy consumption analysis and comparison are done between filters and recommendations are provided from the software (Kimberly-Clark, 2013; Mann-Hummel).

Faulkner (2001) had estimated the costs of different filters used in the HVAC system. The cost of air filters varies for different designs depending on applications and is estimated by

$$Cost\ per\ unit\ air\ flow = \frac{Filter\ Cost + Labor\ Cost\ per\ Filter\ Installation + Energy\ Cost}{Filter\ Lifetime\ \times Air\ Flow\ Rate} \quad \textbf{(2.31)}$$

$$Filter\ lifetime = \frac{Dust\ Holding\ Capacity}{Arrestance \times Inlet\ Particle\ Concentration \times Air\ Flow\ Rate} \quad \textbf{(2.32)}$$

A change in pressure drop is a change of operating point on the fan curve that affects the power consumption of a fan (Zhai & Johnson, 2017). A model is developed by Montgomery et al. (2012) in predicting the energy efficiency and annual operation cost of HVAC air filters at a constant airflow rate using ASHRAE MERV rating filters. The annual cost of operation is the most affected by the dust concentration in air and electricity costs. The annual cost of operation can be reduced if the air filter is changed when it reaches a pressure drop corresponding to minimum annual cost instead of following the final resistance recommended by manufacturers.

Noh and Hwang (2010) studied the effect of ventilation rate and filter performance on the indoor particle concentration and the fan power consumption in a residential housing unit. The power consumption is not much affected by air filter at low ventilation rate as the pressure drop across a filter at a low airflow rate is relatively small compared to the pressure drop across ducting and heat exchanger. The filter performance is better at low ventilation rate.

A predictive cost function for HVAC energy consumption in terms of ventilation and filtration was developed by Ben-David and Waring (2018)

$$J = J_E + J_{IAQ} + J_{filter} \quad \textbf{(2.33)}$$

where J is the pre-occupant cost function; J_E, J_{IAQ} and J_{filter} are costs due to energy consumption, indoor exposure due to PM2.5 and ozone of outdoor origin as well as costs for filter purchase and replacement respectively. Derivatives can be done with respect to ventilation rate or filtration to analyse the respective effect on the cost function.

2.5 Computational Fluid Dynamics

Computational fluid dynamics (CFD) can efficiently the performance of the air filters. It saves costs and time as the full-scale experiments need not be carried out after the simulation results can correlate with experimental results. Besides, flow study within the filter media is hardly achievable by experimental methods (Cai, 1993). A lot of research has been adopting CFD simulation in air filtration research. The purpose of the research and respective models used have been summarized in this section.

2.5.1 Turbulence Models

When solving fluid flow problems with CFD, turbulence behaviours of airflow should be handled carefully during the calculation. For a turbulent flow regime, the Navier-Stokes's equations are modified to consider the fluid interaction with the fluctuating velocity fields due to the turbulence. Turbulence models are introduced in CFD to resolve turbulence fluid flow. There are many types of turbulence models and no one turbulence model is generally accepted to solve every type of problem (Fluent, 2006). Hence, when choosing the turbulence model in CFD analysis, the physics of the flow, level of accuracy required, computational resources, and time have to be considered to achieve an efficient and accurate solution. The turbulence models can be generally categorized into three groups: Reynolds-Averaged Navier-Stokes (RANS), Large Eddy Simulation (LES), and Direct Numerical Simulation (DNS).

Reynolds-Averaged Navier-Stokes (RANS) equations are the most common and oldest approach in turbulence modelling. RANS equations represent the transport equations for the mean flow quantities only, with all the scales of the turbulence being modelled. The computational effort is greatly reduced by permitting a solution for the mean flow variables. The RANS models can be closed in two ways, one is via the Boussinesq hypothesis (Eddy Viscosity Models) and another is via the transport equations for Reynolds stresses (Reynolds-Stress Models) (Fluent, 2006). The governing equations consist of no time derivatives if the mean flow is steady. A steady-state solution can be obtained economically. For an unsteady case, the computational advantage is more obvious as the time step will be determined by the global unsteadiness in the mean flow rather than by the turbulence. Hence, here comes the unsteady Reynolds-Averaged Navier-Stokes (URANS). As long as the time scale of the changes in the mean is large compared to the time scales of the turbulent motion containing most of the energy, the turbulence models used to close the equations are valid. RANS approach is greatly used for practical engineering calculation and industrial fluid simulation due to its robustness. Models such as k-epsilon, k-omega, Spalart-Allmaras are the examples of RANS approach.

Large Eddy Simulation (LES) is an approach in which the large eddies in the turbulence flow are computed in a time-dependent simulation through a set of filtering operations. Eddies that are smaller than the size of the filter will be removed and their effect modelled using sub-grid scale models. During the time-dependent simulation in LES, the data of the mean flow quantities, which are generally most engineering interest will be gathered. Due to this method, the computational cost will greatly reduce. LES requires higher computational resources than the RANS method, but yet far cheaper than Direct Numerical Simulation (DNS).

Direct Numerical Simulation (DNS) captures all the relevant scales of turbulent motion. The Navier-Stokes equations are numerically solved without any turbulent model. The grid size for DNS needs to be very fine to resolve the whole range of spatial and temporal scales of the turbulence. The computational cost for DNS is extremely high as it requires very large memory storage and processing units. The computational cost is proportional to Re^3 and hence it is intractable for flow with complex geometries and high Reynolds number.

2.5.1.1 The Shear-Stress Transport (SST) k-ω Model

There are 2 types of k-ω Turbulence Model which are standard k-ω model and shear-stress transport (SST) k-ω model. SST k-ω model differs from the standard model as follow:

- Shear-stress transport k-ω model has the gradual change from the standard k-ω model in the inner region of the boundary layer to a high Reynolds number version of the k- ε model in the outer part of the boundary layer.
- Modified turbulent viscosity formulation to account for the transport effects of the principal turbulent shear stress.

The standard k-ω model is an empirical model based on model transport equations for the turbulence kinetic energy, k, and the specific dissipation rate, ω, which is the ratio of ε to k. The standard k-ω model in FLUENT incorporates modifications for low-Reynolds number effects, compressibility, and shear flow spreading. It predicts free shear flow spreading rate that is in close agreement with measurements for far wakes, mixing layers and plane, round and radial jets. Hence, it is suitable for wall-bounded flows and free shear flows (Fluent, 2006).

In the SST k-ω model, it effectively blends the robust and accurate formulation of the k-ω model in the near-wall region with the free stream independence of the k-ε model in the far field. The SST k-ω model is similar to the standard k-ω model, but with some refinements as follow:

The standard k-ω model and the transformed k-ε model are both multiplied by a blending function and both models are added together. The blending function is designed to be one in the near-wall region, which activates the standard k-ω model and zero away from the surface, which activates the transformed k-ε model.

The SST model incorporates a damped cross-diffusion derivative term in the ω equation. The definition of the turbulent viscosity is modified to account for the transport of the turbulent shear stress. The modelling constants are different. With the refinements above, the SST k-ω model is more accurate and reliable for a wider class of flows such as adverse pressure gradient flows, airfoils, and transonic shock waves. The k and ω in the SST k-ω model can be obtained from the following transport equations:

$$\frac{\delta}{\delta t}(\rho k) + \frac{\delta}{\delta x_i}(\rho k u_i) = \frac{\delta}{\delta x_j}\left[\left(\mu + \frac{\mu_t}{\sigma_k}\right)\frac{\delta k}{\delta x_j}\right] + G_k - Y_k + S_k \qquad \textbf{(2.34)}$$

$$\frac{\delta}{\delta t}(\rho \omega) + \frac{\delta}{dx_i}(\rho \omega u_i) = \frac{\delta}{dx_j}\left[\left(\mu + \frac{\mu_t}{\sigma_\omega}\right)\frac{\delta \omega}{\delta x_j}\right] + G_w - Y_w + D_w + S_\omega \qquad \textbf{(2.35)}$$

where G_k represents the generation of turbulence kinetic energy die to the mean velocity gradients; G_ω is the generation of ω; Y_k and Y_ω represent the dissipation of k and ω due to turbulence; D_ω represents the cross diffusion term while S_k and S_ω are user-defined source terms.

2.5.2 Pressure Drop and Velocity Field across a Clean Filter

There is a lot of research done in simulating the initial pressure drop of the air filter and velocity profile across the filter using CFD simulation as summarized in Table 2.2. Most of the simulation adopted a 2D domain and one pleat geometry. A porous zone is used to represent the filter media in macroscale simulation. As for the viscous model, various turbulence models are used in previous works such as Detached Eddy Simulation (DES), RNG k-ε model, and RSM model which are proven to accurately predict the initial pressure drop and velocity profile.

Table 2.2: Summary of Input Parameters of Previous Works

References	Purpose of studies	Filter Media Properties	Simulation Domain	Flow model and properties	Outcomes and remarks
Feng et al. (2014)	To predict airflow and pressure drop of a pleated filter	Rectangular pleat $P_w = 50mm$ $h = 50mm$ $B = 8.33 \times 10^{-12} m^2$ $Z = 0.30mm$	- 2D domain - $V_{inlet} = 0.13\ m/s$	Turbulence model - Standard k-ε model - Low Re k-ε model - v2f model - Large Eddy Simulation (LES) models - Detached Eddy Simulation (DES) SIMPLE algorithm in pressure correction equation. Pressure discretization - standard first order upwind Others – second order upwind	- v2f model, LES and DES (Spalart-Allmaras) models accurately predict the pressure drop and flow distribution in pleated filters. - As LES requires high computer capacity, DES (Spalart-Allmaras) and the v2f models are recommended.

Table 2.2, continued

References	Purpose of studies	Filter Media Properties	Simulation Domain	Flow model and properties	Outcomes and remarks
Théron et al. (2017)	To study the pleat geometry on the pressure drop and velocity field	Triangle pleat (pocket filter) $P_w = 11.5, 23.0\ mm$ $h = 20, 40\ mm$ $B = 2.0 \pm 0.5 \times 10^{-9} m^2$ $C = 3344 \pm 1000\ m^{-1}$	- 2D domain - Half pleat - $V_{inlet} = 0.019 - 0.81\ m/s$	Turbulence model (Re=1550 - 45 000) - Standard k-ε model - Reynolds stress model (rsm) Laminar flow in porous media	Both turbulence models give similar pressure drop prediction
Jeon et al. (2020)	To predict the pressure drop through two-stage filtration	$Z = 0.50 - 0.65\ mm$ $B = 10^{-11}\ m^2$	- Triangular mesh (2D), Tetrahedral mesh (3D) - Mesh growth rate = 1.05 - $V_{inlet} = 0.5, 0.75, 1.0\ m/s$	Laminar flow model (Re < 1)	- The relative error of 2D and 3D simulation is small. Pressure drop is not affected by mesh number. - The CFD results agree well with experimental results for both single and two-stage filtration.
Wiegmann et al. (2007)	To show the effect of pleat shape and filter media on pressure drop	$B = 1.1 \times 10^{-10}, 2.5 \times 10^{-11}\ m^2$ $Z = 0.5mm$ $h = 14.07, 8.07\ mm$	- 3D domain	N/A	Precise pressure prediction eases the filter design process.
Chen et al. (1995)	To optimize the pleated filter design	Rectangular pleat	- 2D domain - Half pleat	Laminar flow Flow through filter: Darcy-Lapwood-Brinkman mode	N/A
Schousboe (2017)	To study the velocity distribution across pleat geometries.	Rectangular pleat Pleat density = 6.5, 7, 7.5,8, 8.5 PPI $h = 0.5, 0.75, 1.0\ inches$ $B = 1.23 \times 10^{-12} m^2$ $Z = 0.0145"$	- 2D domain - $V_{inlet} = 10\ ft/min$	Laminar flow	The filtration velocity is non-uniform along the pleat.

Table 2.2, continued

References	Purpose of studies	Filter Media Properties	- Simulation Domain	Flow model and properties	Outcomes and remarks
Fu et al. (2014)	To study pressure drop of pleated air filters	Triangular pleat $B = 11.89 \times 10^{-12} m^2$ $Z = 0.406mm$	- 2D domain - $-V_{inlet} = 0.6\ m/s$	Turbulence model - Standard k-ε model - RNG k-ε model - Reynolds stress model (RSM)	- Standard k-ε model showed greater deviation from experimental results. - RNG k-ε model and RSM model agree with experimental results. - RSM model is fitted better than RNG k-ε model.
Cai (1993)	To study the air flow of filters	Triangular pleat $B = 10^{-8}\ to\ 10^{-6}\ m^2$ $C = 1147.0\ m^{-1}$	- 2D domain $V_{inlet} = 1.0, 5.0\ m/s$	Laminar flow within porous media Turbulence model for flow domain - Standard k-ε model	N/A
Del Fabbro et al. (2002)	To model air flows and pressure d	Rectangular and triangular pleats $h = 27 - 48mm$	- 2D domain	Laminar flow	N/A

P_w = pleat width; h = pleat height; B = media permeability; C = media inertial resistance; Z = media thickness; V_{inlet} = duct air velocity

2.5.3 Dust Loading Simulation

The Eulerian model considers the particles as a continuous phase variable. The effect of particle motion on the airflow is neglected. The Lagrangian method tracks the particle trajectories and is used to model particle motion. These two models are widely used in the literature in simulating the instantaneous pressure drop across the filters which is summarized in Table 2.3.

Table 2.3: Review of Dust Loading Simulations

References	Purpose of studies	Filter Media Properties	Dust Deposition Modelling	Flow model and properties	Outcomes and remarks
Feng and Long (2016)	To model unsteady filtration performance of pleated filter	Rectangular pleat	Lagrangian method Transient particle deposition Eulerian model 2D domain without gravitational force $d_p > 0.5\mu m$, assuming all particles captured on media (100% efficiency)	DES-SA turbulence model Filter media & cake layer – porous zone SIMPLE algorithm to couple the pressure and velocity	Both Lagrangian and Eulerian methods provide accurate results with acceptable error. Eulerian model is used as the computing is faster.

Table 2.3, continued

References	Purpose of studies	Filter Media Properties	Dust Deposition Modelling	Flow model and properties	Outcomes and remarks
Fotovati et al. (2011)	To model instantaneous pressure drop during dust loading (cake filtration)	Rectangular and triangular pleat $h = 25.4\ mm$ $Z = 0.38\ mm$	- Lagrangian particle tracking method - Steady state flow field - Relatively large particles cannot pass through media, only deposition - $d_p = 3, 10\ \mu m$ - Particle rebound neglected - 160 batches of particles (a pseudo-time step each) - $A = 2 \times 10^{13}\ particles/m^3$	2D domain $V_{inlet} = 0.2, 1.0\ m/s$	N/A
Fotovati et al. (2012)	To simulate the particle deposition inside media (depth filtration)	Triangular pleat $h = 25.4\ mm$ $Z = 0.7\ mm$ $\alpha = 5\ \%$ $d_f = 15\ \mu m$	- Lagrangian approach - Discrete Phase Model (DPM) - $A = 2 \times 10^{9}\ particles/m^3$	2D domain Laminar flow Filter media as porous zone $V_{inlet} = 0.05, 0.5\ m/s$	

P_w = pleat width; h = pleat height; B = media permeability; C = media inertial resistance; Z = media thickness; V_{inlet} = duct air velocity; d_p = particle size; A = Aerosol concentration; α = solid volume fraction (SVF); d_f = fibre diameter

2.6 Final Resistance

The final resistance of air filter is defined as the resistance to airflow up to which the filtration performance is measured to determine the average arrestance and test dust capacity according to ISO 16890:2016 Air Filters for General Ventilation (ISO, 2016b). The final resistance is a reference point for the users to replace the filter.

The final resistance value is defined differently in various air filters for general ventilation standards which are EN779:2012, ASHRAE 52.2:2017, and ISO 16890:2016. The final resistance defined for different classes of air filters by various standards is summarized in Table 2.4. The defined value of final resistance in test standards is used to determine the filter performance according to respective standards for filter classification and comparison.

Table 2.4: Final Resistance Defined by Test Standards (ASHRAE, 2017; EN, 2012; ISO, 2016b)

	EN 779:2012	ASHRAE 52.2:2017	ISO 16890:2016
Final Resistance	250 Pa (Filter Class: G1 – G4)	350 Pa (All Filter Classes)	200 Pa (Filter Class: ISO Coarse)
	450 Pa (Filter Class: M5 – F9)		300 Pa (Filter Class: ISO ePM1, 2.5 & 10)

In actual application, the final resistance or the maximum operating resistance to airflow of air filter is normally recommended by the manufacturer (ISO, 2016b). The final resistance is normally recommended to be two times the initial resistance or the pressure drop of a clean filter as recommended in ASHRAE 52.2:2017 (ASHRAE, 2017; Nassif, 2012).

2.7 Summary of Literature Review

The final resistance of the air filter is important to be determined according to different filter designs, media, or applications. If a filter is over-specification and ruptures before the recommended final resistance, the indoor air quality of a building will be drastically affected. The sudden increase of static pressure across the HVAC system as a result of filter ruptures will be disastrous to the system components.

Besides, the energy consumption of the air filter is well depending on the final resistance. As discussed above, the air filter is recommended to be replaced before the

recommended final resistance to optimize the annual operation cost of the HVAC system (Montgomery, 2015). One important factor which affects the energy consumption and lifespan of air filters significantly is the rate of increase in pressure drop of the air filters. The factors affecting the initial pressure drop and pressure drop during dust loaded have been reviewed and it is important to consider the relationship of these factors in setting an optimum final resistance of the air filters. The factors affecting the pressure drop and factors contributing to the life cycle cost are shown in Figure 2.6.

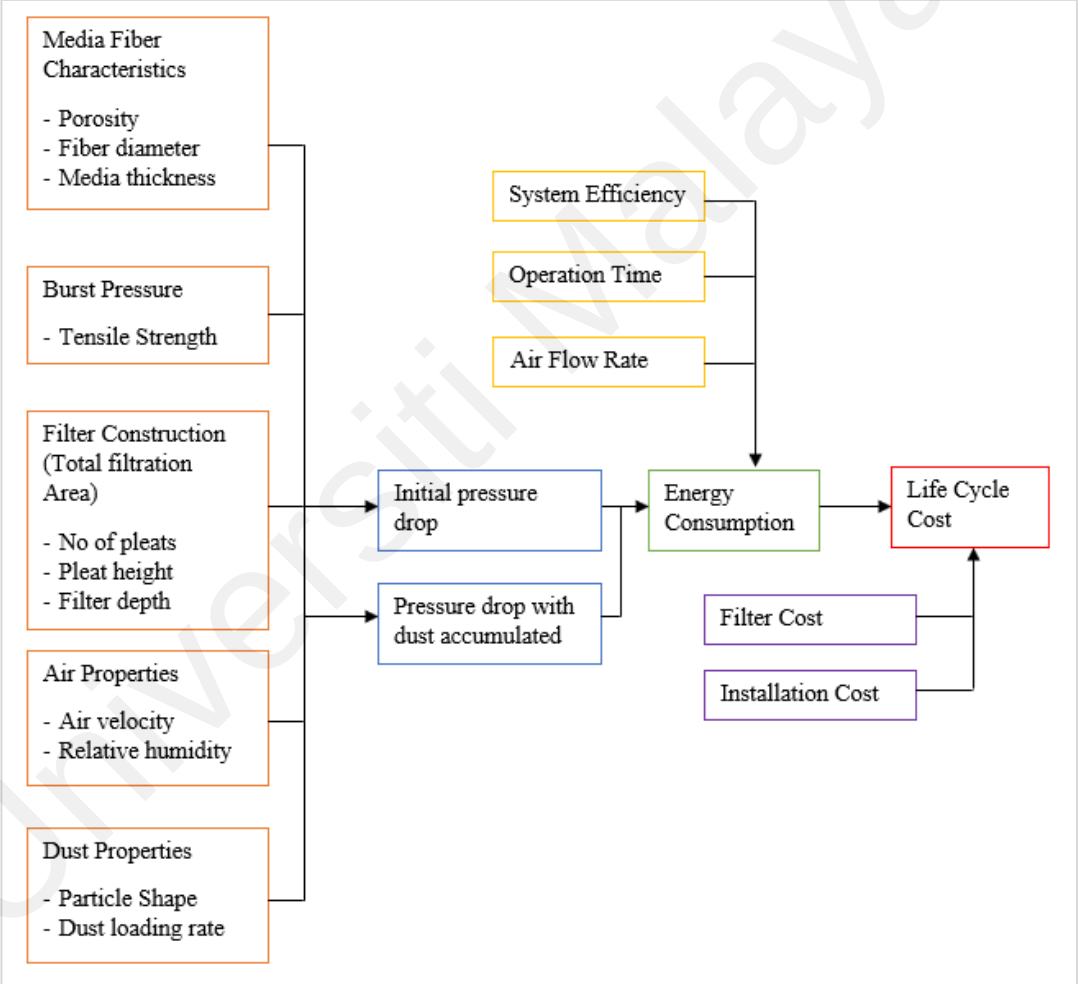

Figure 2.6: Factors Affecting the Filter Pressure Drop

In order to study the factors affecting the filtration performance, the testing procedure according to different test standards which are EN 779, ASHRAE 52.2, and ISO 16890 is compared. The difference between the three test standards discussed in Chapter 3. The test procedure is adopted in determining various parameters affecting the final resistance.

Other than that, CFD is also widely used as a methodology in studying the filtration performance. With experimental validation, CFD can effectively predict the filtration performance, which is time and cost-saving.

In summary, the final resistance is recommended by manufacturers and its relationship is necessary to be developed. If the air filter ruptures before the recommended final resistance, the indoor air quality will be highly contaminated, especially for pharmaceutical industries. Studying various contributing factors experimentally and via simulation, the final resistance relationship is important to ensure that the service period of the air filter can be optimized with high filtration efficiency at optimum energy consumption.

CHAPTER 3: AIR FILTER TEST STANDARDS FOR PARTICULATE MATTER OF GENERAL VENTILATION

Air filters play an important role in an HVAC system to maintain the good indoor air quality of a building. The air filter test standards act as a guideline to evaluate air filter performance. The current global test standard, ISO 16890:2016 adopts particulate matter classification which can be easily understood. The European standard, EN 779:2012 is obsolete and replaced by ISO 16890:2016 in June 2018. ASHRAE 52.2:2017 which adopts Minimum Efficiency Reporting Value (MERV) classification is still widely used in the United States. Some countries in Southeast Asia such as Malaysia, Brunei, and Singapore are applying different standards: EN779, ASHRAE 52.2, and ISO 16890. Standardization of the air filter testing and classification is undoubtedly important in the global air filtration market. This paper can act as a reference and assist these developing countries in adopting the suitable air filter testing standard to develop their national standard. As all three standards have no specifications on energy efficiency classification, the energy rating system can be obtained using Eurovent 4/21-2018. The HVAC system supply air quality can be further improved with the consideration of WHO annual mean pollutant limits and EN 16798-3 air classification to determine the supply air cleanliness.

3.1 Background of Test Standard Development

3.1.1 ASHRAE 52.2

The air filter standard was originated by the American Society of Heating and Ventilating Engineers (ASHVE) in the 1930s with an adopted code in determining the air filter efficiency. The filter efficiency was calculated on the basis of the amount of weight of the synthetic dust which a filter was able to remove (May, 1965). Later in 1953, the Air Filter Institute (AFI), a manufacturers' association adopted Section 1 of a Code for Testing Air Cleaning Devices (Institute, 1954) in determining the filter efficiency. (May,

1965) A final filter was located at the air filter's downstream to trap the unfiltered synthetic dust and this weight of the final filter was used to calculate dust arrestance or efficiency. The dust holding capacity was introduced in the AFI code to estimate the air filter lifespan. The ASHVE and AFI codes worked with a weight method test which was suitable for medium-efficiency filter but found unreliable when the weight efficiency was approaching 100 percent due to experimental error.

Hence, a dust-spot test method was developed by the United States Bureau of Standards and later published by the Air Filter Institute in 1960 (Air Filter Institute, 1960). The dust-spot test method used atmospheric dust from the air and clean filter papers were used to collect upstream and downstream dust at the same sampling rate. The upstream sampler was operated for a shorter time period so that both upstream and downstream could collect the same dust densities on the filter papers. The dust-spot efficiency was defined as a function of the sampling period obtaining the same dust density on filter papers.

The dust-spot efficiency and arrestance test were improved and then published as ASHRAE 52-68: Method of Testing Air Cleaning Devices Used in General Ventilation for Removing Particulate Matter in 1968 as the first official air filter testing standard in HVAC industry (Zhou & Shen, 2007). This standard directed the testing procedures to determine the performance in air cleaning equipment. The ASHRAE 52-68 was then improved and introduced as ASHRAE 52-76 in 1976 by defining a test filter duct section for the pressure drop determination and adding in S.I. units despite merely using English units (National Air Filtration Association, 1993). As ASHRAE 52-76 required a long testing time for atmospheric dust spot efficiency, ASHRAE 52.1-1992 was published. The ASHRAE 52.1 (ASHRAE Standard, 1992) defined a shorter testing method for better

reproducibility and allowing the testing procedure from previous ASHRAE 52-76 (National Air Filtration Association, 1993) at the same time.

The ASHRAE 52.1 focused on the filter performance in protecting machinery and coils and filter's ability to remove staining size particles. The atmospheric dust spot efficiency as well as the ASHRAE dust weight arrestance were calculated and averaged in consideration of the dust loading procedure (Klenk). The dust spot efficiency was determined using light blockage due to atmospheric dust on a target paper (Farr, 2013).

The concern of maintaining good indoor air quality had been increasing, hence the ability of an air filter in removing different particle sizes became more important to judge the filter efficiency. In 1999, ASHRAE 52.2 was introduced with a Minimum Efficiency Reporting Value (MERV) based on a wide particle size range ("ANSI/Standard 52.2-1999, Method of Testing General Ventilation Air-Cleaning Devices for Removal Efficiency by Particle Size," 1999). ASHRAE 52.2 was improved and modified in 2007, 2012, and the latest in 2017. ASHRAE 52.2:2017 (ASHRAE, 2017) is currently widely adopted in worldwide countries especially in the United States.

3.1.2 EN 779

The European standards on air filter test methods and classification started when ASHRAE 52-76 was adopted as Eurovent 4/5 with minor modifications in 1979 (Gustavsson, 1996). Eurovent 4/5 classified filters from EU1 to EU9 based on their dust spot efficiency and arrestance. The test airflow and final pressure drop of air filters were not specified in this standard. The Eurovent 4/5 was later replaced by Eurovent 4/9 before European Committee for Standardization (CEN) introduced EN779. Eurovent 4/9 determined the fractional efficiency of air filters at particle size between 0.2 to 3 μm (Goodfellow & Tahti, 2001). Comparative tests were carried out to find the average particle efficiency from 0.2 - 0.5 μm at a final pressure drop at 300 Pa. The average

particle efficiency was compared to dust spot efficiency, and it showed a good agreement that the particle efficiency at 0.4 μm corresponded approximately to the dust spot efficiency. Therefore, a classification method had been developed in EN779 in 1993 based on 0.4 μm particle average efficiency to replace dust spot efficiency (Gustavsson, 1996). The EN779 was revised in 2002 and officially replaced Eurovent 4/9. The latest revised version was EN779:2012 and this standard was replaced after ISO 16890 was adopted by European in August 2016 (Ginestet, 2017).

3.1.3 ISO 16890

ISO 16890 was introduced in 2016 and it adopts a new classification method based on particulate matter size which is recommended by the World Health Organization. ISO 16890 has replaced EN 779 in Europe as EN 779 focuses on the air filter performance at a particle size of 0.4 μm (Ginestet, 2017). Focusing only on one particle size is not sufficient to reflect the actual filter performance in operation as particulate matter is not uniform in size or shape. Therefore, ISO 16890 tests the air filter performance at a range of particle size from 0.3 μm to 10 μm, where the particles below 10 μm can be inhaled easily into the human body and endanger human health. (Courtey, 2017).

There are four parts of ISO 16890 which have been published in December 2016. The classification of the air filters introduced in this standard gives a clear link between filter efficiency and indoor air quality. The air filer is classified as ePM_1, $ePM_{2.5}$, and ePM_{10}.

3.2 Comparison between Testing Standards

The testing method and procedure for EN 779, ASHRAE 52.2, and ISO 16890 are compared and summarized in Table 3.1.

Table 3.1: Comparison of Clauses and Chapters

	ASHRAE 52.2:2017	EN 779:2012	ISO 16890:2016
Technical specifications, requirements and classification	Section 4 – 9, Section 12	Chapter 5 - 6	Part 1
Efficiency Measurements and Air Flow Resistance	Section 10.1 – 10.6	Chapter 7 – 10.3	Part 2
Determination of Arrestance (Dust Loading Test)	Section 10.7	Chapter 10.4	Part 3
Determination of the minimum efficiency (Conditioning method)	Appendix J (Optional Test)	Chapter 11	Part 4

Table 3.2 is the comparison between the air filter standards for general ventilation which are EN779, ASHRAE 52.2 as well as ISO 16890.

Table 3.2: Technical Comparison

	ASHRAE 52.2	EN 779	ISO 16890
Particle Size	Cover particle range from 0.3 µm to 10 µm	Cover particle range from 0.2 µm to 3.0 µm but efficiency reported at a particle size of 0.4 µm	Cover particle range from 0.3 µm to 10 µm
Test Aerosol	KCl aerosol (0.3 - 10 µm)	DEHS aerosol (0.2 - 3.0 µm)	DEHS aerosol (0.3 - 1.0 µm) KCl aerosol (1.0 - 10 µm)
Test Duct Configuration	• Straight / U shaped duct • Positive Pressure	• Straight duct • Positive / Negative Pressure	• Straight / U shaped duct • Positive / Negative Pressure
Electrostatic Discharge	Optional. Superfine KCl treatment	IPA discharge on media only	IPA discharge on whole filter

Table 3.2, continued

	ASHRAE 52.2	EN 779	ISO 16890
Test Dust	ASHRAE dust	ASHRAE dust	ISO fine dust
Dust Loading Test	Incremental dust feed is necessary for classification.	Incremental dust feed is necessary for classification.	Classification without dust feed
Final Pressure Drop	350Pa	G1 - G4 250Pa M5 - F9 450Pa	ISO Coarse 200Pa ISO ePM1, 2.5 & 10 300 Pa
Filter Classification	Classification against minimum efficiency (MERV) MERV 1 - MERV 16	Classification against average efficiency classes from G1 to F9	Classification against particle size ranges PM1, PM2.5 & PM10
Energy Efficiency Classification	No	No	No

3.3 Test Procedure

3.3.1 ASHRAE 52.2

Firstly, the pressure drop against different airflow rate of a clean air filter is tested with clean atmospheric air which has undergone HEPA filtration. The pressure drop is measured at 50 %, 75 %, 100 %, and 125 % of the rated air flow rate, which is 0.944 m^3/s if not otherwise specified by the manufacturer. Next, it is the particle size efficiency (PSE) test, in which the clean test filter is challenged by aerosol from 0.3 µm to 10.0 µm particle sizes to determine the PSE. During the dust loading test, the test filter is fed with synthetic dust of 30 g or an increase of 10 Pa, whichever comes first. PSE measurement is performed after the dust loading procedure, which is a similar procedure as EN 779. The dust loading and PSE measurement repeat for 4 times until the final resistance is reached. The filter is tested to a final resistance of 350 Pa if not specified by the manufacturer or until the arrestance drops below 85 %, whichever comes first. All efficiency curves are plotted, including the initial efficiency curves of the clean filter and all of the efficiency

curves after each dust loading stage. From all the efficiency curves, the minimum efficiency of different particle sizes can be determined. The air filter is classified based on minimum efficiency reporting value (MERV).

3.3.2 EN779

The test sequence of EN779 starts with a pressure drop against air flow rate determination. This determination of initial resistance or pressure drop is the same as that of ASHRAE 52.2. Next, in order to determine the initial efficiency, the air filter is tested at a range from 0.2 μm to 3.0 μm but reported at the particle size of 0.4 μm only as the particle size of 0.4 μm is the most difficult to be filtered (Courtey, 2017). Most filters have a minimum efficiency of around 0.4 μm. The dust loading procedure is then started after the initial efficiency and pressure drop are determined. After the first stage of 30 g dust loading with ASHRAE 52.2 synthetic dust, the initial arrestance can be obtained. At least four more approximately equal amounts of dust loading stages are done to achieve the final pressure drop of the tested air filter. For air filters of the coarse group (G), the maximum final pressure drop is 250 Pa whereas Medium (M) and Fine (F) group filters are set at 450 Pa. After every dust loading step, efficiency, arrestance, and pressure drop are determined. The classification of the air filter is then done based on the particle size of 0.4 μm.

3.3.3 ISO 16890

The first step of ISO 16890 is the measurement of initial resistance as a function of the airflow rate. The initial fractional efficiency of a clean and unconditioned filter is measured at a range of particle sizes from 0.30 μm to 10.0 μm. Next, the same test filter undergoes an artificial conditioning step with isopropanol (IPA) for 24 hours. The fractional efficiency test of the conditioned test filter is then repeated. This conditioned fractional efficiency is equal to the minimum fractional test efficiency. The ePM efficiencies can be calculated and classified accordingly. If the air filter can be classified

in ISO ePM 10, ePM 2.5, or ePM 1, the following dust loading test is optional, whereas the test is necessary for ISO Coarse group. In the dust loading test, only arrestance, test dust capacity, and airflow resistance are determined. No efficiency test is carried out after the dust loading process. For filters with particulate efficiency less than 50 % at PM_{10} particle range, the final pressure drop is 200 Pa while for other filters, the final resistance to airflow is 300 Pa.

3.4 Filter Classifications

Generally, there are three classes of air filters – coarse filters which are normally used as the primary stage of filtration, medium grade filters or normally called secondary filters and fine filters which are able to remove particles at high efficiency and used at the final stage of filtration(National Air Filtration Association, 1993). The classification of air filters is important to compare the air filter performance and act as a reference for users to select suitable air filters depending on applications.

3.4.1 ASHRAE 52.2

The particle size efficiency is determined at a size range of 0.3 µm to 10.0 µm. ASHRAE 52.2 uses the resulting size-resolved removal efficiency data to classify the average filter efficiency in three aggregate particle bins (Stephens, 2018). As shown in Table 3.3, the efficiency is analysed at size ranges, from 0.3 to 1.0 µm, 1.0 to 3.0 µm, and 3.0 to 10.0 µm. The minimum efficiency at different sizes within the 3 respective small ranges are averaged and classified according to the Minimum Efficiency Reporting Value (MERV). For efficiency of less than 20 % of the range of 3.0 µm to 10.0 µm, the filter is classified based on the average arrestance.

Table 3.3: Classification of ASHRAE 52.2 (ASHRAE, 2017)

Standard 52.2 Minimum Efficiency Reporting Value (MERV)	Composite Average Particle Size Efficiency, % in Size Range, µm			
	Range 1	Range 2	Range 3	Average Arrestance
	0.30 to 1.0	1.0 to 3.0	3.0 to 10.0	%
1	N/A	N/A	$E_3 < 20$	$A_{avg} < 65$
2	N/A	N/A	$E_3 < 20$	$65 \leq A_{avg}$
3	N/A	N/A	$E_3 < 20$	$70 \leq A_{avg}$
4	N/A	N/A	$E_3 < 20$	$75 \leq A_{avg}$
5	N/A	N/A	$20 \leq E_3$	N/A
6	N/A	N/A	$35 \leq E_3$	N/A
7	N/A	N/A	$50 \leq E_3$	N/A
8	N/A	$20 \leq E_2$	$70 \leq E_3$	N/A
9	N/A	$35 \leq E_2$	$75 \leq E_3$	N/A
10	N/A	$50 \leq E_2$	$80 \leq E_3$	N/A
11	$20 \leq E_1$	$65 \leq E_2$	$85 \leq E_3$	N/A
12	$35 \leq E_1$	$80 \leq E_2$	$90 \leq E_3$	N/A
13	$50 \leq E_1$	$85 \leq E_2$	$90 \leq E_3$	N/A
14	$75 \leq E_1$	$90 \leq E_2$	$95 \leq E_3$	N/A
15	$85 \leq E_1$	$90 \leq E_2$	$95 \leq E_3$	N/A
16	$95 \leq E_1$	$95 \leq E_2$	$95 \leq E_3$	N/A

3.4.2 EN779

EN779:2002 has been revised the classification system from only F and G group filters to three groups (F, M, and G filters). As shown in Table 3.4, a filter with less than 40% average efficiency at 0.4 µm particles is grouped as coarse filter or group G. G group filters are classified from G1 to G4 based on their average arrestance with the loading dust. Medium (M) group filters require an average efficiency from 40% to less than 80% at 0.4µm and are classified in M5 or M6 based on their average efficiency. For average efficiency of 80 % or more, the filter is grouped as fine (F) filter from F1 to F9 based on their average efficiency as well as the minimum efficiency throughout the test.

Table 3.4: Classification of EN 779 (EN, 2012)

Group	Class	Final test pressure drop Pa	Average efficiency (A_m) of synthetic dust %	Average efficiency (E_m) of 0.4 µm particles %	Minimum efficiency [a] of 0.4 µm particles %
Coarse	G1	250	$50 \leq A_m < 65$	-	-
	G2	250	$65 \leq A_m < 80$	-	-
	G3	250	$80 \leq A_m < 90$	-	-
	G4	250	$90 \leq A_m$	-	-
Medium	M5	450	-	$40 \leq E_m < 60$	-
	M6	450	-	$60 \leq E_m < 80$	-
Fine	F7	450	-	$80 \leq E_m < 90$	35
	F8	450	-	$90 \leq E_m < 95$	55
	F9	450	-	$95 \leq E_m$	70
[a] Minimum efficiency is the lowest efficiency among the initial efficiency, discharged efficiency, and the lowest efficiency throughout the loading procedure of the test.					

3.4.3 ISO 16890

In order to determine the particulate matter efficiencies, ePM of air filters, standardized volume distribution functions are used in this standard. The functions are used globally to represent the average ambient air of urban and rural areas (Ginestet, 2017). The fine filters which can filter PM_1 and $PM_{2.5}$ particle size fractions are evaluated with an urban area size distribution, whereas filters for PM_{10} fraction are evaluated with the rural area size distribution. The initial and conditioned fractional efficiencies are averaged as the real performance of the air filters lays between the initial and conditioned fractional efficiencies. The average fractional efficiencies are used for calculation of particulate matter efficiencies, ePM. The particle size range is 0.30 µm to 1.0 µm for ePM_1, 0.30 µm to 2.50 µm for $ePM_{2.5}$ and 0.30 µm to 10.0 µm for ePM_{10}. The classification of the air filters is done based on ePM calculations, as shown in Table 3.5.

Table 3.5: Classification of ISO 16890 (ISO, 2016b)

Group designation	Requirement			Class reporting value
	$ePM_{1,min}$	$ePM_{2.5,min}$	ePM_{10}	
ISO Coarse	-	-	<50 %	Initial grav. Arrestance
ISO ePM10	-	-	≥50 %	ePM_{10}
ISO ePM2.5	-	≥50 %	-	$ePM_{2.5}$
ISO ePM1	≥50 %	-	-	ePM_1

The reporting of the ePM classes is done by rounding downwards the class reporting values to the nearest 5% points whereas it is reported as ">95%" for values larger than 95%. The ISO Coarse filters which have an ePM_{10} less than 50% are reported with their initial gravitational arrestance, whereas other filter groups are reported at their respective particulate matter efficiencies.

3.5 Test Aerosols and Particle Counter

An aerosol is a suspension of fine solid or liquid particles in the air (Carrier, 2005). Test aerosol is particles generated either in the solid or liquid phase to determine the particle size efficiency. The number and size of particles generated from the test aerosol are determined using an optical particle counter or spectrometer.

3.5.1 ASHRAE 52.2

The test aerosol used in ASHRAE 52.2 is polydisperse solid-phase potassium chloride (KCl) generated from an aqueous solution. The reasons for choosing KCl aerosol are because KCl particles, which are not hazardous to human health, are easy to generate and available at low cost. Solid-phase KCl particles provide a more severe challenge to test devices as they are easy to bounce off collection surfaces, increasing the chance of penetration.

The aerosol generated is in a range from 0.3 μm to 10 μm. The aerosol is discharged with a radiation generator before being introduced into the test duct. According to ASHRAE 52.2:2017, the reason for setting the upper particle size limit as 10 μm is because particles of this size may affect human health and air handling equipment. The particles can affect human health as the particle size may be trapped in the nose, causing irritation or allergy. Besides, the particles can soil surfaces, equipment, and ductwork system, affecting the indoor air quality (IAQ). Many allergens, fungi, and bioaerosols are also within a size range of 3.0 μm to 10 μm. Choosing 0.30 μm as the lower size limit is

because the available optical particle counters in the commercial market have a good monotonic response to polydisperse aerosol and are able to achieve 0.30 μm particle size counting. The particle counters used to measure particle range from 0.3 μm to 10 μm shall consist of 12 channels.

3.5.2 EN779

In EN 779:2012, liquid aerosol which is DEHS or any equivalent aerosol is used. The liquid aerosol is chosen in this standard based on experience gained from EN779:2002 and Eurovent 4/9 techniques as a liquid aerosol is easy to generate particles at a required size range with a high degree of consistency. As the particle counters are calibrated with spherical latex particles, calculation spherical liquid particle size in particle counters is more accurate compared to using solid particles of salt with a non-spherical shape. Undiluted DEHS is used to generate a non-charged aerosol. The aerosol generated for filtration efficiency as a function of particle size at a range of 0.2 μm to 3.0 μm. The optical particle counter (OPC) required should have at least 5 size channels at equidistant logarithmic scale from 0.2 μm to 3.0 μm.

3.5.3 ISO 16890

There are 2 types of test aerosol used in this standard, combining both test aerosols from EN 779 and ASHRAE 52.2. The first type is liquid phase aerosol which is DEHS and other equivalents. This liquid phase aerosol is used to generate a particle size range of 0.30 μm to 1.0 μm. Another type is the polydisperse solid-phase potassium chloride (KCl) generated from aqueous solution. The particle size range generated by KCl aerosol is 1.0 μm to 10.0 μm. The KCl aerosol is required to pass through the discharge ionizer to achieve Boltzmann electrostatic charge distribution.

The optical particle counter requires a minimum of 12 logarithmically spaced particle size channels for full data set collection. It requires a minimum of three size channels in ranges of 0.3 µm to 1.0 µm, 1.0 µm to 3.0 µm and 3.0 µm to 10.0 µm respectively.

3.6 Test Duct Configuration

The test duct configuration can be designed according to specifications described in the standards. Generally, the cross-section of ducts is 610 mm x 610 mm. For ASHRAE 52.2, the test duct must be operated at positive pressure in either a straight or U-bend configuration. The blower is located at the duct upstream of the test filter and draws air into the duct. As for EN 779, the test rig can be designed with negative or positive pressure in a straight configuration. ISO 16890 allows a straight test rig or a U-shaped test rig configuration. It can be in a negative or positive pressure airflow arrangement. In order to determine the fan location for EN 779 and ISO 16890, the effect of using pressure or negative pressure operation should be considered. For the fan located upstream, a positive pressure operation could cause the test aerosol and loading dust leak into the room while the particles could leak into the test rig at negative pressure. In Figure 3.1 and Table 3.6, the instruments and devices required for different standards are summarized.

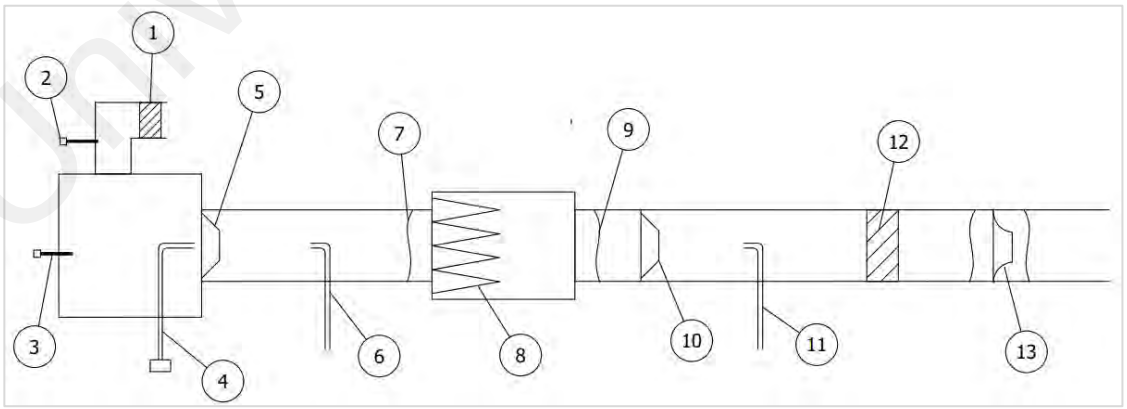

Figure 3.1: Test Rig Configuration(ISO, 2016b)

Table 3.6: Summary of Instruments and Devices Required for Testing (ASHRAE, 2017; EN, 2012; ISO, 2016b)

Label	Items	Applicable to		
		ASHRAE 52.2	EN 779	ISO 16890
1	Upstream High-Efficiency Particulate Air (HEPA) Filtration	✓	✓	✓
2	Liquid Aerosol Injection		✓	✓
3	Solid Aerosol Injection	✓		✓
4	Dust Injection	✓	✓	✓
5	Upstream Mixing Orifice	✓	✓	✓
6	Upstream Aerosol Sampling Head	✓	✓	✓
7	Upstream Test Device Pressure Tap	✓	✓	✓
8	Test Device	✓	✓	✓
9	Downstream Test Device Pressure Tap	✓	✓	✓
10	Downstream Mixing Orifice (Efficiency Test)			✓
	Downstream Final Filter (Dust Loading Test)	✓	✓	✓
11	Downstream Aerosol Sampling Head	✓	✓	✓
12	Downstream High-Efficiency Particulate Air (HEPA) Filtration	Optional	Optional	Optional
13	Air Flow Measurement Device	✓	✓	✓

3.7 Electrostatic Discharge

An electrostatic enhanced air filter can achieve high efficiency as the particles can be easily removed when they pass through the charged media surface (Feng & Cao, 2019; Tian et al., 2018). Therefore, electrostatic discharge is important to determine the minimum efficiency of air filters.

3.7.1 ASHRAE 52.2

ASHRAE Technical Committee 2.4 had developed a method of conditioning that has been demonstrated in limited cases to predict the air filter performance more closely in the actual use. This conditioning method is an optional method described in Appendix J of this standard to predict the efficiency loss. If desired, both the compulsory test described in ASHRAE 52.2 and the optional conditioning test are required to be done

respectively on two similar test devices. This optional test requires potassium chloride (KCl) as a conditioning aerosol. The conditioning aerosol of KCl does not go through discharge ionizer whereas the test aerosol does.

The test sequence with the conditioning procedure is as well started with the pressure drop test at various airflow rates. The particle size efficiency (PSE) test of the clean filter is done as described in the compulsory test using test aerosol. Next, the test device is exposed to conditioning aerosol with the airflow rate used in the PSE test. The upstream concentration of the conditioning aerosol is measured using a condensation particle counter (CPC). The conditioning is done in incremental steps with a PSE taken after each increment. The conditioning process is stopped when the measurement shows no further significant drop or when the cumulative exposure time of the filter to conditioning aerosol reaches a certain value. After that, the PSE test and dust loading process are done as described in ASHRAE 52.2 standard. The test filter with conditioning step is classified with minimum efficiency reporting value (from MERV 1-A to MERV 16-A) according to a different table in Appendix J in ASHRAE 52.2, as shown in Table 3.7.

Table 3.7: Classification with Conditioning Step of ASHRAE 52.2 (ASHRAE, 2017)

Standard 52.2 Minimum Efficiency Reporting Value (MERV-A)	**Composite Average Particle Size Efficiency, % in Size Range**			**Average Arrestance (%) %**
	Range 1	Range 2	Range 3	
	0.30 to 1.0 µm	1.0 to 3.0 µm	3.0 to 10.0 µm	
1-A	N/A	N/A	E_3-A < 20	A_{avg} < 65
2-A	N/A	N/A	E_3 -A < 20	65 ≤ A_{avg}
3-A	N/A	N/A	E_3-A < 20	70 ≤ A_{avg}
4-A	N/A	N/A	E_3 -A < 20	75 ≤ A_{avg}
5-A	N/A	N/A	20 ≤ E_3-A	N/A
6-A	N/A	N/A	35 ≤ E_3-A	N/A
7-A	N/A	N/A	50 ≤ E_3-A	N/A

Table 3.7, continued

Standard 52.2 Minimum Efficiency Reporting Value (MERV-A)	Composite Average Particle Size Efficiency, % in Size Range			Average Arrestance (%) %
	Range 1	Range 2	Range 3	
	0.30 to 1.0 μm	1.0 to 3.0 μm	3.0 to 10.0 μm	
8-A	N/A	$20 \leq E_2$-A	$70 \leq E_3$-A	N/A
9-A	N/A	$35 \leq E_2$-A	$75 \leq E_3$-A	N/A
10-A	N/A	$50 \leq E_2$-A	$80 \leq E_3$-A	N/A
11-A	$20 \leq E_1$-A	$65 \leq E_2$-A	$85 \leq E_3$-A	N/A
12-A	$35 \leq E_1$-A	$80 \leq E_2$-A	$90 \leq E_3$-A	N/A
13-A	$50 \leq E_1$-A	$85 \leq E_2$-A	$90 \leq E_3$-A	N/A
14-A	$75 \leq E_1$-A	$90 \leq E_2$-A	$95 \leq E_3$-A	N/A
15-A	$85 \leq E_1$-A	$90 \leq E_2$-A	$95 \leq E_3$-A	N/A
16-A	$95 \leq E_1$-A	$95 \leq E_2$-A	$95 \leq E_3$-A	N/A

3.7.2 EN779

In order to determine the effect of electrostatic removal mechanism on the filter efficiency, the filter material is tested before and after being discharged with isopropanol (IPA). The filter material sample must be identical to the material of the tested filter. The material sample shall be selected by cutting to represent the complete filter. The media sample is discharged by immersing it in IPA for two minutes and dried on the inert surface for 24 hours. The test aerosol, the particle size range, and efficiency measurement procedure are similar to the testing procedure of full filter. The average discharged efficiency is reported at 0.4 μm particle size.

3.7.3 ISO 16890

The conditioning test is to determine the minimum test efficiency of the air filters and the effect of the electrostatic removal mechanism on air filter performance. The conditioning material used is isopropanol (IPA). IPA is placed in a cabinet for evaporation until the equilibrium of IPA vapour in the ambient air of the cabinet is reached. The conditioning

time for the test filter is 24 hours. After the conditioning time is reached, the test device is placed under standard climatic conditioned for at least 30 mins before carrying out the conditioned fractional efficiency test (ISO, 2016e).

3.8 Test Dust

Test dust or loading dust is synthetic dust formulated specifically in different standards and used to determine the dust holding capacity and arrestance of air filters. The efficiency of air filters due to the dust loading effect can be studied with a simulated test using test dust.

Both EN 779 and ASHRAE 52.2 use synthetic dust as defined in ASHRAE 52.2 which consists of

- 72% by weight of ISO 12103-1, A2 Fine Test Dust
- 23% by weight of powdered black carbon
- 5% by weight of milled cotton linters.

ISO 16890 uses the synthetic loading dust, L2 as specified in ISO 15957(ISO, 2016d).

3.9 Energy Efficiency Classification

The differential pressure across air filters can cause high energy consumption of the HVAC system (Montgomery et al., 2012; Sun & Woodman, 2009; Zhai & Johnson, 2017). Therefore, energy efficiency classification is important to evaluate the performance of air filters. However, all three test standards have no specifications on the energy consumption calculation of air filters until the recommended final resistance. The comparison of air filters in terms of energy efficiency is not possible as there is no guideline described in test standards.

3.10 Discussion

3.10.1 Standardization with ISO 16890

Before ISO 16890 is introduced, the European standard, EN 779, and the American standard, ASHRAE 52.2 have been widely used in their respective region while other regions such as Asia and the Middle East countries have used both of the standards (Courtey, 2017). A standardization of air filter test method and classification is aimed to be achieved by the introduction of ISO 16980 in global air filtration industries. As EN 779 is obsolete, ISO 16890 is adopted in Europe while ASHRAE 52.2 is still a preferred standard for the US.

3.10.2 Classification Method

EN 779 is obsolete as the European has adopted ISO 16890 as the new official air filter testing standard. Comparing ISO 16890 and ASHRAE 52.2, the main concern of the public is their classification method. The previous EN 779 testing only reports the efficiency at 0.4 μm to determine filter classification. Both ISO 16890 and ASHRAE 52.2 focus on the particle size range of 0.3 μm to 10.0 μm, covering particle size which could endanger human health. ASHRAE 52.2 classifies the air filters with Minimum Efficiency Reporting Value (MERV) while ISO 16890 uses particulate matter (PM) classes. Reporting with the MERV method, the filter users need to refer to the classification table to get a better picture of the air filter performance. Classification with particulate matter can better represent the actual dirty air in the outdoor environment and provide a better understanding of the users on the actual performance of air filters from the filter reporting value. The classification by using particulate matter also aligns with the World Health Organization and Environmental Protection Agency, focusing on the effect of particulate matter such as $PM_{2.5}$ on human health as well as the importance of indoor air quality (IAQ) nowadays.

ASHRAE 52.2 and ISO 16890 are using the measurement of size-resolved particle removal efficiency from 0.3 μm to 10 μm. ASHRAE 52.2 uses the resulting size-resolved particle removal efficiency to classify the filter efficiency into three particle size bins and determine the minimum removal efficiency in each bin for MERV classification. ISO 16890 uses the resulting size-resolved particle removal efficiency to estimate the mass-based particle removal efficiencies at PM_1, $PM_{2.5}$, and PM_{10}. Efficiency at PM_1 (ePM_1) covers the particle range from 0.3 μm to 1.0 μm; $ePM_{2.5}$ covers from 0.3 μm to 3.0 μm whereas ePM_{10} considers particle size of 0.3 μm to 10 μm. The ambient air is bimodally distributed with particles in fine and coarse mode. Bimodal volume distribution functions are used in ISO 16890 to represent the outdoor air in urban and rural globally. Assuming the ambient particles are spherical with constant unit density, the volume-based removal efficiencies are equivalent to mass-based efficiencies (Stephens, 2018). ISO 16890 uses a mass particle efficiency similar to ASHRAE 52.1 but with consistent particle mass compared to the ambient air (*Comparing ISO 16890 and ASHRAE 52.2/MERV*).

3.10.3 Electrostatic Discharge

The electrostatic effect can significantly increase the filter efficiency as the dust particles can be held by strong electrostatic forces when they come in contact with filter media (National Air Filtration Association, 1993). However, if the filter is not electrostatically charged continuously, the air filter performance will drop intensely after the filter is fully discharged with dust particles. Therefore, in order to determine the minimum efficiency of the air filters, the electrostatic discharge can be carried out on the test filter. In EN 779, the discharge procedure is done on filter material by immersing the media in isopropanol solution. The discharge treatment which is included in Appendix J is optional for ASHRAE 52.2 and it is done using charged aerosol. In ISO 16890, the electrostatic discharge is done on the whole test filter by exposing the filter in isopropanol vapour. The normal MERV classification of ASHRAE 52.2 does not take into account the effect of

electrostatic discharge. The efficiency obtained from ASHRAE 52.2 testing might be higher than its actual performance due to the electrostatic effect. Although the discharge procedure is included as an option, most companies do not carry out electrostatic discharge, causing a misrepresentation of the real-world filter performance (*Comparing ISO 16890 and ASHRAE 52.2/MERV*). Electrostatic discharge on filter media itself in EN 779 might not be sufficient as the performance may vary after the whole filter is fully assembled with the filter frame. A full filter discharge introduced in ISO 16890 can efficiently remove all the charged particles and determine the minimum efficiency of the air filter. Both efficiencies before and after discharged are reported and compared in ISO 16890.

3.10.4 Energy Calculation

It is important to consider the energy consumption calculation of the air filters. All three standards have no specification on the calculation method for the energy of an air filter to be consumed until the final resistance is reached. Eurovent 4/21-2014 was the guideline published in Europe to define a method of air filter classification in consideration of energy efficiency. This guideline makes use of the test result from EN 779 to further analyse for the energy consumption of air filters. The latest version is Eurovent 4/21-2018 which implements the energy efficiency according to ISO 16890 classification after EN 779 is obsolete in Europe.

The energy consumption of air filters described in Eurovent 4/21 is determined by

$$W = \frac{q_v \cdot \overline{\Delta P} \cdot t}{\eta \cdot 1000} \quad \textbf{(3.1)}$$

$$\overline{\Delta P} = \frac{1}{M}\int_0^M \Delta P(m)dm \quad \textbf{(3.2)}$$

where W is the energy consumption in kWh; q_v is the airflow rate at 0.944m^3/s; t is the operation time at 6000 hours; ɳ is the system energy efficiency at 0.50, which is the average fan efficiency in an air handling unit and $\overline{\Delta P}$ is the average pressure drop of air filter until the final resistance in Pa. $\overline{\Delta P}$ is calculated from equation (3.2) where $\Delta P(m)$ is the instantaneous pressure drop across filter; M is the total mass of dust loading in g, m is the variable of loaded dust (Eurovent, 2018).

3.11 Summary

Comparing different factors, ISO 16890 provides a guideline in air filter testing at general ventilation. The classification with the particulate method approach is easy to understand even for the users who are not air filter specialists. This can increase the public awareness of the surrounding air quality by selecting suitable air filters accordingly. However, it is recommended to introduce an energy consumption calculation method in the test standard with Eurovent 4/21 (Liu et al., 2017). Besides, in order to maintain good indoor air quality, the World Health Organization annual mean pollutant limits and EN 16798-3:2017 (CEN, 2017) which describes air classification can be taken into account for building supply air system. The air filtration and ventilation system design can be holistic in consideration of air filter performance with ISO 16890:2016, filter energy consumption with Eurovent 4/21 as well as air quality with WHO annual mean pollutants limits and EN 16798-3:2017

A common air filter classification method enables manufacturers and consumers to compare filter performance like-for-like. The introduction of ISO 16890 provides a classification method using particulate matter which can be adopted globally and acts as a universal guideline for air filter comparison. Reporting efficiency in particulate matter

can be easily understood by the end-users who are not air filter experts. ISO 16890 focuses on a classification related to air pollutant levels and indoor air quality which aligns with World Health Organization. Europe has adopted ISO 16890 in replacement of EN 779 while ASHRAE 52.2 is still widely used especially in the United States. Standardization of the air filter standard is necessary, especially for countries in Southeast Asia such as Malaysia, Brunei, and Singapore. The adoption of ISO 16890 in global countries for air filter testing and classification, at the same time embedding Eurovent 4/21 for energy efficiency calculation, WHO guidelines for annual air pollutant limits and EN 16798-3 for building supply air quality, will bring a significant effect in the air filtration and building ventilation systems.

CHAPTER 4: METHODOLOGY

In this chapter, the methodology used in this research study is discussed. CFD simulation is used to study the effect of pleat shape on the initial pressure drop. Experimental data collection is conducted to study the influence of the type of fibre media, filtration velocity, pleat depth and pleat density on the filtration performance. Besides, the physical properties of the filter media are also determined using SEM scan and tensile strength measurements. The experimental data analysis is performed using linear multiple regression to find the empirical models for the filtration performance parameters.

4.1 Project Workflow

Figure 4.1 shows the workflow planning of the study. A literature review is conducted thoroughly to identify the research niche. Factors affecting the final resistance are studied comprehensively. Different air filter test standards are studied to adopt a suitable experimental procedure. Next, the various CFD modelling techniques applied in air filtration simulations are studied, and suitable models are applied in this project.

A test rig is built for experimental data collection based on the international air filter test standard, ISO 16890:2016 as described in Section 4.2. The ducts and mechanical parts are designed using Computer-Aided Design (CAD) and fabricated accordingly. The measuring devices and instruments are selected based on the requirements of the standard and installed accordingly.

CFD simulation is conducted to study the pleat shape of the filter. The steady-state simulation is used to study the pressure drop across the clean air filter. The experiments are carried out to study the effect of filter media, filtration velocity, pleat depth and pleat density on the filtration performance. After that, the experimental data collected are analysed to form empirical models for each filtration performance parameter using linear

multiple regressions. Then, the formulation in defining final resistance is determined in consideration of the filter's predicted lifespan and energy cost.

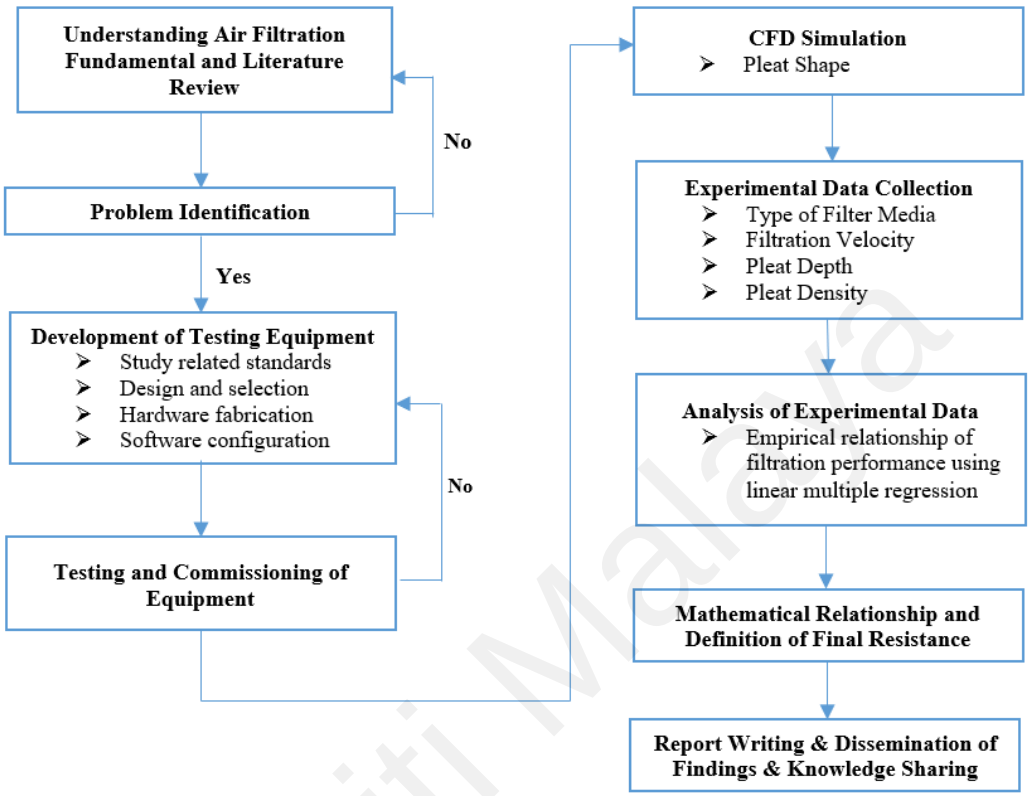

Figure 4.1: Workflow Chart

4.2 Computational Fluid Dynamics

Computational fluid dynamics (CFD) is used to study the effect of the pleat shape on the initial pressure drop. Six different pleat shapes are studied, which are depicted in Figure 4.2. Each pleat shape is fixed at a pleat depth of 44 mm and a pleat density of 4.0 pleats per inch (PPI), while the total filtration area is maintained at about 443 mm per unit length. The thickness of the porous zone is 0.32 mm, which is the fibreglass media thickness used in this study.

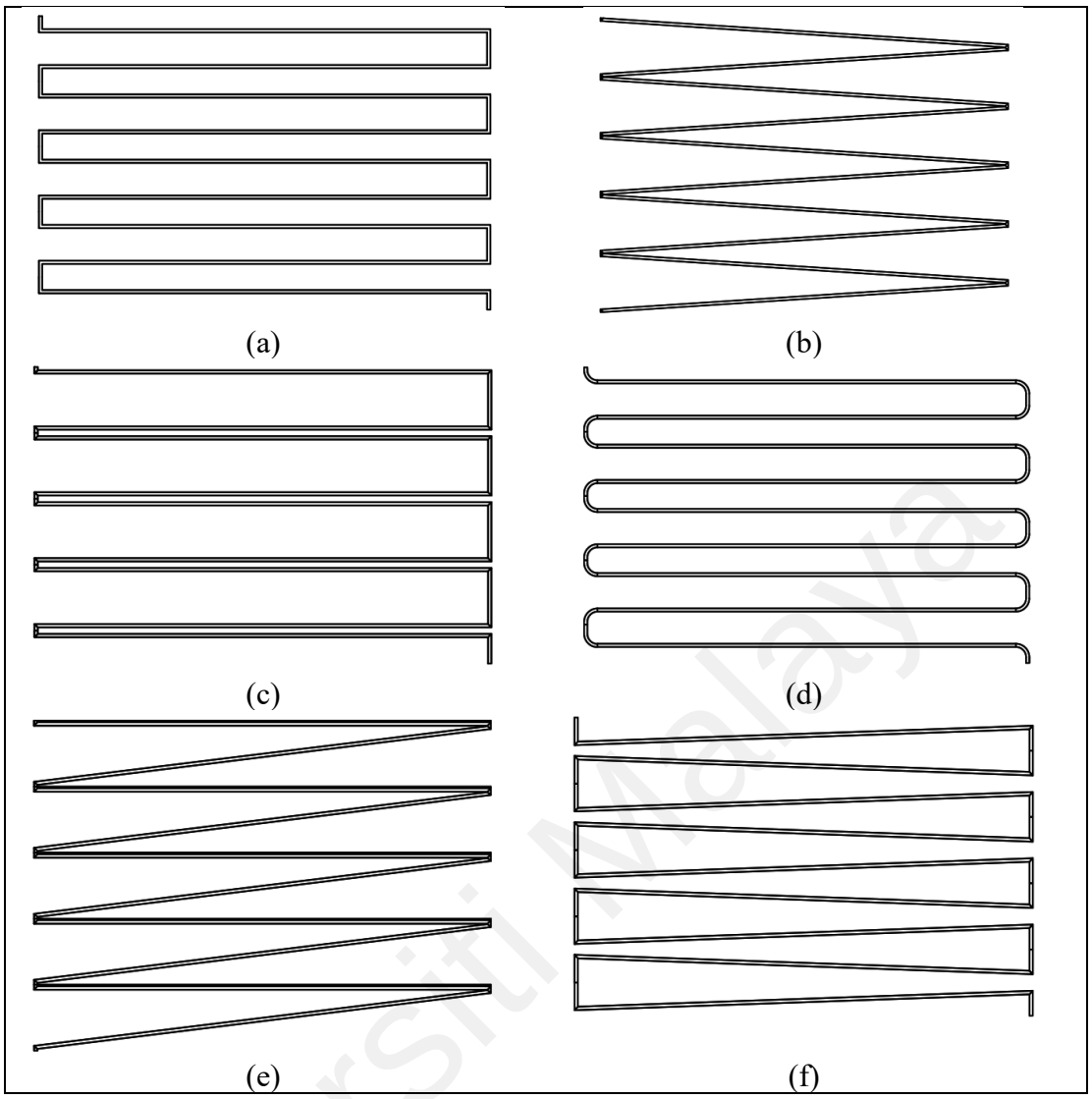

Figure 4.2: Type of Pleat Shapes (a) Rectangular (b) Triangular (c) U-shaped (d) S-shaped (e) Z-shaped (f) Box-shaped

4.2.1 Computational Domain, Mesh, and Boundary Conditions

Both 2D simulation and 3D simulation are carried out to simulate the airflow through a flat sheet, while 2D simulations are used to simulate the flow behaviours for different pleat shapes. The length of the fluid domain is set to be at least three times the model dimension for the upstream domain and at least five times for the downstream to ensure the flow will not be disturbed due to the limit of the computational domain and the boundary conditions. Figure 4.3 shows the computational domain and the boundary conditions used in the simulation.

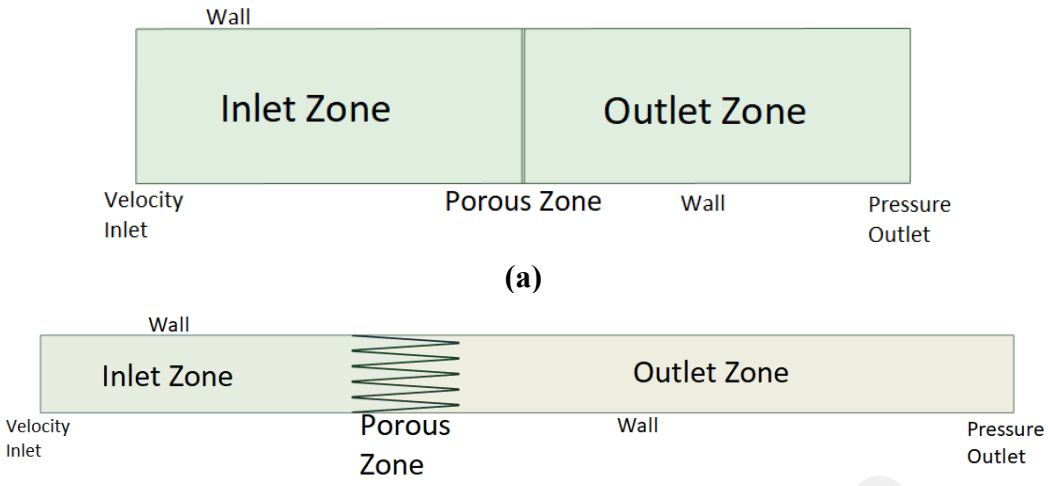

Figure 4.3: Computational Domain and Boundary Conditions (a) Flat Shape (b) An Example of Pleat Shape

ANSYS Mesh is used as the meshing tool to generate the mesh for the computational domain. The quality of the mesh is important in order to simulate a reliable result. As shown in Figure 4.4, structured meshes are generated for all study cases by using the surface slicing technique in order to get a low skewness mesh. The maximum skewness for all cases is controlled at 0.5, and the minimum orthogonal quality is at 0.7, in which the mesh quality is good compared with Figure 4.5.

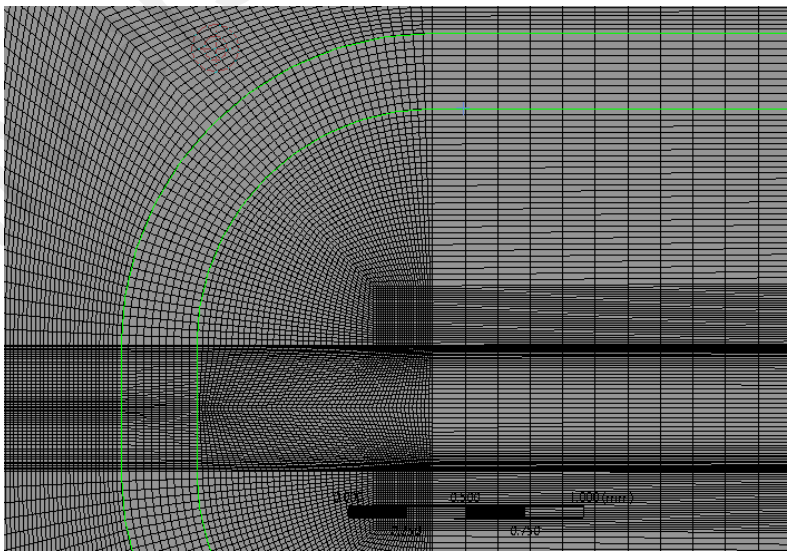

Figure 4.4: Structured Mesh Technique

Skewness mesh metrics spectrum:

Excellent	Very good	Good	Acceptable	Bad	Unacceptable
0-0.25	0.25-0.50	0.50-0.80	0.80-0.94	0.95-0.97	0.98-1.00

Orthogonal Quality mesh metrics spectrum:

Unacceptable	Bad	Acceptable	Good	Very good	Excellent
0-0.001	0.001-0.14	0.15-0.20	0.20-0.69	0.70-0.95	0.95-1.00

Figure 4.5: Mesh Metrics Spectrum

Mesh independence studies are carried out for each case to ensure the simulation result is independent of the grid size used. The scaled residual is observed, and the solution is considered converged to at least 0.001. Figure 4.6 summarizes the graphs of the mesh independence test for each case. The selected total element number for each case is tabulated in Figure 4.6.

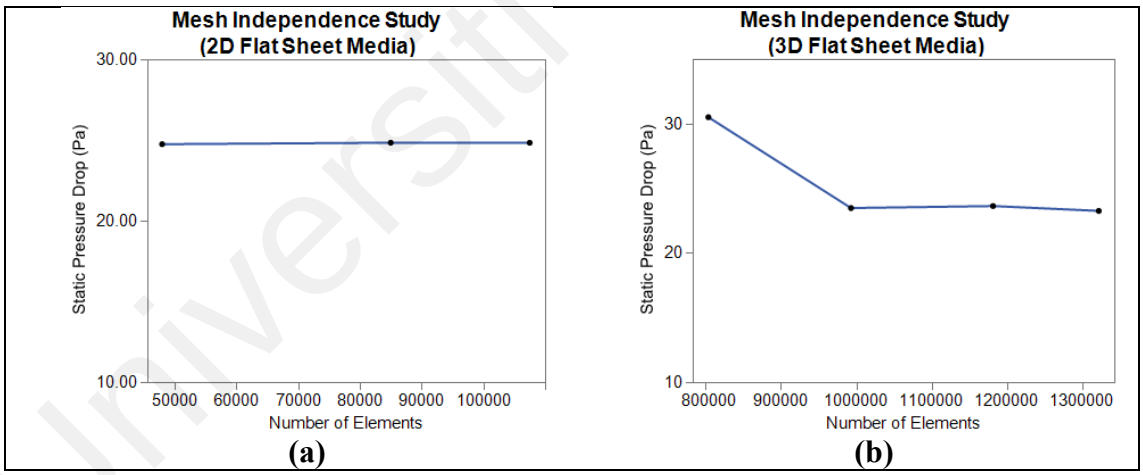

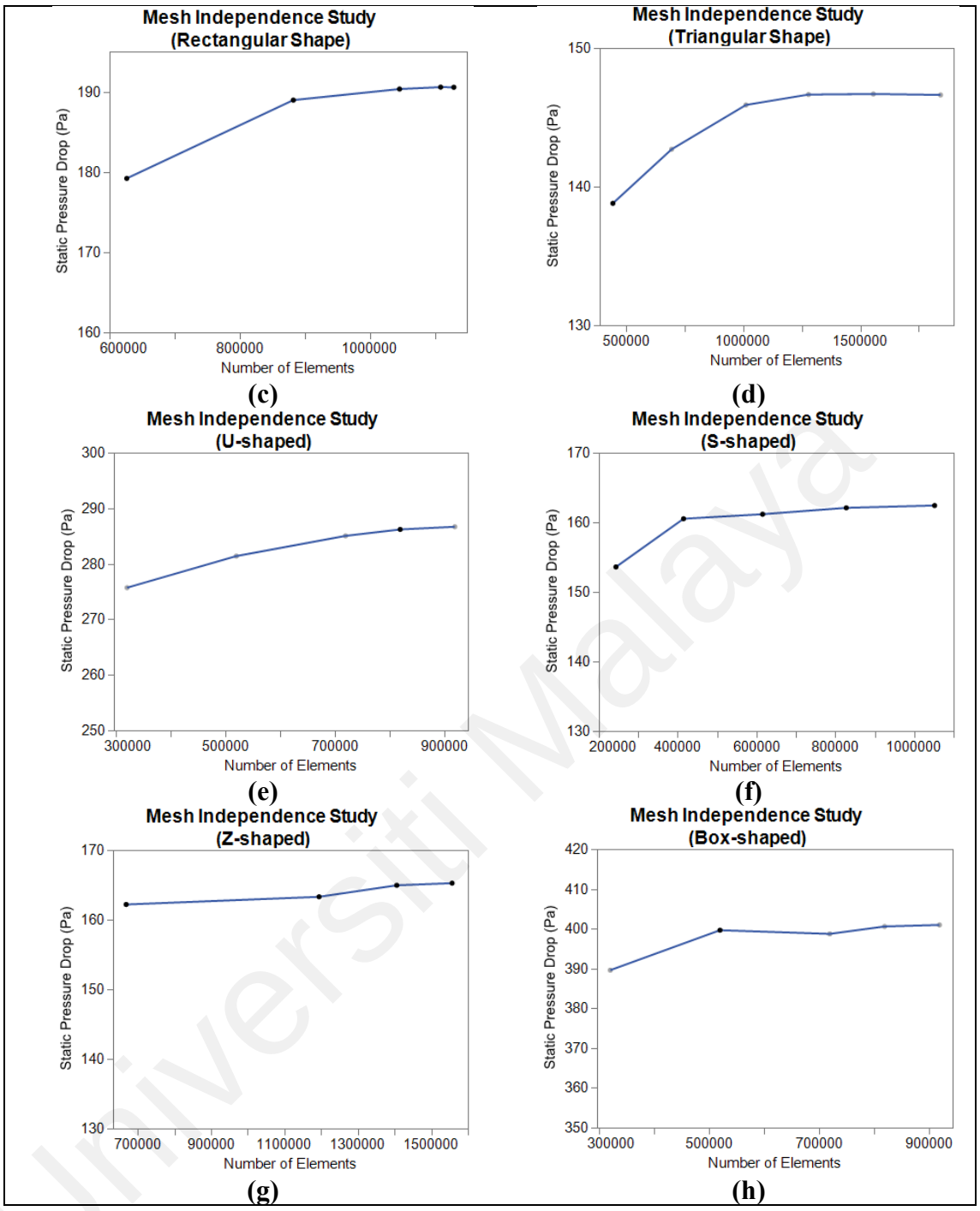

Figure 4.6: Independence Mesh Study (a) 2D Flat Sheet Media (b) 3D Flat Sheet Media (c) Rectangular (d) Triangular (e) U-shaped (f) S-shaped (g) Z-shaped (h) Box-shaped

Table 4.1: Number of Elements with Respective Skewness and Orthogonal Quality

Study Case	Number of Elements Used	Maximum Skewness	Minimum Orthogonal Quality
2D Flat Shape Media	48,000	8.9121×10^{-6}	1.0000
3D Flat Shape Media	992,768	0.0228	0.9939
Rectangular	1,045,636	0.5000	0.7071
Triangular	1,278,000	0.4794	0.7242
U-shaped	819,360	0.5000	0.7032
S-shaped	827,640	0.5000	0.7088
Z-shaped	1,405,920	0.5000	0.7183
Box-shaped	819,360	0.5000	0.7047

4.2.2 CFD Models

4.2.2.1 Viscous Model

The Reynolds number for the rectangular and triangular pleat shape is 5364 whereas the Reynolds number for box-shaped, U-shaped, S-shaped and Z-shaped is 4828. Therefore, the Shear-Stress Transport (SST) k-ω turbulence model is used as the viscous model is applied to compute the turbulence behaviours of the air flow across filter media pack. Shear-Stress Transport (SST) k-ω turbulence model is the refinement of the standard k-ω model, and it is suitable to simulate for the flow that involves flow separation and adverse pressure gradient. The Shear-Stress Transport (SST) k-ω turbulence model is able to give reasonable accuracy by using less computational resources and time (Ferziger et al., 2002; Fluent, 2017). The accuracy of the results can be further increased by applying the second upwind scheme discretization method.

4.2.2.2 Porous Media Model

Darcy Forchheimer equation is used to predict the pressure drop across a porous region, ΔP. Two parameters are included in the Equation (4.1) which is the viscous and inertial

resistance to the airflow (Théron et al., 2017) where Z is the media thickness; μ and ρ are the air dynamic viscosity and density; B is the media permeability; C is the inertial resistance coefficient and V_f is the air velocity.

$$\frac{\Delta P_0}{Z} = \frac{\mu}{B} \cdot V_f + \frac{C}{2} \rho \cdot {V_f}^2 \quad \textbf{(4.1)}$$

B is calculated to be $1.23 \times 10^{-11}\, m^2$ and C is $1.24 \times 10^{6}\, m^{-1}$ based on the data extracted from manufacturer's technical sheet, which is attached in Appendix A. The flow inside the porous zone is laminar as the Reynolds number is small (Cai, 1993; Feng & Long, 2016; Théron et al., 2017).

4.3 Construction of Testing Equipment

Full-scale testing equipment according to air filter testing standard, ISO 16890:2016 with burst pressure testability is constructed to test air filter performance. This standard is chosen as a reference for the test rig design because ISO 16890:2016 is now widely used in the industry due to the new classification method as discussed in Chapter 3.

The testing equipment is able to determine the filtration efficiency with the aid of aerosol generation system, airflow resistance with variable airflow system, the classification of each air filter based on fractional efficiency of the air filter of a specific size range and burst pressure of air filter with increased airflow across the filter or by feeding additional synthetic test dust to filter. The cross-sectional area of the test duct is 610 mm x 610 mm, which is the typical size of an air filter. Figure 4.7 shows the location of the instruments in the testing equipment. The components and their functions are summarized in Table 4.2. The measuring devices are the important components for testing. To ensure the measurement accuracy, all measuring devices are calibrated by third party laboratory complied with ISO 17025.

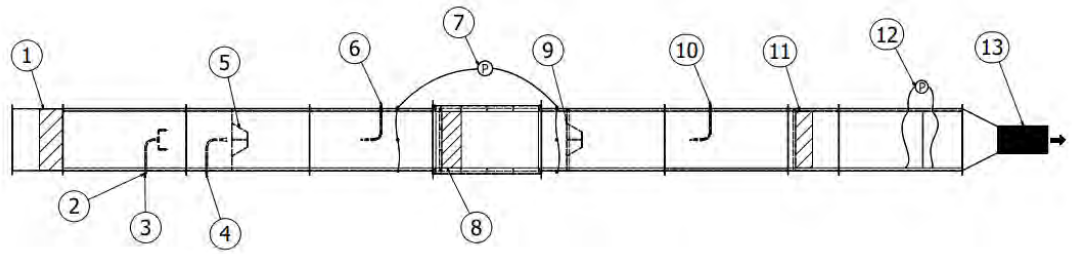

1	HEPA Filter	8	Test Filter
2	DEHS Aerosol Probe (Connected to DEHS Aerosol Generator)	9	Mixing Orifice (For Efficiency Test) Final Filter (For Dust Loading Test)
3	KCl Aerosol Probe (Connected to KCl Aerosol Generator)	10	Downstream Particle Counter (Connected to Optical Particle Counter)
4	Dust Injection Probe (Connected to Dust Feeder)	11	HEPA Filter
5	Mixing Orifice	12	Air Flow Meter
6	Upstream Particle Counter (Connected to Optical Particle Counter)	13	Connect to Blower
7	Differential Pressure Gauge		

Figure 4.7: Schematic Drawing of Testing Equipment

Figure 4.8: Complete Testing Equipment

Table 4.2: List of Instruments and Measuring Devices

Component	Model	Function
Pre-Filters, Secondary Filters & HEPA Filter Section	2 units of JAF Deakleen SU 594x594x44 mm 2 units of JAF Miracel II MH 594x594x95 mm 1 unit of JAF Lunacel HC 600x1200x149 mm	To filter entering air and make sure air is clean before the aerosol purge
DEHS Aerosol Generator and Probe	ATM 231 Atomizer Aerosol Generator	Liquid phase aerosol which is to generate particle size range from 0.3 μm to 1.0 μm.
KCl Aerosol Generator and Probe	TSI Model 8108-1	Solid-phase aerosol which is to generate particle size range from 1.0 μm to 10.0 μm.
Dust Feeder	-	To feed air into the test duct to determine arrestance of the air filter
Mixing orifice and Perforated Plate	-	To ensure even distribution of air particles in laminar airflow.
Optical Particle Counter	2 units of LAP 340 Laser Aerosol Particle Counter	Device for detecting and counting the number of air particle present in the sample air
Differential Pressure Gauge	Beck 984M	To determine the pressure drop across the test filter.
Test Filter Section	-	To install a test filter
Final Filter	-	To capture dust which cannot be filtered by test filter
Downstream HEPA Filter	1 unit of JAF Lunacel TS 600x600x292 mm	To ensure air is clean before it is released to the environment
Air Flow Meter	Beck 984M with AFG-1 Averaging Flow Grid	To measure volumetric airflow in the test duct
Blower with VSD controller	VCM 561 N	To suck and control the required airflow

4.4 Experimental Data Collection

In order to determine the final resistance, the factors affecting the filtration performance such as type of fibreglass media, filtration velocity, pleat density and pleat depth are studied. The performance of air filters is evaluated at its clean state and followed by a dust loading procedure.

4.4.1 Test Aerosol

Test aerosol is used to generate fine particles to determine filtration efficiency. Two types of aerosol are used in this study which are the liquid phase aerosol of DEHS (DiEthylHexylSebacate) and the solid phase aerosol of potassium chloride (KCl) (ISO, 2016c). DEHS droplets are generated using a Laskin nozzle by ATM 231 Atomizer Aerosol Generator. DEHS is used in the particle size range of 0.3 µm to 1.0 µm. The solid phase aerosol or KCl aerosol is used in a relatively larger particle range from 1.0 µm to 10.0 µm. The KCl aerosol is generated using TSI Model 8108-1 aerosol generator.

The aerosol particle generated is counted using optical particle counters. Two similar units of LAP 340 Laser Aerosol Particle Counter are used to measure the upstream and downstream aerosol particles. There are 12 particle size channels used to cover the particle size range from 0.3 µm to 10.0 µm, as shown in Table 4.3.

Table 4.3: Particle Counter Channel Size Range

Size Range Channel	Lower Limit of Particle Channel (µm)	Upper Limit of Particle Channel (µm)
1	0.30	0.40
2	0.40	0.55
3	0.55	0.70
4	0.70	1.00
5	1.00	1.30
6	1.30	1.30
7	1.30	2.20
8	2.20	3.00
9	3.00	4.00
10	4.00	5.50
11	5.50	7.00
12	7.00	10.00

4.4.2 Synthetic Test Dust

ISO 15957-L2 test dust is used for the dust loading process. This test dust is as known as ISO 12103-A2 fine dust, with an approximate bulk density of 900 kg/m^3 (ISO, 2015).

Table 4.4 shows the dust particle size distribution of ISO 15957-L2 test dust, while Figure 4.9 is plotted using the median value of the maximum volume fraction.

Table 4.4: Dust Particle Size Distribution (ISO, 2016a)

Size (µm)	Maximum Volume Fraction (%) for ISO 15957-L2/ ISO 12103-A2 test dust
1	2.5 to 3.5
2	10.5 to 12.5
3	18.5 to 22.0
4	25.5 to 29.5
5	31 to 36
7	41 to 46
10	50 to 54
20	70 to 74
40	88 to 91
80	99.5 to 100
120	100

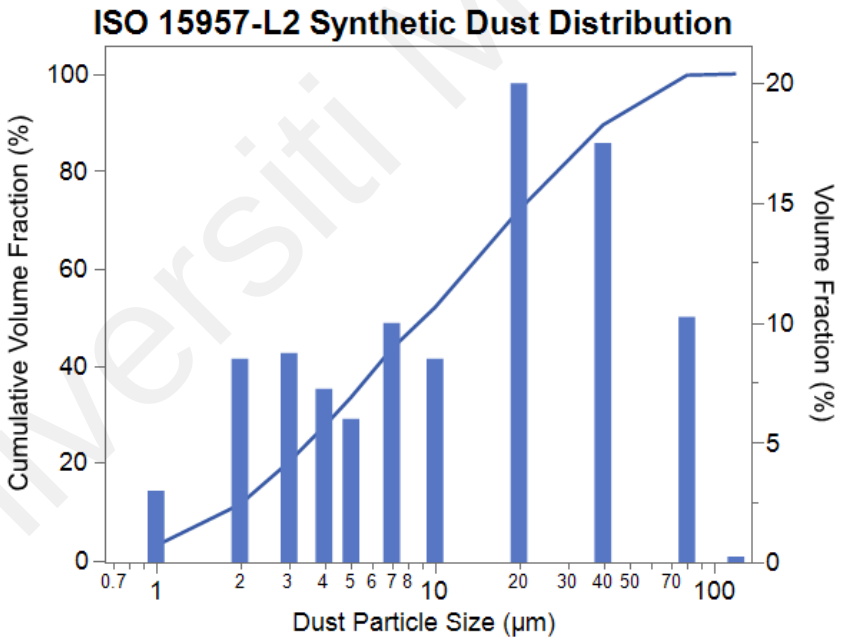

Figure 4.9: Dust Particle Size Distribution

4.4.3 Testing Procedure

To determine the filter performance, the test sequence is described below. The full test sequence is repeated three times with new filters of a similar model to ensure the repeatability of the experiment. The assumptions made for the test procedures are the airflow is in a steady-state condition, and the system is under isothermal condition.

(a) ***Determination of Initial Pressure Drop***

1. The test filter is installed accordingly
2. The pressure drop is measured at 50 %, 75 %, 100 %, and 125 % of the rated air flow rate, which is 0.944 m^3/s. This corresponds to filtration velocity of 1.27 m/s, 1.90 m/s, 2.54 m/s and 3.17 m/s.

(b) ***Determination of Initial Fractional Efficiency***

(i) Correlation Counts (Without test filter installed)

3. The test filter is removed from the test duct. The beginning background counts are measured for upstream, $U_{B,c,b,ps}$ and downstream, $d_{b,c,ps}$.
4. The DEHS aerosol generator is started and stabilized.
5. The efficiency counts (without test filter installed, but with DEHS aerosol started) are measured for upstream, $U_{c,i,ps}$ and downstream, $D_{c,i,ps}$ at a particle size range of 0.3 µm to 1.0 µm. 5 samples ($i = 1,2, \dots ,5$) of 30 seconds measurements are taken for upstream and downstream counts. The DEHS aerosol is then stopped.
6. The KCl aerosol generator is started and stabilized.
7. The efficiency counts (without test filter installed, but with KCl aerosol started) are measured for upstream, $U_{c,i,ps}$ and downstream, $D_{c,i,ps}$ at particle size range of 1.0 µm to 10.0 µm. 5 samples ($i = 1,2, \dots ,5$) of 30 seconds measurements are taken for upstream and downstream counts. The KCl aerosol generator is then stopped
8. The final background counts are measured for upstream, $U_{B,c,f,ps}$ and downstream, $d_{c,f,ps}$. Step 3 to step 8 is used to determine the correlation ratio for the efficiency calculation later.

(ii) Efficiency Counts (With test filter installed)

9. The test filter is then installed. The beginning background counts are measured for upstream, $U_{B,b,ps}$ and downstream, $d_{b,ps}$.
10. The DEHS aerosol generator is started and stabilized.
11. The efficiency counts (with test filter installed and DEHS aerosol started) are measured for upstream, $U_{i,ps}$ and downstream, $D_{i,ps}$ at particle size range of 0.3 µm to 1.0 µm. 5 samples ($i = 1,2, \dots ,5$) of 30 seconds measurements are taken for upstream and downstream counts. The DEHS aerosol is then stopped.
12. The KCl aerosol generator is started and stabilized.
13. The efficiency counts (with test filter installed and KCl aerosol started) are measured for upstream, $U_{i,ps}$ and downstream, $D_{i,ps}$ at a particle size range of 1.0 µm to 10.0 µm. 5 samples ($i = 1,2, \dots ,5$) of 30 seconds measurements are taken for upstream and downstream counts. The KCl aerosol generator is then stopped
14. The final background counts are measured for upstream, $U_{B,f,ps}$ and downstream, $d_{f,ps}$.

(c) *Conditioning Procedure*

15. The test filter is then placed inside a cabinet filled with isopropanol (IPA) vapour to carry out discharge process of the test filter for 24 hours.
16. After 24 hours, the test filter is placed under standard climatic conditions for at least 30 minutes.

(d) *Determination of Discharged Fractional Efficiency*

17. To determine the discharged fractional efficiency, Steps 3 to 14 are repeated by using the discharged test filter.

(e) ***Determination of Arrestance, Dust Holding Capacity & Final Pressure Drop***

18. The final filter is weighed and recorded. The test filter and final filter are installed to the duct. The final filter is installed downstream of the test filter, which is installed as Item 9 from Figure 4.7, to recapture penetrated dust of the test filter.
19. The test filter is progressively loaded with ISO 15957 L2 synthetic. The first stage of dust feeding is stopped after 30g of dust is loaded or an increase of 10 Pa of the test filter. This gives the initial arrestance of the test filter.
20. Before stopping each stage of the dust feeding, the leftover dust which remains in the feeder tray to the dust pickup tube is brushed, and the dust feeder is vibrated for 30 seconds to entrain the dust into the duct airflow. The total dust loaded and the consequent pressure drop of the test filter is recorded after each feeding stage.
21. The dust feeding is stopped, and the final filter is reweighed. The dust left between the test filter, and the final filter is collected and included in the final filter weight.
22. The dust feeding cycle is repeated from steps 19 to 21 to obtain a smooth dust loading curve until the filter media breaks or a drop of arrestance more than 2%.

A similar procedure is used to investigate other factors affecting the filtration performance such as type of fibreglass media, filtration velocity, pleat density and the pleat depth.

4.4.4 Calculation Formulae

4.4.4.1 Filtration Efficiency

As described in Section 4.4.3(b), the background counts (both correlation and efficiency) are averaged.

The correlation ratio, R is used to correct any bias that happened due to probably systematic errors in the experiments between upstream and downstream sampling systems. The correlation ratio is calculated from the ratio of downstream to upstream

particle counts when only aerosol generator is on and without any test filter installed. These particle counts are recorded in Steps 5 and 7 in Section 4.4.3(b). The individual correlation ratios calculated from each sampling repetition, $R_{i,ps}$ are averaged to obtain a final correlation ratio for each particle size, $\bar{R}_{ps}$. The standard deviation of the correlation ratio, $\delta_{c,ps}$ is determined. The particle size channel is summarized in Table 4.3. The geometrical mean diameter, $\bar{d}_{ps}$ is used to represent the particle size, ps.

$$\bar{d}_{ps} = \sqrt{d_{ps} + d_{ps+1}} \quad \textbf{(4.2)}$$

where d_{ps} is the lower limit of the particle size channel and d_{ps+1} is the upper limit of the particle size channel.

The fractional efficiency is the percentage of particles a test filter can remove from the air and is calculated from the penetration of the particles. The observed penetration of particles, $P_{i,o,ps}$ is calculated from the ratio of downstream to upstream particle counts when only aerosol generator is on and with the test filter installed. These particle counts are recorded in Step 11 and 13 in Section 4.4.3(b). These penetrations are averaged to find the observed penetration value for each particle size $\bar{P}_{o,ps}$. The standard deviation of the observed penetration, $\delta_{o,ps}$ is determined.

The final penetration of each particle size, $\bar{P}_{ps}$ is obtained by correcting the observed penetration, $\bar{P}_{o,ps}$ with the correlation ratio, $\bar{R}_{ps}$. This is to reduce the bias that happened due to the systematic error in the experiments. The total error is calculated by combing the standard deviation of the correlation ratio and observed penetration.

The fractional efficiency, η_{ps} can be calculated from the final penetration values, $\bar{P}_{ps}$. The same calculation method is used for both initial and discharged efficiencies. The filtration efficiency is taken from the average of the initial and the discharged efficiencies

of the test filter. Table 4.5 and Table 4.6 summarizes the formulae used in fractional efficiency calculation and the respective nomenclature used.

Table 4.5: Formulae in Calculating Fractional Efficiency (ISO, 2016c)

Description			**Formulae**	
Referring to Section 4.4.3(b)	**Terms**			
Step 3 & 8	Correlation background count	Upstream	$U_{B,c,ps} = \frac{U_{B,c,b,ps} + U_{B,c,f,ps}}{2}$	**(4.3)**
		Downstream	$D_{B,c,ps} = \frac{d_{b,c,ps} + d_{c,f,ps}}{2}$	**(4.4)**
Step 9 & 14	Efficiency background count	Upstream	$U_{B,ps} = \frac{U_{B,b,ps} + U_{B,f,ps}}{2}$	**(4.5)**
		Downstream	$D_{B,ps} = \frac{d_{b,ps} + d_{f,ps}}{2}$	**(4.6)**
Step 5 & 7	Correlation Ratio	Each sampling	$R_{i,ps} = \frac{D_{c,i,ps}}{U_{c,i,ps}}$	**(4.7)**
		Average	$\bar{R}_{ps} = \frac{\sum_{i=1}^{n} R_{i,ps}}{n}; n = 5$	**(4.8)**
		Standard Deviation of Each Sampling	$\delta_{c,ps} = \sqrt{\frac{\sum_{i=1}^{n}(R_{i,ps} - \bar{R}_{ps})^2}{n-1}}$	**(4.9)**
Step 11 & 13	Observed Penetration	Each observed penetration sampling	$P_{i,o,ps} = \frac{D_{i,ps}}{U_{i,ps}}$	**(4.10)**
		Average observed penetration	$\bar{P}_{o,ps} = \frac{\sum_{i=1}^{n} P_{i,o,ps}}{n}; n = 5$	**(4.11)**
		Standard Deviation of Each Penetration Sampling	$\delta_{o,ps} = \sqrt{\frac{\sum_{i=1}^{n}(P_{i,o,ps} - \bar{P}_{o,ps})^2}{n-1}}$	**(4.12)**
-	Final Penetration	Each particle size	$\bar{P}_{ps} = \frac{\bar{P}_{o,ps}}{\bar{R}_{ps}}$	**(4.13)**
		Total error	$\delta_{ps} = \bar{P}_{ps}\sqrt{(\frac{\delta_{c,ps}}{\bar{R}_{ps}})^2 + (\frac{\delta_{o,ps}}{\bar{P}_{o,ps}})^2}$	**(4.14)**
	Fractional Efficiency	Each particle size	$\eta_{ps} = (1 - \bar{P}_{ps}) \times 100\%$	**(4.15)**

Table 4.6: Nomenclature used in Filtration Efficiency Calculation Formula

Symbol	Description
$U_{B,c,ps}$	Upstream background average correlation count for each particle size
$U_{B,c,b,ps}$	Beginning upstream background average correlation count for each particle size
$U_{B,c,f,ps}$	Final upstream background average correlation count for each particle size
$D_{B,c,ps}$	Downstream background average correlation count for each particle size
$d_{b,c,ps}$	Beginning downstream background average correlation count for each particle size
$d_{c,f,ps}$	Final downstream background average correlation count for each particle size
$U_{B,ps}$	Upstream background average efficiency count for each particle size
$U_{B,b,ps}$	Beginning upstream background average efficiency count for each particle size
$U_{B,f,ps}$	Final upstream background average efficiency count for each particle size
$D_{B,ps}$	Downstream background average efficiency count for each particle size
$d_{b,ps}$	Beginning downstream background average efficiency count for each particle size
$d_{f,ps}$	Final downstream background average efficiency count for each particle size
$R_{i,ps}$	Correlation ratio for each sample i and each particle size
$D_{c,i,ps}$	Downstream correlation count for each particle size
$U_{c,i,ps}$	Upstream correlation count for each particle size
$\bar{R}_{ps}$	Final correlation ratio for each particle size
n	Number of samples
$\delta_{c,ps}$	Standard deviation of the correlation ratio for each particle size
$P_{i,o,ps}$	Observed penetration for each sample i and each particle size
$D_{i,ps}$	Downstream efficiency particle count for each particle size
$U_{i,ps}$	Upstream efficiency particle count for each particle size
$\bar{P}_{o,ps}$	Observed penetration for each particle size
$\delta_{o,ps}$	Standard deviation of the observed penetration for each particle size
$\bar{P}_{ps}$	Final penetration for each particle size
δ_{ps}	Standard deviation of the final penetration for each particle size
η_{ps}	Fractional efficiency for each particle size

4.4.4.2 Arrestance

Arrestance, A_j is calculated after each dust loading step, j with

$$A_j = \left(1 - \frac{m_j}{M_j}\right) \times 100\% \tag{4.16}$$

where m_j is the mass of dust passing the filter (total mass gain of final filter and the dust collected between the test filter and final filter and M_j is the mass of loaded dust during the dust loading stage j.

4.4.5 Test Filters Used

The test filter model selected is a pleated secondary filter, as shown in Figure 4.10(a). The filter media used is fibreglass with hot-melt separator. The cross-sectional filter size is 594 mm (Width) × 594 mm (Height). The pleat depth used is 44 mm, 60 mm, 75 mm, 85 mm, and 95 mm. There are four types of fibreglass media used, namely media A, B, C, and D. As for pleat density, which is defined by the number of pleats per inch media, 3.5 pleats per inch (PPI), 4.0 PPI, 4.5 PPI, 5.0 PPI, 6.0 PPI and 6.5 PPI are tested. Figure 4.10(b) defines the pleat geometry, and the pleat width can be calculated with Equation (4.17).

$$Pleat\ width, P_w(mm) = \frac{25.4}{no.of\ pleats\ per\ inch} \tag{4.17}$$

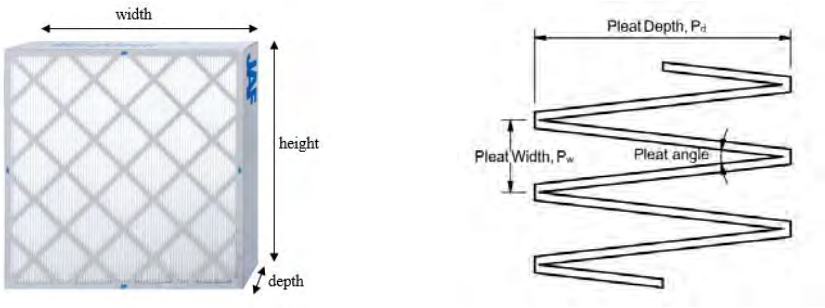

(a) **(b)**

Figure 4.10: (a) Test Filter Model (b) Pleat Geometry

4.4.6 Physical Properties of Media Used

As mentioned earlier, there are four types of different filter fibreglass media investigated in this study, namely media A, B, C and D. The physical properties of the media used are analysed on their effect on the filter performance. The tensile strength of the media, fibre diameter, media thickness and filter packing density are determined. The specification sheets of each media are attached in Appendix A.

4.4.6.1 Scanning Electron Microscope

A scanning electron microscope (SEM) uses a beam of focused electrons over a surface to gain information about the surface composition and topography, creating an image of the surface. The four filter fibre samples are scanned for their microstructure using SEM. The Quanta 200 FEG Scanning Electron Microscope is used. A high vacuum of 70 Pa and a high voltage of 5.00 kV are used.

The SEM images generated are analysed using software Image J to study the microstructure of the filter media, which is the fibre diameter. The geometric mean diameter of the fibre is calculated from 150 fibres in the image (Baheti & Tunák, 2017; Shin et al., 2008). Figure 4.11 shows the labelling of the measurements in the SEM images.

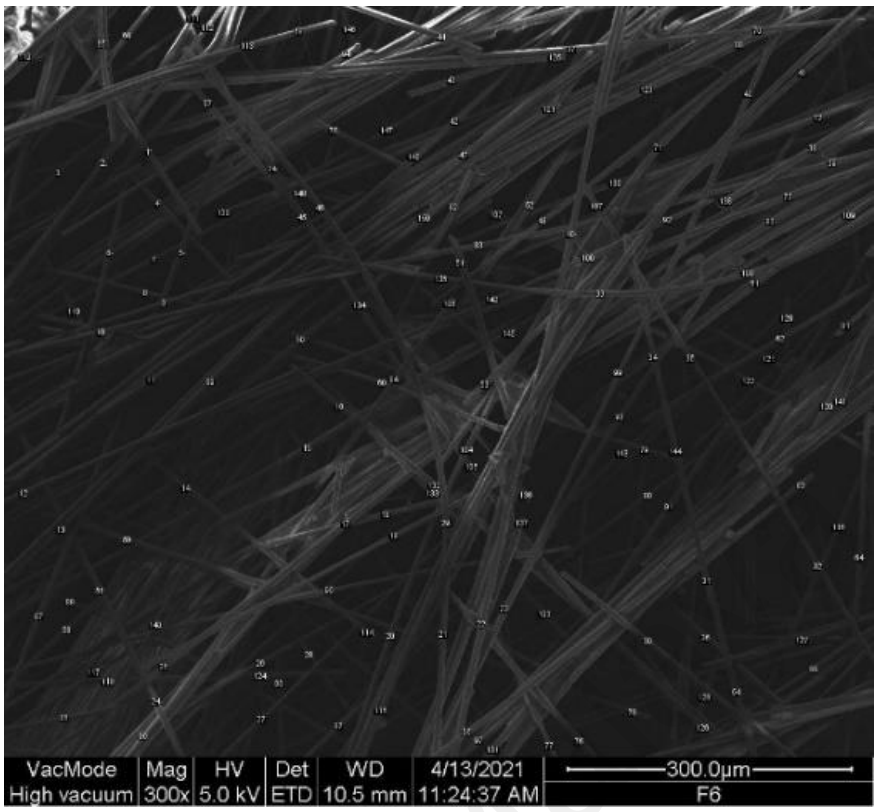

(a)

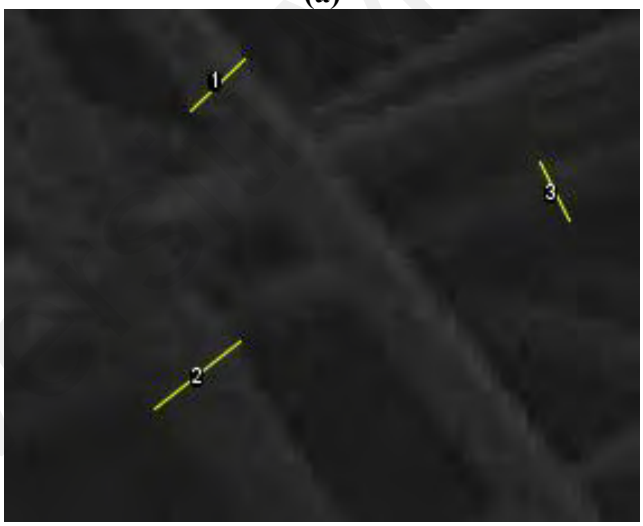

(b)

Figure 4.11: Labelling of Measurements in SEM Image (a) Overall (b) Zoom-in

4.4.6.2 Tensile Strength

The tensile strength of each media type is tested using Victor Manufacturing Electromechanical Benchtop Type Tensile Machine VEW 220 Series. A total of 3 samples in the machine direction (MD) and 3 samples in the cross direction (CD) are cut from the fibre media roll and labelled accordingly, as shown in Figure 4.12 with dimensions of 25 mm × 350 mm. The sample is fixed in an upright position with a test span gap of 180 ± 5 mm in the test machine, as shown in Figure 4.13(b). The elongation

speed used in this test machine is 25 mm/min. Raw data collected is extracted from the software for data analysis.

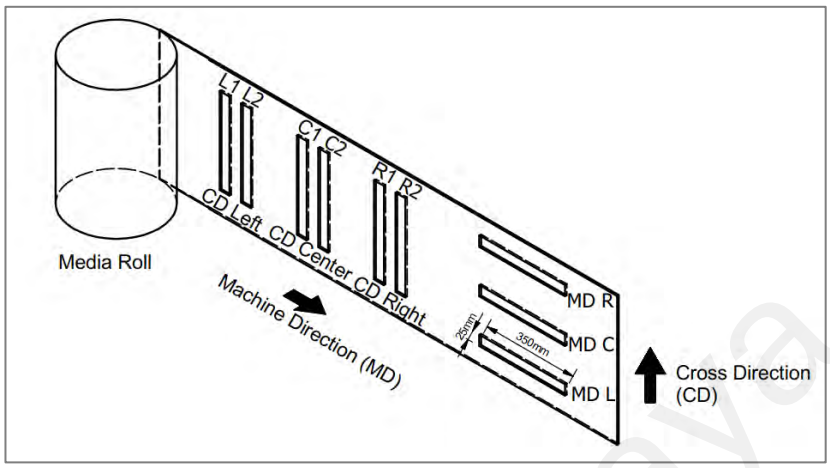

Figure 4.12: Media Samples Preparation for Tensile Test

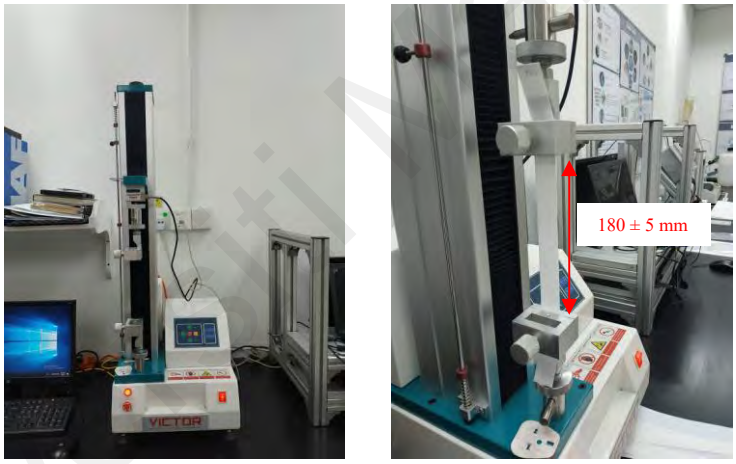

(a) (b)

Figure 4.13: (a) Tensile Machine (b) Installation of Media Sample

4.5 Linear Multiple Regression for Data Analysis

Linear multiple regression is used to study the empirical models of the filtration performance parameters, which are filtration efficiency, initial resistance, pressure drop across dust cake and dust holding capacity, using 51 sets of experimental data obtained in this study. The filtration performance parameter is the predicted dependent variable used in linear multiple regression modelling, whereas the independent predictor variables or the filter design parameters in this study are the fibre diameter, d_f filter packing

solidity, $\propto_f$, filtration velocity, V_f, pleat depth, P_d and pleat density P_ρ. The analysis software used in the linear multiple regression is JMP Pro 15.

Equation (4.18) shows the general formula of the linear multiple regression, where y is the predicted dependent variable, β_0 is the y-intercept, β_1 is the regression coefficient of the first independent variable, X_1 and β_n is the regression coefficient of the last independent variable, X_n.

$$y = \beta_0 + \beta_1 X_1 + \ldots + \beta_n X_n \quad \textbf{(4.18)}$$

The multicollinearity between the independent variables is first tested using variance inflation factor (VIF) using Equation (4.19) where VIF_j is the VIF value for independent predictor variable j and R_j^2 is the coefficient of determination. A high VIF shows that the independent variable is highly collinear with another variable in the model. When multicollinearity exists, the precision of the estimated coefficients will reduce and weaken the statistical power of the regression model. According to Daoud (2017), when VIF = 1, the parameters are not correlated, and there are no multicollinearity issues; for 1 < VIF ≤ 5, the parameters are moderately correlated, and the results are acceptable; for VIF ≥ 5, the parameters are highly correlated, and the multicollinearity should be resolved by omitting the redundant variable with higher VIF from the regression model.

$$VIF_j = \frac{1}{1 - R_j^2} \quad \textbf{(4.19)}$$

Then, the analysis of variance using the F-test is carried out to compare the fits between the linear models. If the p-value obtained from F-test is below 0.05, it can be concluded that there is a significant linear relationship between the predicted and predictor variables and the model provides an acceptable fit (Siegel, 2016).

CHAPTER 5: INVESTIGATION OF THE EFFECT OF PLEAT SHAPE ON THE INITIAL PRESSURE DROP USING CFD SIMULATION

Computational Fluid Dynamics (CFD) is efficient in predicting and analysing the fluid flow performance as it is a cost and time-saving method with careful justification. CFD has been useful in determining the air filtration performance (Fan et al., 2018; Feng et al., 2014; Fotovati et al., 2011; Qian et al., 2013). The validated simulation results which have been studied in the literature have proven the reliability of the CFD models. In this chapter, computational fluid dynamics (CFD) is used to study the effect of the pleat shape on the initial pressure drop of the filters. Due to the complexity of fibre media structure, a computational affordable macroscale model is used to determine the pressure drop of the air filters. The filter media is modelled as a porous medium. Firstly, a flat sheet filter media is modelled in 2D and 3D. The simulated result is compared with the datasheet provided by the manufacturer. The same settings are used to study the effect of pleat shape on the initial pressure drop. Six different types of pleat shapes (triangular, rectangular, S-shaped, U-shaped, Z-shaped and box pleats) are investigated in this chapter.

5.1 Model Validations using a Flat Sheet Media

A porous medium model is used to simulate the filter media with the parameters input calculated using Equation (4.1). A flat sheet of filter media in the centre of a computational domain is simulated in 2D and 3D environments.

Figure 5.1 and Figure 5.2 show the pressure drop contour of the flat sheet 2D and 3D models respectively. The air velocity is set at 0.033 m/s, 0.0533 m/s, 0.0667 m/s and 0.0833 m/s to obtain the air resistance curve of the porous media. As depicted in Figure 5.3, it can be observed that 2D simulation provides an acceptable pressure drop compared to the experimental data given by the media datasheet (attached in Appendix A) with a

deviation of less than 5.2 %. However, the 3D simulation shows a higher deviation from the experimental data, which is at a deviation of 15.5%. As the 3D-domain requires high computational demand, 2D-domain with a better prediction is chosen and sufficient for simulation. 2D simulation is widely used in the filtration simulation (Feng et al., 2014; Fotovati et al., 2011; Schousboe, 2017; Théron et al., 2017).

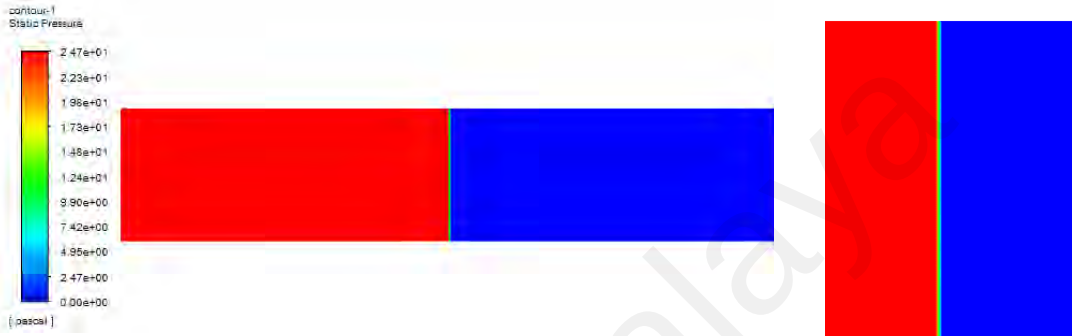

(a) **(b)**

Figure 5.1: Static Pressure of Flat Sheet Model (2D) at Filtration Velocity of 5.33 cm/s (a) Full View (b) Closed-up View

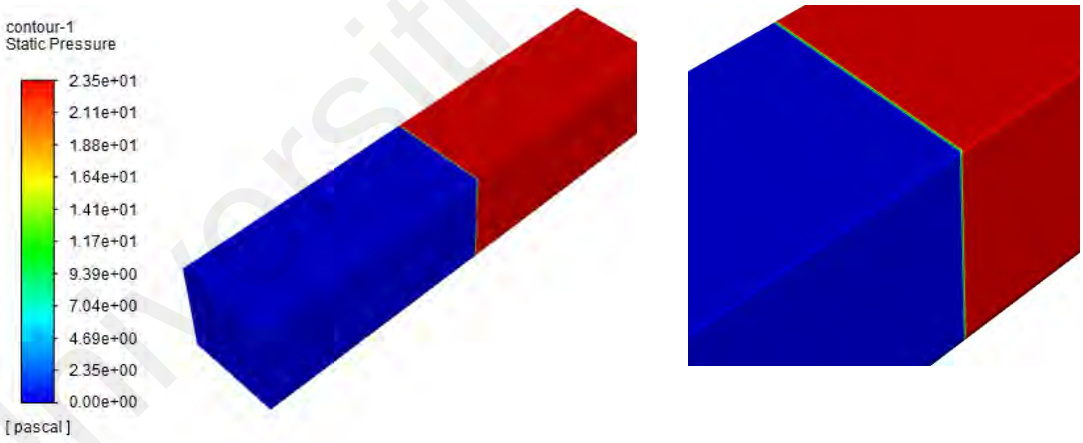

(a) **(b)**

Figure 5.2: Static Pressure of Flat Sheet Model (3D) at Filtration Velocity of 5.33 cm/s (a) Full View (b) Closed-up View

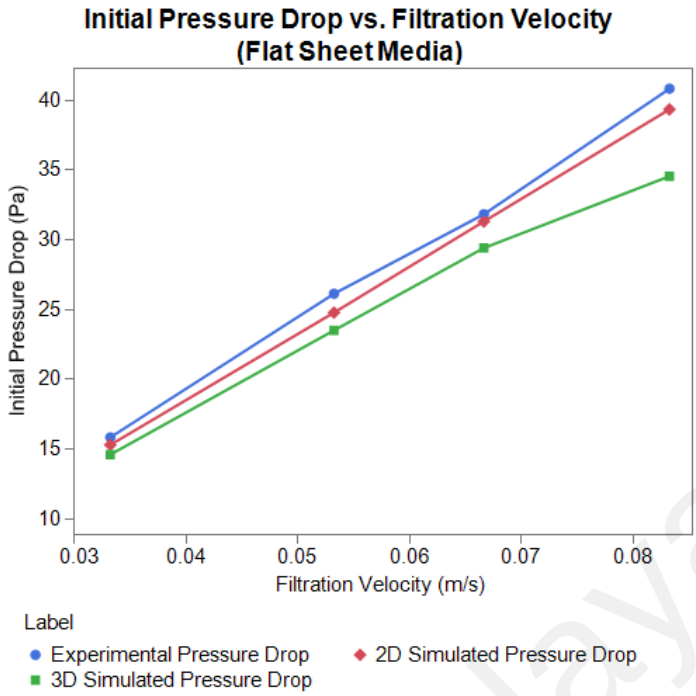

Figure 5.3: Air Resistance Curve of Porous Media

5.2 Effect of Pleat Shapes on Initial Pressure Drop

In the filter application, the flat sheet media is always pleated to increase the filtration area so that it can collect more dust particles within a limited filter cross-sectional area. Besides, a pleated filter is able to increase the physical strength of the filter against a high airflow rate. The pleat shape of the filter can significantly affect the initial pressure drop of the filter, even with the same pleat density, pleat depth and total filtration area. Hence, in this section, six different pleat shapes of the filters, including triangular, rectangular, S-shaped, U-shaped, Z-shaped and box pleats, have been generated, and their effect on the initial pressure drop across filters are studied.

Figure 5.4 shows that the triangular pleat has the lowest pressure drop, followed by S-shaped, Z-shaped, rectangular and U-shaped pleats while the box pleat has the highest pressure drop.

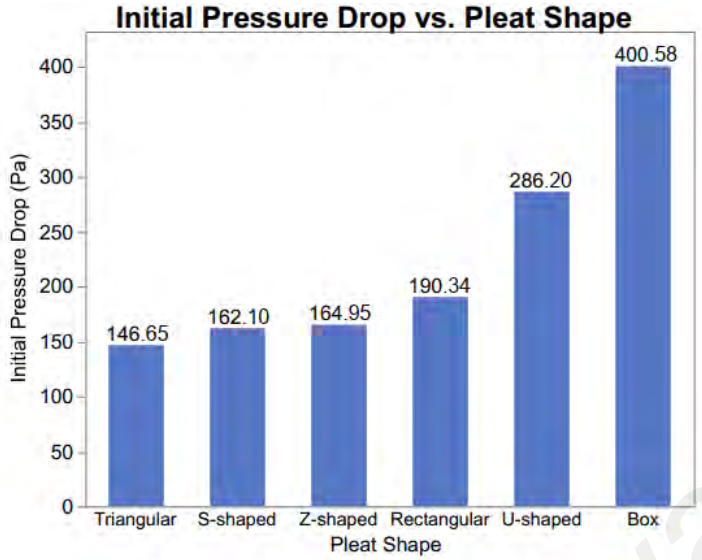

Figure 5.4: Chart of Initial Pressure Drop at Different Pleat Shapes at Filtration Velocity of 2.54 m/s

The triangular pleat shape has the lowest initial pressure drop of 146.65 Pa at the filtration velocity of 2.54 m/s, while the box pleat has the highest initial pressure drop of 400.58 Pa. Observing the pressure contour of the box pleat in Figure 5.5, the airflow from the upstream is halted when reaching the small opening of the porous media zone, causing the pressure building up in the upstream porous area. This halt of airflow is due to the small gap between the box pleats, which blocks the air from passing through, as shown in the velocity vector in Figure 5.6. Compared with the triangular pleat using the velocity vector in Figure 5.8, it shows that the flow is slowly converging into a V-shaped channel, resulting in an overall smooth flow across the porous media. From Figure 5.8(d), the turbulence after the triangular pleat is also minimum. This causes the triangular shape to have the lowest pressure drop of 146.65 Pa among the pleat shapes, as depicted in Figure 5.7.

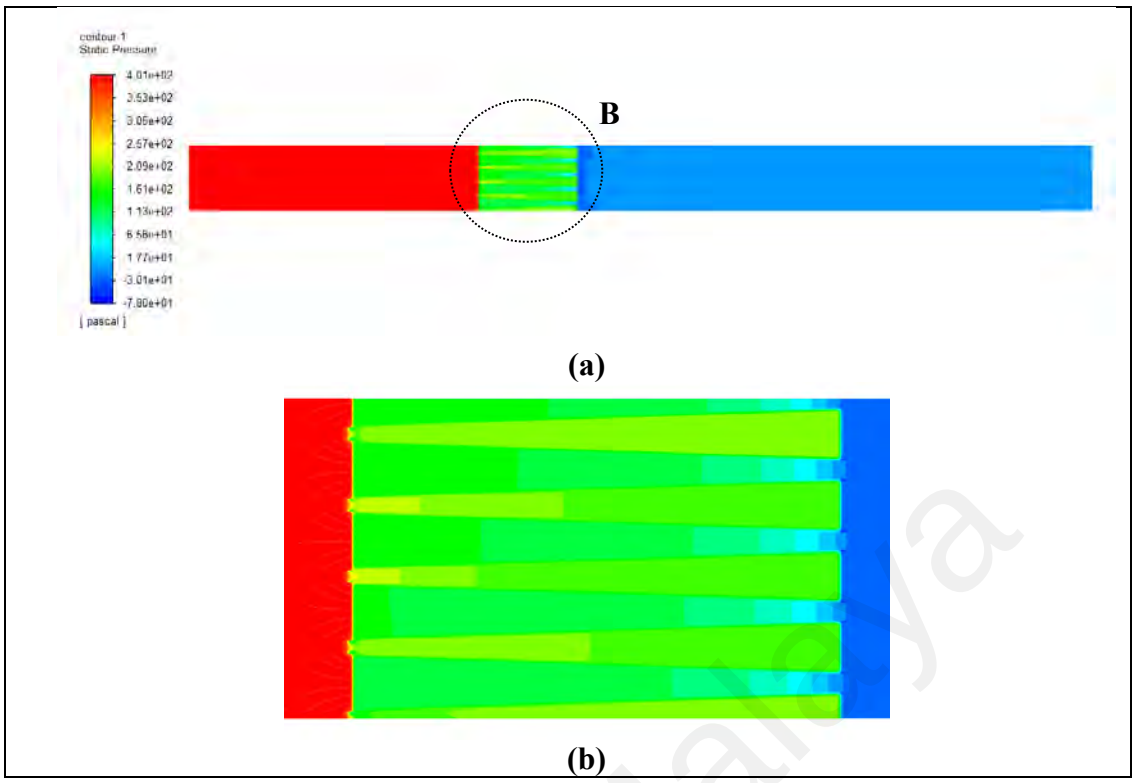

Figure 5.5: Pressure Contours for Box Pleats (a) Overview (b) Detail View B

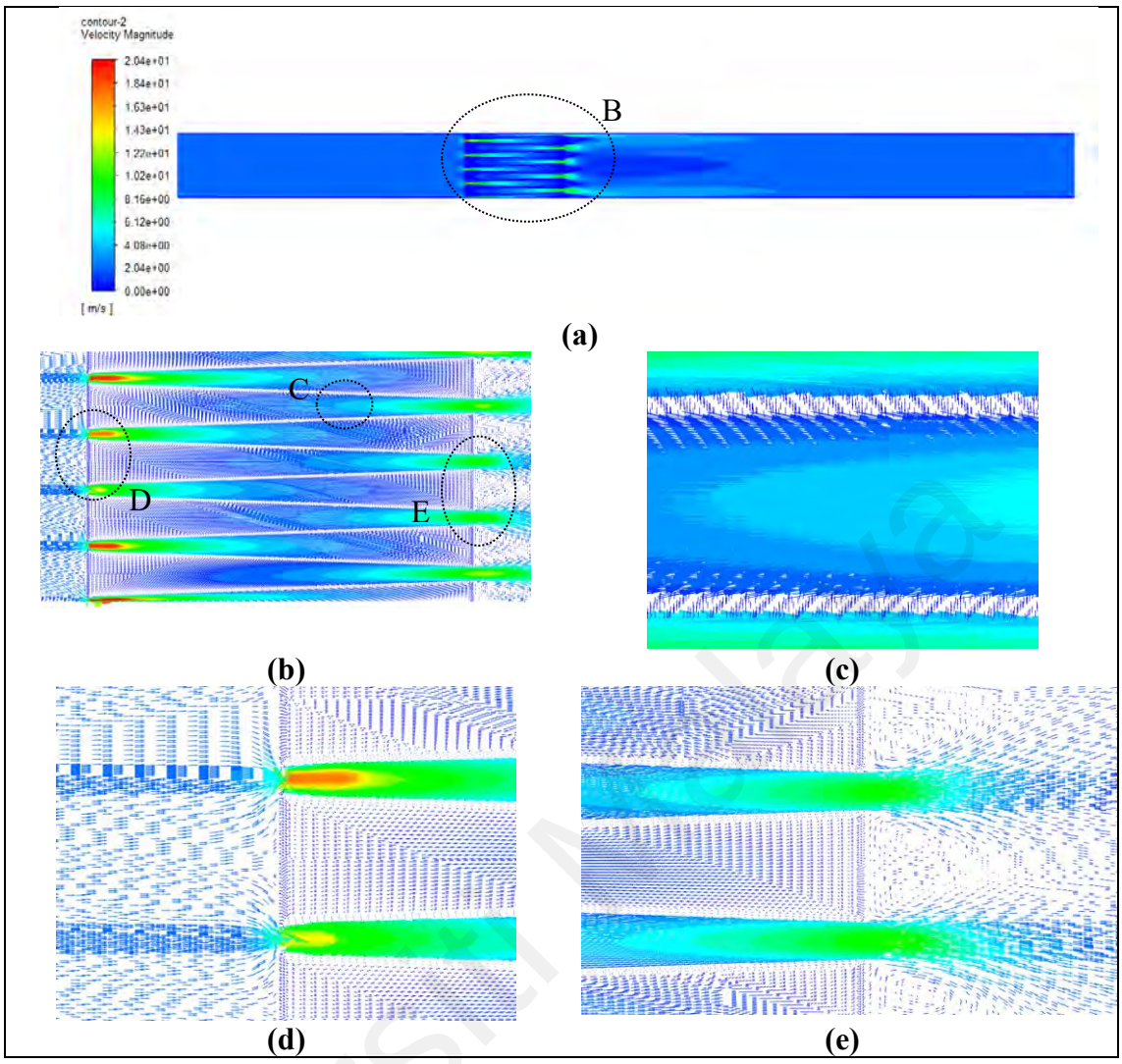

Figure 5.6: Velocity Vectors for Box Pleats (a) Overview (b) Detail View B: Full Pleats (c) Detail View C: Pleat Side (d) Detail View D: Pleat Upstream (e) Detail View E: Pleat Downstream

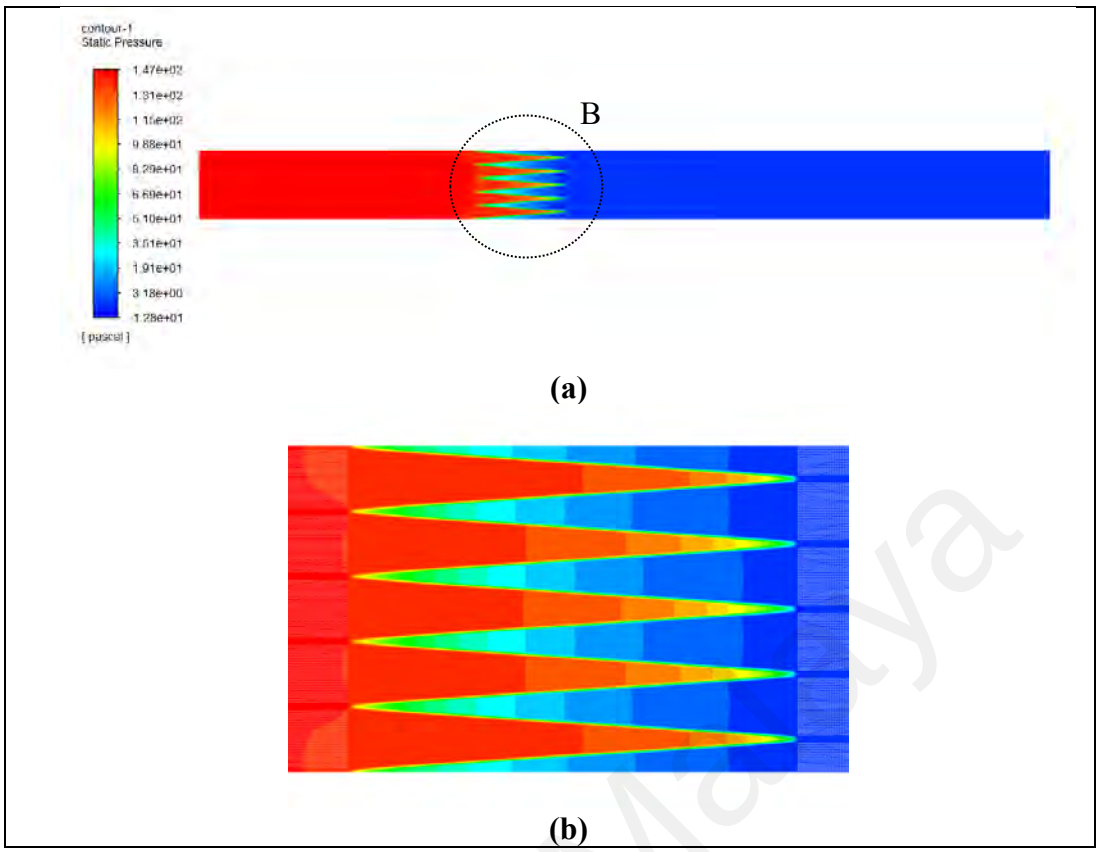

Figure 5.7: Pressure Contours for Triangular Pleats (a) Overview (b) Detail View B

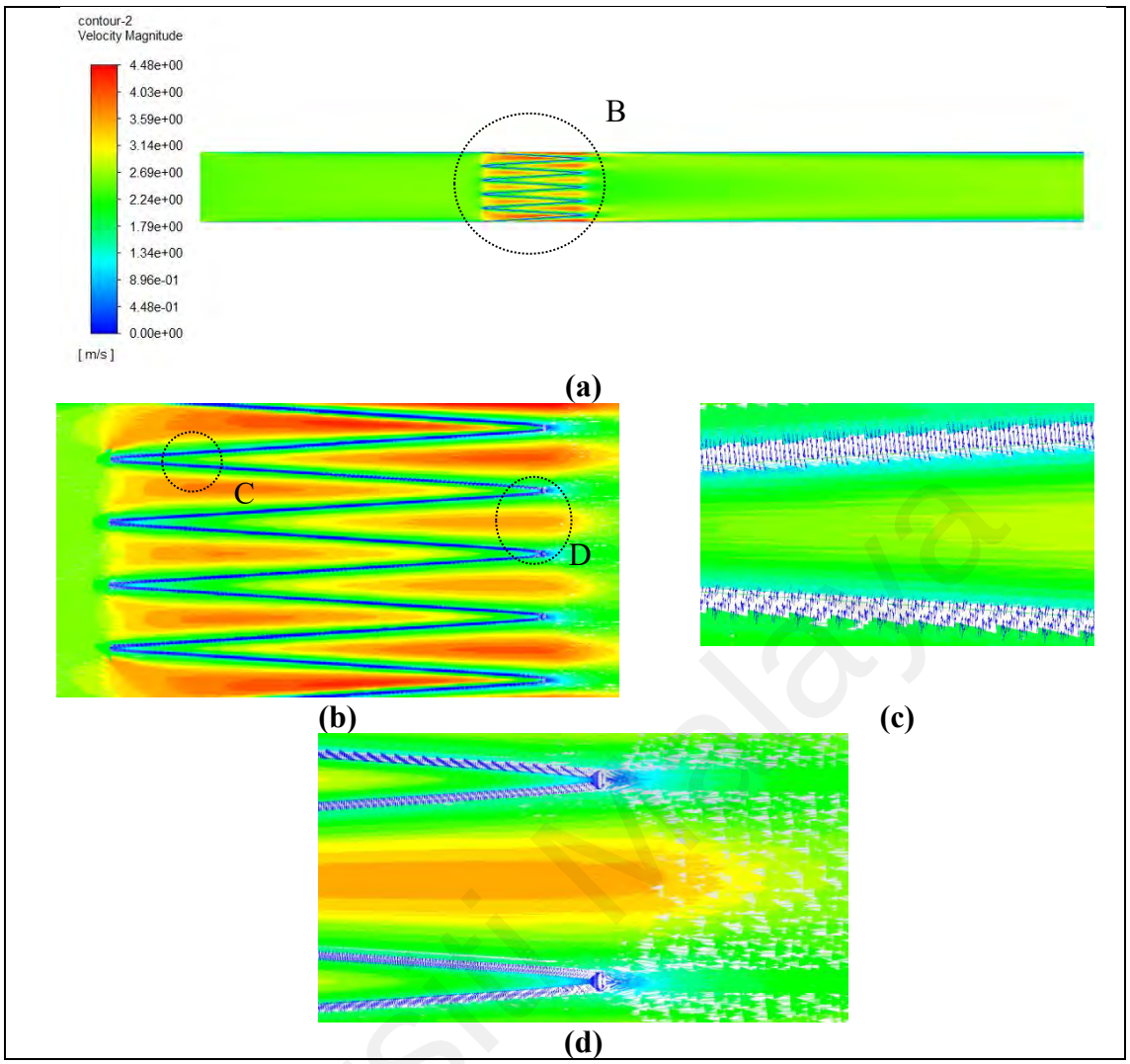

Figure 5.8: Velocity Vectors for Triangular Pleats (a) Overview (b) Detail View B: Full Pleats (c) Detail View C: Pleat Side (d) Detail View D: Downstream Pleat

Comparing the simulation results of Z-shaped pleat from Figure 5.9 and Figure 5.10, Z-shaped pleat has a similar shape configuration to the triangular pleat but with a different pleat angle. This also brings a relatively smooth flow across the slanted pleat of the Z-shaped, but a slight flow blockage happened on the horizontal pleat. Therefore, the Z-shaped pleat has a slightly higher pressure drop of 164.95 Pa at a velocity of 2.54 m/s compared with the triangular pleat at 146.65 Pa.

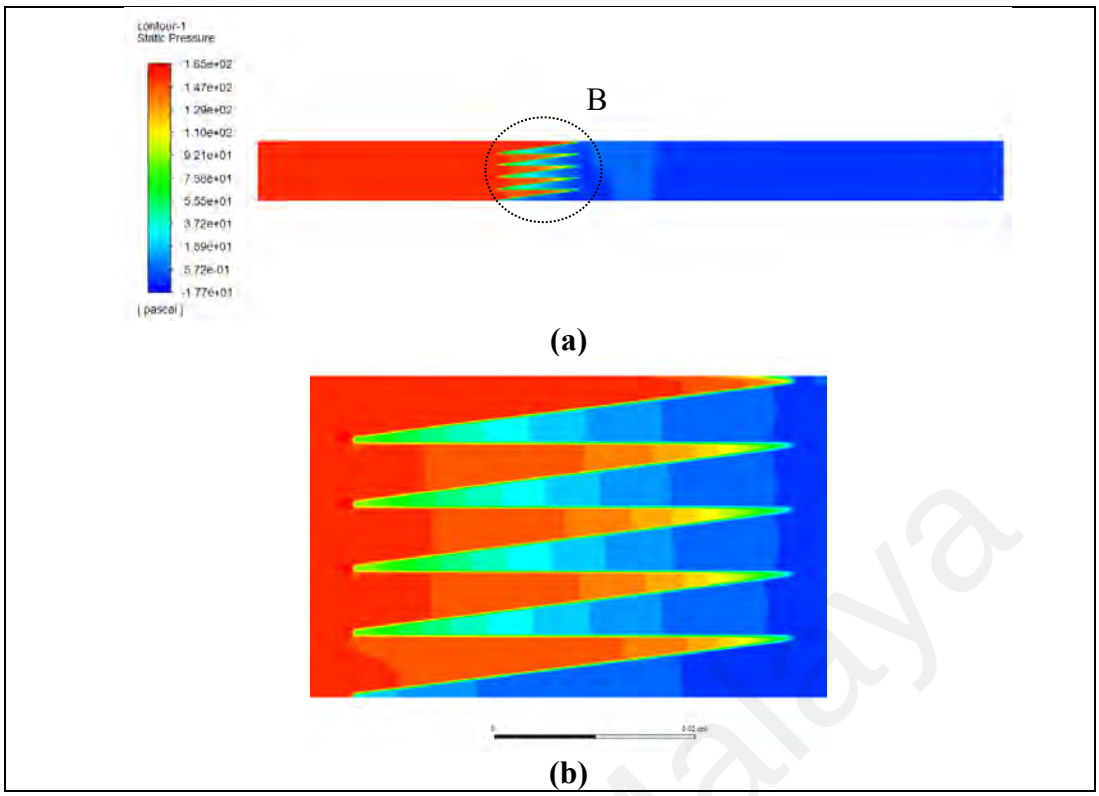

Figure 5.9: Pressure Contours for Z-shaped Pleats (a) Overview (b) Detail View B

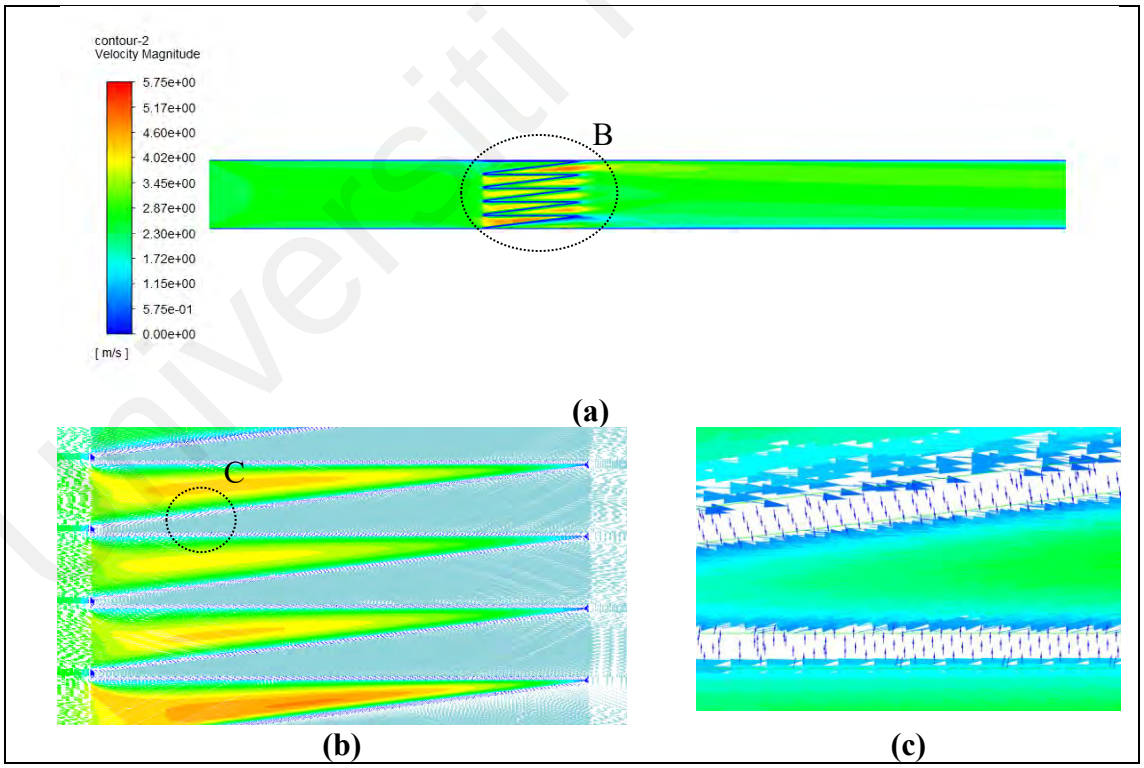

Figure 5.10: Velocity Vectors for Z-shaped Pleats (a) Overview (b) Detail View B: Full Pleats (c) Detail View C: Pleat Side

Observing the pressure contours in Figure 5.11 and Figure 5.13, both rectangular pleat and U-shaped pleat have a higher pressure drop, which is 190.34 Pa and 286.30 Pa at an

air velocity of 2.54 m/s, compared with the triangular and Z-shaped pleats. The rectangular pleat and U-shaped pleat have a similar pleat configuration, but the rectangular pleat has an equal pleat opening while the U-shaped has narrower pleating at one side. It can be clearly seen in the velocity vector from Figure 5.12 that there is high turbulence in flow downstream of the rectangular pleat, forming a wake region after the pleat. The turbulence flow and wake will cause a drag to the overall airflow, hence increasing the flow resistance and pressure drop across the porous media. As depicted in the velocity vector from Figure 5.14, the U-shaped pleat has a larger surface area downstream, which has caused the formation of a bigger wake region. This has resulted in a higher pressure drop across the filter compared with the rectangular pleat. An S-shaped pleat is an improved version of the rectangular pleat, by curving the corner of the rectangular shape. As shown in Figure 5.15, the pressure drop across this S-shaped pleat is 162.10 Pa at a velocity of 2.54 m/s, which has reduced 14.84 % from the rectangular pleat's pressure drop at 190.34 Pa. Observing the velocity vector in Figure 5.16(c), the flow downstream of this filter pleat is relatively smoother, and the wake region is minimized as compared with the rectangular shape, which results in a lower pressure drop.

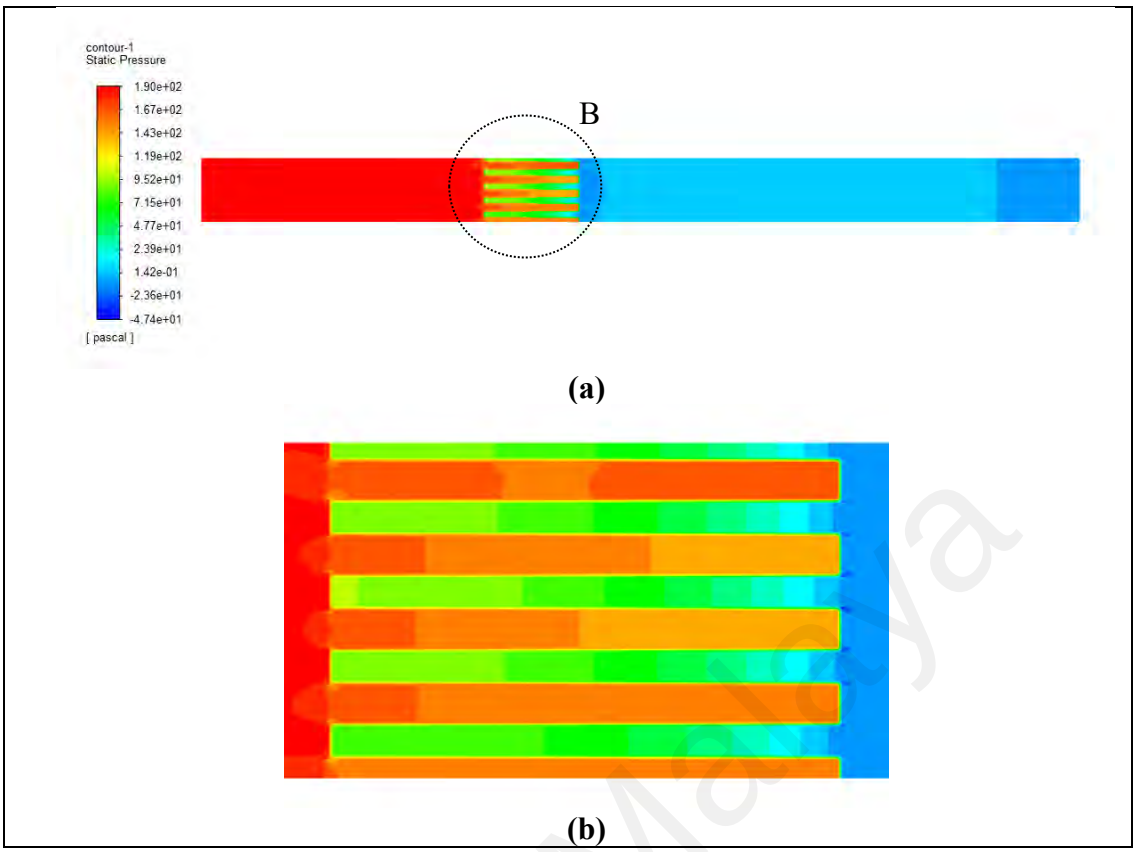

Figure 5.11: Pressure Contours for Rectangular Pleats (a) Overview (b) Detail View B

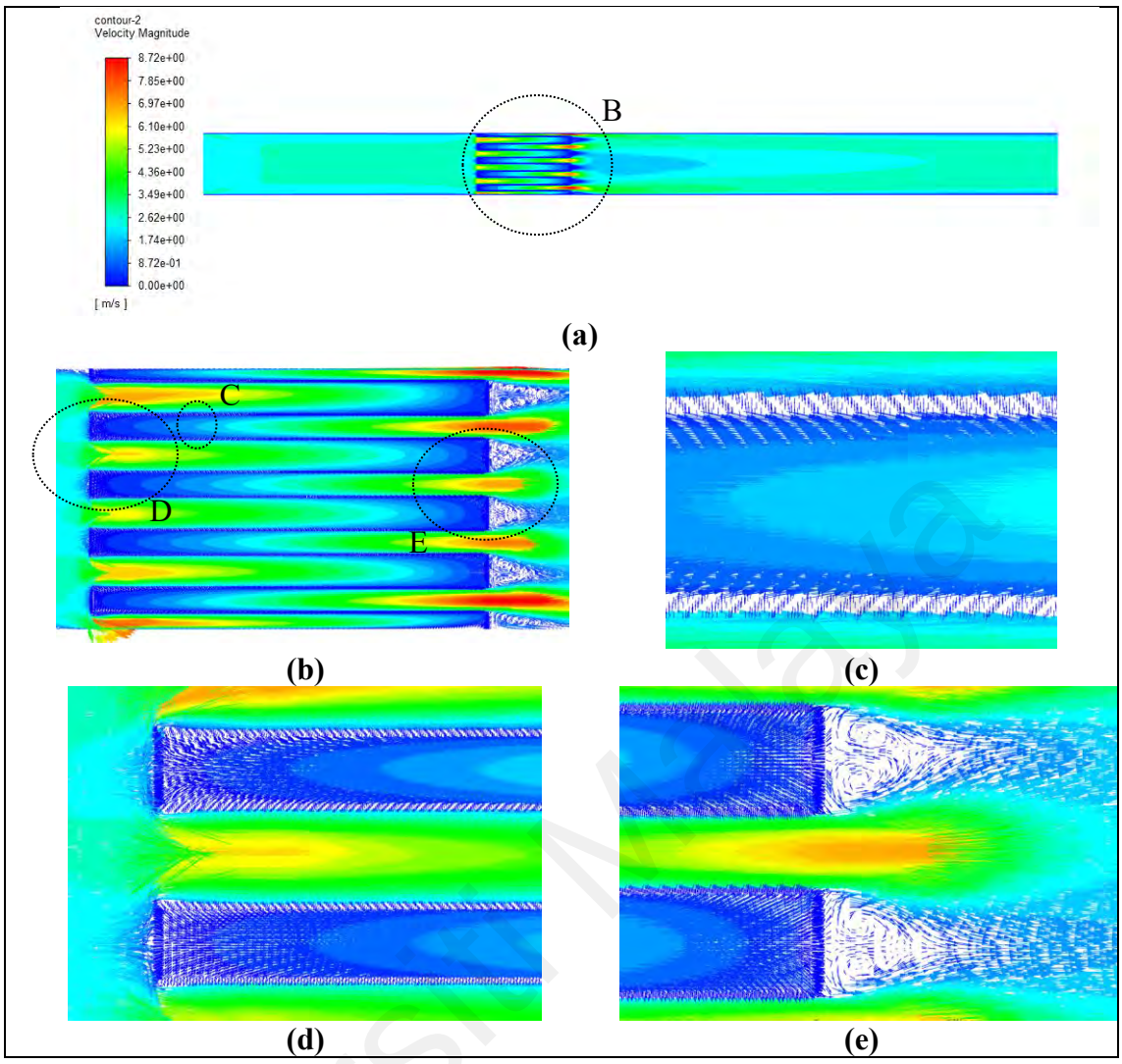

Figure 5.12: Velocity Vectors for Rectangular Pleats (a) Overview (b) Detail View B: Full Pleats (c) Detail View C: Pleat Side (d) Detail View D: Pleat Upstream (e) Detail View E: Pleat Downstream

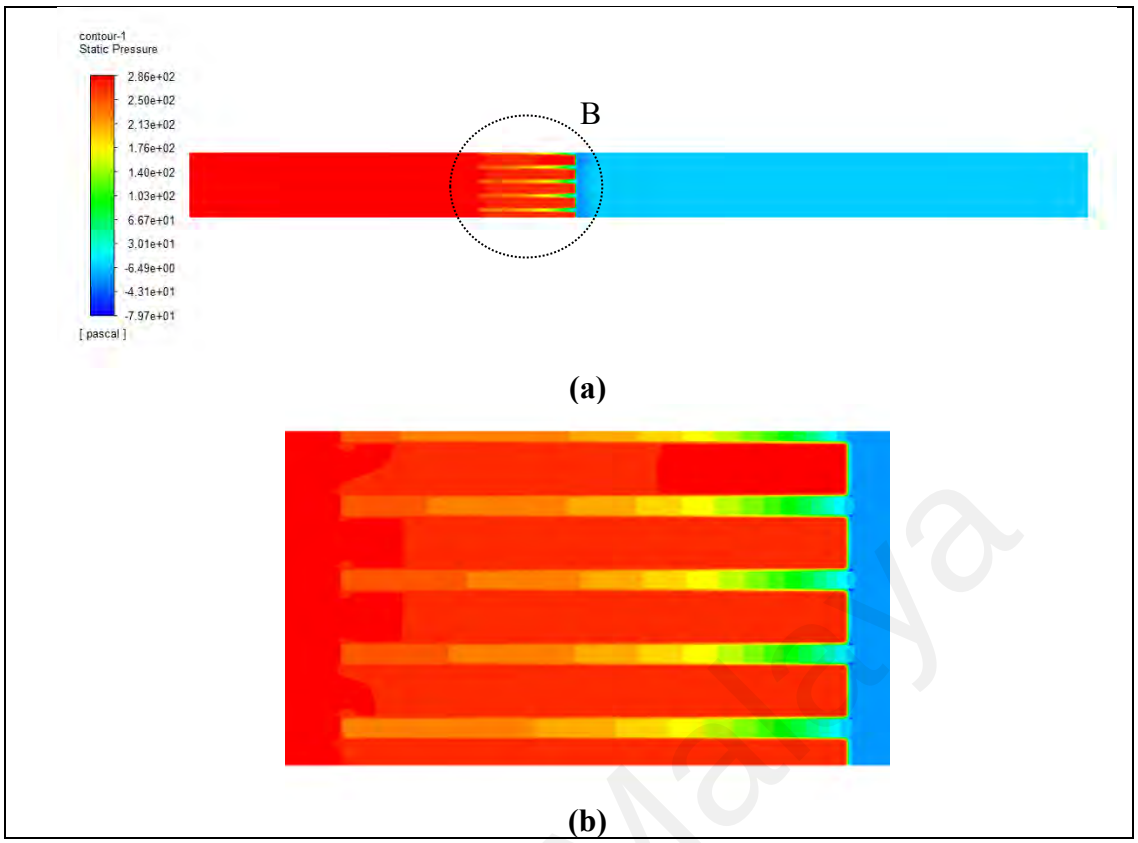

Figure 5.13: Pressure Contours for U-shaped Pleats (a) Overview (b) Detail View B

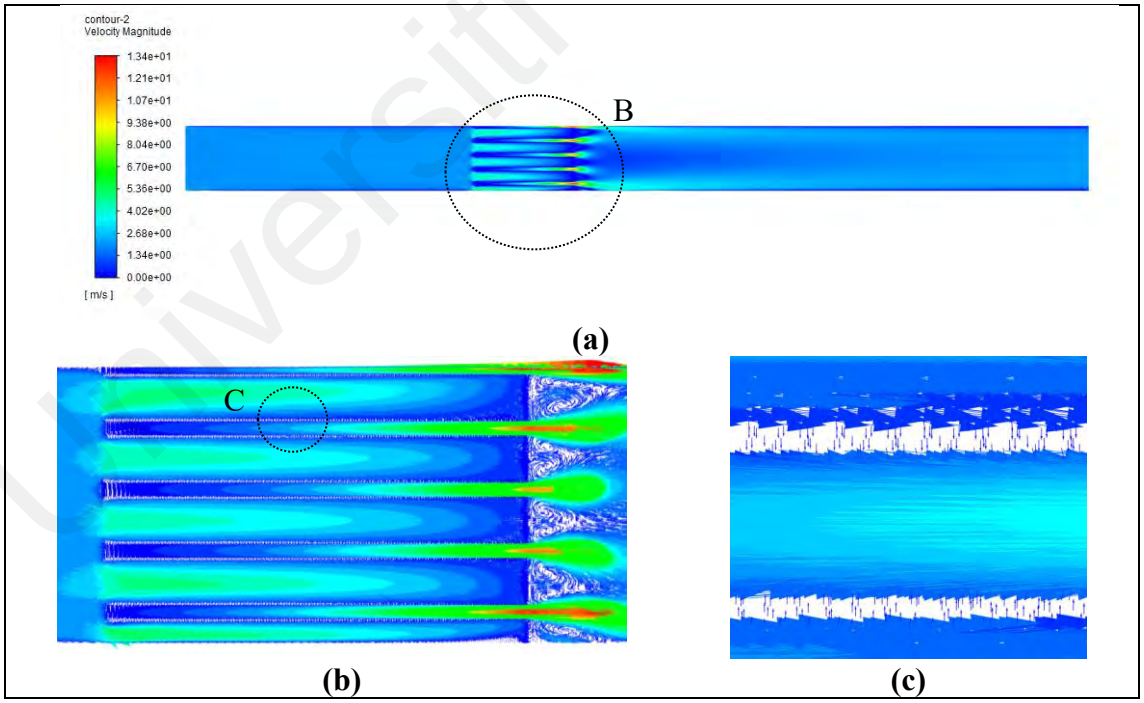

Figure 5.14: Velocity Vectors for U-shaped Pleats (a) Overview (b) Detail View B: Full Pleats (c) Detail View C: Pleat Side

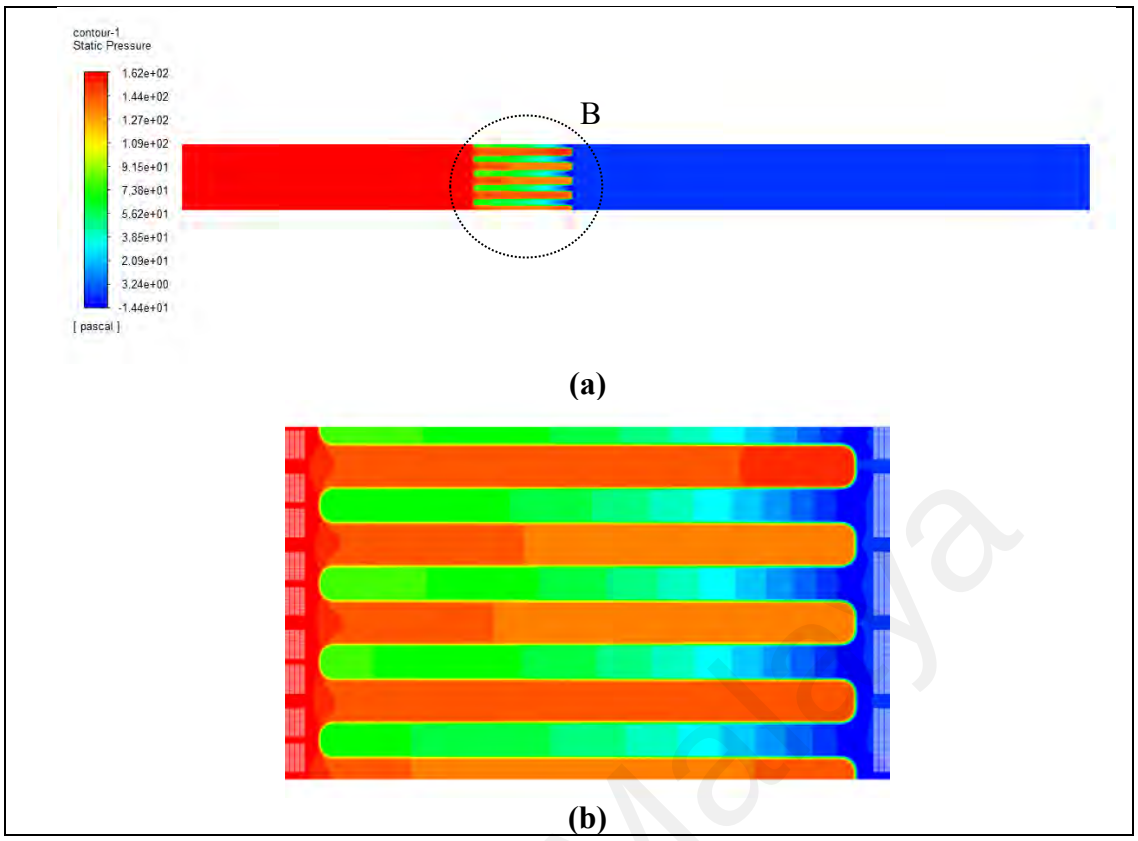

Figure 5.15: Pressure Contours for S-shaped Pleats (a) Overview (b) Detail View B

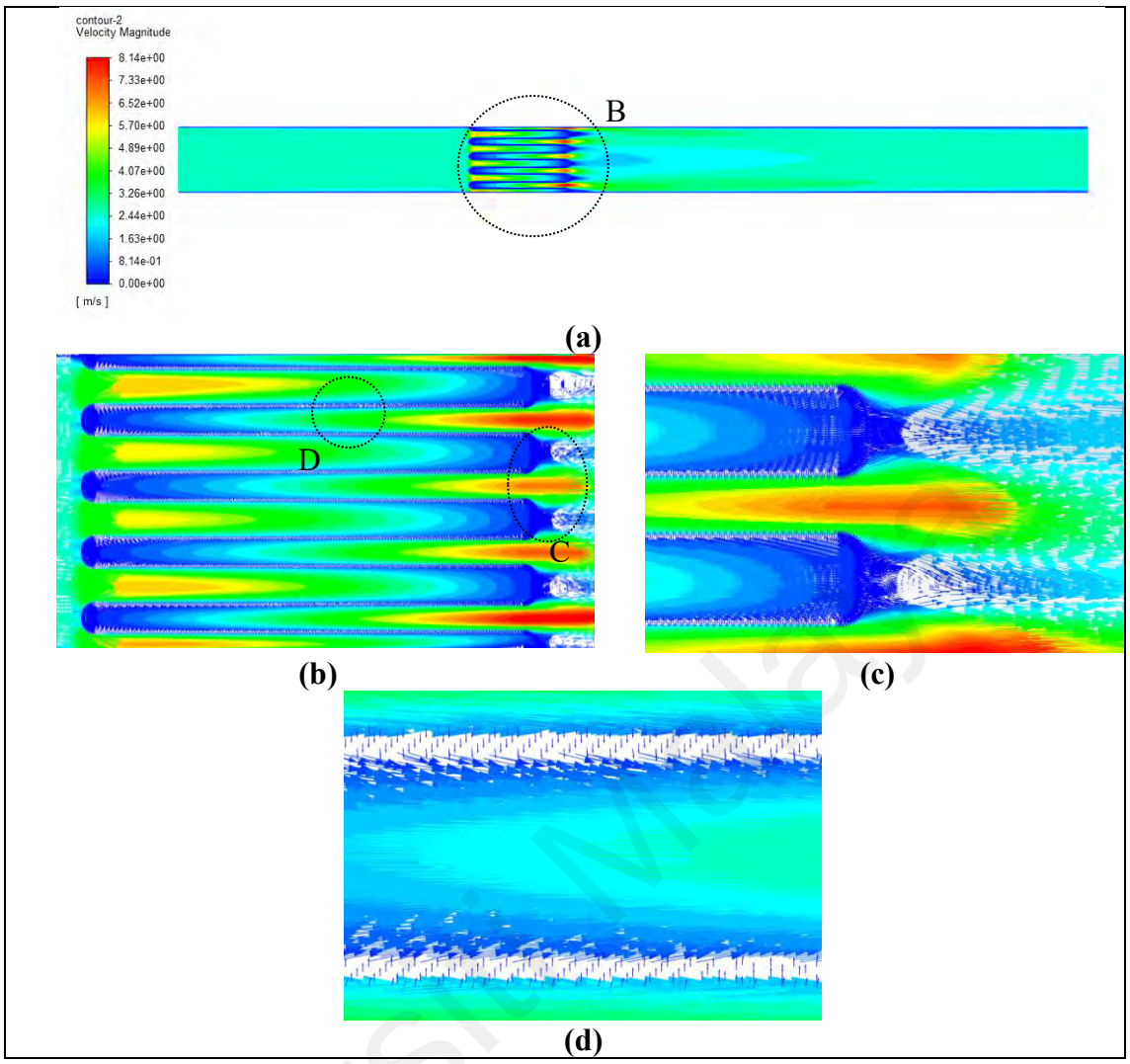

Figure 5.16: Velocity Vectors for S-shaped Pleats (a) Overview (b) Detail View B: Full Pleats (c) Detail View C: Pleat Downstream (d) Detail View D: Pleat Side

For the completeness of the study, different flow velocities across the filter pleats are also simulated to study the initial resistance curve for different pleat shapes. From Figure 5.17, it can be observed that the gradient of the graphs increases from triangular, S-shaped, Z-shaped, rectangular, and U-shaped to box pleats. The viscous drag effect increases with increasing air velocity, and the effect is more pronounced for the U-shaped pleat and the box pleat. The wake regions become bigger downstream of the pleats, especially for the U-shaped and box pleats, causing the differential pressure across the pleats to increase significantly. This causes the initial pressure drop against the air velocity curve to increase in a steeper gradient from the triangular towards the box pleat.

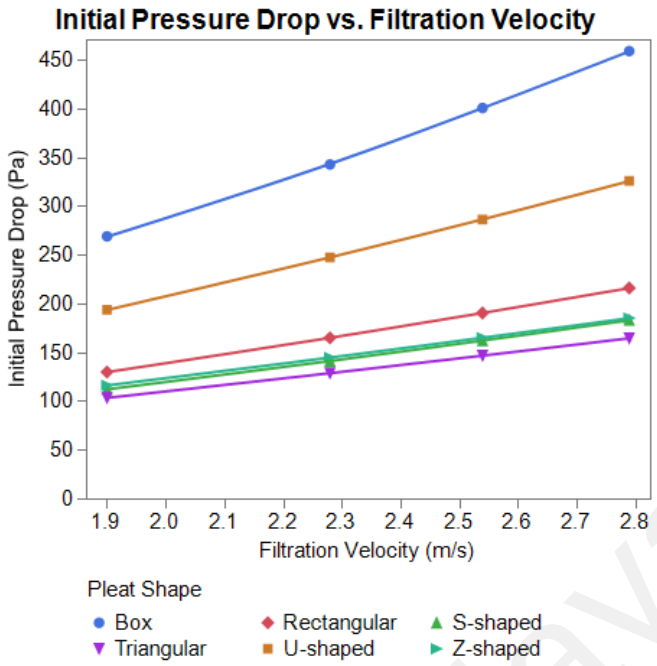

Figure 5.17: Comparison of Initial Pressure Drop for Different Pleat Shape at Filtration Velocity of 2.54 m/s

5.3 Summary

Based on the CFD simulation results, it can be concluded that the pressure drop across the porous media will be affected by the pleat shapes. Different pleat shapes will impose different resistance toward the airflow, causing the pressure drop across the filter to vary. Besides, the pleat shape also causes the flow to be turbulent after the porous media. The turbulence in flow will dissipate the flow energy and cause the differential pressure to be higher. Among all the pleat shapes in this study, the triangular pleat produces the least resistance against air flow upstream and the minimum turbulence downstream, causing the lowest pressure drop across it. This explains why the triangular pleats are typically used in filter applications in the filtration industry. Therefore, the triangular pleats are selected and used in the physical filter construction for experimental data collection in the following chapters.

CHAPTER 6: EFFECT OF FILTER MEDIA ON THE FILTRATION PERFORMANCE

In this chapter, the effect of filter media characteristics on the filtration performance of the pleated fibrous media is studied experimentally. The filter flat sheet media are constructed into filters of similar construction as described in Section 4.4.5 with triangular pleats to determine the filtration performance, including the initial pressure drop, filtration efficiency and pressure drop across the dust cake. Previous studies are limited to using flat sheet media in studying the effect of filter media on filtration performance. The filtration performance of pleated media is incomparable with flat sheet media, especially on the dust cake performance. Section 6.1 summarizes the physical characteristics of the fibreglass media, while Section 6.2 discusses the effect of electrostatic charges on fibreglass media before looking into the effect of fibreglass media on the filtration performance.

6.1 Physical Properties

6.1.1 Scanning Electron Microscope

There are four different fibreglass media (media A, B, C and D) used to study the filtration performance. The filter media is scanned using a scanning electron microscope to study the microscopic porosity. The SEM images in Figure 6.1 depicts the morphology of the fibreglass media tested at a magnification factor of 300.

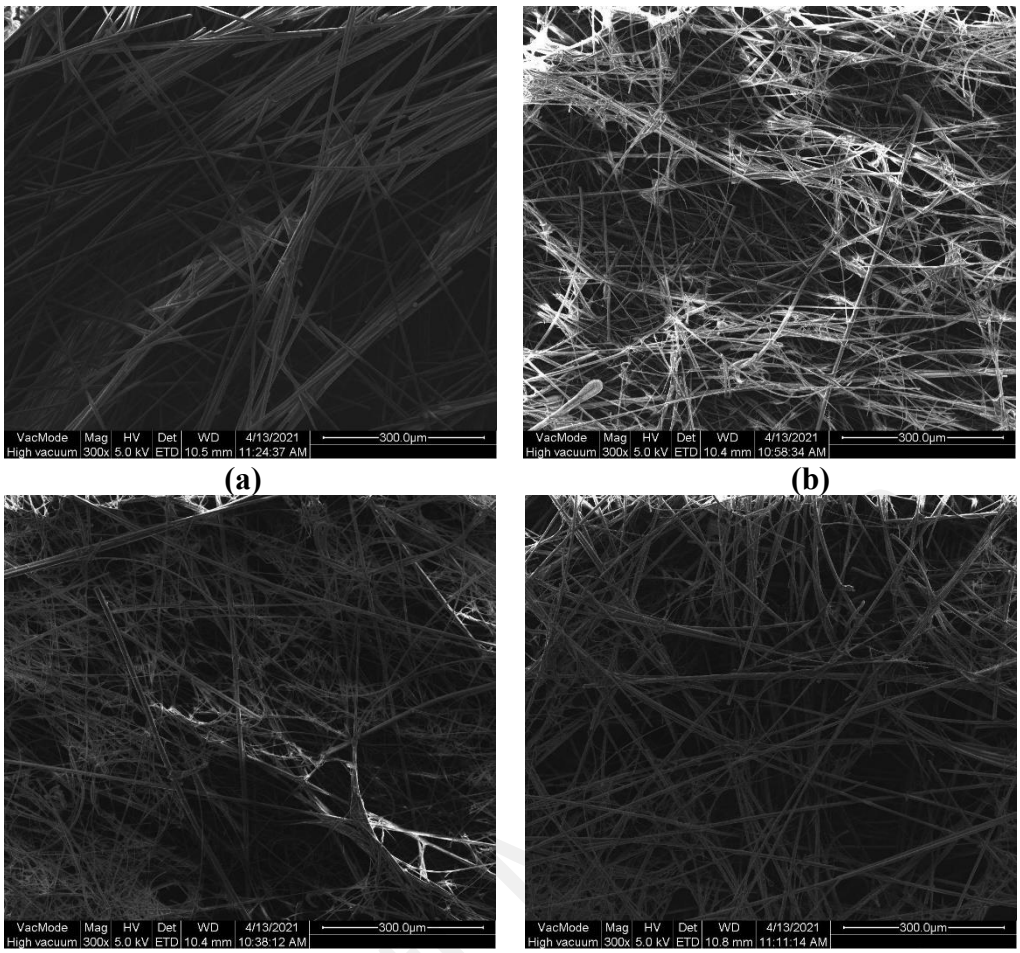

Figure 6.1: SEM Images of Fibreglass Media (x300) (a) Media A (b) Media B (c) Media C (d) Media D

6.1.2 Fibre Diameter

The geometric fibre diameter, d_{fg} is estimated by averaging 150 fibre diameters from the SEM images using Image J software. Figure 6.2 depicts the media fibre diameter distribution. As the fibre size distribution follows a lognormal distribution, the mean fibre diameter, d_f and its standard deviation, σ_f is calculated using Equations (6.1) and (6.2), where σ_g is the geometric standard deviation.

$$d_f = d_{fg} \cdot \exp(0.5 \ln^2 \sigma_g) \quad \textbf{(6.1)}$$

$$\sigma_f = \sqrt{-1 + \exp(\ln^2 \sigma_g)} \quad \textbf{(6.2)}$$

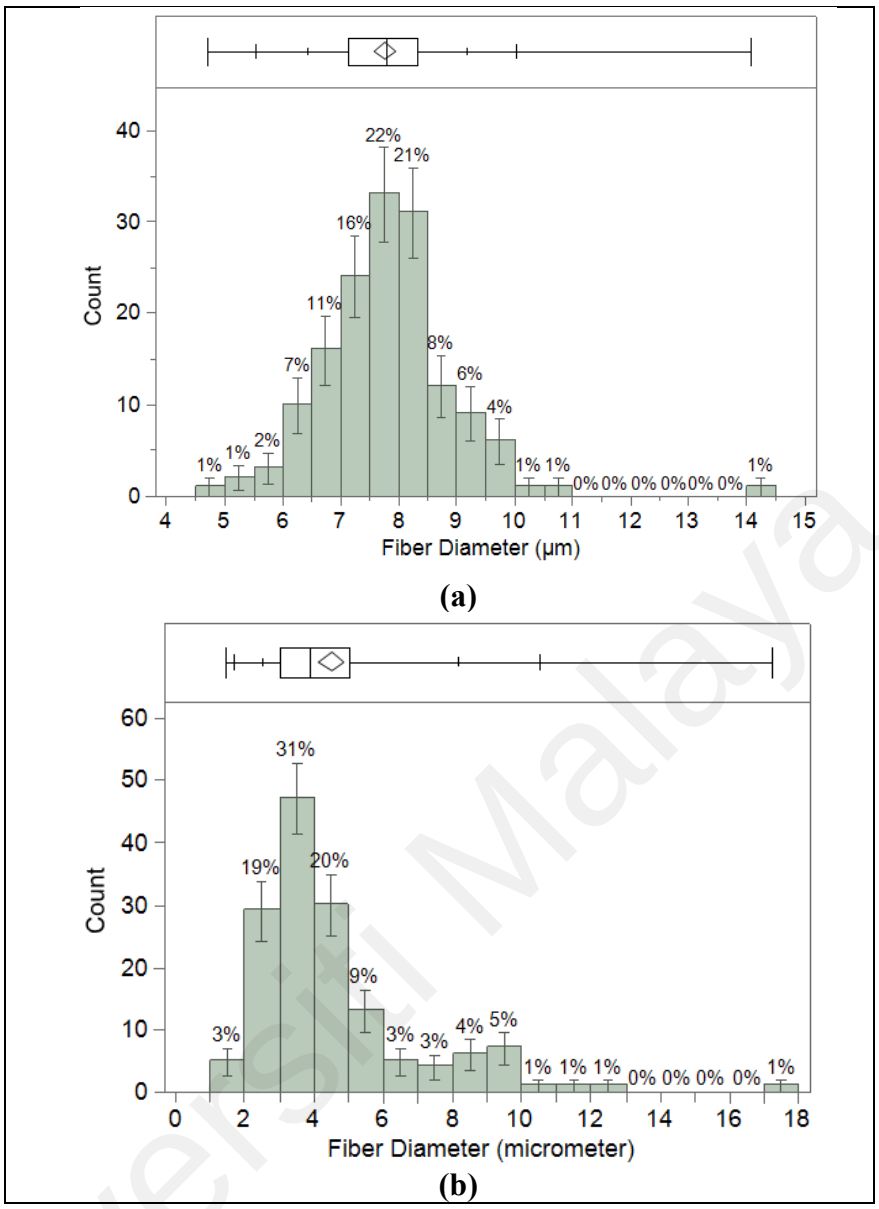

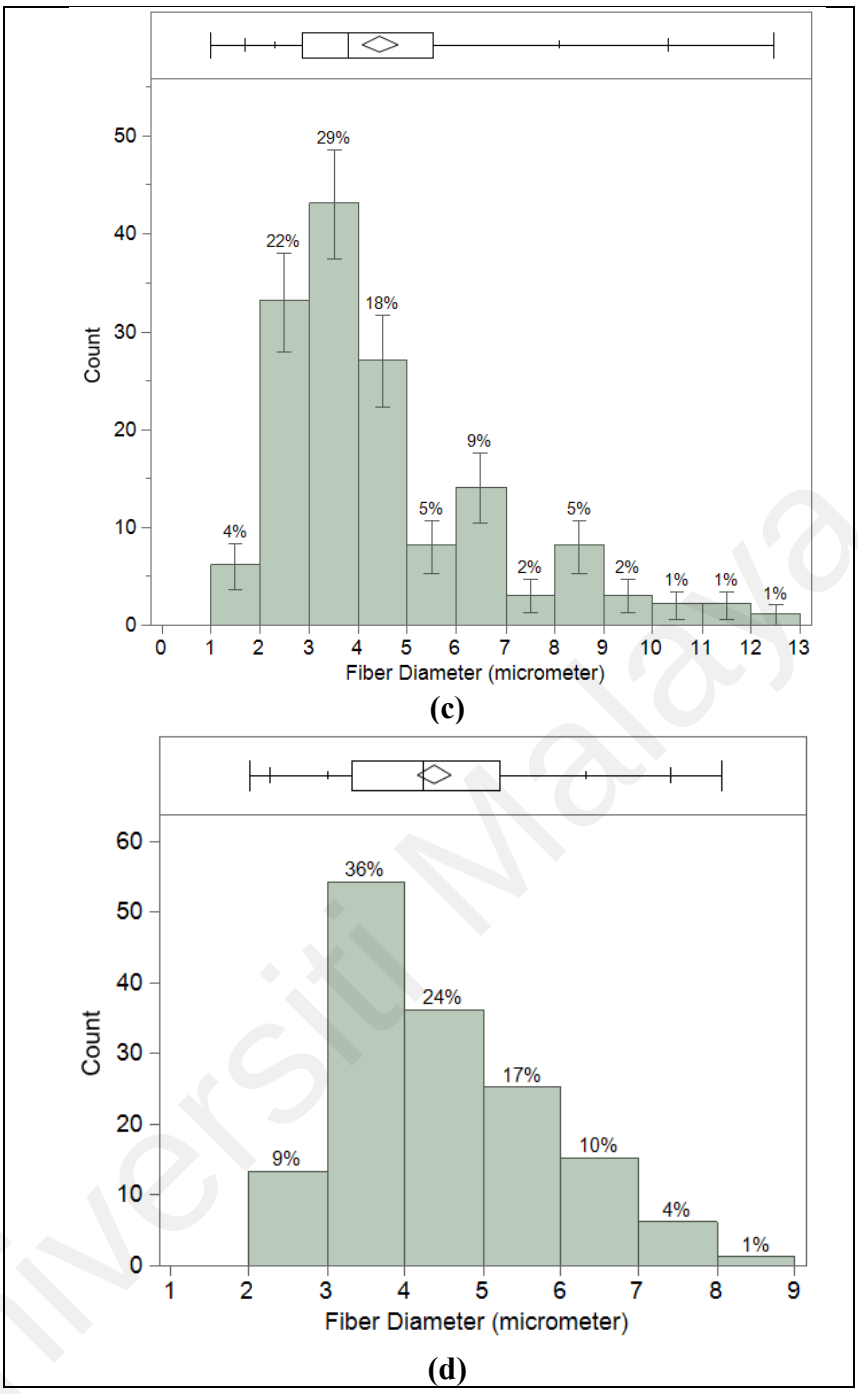

Figure 6.2: Media Geometric Fibre Diameter Distribution (a) Media A (b) Media B (c) Media C (d) Media D

The mean fibre diameters, d_f are 7.86 µm, 6.53 µm, 6.16 µm and 4.57 µm, respectively for media A, B, C and D.

6.1.3 Filter Packing Density

The filter packing density is the volume fraction of fibres in a filter, also known as solid volume fraction (SVF) or filter solidity. Filter packing density, $\propto_f$ is calculated using Equation (6.3)

$$\propto_f = \frac{W_f}{\rho_f Z} \tag{6.3}$$

where W_f is the basis weight of the fibre media or the mass of fibre media per unit filter area; ρ_f is the fibreglass density and Z is the media thickness.

The fibre thickness, Z is measured using a micrometre for 15 repetitions, and the average values are recorded as 0.39 mm, 0.31 mm, 0.31 mm and 0.30 mm for media A, B, C and D, respectively. Five samples of 10 cm × 10 cm of each media type are weighed, and the average basis weight is 79.34 g/m^2, 67.24 g/m^2, 70.94 g/m^2 and 74.01 g/m^2 for media A to D, respectively.

The density of fibreglass, ρ_f is 2.48 g/cm^3 (Shrivastava, 2018). After calculation, the $\propto_f$ of filter media are 0.08203, 0.08746, 0.09227 and 0.09952 respectively for media A to D.

6.1.4 Tensile Strength

Tensile tests are carried out on the flat sheet media. The tensile test is carried out to determine the tensile strength of media in both machine direction and cross direction. Figure 6.3 and Figure 6.4 show the samples of the force-deformation curve of different media types. When the force is increased until the media's ultimate strength, the media fractures, thus causing the sudden drop in the graph of force against deformation.

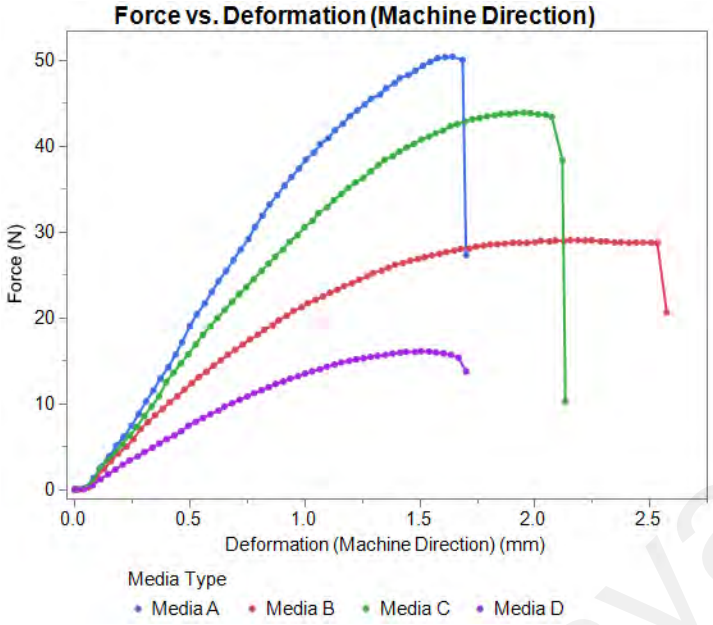

Figure 6.3: Force against Deformation in Machine Direction

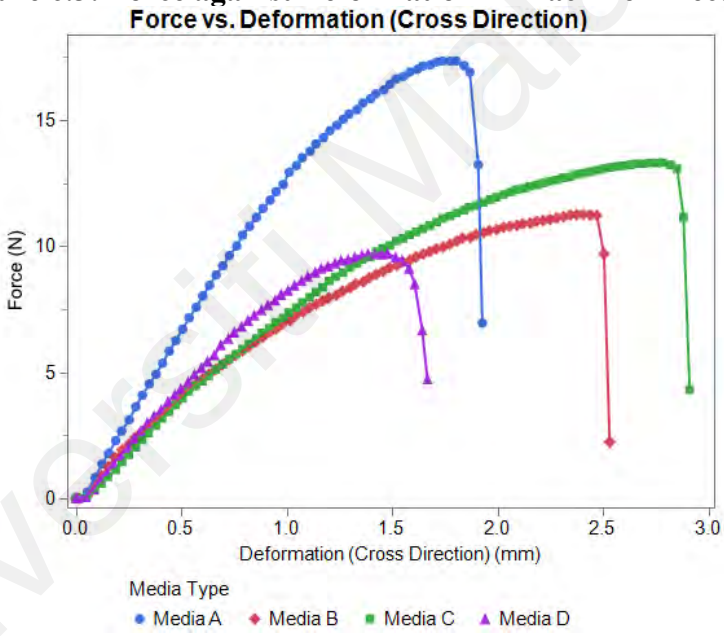

Figure 6.4: Force against Deformation in Cross Direction

The tensile strength of fibreglass media is calculated using Equation (6.4) (Bajpai, 2018). The fibrous media network is manufactured with more fibres are aligned in parallel to the direction of the media machine, which is known as the machine direction (MD). This causes the media to have directional-dependent physical properties. This explains why the tensile strength is higher in the machine direction than in the cross direction for all four types of media in Figure 6.5. In other words, the media has a stronger strength or is stiffer in the machine direction; this also causes the deformation in CD to be larger than

MD by comparing Figure 6.3 and Figure 6.4. The tensile strength is highest for media A, followed by C, B and D.

$$Tensile\ Strength\ (N/mm) = \frac{Ultimate\ Force}{Sample\ Width} \quad \textbf{(6.4)}$$

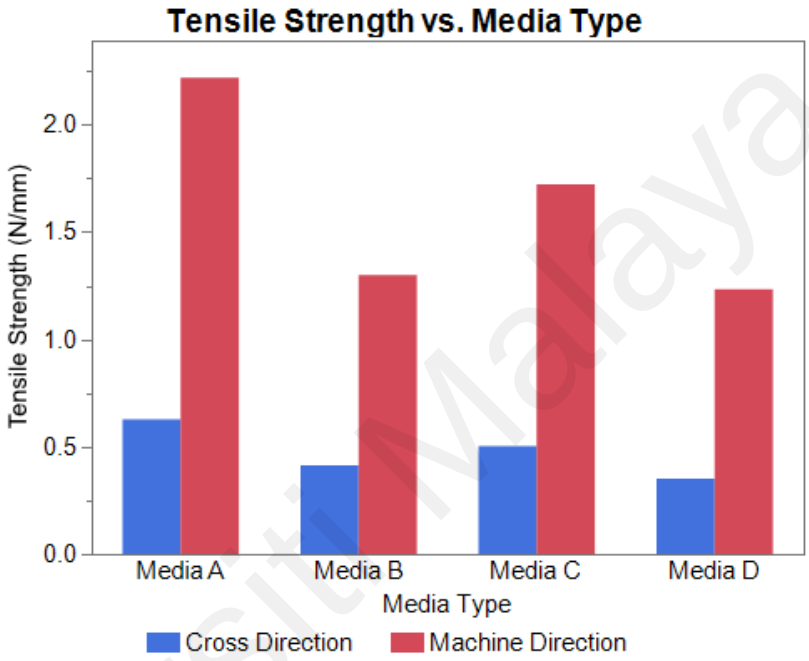

Figure 6.5: Chart of Tensile Strength of Flat Sheet Media in Cross and Machine direction

6.1.5 Summary of Media's Physical Properties

Table 6.1 summarizes the physical properties found experimentally for all 4 media.

Table 6.1: Physical Properties of Filter Media

Media	Fibre Mean Diameter, d_f (µm)	Basis Weight, W_f (g/m^2)	Thickness Measured (mm)	Filter Packing Density, $\propto_f$	Tensile Strength in Machine Direction (N/mm)	Tensile Strength in Cross Direction (N/mm)
A	7.86 ± 0.14	79.34	0.39 ± 0.03	0.0820	2.2180	0.6263
B	6.53 ± 1.04	67.24	0.31 ± 0.02	0.0875	1.2990	0.4167
C	6.16 ± 0.96	70.94	0.31 ± 0.03	0.0923	1.7230	0.4953
D	4.57 ± 0.29	74.04	0.30 ± 0.02	0.0995	1.2340	0.3537

6.2 Effect of Electrostatic Charges on Fibre Media

The electrostatic effect is one of the significant contributing factors to improving filter efficiency. However, the efficiency of the charged filter will decrease with time as the charged particles are neutralized by the dust particles, giving the minimum efficiency when the electrostatic charges are at a steady-state (Ji et al., 2003).

In order to study the effect of the electrostatic mechanism on the filtration efficiency at different types of fibre media, the initial efficiency and the discharged efficiency are determined. The initial efficiency of a test filter is measured before the whole filter is placed in a discharged cabinet filled with isopropanol vapour for 24 hours. This discharging method is advised in the air filter testing standard, ISO 16890-4 (ISO, 2016e).

From Figure 6.6, it can be observed that the difference between initial and discharged fractional efficiencies is very minimal, less than four percentage points. This shows that the electrostatic removal mechanism is negligible in the fibreglass media. Due to the finer fibre diameter in fibreglass media, the filtration mechanisms are dominant in the interception, the inertial impaction and Brownian diffusion. Compared to synthetic filter media, the fibre diameter is larger than the fibreglass media, causing the synthetic media to have larger voids (Vaughn & Ramachandran, 2002). The collision and interception between fibres and particles reduce in the large voids. Therefore, synthetic media is normally charged to increase the filtration efficiency, but not fibreglass media.

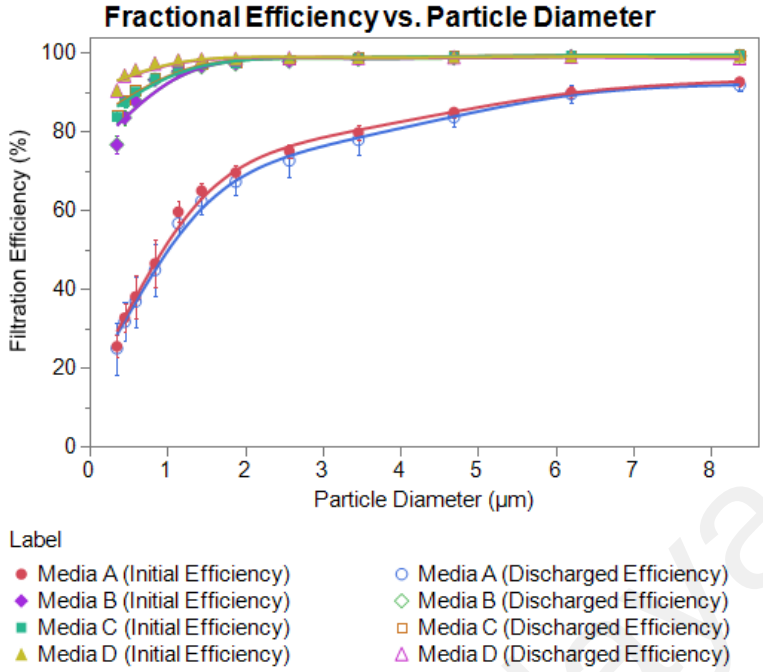

Figure 6.6: Electrostatic Effect on Filtration Efficiency

However, there are still some minor possibilities for the charge accumulation on the fibreglass when the filter is exposed to charged aerosol particles. In order to minimize this effect, the filtration efficiency is taken as the average of the initial and discharged efficiencies in the following study.

6.3 Filtration Performance

The relationship between the physical properties and the filtration performance, including the filtration efficiency, initial pressure drop and the pressure drop across the dust cake is discussed in this section.

6.3.1 Effect of Physical Properties on Clean Filters

6.3.1.1 Filtration Efficiency

The filtration performance of a clean pleated filter is evaluated with the filtration efficiency and initial pressure drop. The filtration efficiency is plotted against particle sizes ranging from 0.3 µm to 10.0 µm in Figure 6.7. It can be observed that the filtration efficiency curve shifts upwards from media A to D. This can be related to the fibre diameter and filter packing density of the fibreglass media. As shown in Table 6.1 earlier,

the fibre mean diameter decreases while the filter packing density increases from media A to D. The collection mechanism is dominant by diffusion and interception for particle size range < 0.5 μm, where the filtration mechanisms are stronger with decreasing fibre diameter (Kim et al., 2021). This explains why the filtration efficiency increases with decreasing fibre diameter, as shown in Figure 6.8(a), and this result is in agreement with Payen et al. (2012). Figure 6.8(b) displays that the filtration efficiency increases when the filter packing density increases. The filter packing density, $\propto_f$ is the ratio of fibreglass's volume to the filter's volume. When the filter packing density is higher, the trapping probability can also be increased with a higher $\propto_f$, resulting the filtration efficiency to increase.

Besides, in Figure 6.7, the filtration efficiency increases with particle diameters and the minimum efficiency occur at the particle size of 0.3 μm for all fibreglass media. This is because the particle size of 0.3 μm is the most penetrating particle size (MPPS) as defined by the United States Environmental Protection Agency (EPA) (EPA, 2022). At MPPS, the particle size is the hardest to be captured by filter fibre as it is too big to be collected by Brownian's diffusion (< 0.1 μm) and too small to be collected by interception (> 0.5 μm).

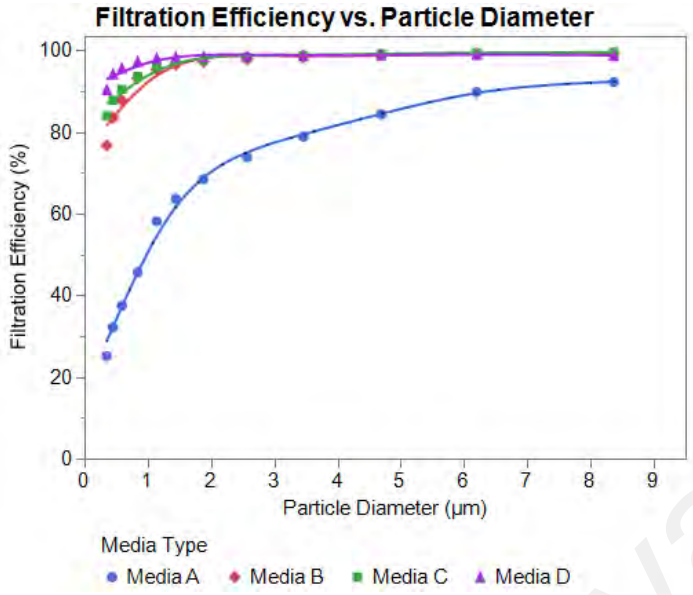

Figure 6.7: Filtration Efficiency against Particle Diameter at Different Media Types

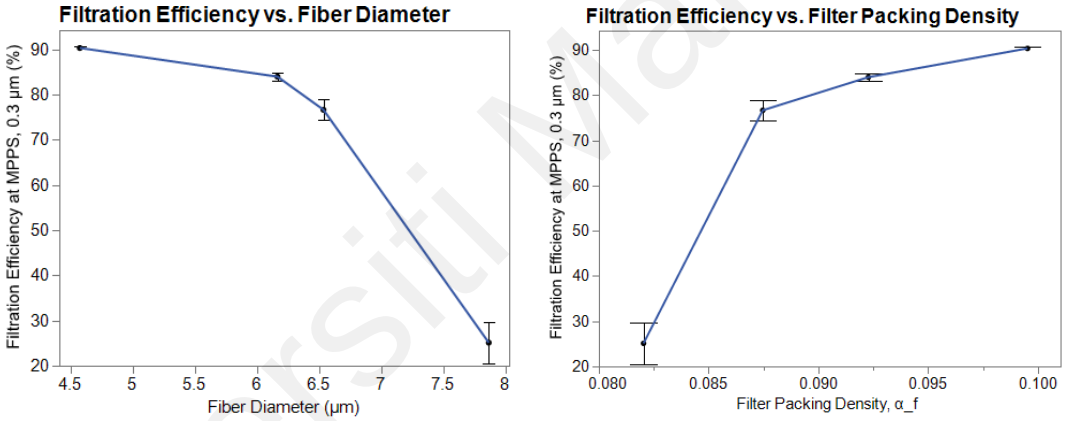

(a) **(b)**

Figure 6.8: Effect of (a) Fibre Diameter and (b) Filter Packing Density on Filtration Efficiency

6.3.1.2 Initial Pressure Drop

Next, the initial pressure drop is an important parameter in evaluating the filtration performance, as the initial pressure drop can significantly affect the energy consumption. Figure 6.9 shows that the initial pressure drop increases with increasing filtration velocity for all fibreglass media and also increases from media A to D. Figure 6.10 shows that the initial pressure drop decreases with increasing fibre diameter and increases with filter packing density. This can be explained as a denser network can be formed with a smaller fibre diameter (Bian et al., 2020). The denser network has created a greater resistance to airflow, causing the initial pressure drop to increase with decreasing fibre diameter.

Similarly, as the filter packing density increases, the air permeability also decreases due to the fibre's blockage, causing the initial pressure drop also increase.

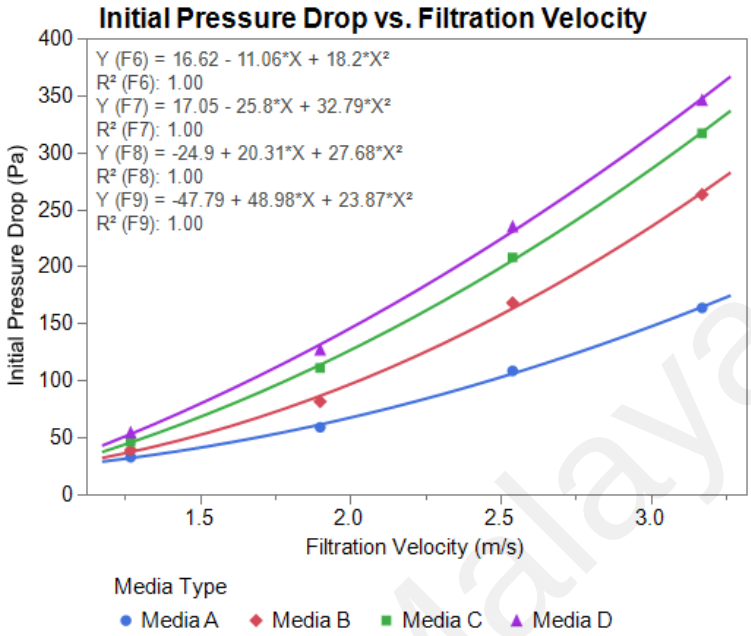

Figure 6.9: Initial Pressure Drop against Filtration Velocity for Different Media Types

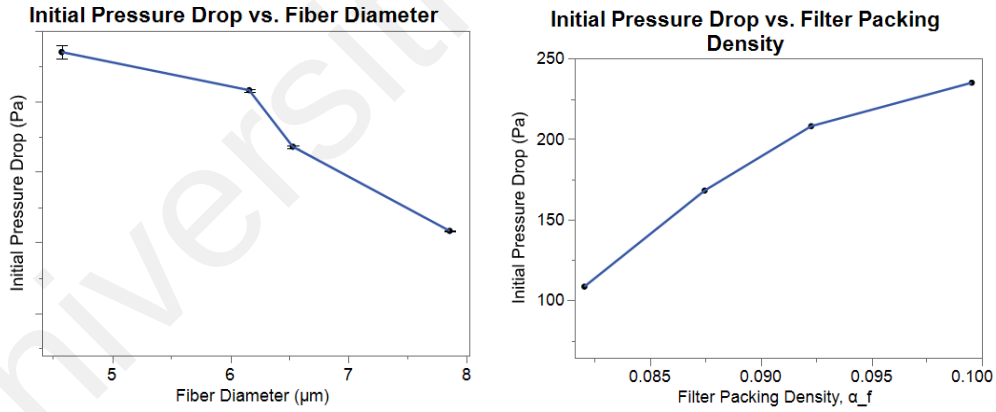

(a) **(b)**

Figure 6.10: Effect of (a) Fibre Diameter and (b) Filter Packing Density on Initial Pressure Drop

6.3.1.3 Quality Factor

A good filtration performance gives a high filtration efficiency and low initial pressure drop. This can be evaluated using the quality factor, QF, as defined in Equation (6.5), where P is the filtration penetration, η_T is the filtration efficiency and ΔP is the initial pressure drop across the filter.

$$QF = \frac{-\ln P}{\Delta P_0} = \frac{-\ln(1-\eta_T)}{\Delta P_0} \quad (6.5)$$

Figure 6.11 shows the quality factor of the fibreglass media filters as a function of fibre diameter and filter packing density. It can be observed that the quality factor decreases with increasing fibre diameter but increases with increasing filter packing density. Hence, it is desirable to use a greater fibre diameter and higher filter packing density in order to maximize the filtration performance of a clean filter.

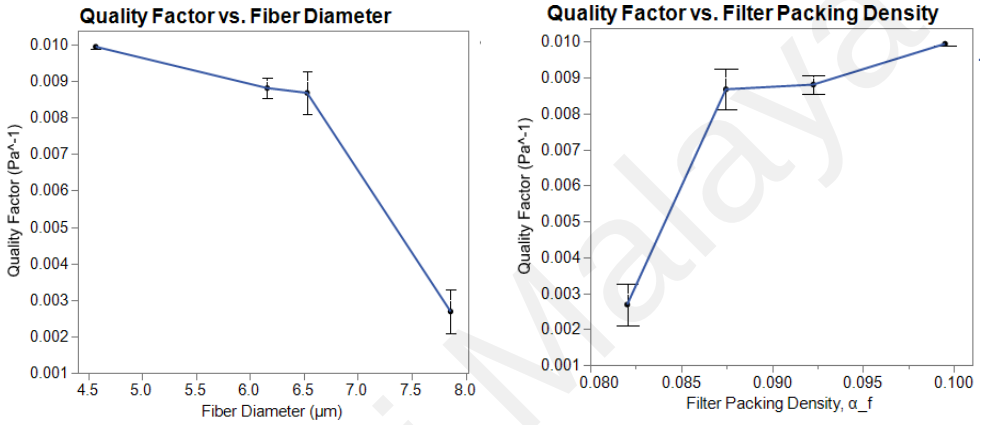

(a) **(b)**

Figure 6.11: Effect of (a) Fibre Diameter and (b) Filter Packing Density on the Quality Factors

6.3.2 Pressure Drop across Dust Cake

Figure 6.12 shows an example of a filter before and after the dust loading process. Dust is fed consistently into the filter at the tested filtration velocity, which is 2.54 m/s. At the point when the arrestance starts to drop, it indicates the filter media reaches its maximum dust holding capacity, which can be seen in Figure 6.13. The filter media deforms at the end of the testing due to the high pressure incurred by the airflow. The drop in arrestance occurs when the filter media starts to break, so the dust particle can easily pass through the media. As the arrestance is defined as the amount of dust a filter can hold while retaining the required filter's efficiency (Legg, 2017), a drop in arrestance indicates the failure of the test filter as the filter's efficiency is no longer retained. The dust loading process will stop upon reaching the test filter's failure and the final pressure drop will be recorded.

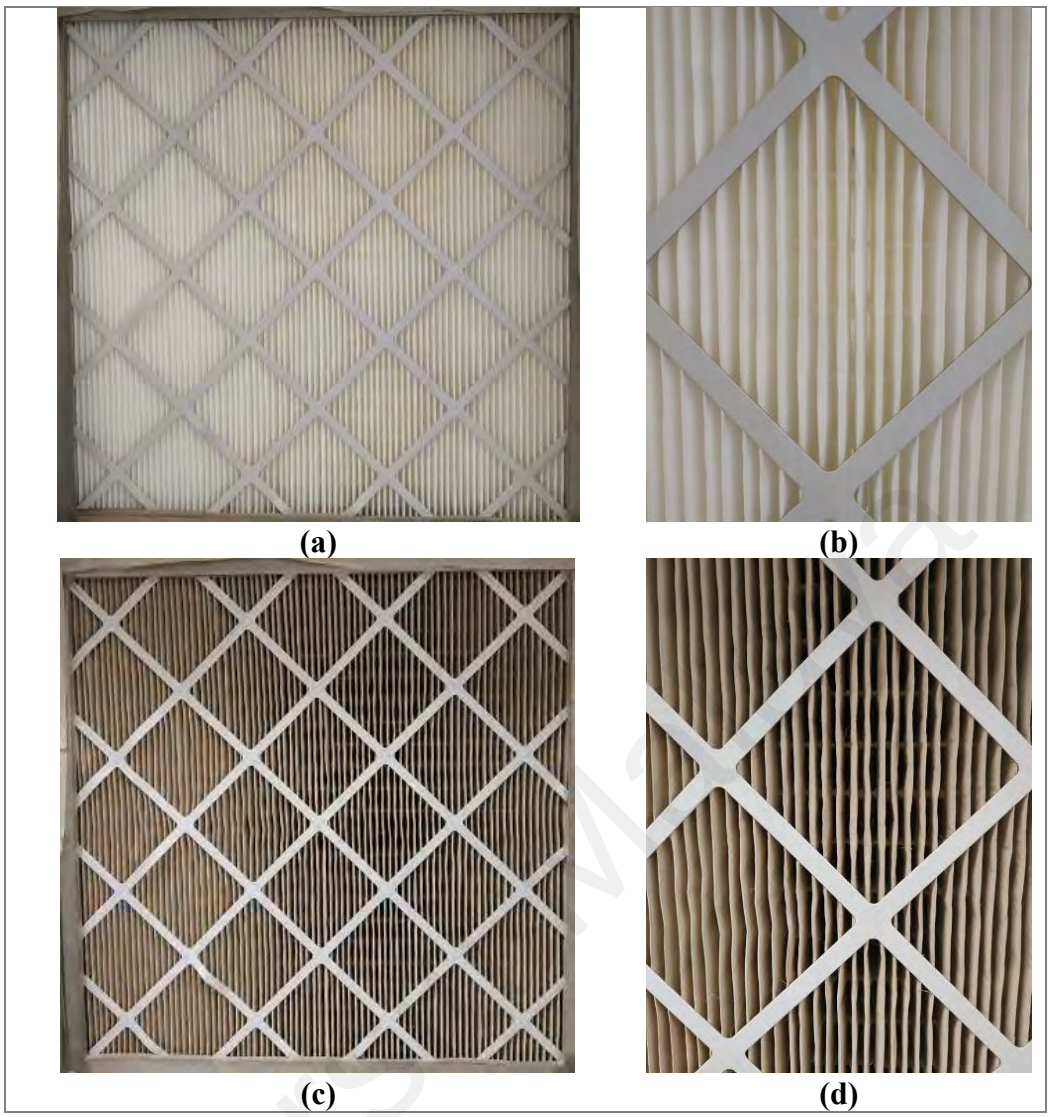

Figure 6.12: (a) Clean Filter (b) Close-up of Clean Filter Media (c) Tested Filter (d) Close-up of Tested Filter Media

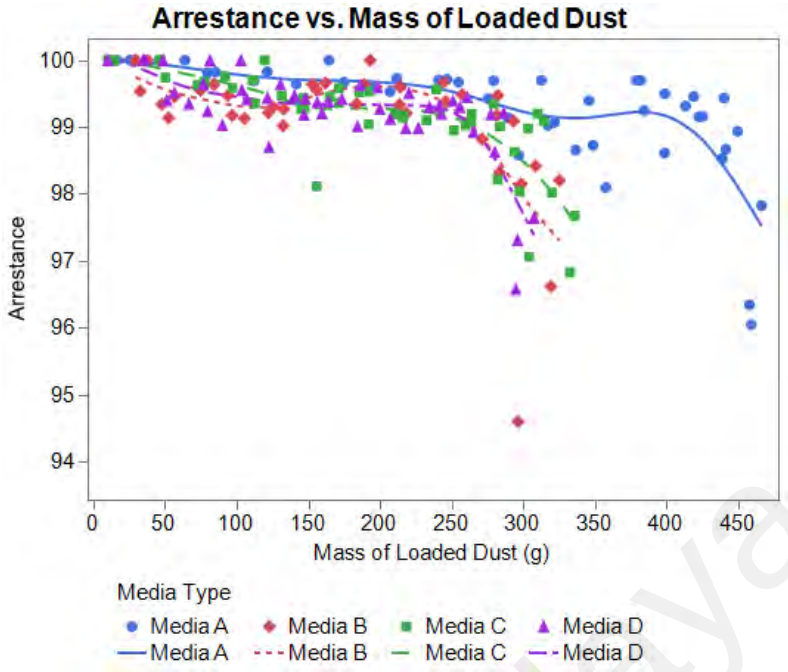

Figure 6.13: Arrestance against Mass of Loaded Dust at Different Media Types

Figure 6.14 shows the graph of total pressure drop against the mass of loaded dust on the test filters with different media types, while Figure 6.15 is the graph of pressure drop across dust cake against the mass of loaded dust and plotted by subtracting the initial pressure drop from the total pressure drop from Figure 6.14. From Figure 6.15, the results illustrate that the curves of dust cake pressure drop increase in three different stages: constant increase stage at a low gradient, accelerating increase stage and lastly, constant increase stage at the steepest slope, which follows the typical dust loading behaviours (depth filtration, transitional filtration and surface filtration).

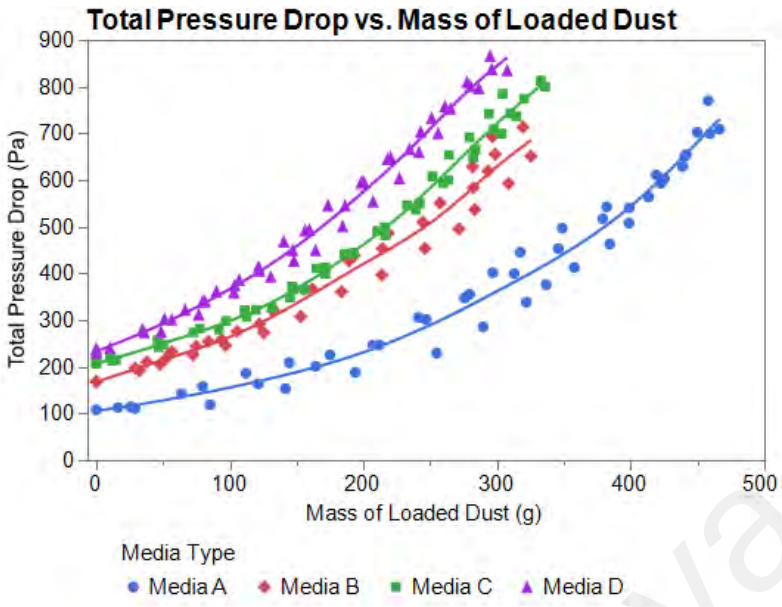

Figure 6.14: Total Pressure Drop against Mass of Loaded Dust at Different Media Types

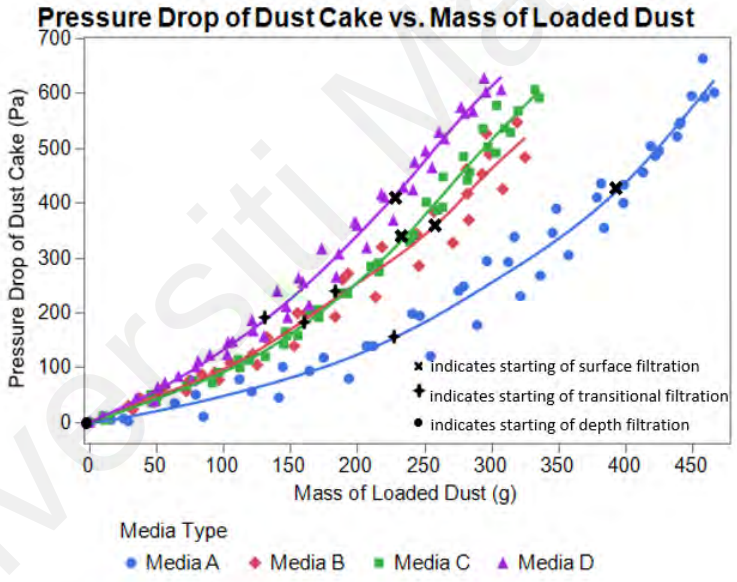

Figure 6.15: Pressure Drop across Dust Cake against Mass of Loaded Dust at Different Media Types

Table 6.2 summarizes the effect of the physical properties of fibreglass media on dust cake formation. It shows that the mass of loaded dust in depth filtration increases as the fibre diameter increases. This might be because as the fibre diameter is bigger, the fibre network is lesser dense, which causes a bigger average pore diameter. The amount of dust that can be deposited within the fibre media will be greater, which leads to a bigger mass of loaded dust in the depth filtration, and eventually, a higher dust holding capacity.

However, compared with the filtration efficiency in Section 6.3.1.1, the filtration efficiency of the media increases, and the respective dust holding capacity decreases, except for Media B and C having relatively similar dust holding capacity with a minor difference of 10 g, which can be shown in Figure 6.16. The bigger average pore diameter has decreased the impact probabilities between fibres and dust particles, decreasing the filtration efficiency, even though the dust holding capacity is high. This shows a compromise in the filtration performance.

Table 6.2: Effect of Physical Properties on Dust Cake Formation

Media Types	Mean Fibre Diameter, d_f (µm)	Mass of Loaded Dust in Depth Filtration (Pa)	Dust Holding Capacity (g)
A	7.86 ± 0.14	230	461
B	6.53 ± 1.04	180	314
C	6.16 ± 0.96	160	324
D	4.57 ± 0.29	130	299

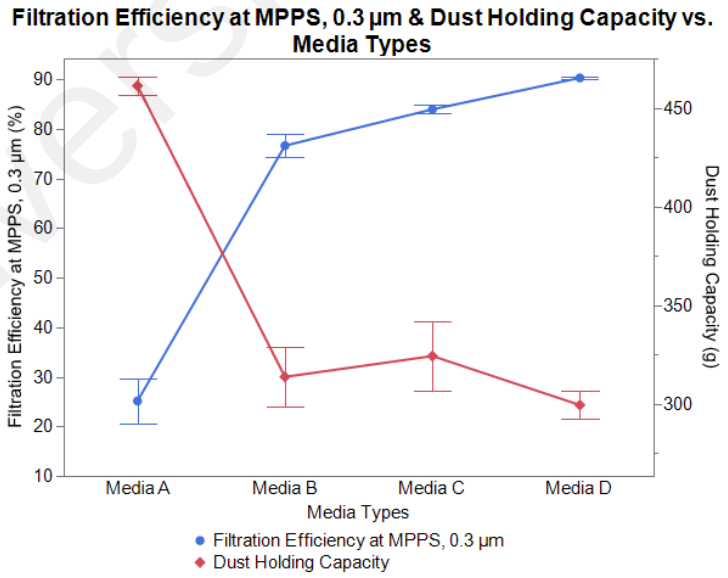

Figure 6.16: Filtration Efficiency and Dust Holding Capacity at Different Media Types

The tensile strength of the fibreglass media is expected to be influencing the final pressure drop of the filter and pressure drop across the dust cake. However, the high *p*-

values, as shown in Table 6.3 indicate no obvious relationship between tensile strength and the pressure drop across dust cake and the final pressure drop. The relationship is significant when the *p*-values are less than 0.05 (Siegel, 2016). Therefore, it can be concluded that the tensile effect has no clear correlation with the pressure drop of the filter.

Table 6.3: *p*-Values of Tensile Strength and Pressure Drop

***p*-Values**	**Pressure Drop across Dust Cake**	**Final Pressure Drop**
Tensile Strength in Machine Direction	0.4905	0.7374
Tensile Strength in Cross Direction	0.6366	0.5877

6.4 Summary

In this chapter, the effect of electrostatic charges on fibreglass media and the effect of physical properties of fibreglass media on filtration performance is studied. It can be concluded that the electrostatic removal mechanism is negligible on the fibreglass media. As for the physical properties of the fibreglass media, the initial pressure drop and filtration efficiency increase (in overall, quality factor increases) with decreasing fibre diameter and increasing filter packing density. The filtration efficiency increases, and the dust holding capacity decreases with decreasing fibre diameter. This is because as the fibre diameter decreases, the fibre network formed is denser, which leads to smaller pore size. The smaller pore size and higher filter packing density increase the trapping probability, subsequently increasing the filtration efficiency. However, the smaller pore size decreases the air permeability, which increases the initial pressure drop. The dust holding capacity also decreases as the amount of dust deposited within the fibre media decreases with a smaller average pore size. Besides, the tensile strength is proven not to influence the pressure drop of filters as the correlation coefficient is low.

CHAPTER 7: THE INFLUENCE OF FILTRATION VELOCITY ON THE FIBROUS FILTER PERFORMANCE

The air filtration velocity is one of the important parameters contributing to the filtration performance of a fibre filter. This chapter discusses the effect of the filtration velocity on the filtration efficiency, initial pressure drop and the pressure drop across dust cake.

The filter model used remains constant in this part of investigation. The test filter used are constructed the same with fibreglass media with a pleat density of 4.0 PPI at dimension of $594mm$ (H) $\times$ $594mm$ (L) $\times$ $95mm$ (D). These parameters are used typically in industrial practice. The test filters are tested using similar methodology as described in Chapter 4 but at different filtration velocities. A full test of determination of the filtration efficiencies and the pressure drop across dust cake are repeated at 1.27 m/s, 1.90 m/s, 2.28 m/s, 2.54 m/s and 2.79 m/s. The selected filtration velocity is within the recommended range of initial resistance test (1.27 m/s – 3.17 m/s) in ISO 16890.(ISO, 2016c) Due to the physical structure of the fibreglass media is unable to support the prolonged full test of the dust loading procedure at 3.17 m/s, the filtration velocity is taken at 50%, 75 %, 90 %, 100 % and 110 % of the recommended HVAC operating velocity, which is 2.54 m/s (ASHRAE, 2017). Each full test at different filtration velocities is repeated 3 times.

7.1 Filtration Efficiency

In Figure 7.1, the graph of filtration efficiency is plotted against the geometrical mean diameter of the aerosol particles. It shows the overall filtration efficiency is higher when the filtration velocity increases. The inertial impaction becomes more significant when the filtration velocity increases which can also be seen in the increasing trend in Figure 7.2. This causes the filtration efficiencies to increase when more particles are trapped at increasing filtration velocity. The aerosol particle investigated are within the range of 0.3

μm and 10.0 μm, which is at the inertial impaction and interception dominant stage. As shown in the finding of Zhu et al. (2000), diffusion is dominates the particle collection for particle diameter < 0.1 μm while inertial impaction and interception are collecting particle of diameter > 0.5 μm dominantly.

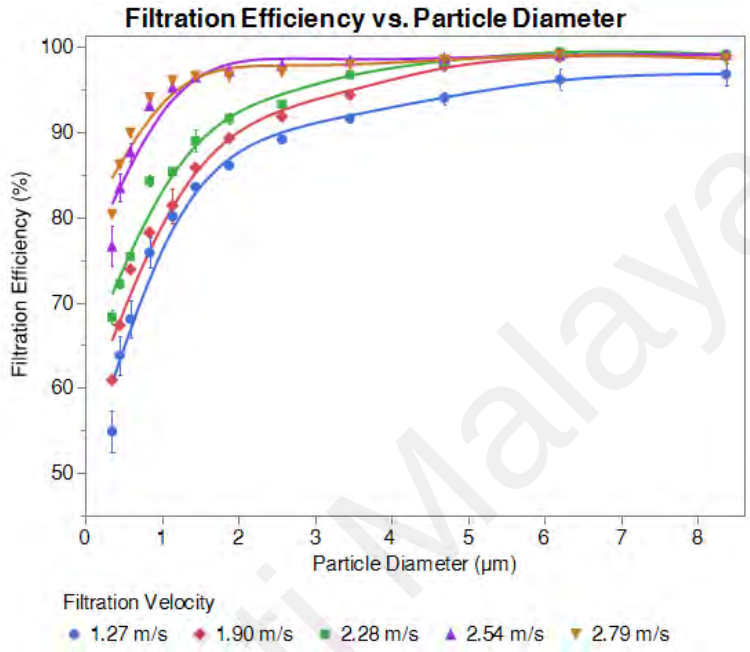

Figure 7.1: Filtration Efficiency against Particle Diameter at Different Filtration Velocities

Observing Figure 7.2, the overall trend shows an increasing filtration efficiency with increasing filtration velocities and the increasing trend is more pronounced when the particle mean diameter is smaller. This has been demonstrated that the inertial impaction is dominating at relatively smaller particle size. A greater force of inertia is brought by high air velocity, and this increases the possibility of collision between the particles and the media fibre. The gradient of increasing filtration efficiency becomes less steep at the higher particle size. The efficiency in removing large particles is high due to interception. This happens because the interception collection is more significant when the particle diameter is getting nearer to the fibre diameter, which is 4.52 μm in this case (Zhang, 2004). A larger particle can be intercepted easily within the fibre media. The phenomenon is in contrast, which happens typically at HEPA filters tackling the fine particles with

diameter below 0.1 μm. The filtration efficiency is found to be decreasing with an increasing filtration velocity (Alderman et al., 2008) and this is because the diffusion mechanism is dominant at the nanoparticle size range.

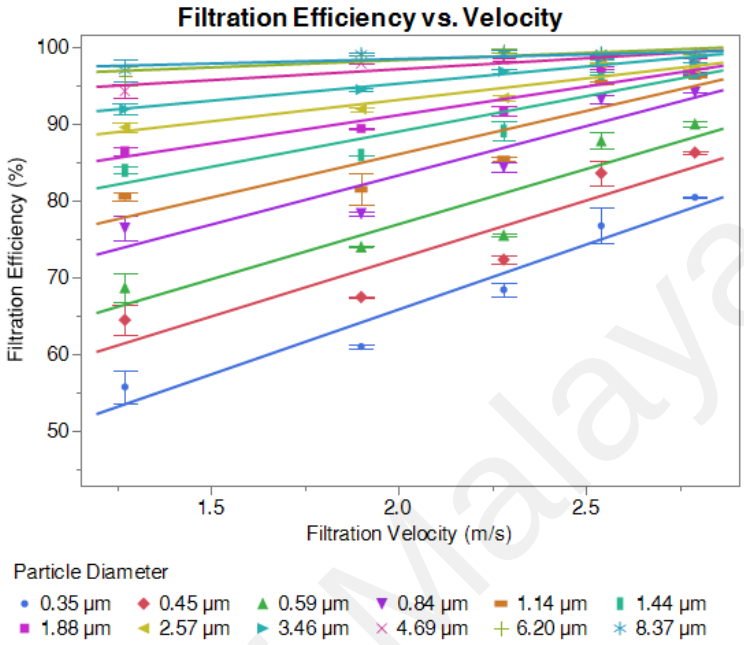

Figure 7.2: Filtration Efficiency against Filtration Velocity at Different Particle Diameters

Therefore, it is concluded that the filtration efficiency is dependent on the filtration velocity where the filtration efficiency increases with increasing velocity as the inertial impaction collection is more dominating at higher filtration velocity.

7.2 Initial Pressure Drop

The total pressure drop across filter is the summation of the initial pressure drop and the pressure drop across dust cake, as shown in Equation (2.18) $\Delta P = \Delta P_0 + \Delta P_c$. According to Equation (2.19) $\Delta P_0 = K_1 V_f$, the clean filter pressure drop is proportional to the filtration velocity based on Darcy's Law. This relationship is proven in the experiments by Li et al. (2019) at a range of tested velocities of 0 cm/s to 10.10 cm/s.

Figure 7.3 is the graph of initial pressure drop against filtration velocity. The graph is plotted based on the average of 15 repetitions on 15 test filters of similar model while the

error bar is constructed based on the standard deviation. The initial pressure drop increases in quadratic form with the filtration velocity. The relationship between the initial pressure drop, ΔP_0 and filtration velocity, V_f found in this study is

$$\Delta P_0 = 36.8\, {V_f}^2 - 42.69\, V_f + 28.92 \quad \textbf{(7.1)}$$

which is not consistent with Darcy Law. In HVAC system, the air face velocity is set in the range of 2.0 to 2.5 m/s for the dehumidifying coils (Handbook, 2005) and this subsequently causes the air filter experiencing similar high air velocity in actual application. Therefore, Darcy's Law is no longer applicable to explain the filter initial pressure drop.

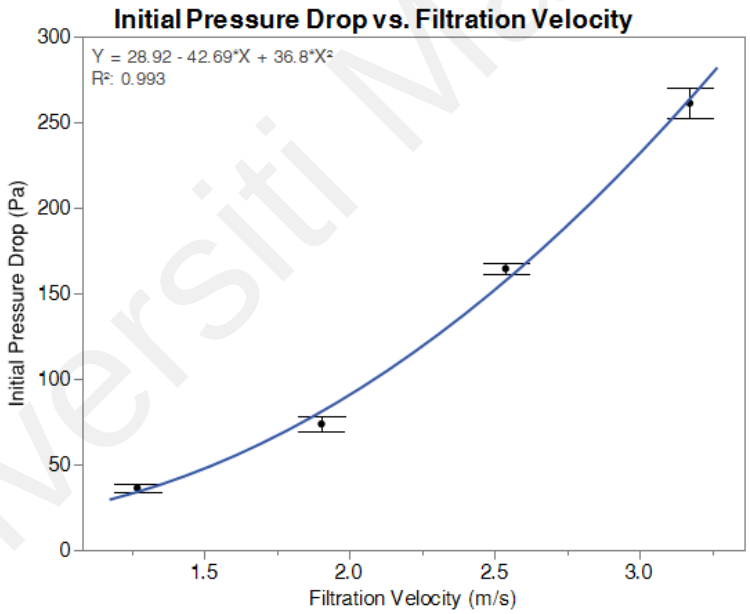

Figure 7.3: Initial Pressure Drop against Filtration Velocity

Darcy Forchheimer equation is used to predict the pressure drop across a porous region, ΔP. Two parameters are included in the equation which is the viscous and inertial resistance to the airflow (Théron et al., 2017):

$$\frac{\Delta P_0}{Z} = \frac{\mu}{B} \cdot V_f + \frac{C}{2} \rho \cdot {V_f}^2 \quad \textbf{(7.2)}$$

where Z is the media thickness; μ and ρ are the air dynamic viscosity and density; B is the media permeability; C is the inertial resistance coefficient and V_f is the air velocity. According to Dake (1983), the non-Darcy component which is the inertial resistance is negligible at low flow velocities.

The test filtration velocities in this study are relatively high, which is 1.27 m/s, 1.90 m/s, 2.54 m/s and 3.17 m/s. The selected test filtration velocities correspond to the 50%, 75%, 100% and 125% of the rated air flow rate, which is 0.944 m^3/s for a filter size with cross-sectional area of 610 mm × 610 mm at 0.944 m^3/s as described in ISO 16890:2017 (ISO, 2016c). Therefore, the inertial resistance effect is significant in this study, as shown in the data-fitted equation according to Equation (7.2) in Figure 7.3. This justifies the difference in clean filter pressure drop curve against filtration velocities of this study with the literature findings.

In short, it is found that the initial pressure drop shows a quadratic relationship of $\Delta P_0 = 36.8\, {V_f}^2 - 42.69\, V_f + 28.92$ with filtration velocity which is because the inertial resistance is accounted at high filtration velocity.

7.3 Pressure drop across dust cake

In this section, the pressure drop across dust cake, ΔP_c will be investigated based on the effect of the filtration velocities. The filters with same fibreglass media at 4.0 PPI and a pleat depth of 95 mm are tested at different velocities which are 1.27 m/s, 1.52 m/s, 1.90 m/s, 2.28 m/s and 2.54 m/s. Figure 7.4 shows the arrestance of the filters at different filtration velocities. When the arrestance drops more than 2 percentage points, it indicates the filter media starts to break and the respective mass of loaded dust on the filter is the maximum dust holding capacity.

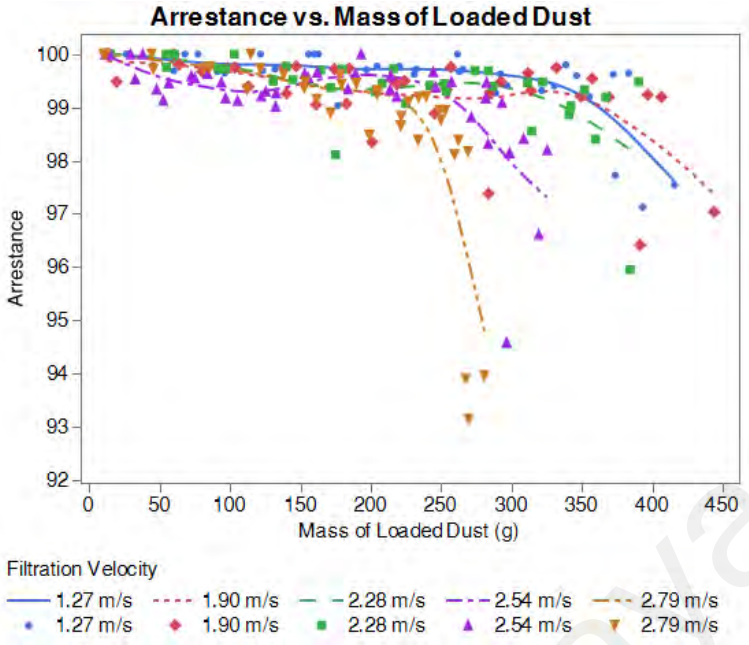

Figure 7.4: Arrestance against Mass of Loaded Dust at Different Filtration Velocities

7.3.1 Effect on K_c in Different Transitional Regimes

As shown in Figure 7.5, the total pressure drop is plotted against the mass of dust loaded to the filter. The total pressure drop, ΔP is the summation of initial pressure drop of the filter, ΔP_0 and the pressure drop across dust cake, ΔP_c which can be expressed as

$$\Delta P = \Delta P_0 + \Delta P_c = \Delta P_0 + K_c \mu \frac{m V_f}{S_f} \tag{7.3}$$

where K_c is the specific dust cake resistance coefficient, μ is the dynamic viscosity of air, m is the mass of dust loaded on the filter, V_f is the filtration velocity and S_f is the filtration area.

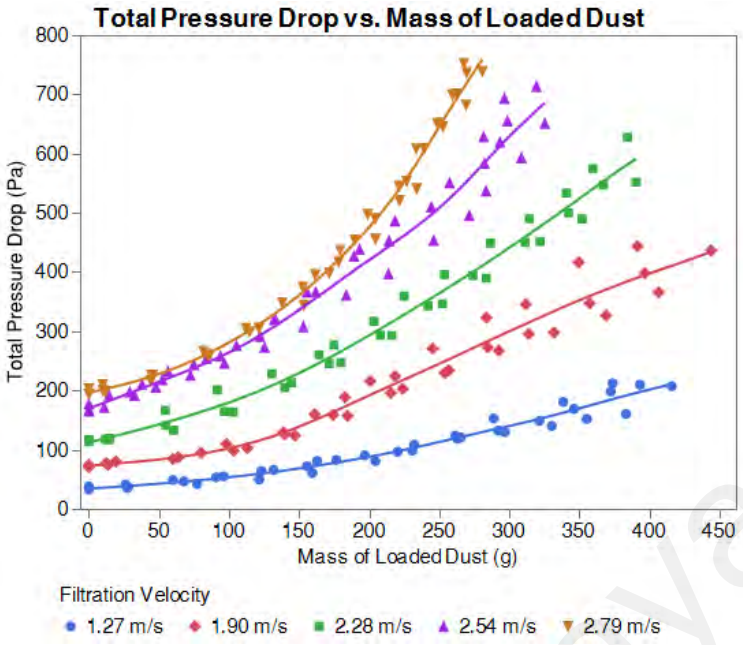

Figure 7.5: Total Pressure Drop against Mass of Loaded Dust based on Filtration Velocity

Figure 7.6 is showing the relationship of dust cake pressure drop against mass of loaded dust with the deduction of initial pressure drop. It can be observed that the curve gradient of the trendline is increasing along with the mass of loaded dust, at three distinct stages: constant increase stage at a low gradient, accelerating increase stage and lastly constant increase stage at the steepest slope. It is further categorized into three different filtration regimes based on the obvious increase in curve gradient: depth filtration, transitional filtration, and surface filtration. The specific resistance coefficient of dust cake, K_c represents a measure of the difficulty of air permeation through the filter. Figure 7.7 is transformed from Figure 7.6 using Equation (7.3)(7.2) to determine K_c based on three different filtration regimes. The K_c value in each regime is determined in linear regression (Cheng & Tsai, 1998). Table 7.1 summarizes the specific resistance coefficient of dust cake at different filtration regimes.

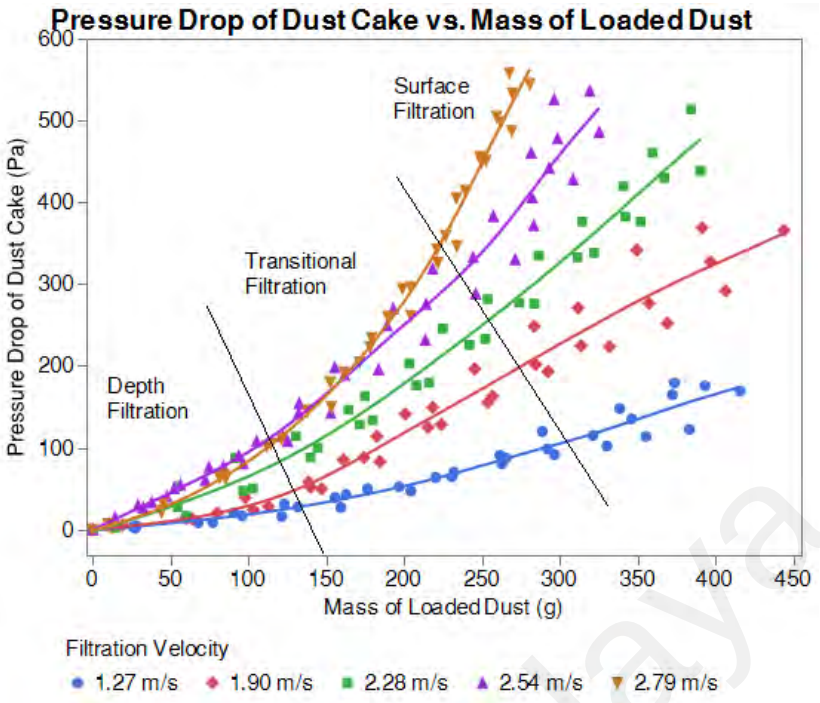

Figure 7.6: Pressure drop across Dust Cake against Mass of Loaded Dust based on Filtration Velocity

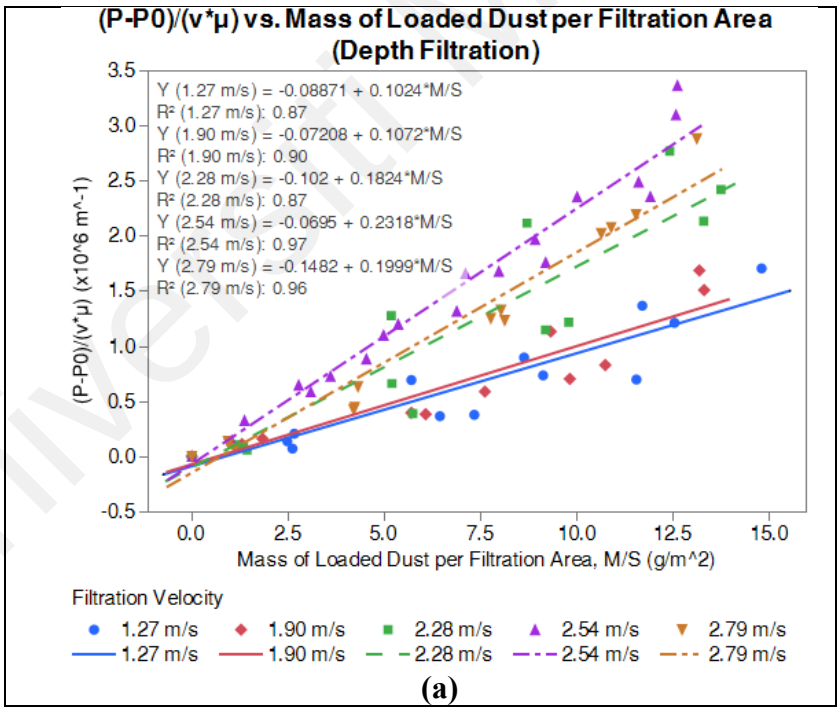

(a)

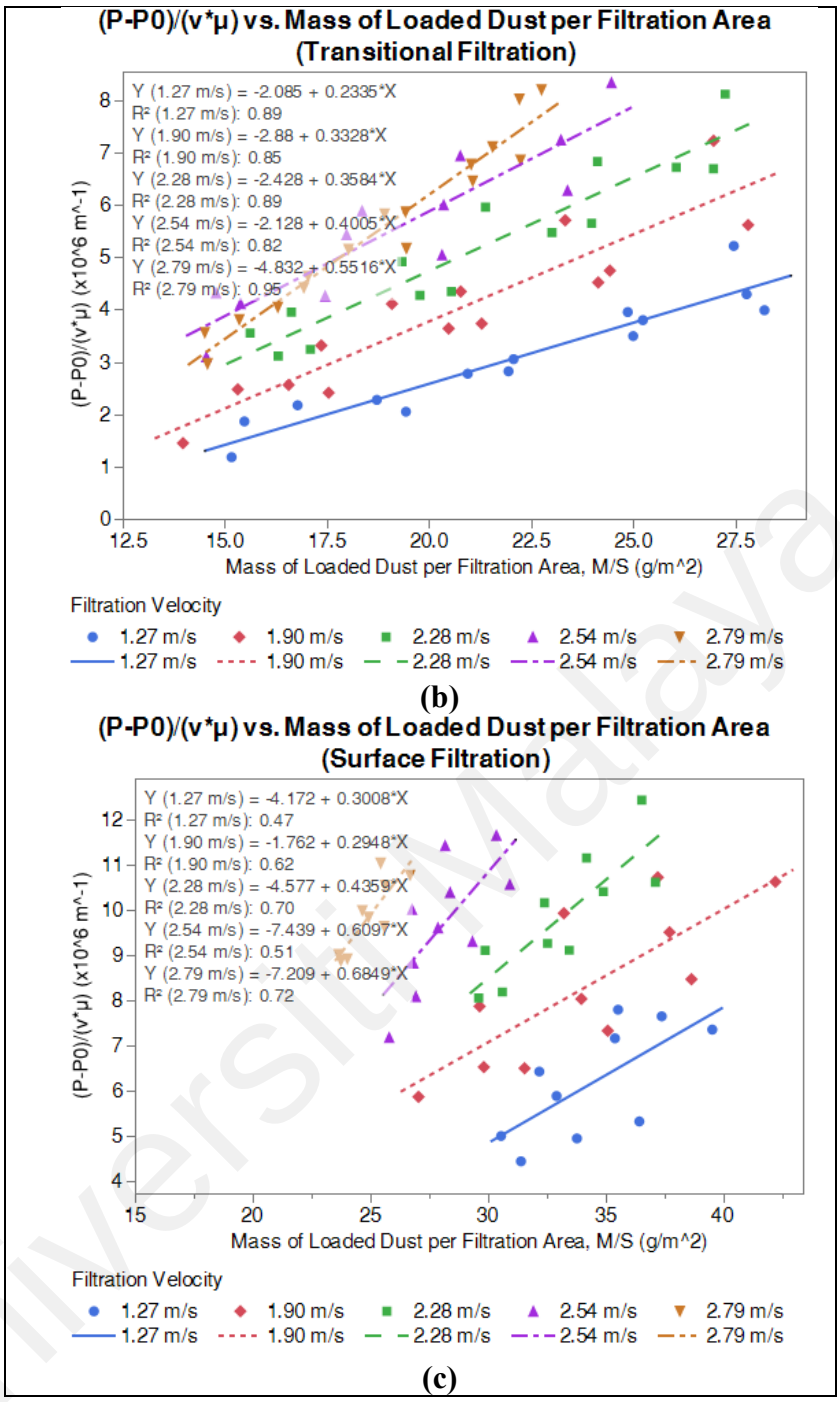

Figure 7.7: Effect of the Dust Cake Specific Resistance Coefficient at Different Filtration Stages (a) Depth Filtration (b) Transitional Filtration (c) Surface Filtration

Table 7.1: Specific Resistance Coefficient of Dust Cake at Different Filtration Regimes

Filtration Velocity (m/s)	Specific Resistance Coefficient of Dust Cake, K_c ($\times 10^6$ m/g)		
	Depth Filtration	Transitional Filtration	Surface Filtration
1.27	0.1024	0.2335	0.3008
1.90	0.1072	0.3328	0.2948
2.28	0.1824	0.3584	0.4359
2.54	0.2318	0.4005	0.6097
2.79	0.1999	0.5516	0.6849

Figure 7.8 depicts the close-up pictures of the filter media during depth filtration, transitional filtration and surface filtration. It can be observed that the colour of the filter media becomes more brownish, and the pleat structure becomes curvier as the dust accumulated on the surface increases along the filtration stages. In the early stage, which is called depth filtration in Figure 7.7(a), it can be observed that the gradient, K_c is less steep than other two stages. This can also be seen from Table 7.1 that the K_c values at the depth filtration are the lowest compared to other regimes. The dust particles have accumulated on the surface of each filter fibre. As the amount of dust is limited in the early stage trapped within the filter media, which is less than 150 g of loaded dust, the airflow is not obviously affected and therefore, the change in pressure drop is increasing gradually at the lowest K_c values. K_c values of transitional region, which is shown in Table 7.1, is higher that of the depth filtration but lower than the surface filtration. This happens due to the thin properties of the fibreglass media, most of the void space is filled quickly by dust particles within the filter media and it enters transitional stage when the dendritic structures start to form. The pressure drop of the filter in this transitional stage increases faster than the depth filtration. The dendritic structures gradually grow in the transitional stage until the dendrites intercept others' grow paths. At this stage, the filter enters surface filtration when the dust cake is formed. The pressure drop curve in this stage increase steeply compared to the previous two stages, causing the K_c values to be highest.

Figure 7.8: Samples of Close-up Pictures for Filter Media during (a) Depth Filtration (b) Transitional Filtration (c) Surface Filtration

7.3.2 Effect on K_c in Full Range of Mass of Loaded Dust

Besides seeing in filtration regimes, the specific resistance coefficient of dust cake, K_c is also analysed in a full range of mass of loaded dust. Figure 7.9(a) is the graph of $\frac{\Delta P - \Delta P_0}{V_f \cdot \mu}$ against $\frac{m}{S_f}$ where the gradient of the graphs represents the specific resistance coefficient of dust cake, K_c. It exhibits quadratic growth with increasing mass of dust per filtration area, $\frac{m}{S_f}$. The rate of change of $\frac{\Delta P - \Delta P_0}{V_f \cdot \mu}$ with respect to $\frac{m}{S_f}$ is shown in Figure 7.9(b). It also can be seen that the K_c values are increasing when the mass loaded on the filter surface area increases and it behaves as linear relationship. This can be explained that the porosity of dust cake decreases when more dust is accumulated on the filter surface, hence exerting a higher blockage to the air flow.

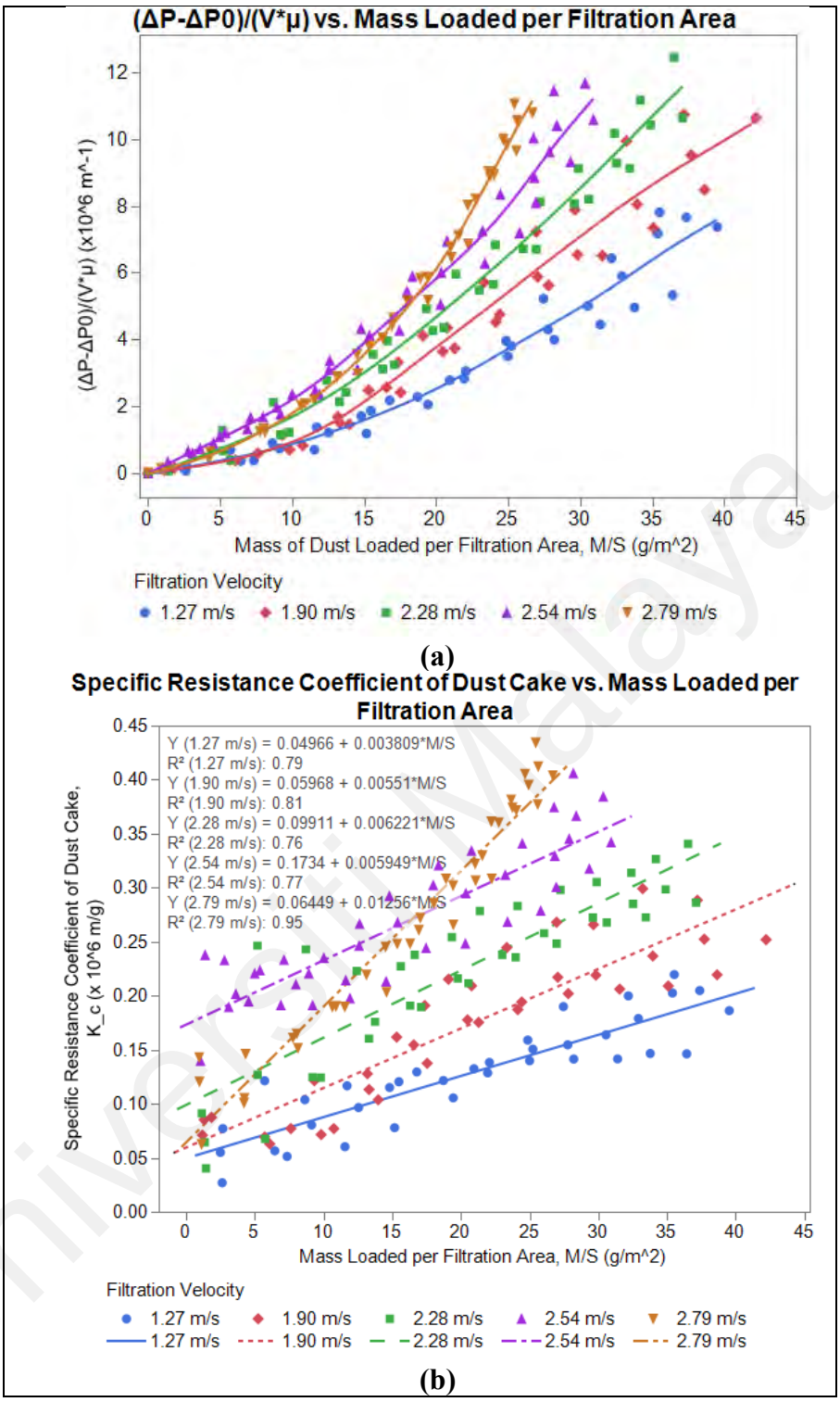

Figure 7.9: Effect of the Filtration Velocity on the Dust Cake Specific Resistance Coefficient, K_c (a) $\frac{\Delta P-\Delta P_0}{V_f \cdot \mu}$ against $\frac{m}{S_f}$ where gradient is K_c (b) $\frac{(\Delta P-\Delta P_0)S_f}{V_f \cdot \mu \cdot m}$ against $\frac{m}{S_f}$ where y-axis is K_c

As shown in Figure 7.9(a), the pressure drop across dust cake is divided by the filtration velocity to study the effect of the filtration velocity on the K_c. It shows that the filtration velocity is a contributing factor in dust cake formation, as at different velocities,

the rate of change with respect to mass of loaded dust is different instead of overlaying of each other. The slope of the dust cake specific resistance coefficient, K_c is steeper at the higher filtration velocity, with the increasing of loaded dust mass as shown in Figure 7.9(b). This is proven by Cheng and Tsai (1998) and Choi et al. (2004) that the dust cake formed tends to be relatively thinner at a higher filtration velocity, as the old dust cake is compressed by the new dust cake layer to be denser, and this decreases the dust cake porosity. As a result, the pressure drop across dust cake increases at increasing velocity.

However, the K_c values for filtration velocity of 2.79 m/s increase significantly at a steeper slope compared to other velocities. This happens might be due to the strong turbulence effect at a high filtration velocity. The turbulence effect brings to an uneven dust distribution in the air flow, causing the dust hardly deposited on the filter. The low amount of dust deposited in the depth filtration and beginning of the transitional filtration causes the K_c to be lower than that of filtration velocity of 2.54 m/s. When the dust cake starts to develop at the later stage, the effect of filtration velocity across the dust cake becomes significant. This causes K_c to increase significantly at a steeper slope, starting from a lower K_c value which corresponds to a lower mass of loaded dust, as shown in Figure 7.9(b) compared with other filtration velocities.

Therefore, it can be summarized that the specific resistance coefficient of dust cake, K_c increases linearly with mass of loaded on filter. K_c increases with the increasing filtration velocity due to the denser dust cake formed at a higher filtration velocity. The effect of filtration velocity on K_c is further analysed by fixing the mass of loaded dust or dust concentration as shown in the following.

7.3.3 Effect on K_c at Constant Dust Concentration

Figure 7.10 illustrates the relationship of K_c and filtration velocity at constant dust concentration. The dust concentrations are taken at 4.75 g/m^2, 9.51 g/m^2, 14.26 g/m^2,

19.01 g/m^2, 23.76 g/m^2 and 28.52 g/m^2, which correspond to the mass of dust loaded of 50 g, 100 g, 150 g, 200 g, 250 g and 300 g on the test filters. When the dust concentration is lower than 19.01 g/m^2, K_c is increasing linearly with filtration velocity while the relationship turns into quadratic growth as the dust concentration increases. When the dust concentration is lower than 19.01 g/m^2, which is in the depth filtration region and the beginning of the transitional filtration region, dust is accumulated within the filter bed and dust cake formation is low. This causes the effect of filtration velocity on dust cake resistance to air flow is not significant due to low dust cake formation. When the dendritic structures form into dust cake since the middle stage of transitional regime, the dust cake resistance becomes higher and increases in higher gradient along the increasing velocity. The filtration velocity becomes a major factor on pressure drop across dust cake, when the dust cake formation is getting thicker.

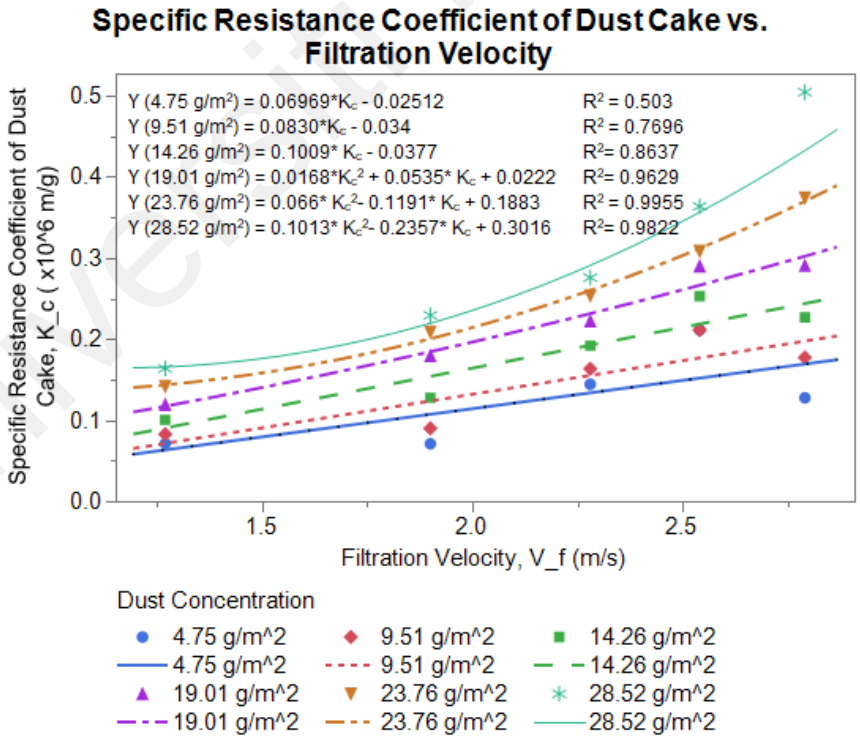

Figure 7.10: Relationship between K_c and Filtration Velocity at Constant Dust Concentration

Thus, the empirical relationships of K_c and filtration velocity, V_f can be concluded as

$$K_c = aV_f + b \tag{7.4}$$

for depth filtration and beginning of transitional filtration and

$$K_c = aV_f{}^2 + bV_f + c \tag{7.5}$$

for middle of transitional filtration and surface filtration where a, b and c are empirical constants.

7.3.4 Effect on Dust Holding Capacity & Final Pressure Drop

Next, the effect of filtration velocity on the dust holding capacity and the final pressure drop is also studied, as depicted in Figure 7.11. The final pressure drop is the resistance to air flow when the filter reaches its maximum dust holding capacity. It reveals that as the dust holding capacity decreases and the final pressure drop increases as the filtration velocity increases. The reason behind is that when the filtration velocity is high, a higher force will be incurred on the filter media, causing the filter media to deform easily. This leads the media to fail at a lower dust holding capacity at higher filtration velocity. As discussed earlier, the pressure drop across filter is significantly dependent on the filtration velocity. Therefore, the final pressure drop increases with filtration velocity, even when total mass of dust loaded is low. Therefore, the dust holding capacity is low with high final pressure drop at a higher filtration velocity.

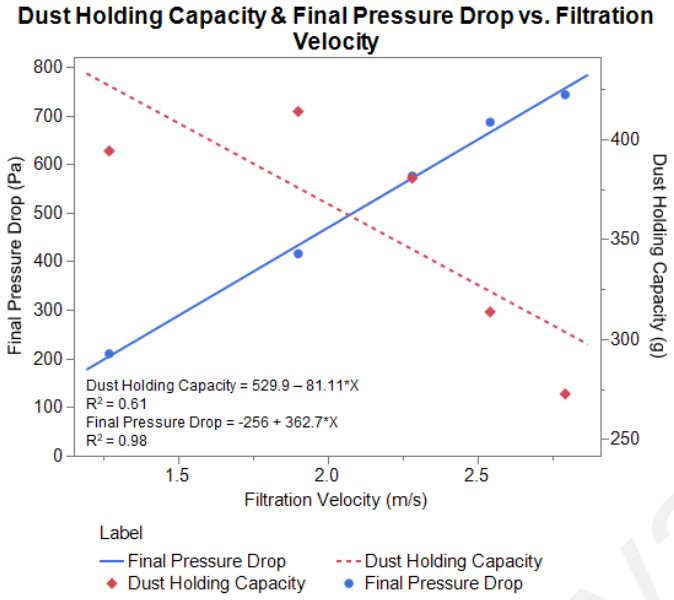

Figure 7.11: Effect of Filtration Velocity on Dust Holding Capacity and Final Pressure Drop

7.4 Summary

The experimental findings indicate that the influence of the filtration velocity is significant to the filtration performance including filtration efficiency, initial pressure drop and pressure drop across dust cake. The filtration efficiency increases with increasing filtration velocity as the inertial impaction becomes more dominating at high filtration velocity.

The initial pressure drop exhibits quadratic growth with increasing filtration velocity, corresponding to Darcy Forchheimer equation at the relationship expressed as $\Delta P_0 = 36.8\, {V_f}^2 - 42.69\, V_f + 28.92$ as the inertial resistance is significant at high filtration velocity.

The dust cake specific resistance coefficient, K_c increases at an increasing velocity, V_f. The dust cake tends to be compressed into a denser form at a high filtration velocity, which subsequently increasing the pressure drop across dust cake. At constant dust concentration, the relationship between K_c and V_f is in a linear relationship for depth filtration and the starting of transitional filtration at an empirical equation of $K_c = aV_f +$

b. Since the middle of transitional filtration and the surface filtration, K_c shows a quadratic growth with increasing V_f at an empirical equation of $K_c = aV_f{}^2 + bV_f + c$ where a, b and c are empirical constants.

The dust holding capacity decreases and the final pressure drop increases with increasing filtration velocity. The greater force incurred by the higher velocity or greater air flow causes the filter media deforms and ruptures easily, causing a low dust holding capacity.

The filtration efficiency is the most important factor in consideration of the indoor air quality as well as the air filter design. If the filtration efficiency can achieve the minimum required indoor air quality according to different industrial applications, such as hospitals, office buildings or semiconductor factories, the operation of the HVAC filtration systems can be maintained at a lower filtration velocity, considering that the higher air velocity will increase the pressure drop across the filter and subsequently increases the system energy consumption. Therefore, the selection of the operational air velocity across the air filters shall take into consideration of both the filtration efficiency and the system energy consumption.

CHAPTER 8: EFFECT OF THE PLEAT GEOMETRY ON THE FIBROUS FILTRATION PERFORMANCE

Filter media is often pleated to maximize the effective filtration area in a limited filter dimension. The pleat geometrical parameters are important to be considered as the filtration performance is strongly dependent on the pleat geometry such as pleat depth and pleat density or pleat width. The aim of this chapter is to study the effect of the pleat geometry of the full-sized industrial filters on the filtration performance, including the initial filtration efficiency, initial pressure drop and the pressure drop of the dust cake.

In order to find the effect of pleat density on the filtration performance, the filter media used is fixed with same fibreglass media at a pleat depth of 95 mm. Different filters at different pleat densities of 3.5 PPI, 4.0 PPI, 4.5 PPI, 5.0 PPI, 6.0 PPI and 6.5 PPI are tested at the different filtration velocities. The investigation of the influence of pleat depth on the filtration performance is carried out at different pleat depths of 44 mm, 60 mm, 75 mm, 85 mm and 95 mm, keeping the pleat density constant at 4.0 PPI. The filtration velocity is maintained at 2.54 m/s for filtration efficiency and dust loading procedure in this study of pleat geometry.

8.1 Filtration Efficiency

The effect of the pleat geometry on the filtration efficiency is studied. The graphs of filtration efficiency against particle diameters at different pleat densities and pleat depths are plotted in Figure 8.1 and Figure 8.2, respectively. The figures show that as the particle diameter increases, the filtration efficiency also increases due to as the interception collection become more dominate at a larger particle size larger than 0.5 μm (Zhu et al., 2000). As discussed earlier in Chapter 2, there are three particle capture mechanisms: Brownian diffusion (particle size $< 0.1\ \mu m$), interception (particle size $> 0.5\ \mu m$) and inertial impaction (particle size $> 5\ \mu m$). The most penetrating particle size which

normally happens in the particle size of 0.1 to 1 μm (Wang & Zhao, 2015), which are in the interception mechanism range, is difficult to be captured by the fibres. This has caused the filtration efficiency to be relatively lower at the smaller particle range as shown in Figure 8.1 and Figure 8.2.

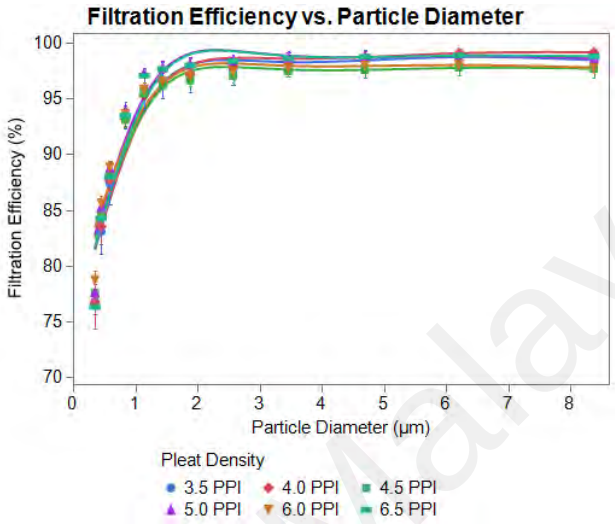

Figure 8.1: Filtration Efficiency against Particle Diameter at Different Pleat Densities

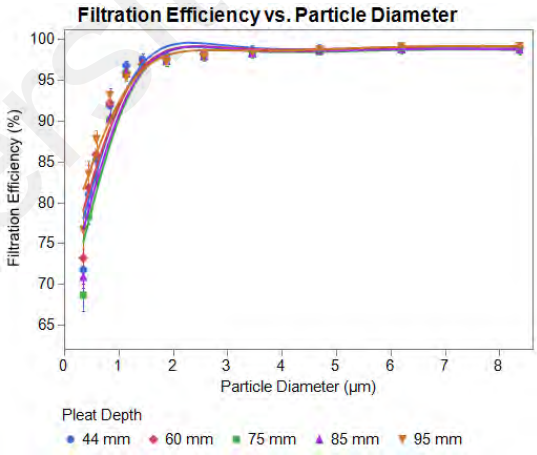

Figure 8.2: Filtration Efficiency against Particle Diameter at Different Pleat Depths

Besides, it can be observed from Figure 8.1 and Figure 8.2 that the pleat densities and pleat depths show insignificant relationship with the filtration efficiency as the filtration efficiencies are very close to each other at different pleat densities and pleat depths. The difference between the maximum and minimum efficiency values against various particle diameters are only less than 3 percentage points within different pleat densities, and less

than 8 percentage points within different pleat depths. The insignificant relationship between the pleat geometry and filtration efficiency corresponds with the literature findings as the filtration efficiency is pronouncedly affected by media fibre properties and filtration velocity (Bian et al., 2020; Leung et al., 2010; Payen et al., 2012), which are discussed in Chapters 6 and 7, while the pleat geometry is significantly influencing the pressure drop of the filters (Théron et al., 2017). Hence, it can be concluded that the pleat geometry is a negligible contributing factor in filtration efficiency.

8.2 Initial Pressure Drop

8.2.1 Pleat Density of Filter Media

Figure 8.3 illustrates the relationship between the initial pressure drop and filtration velocity at different pleat densities. The initial pressure drop shows a quadratic growth with the filtration velocity for all pleat densities, corresponding to the Darcy Forchheimer equation discussed in Section 7.2. Equation (8.1) shows the curve-fitted expression of the relationship

$$\Delta P_0 = K_i V_f^{\,2} - K_1 V_f + c \qquad \textbf{(8.1)}$$

where ΔP_0 is the initial pressure drop, V_f is the filtration velocity, K_i represents the inertial resistance coefficient to airflow, K_1 is the viscous resistance coefficient to airflow, and c is the empirical constant. As the pleat density increases, the gradient of the graphs, which represents the inertial resistance coefficient, K_i also increases. This is better depicted in Figure 8.4, which shows a substantial effect of the pleat density on the initial pressure drop. As the pleat density increases, the initial pressure drop also increases. This happens because pleating is an efficient way to increase the total filtration area in limited filter size. A higher total filtration area is able to allow more air to pass through easily. However, when the pleat density is too high, the compact media pack will in fact decrease the pleat channel and form a high blockage to the airflow from passing through. The high

pleat density media has caused a low air permeability and thus an increased airflow resistance. This explains the phenomenon in which the initial pressure drop increases with increasing pleat density in Figure 8.4.

It has shown that at lower filtration velocities which are 1.27 m/s and 1.90 m/s, the initial pressure drop increases linearly with increasing pleat density while showing an accelerating increase of initial pressure drop at higher filtration velocities of 2.54 m/s and 3.17 m/s. The effect of the pleat density on the initial pressure drop becomes more pronounced at higher velocity. This happens because of the increasing inertial effect of airflow on the initial pressure drop across the higher pleat density (Maddineni et al., 2019).

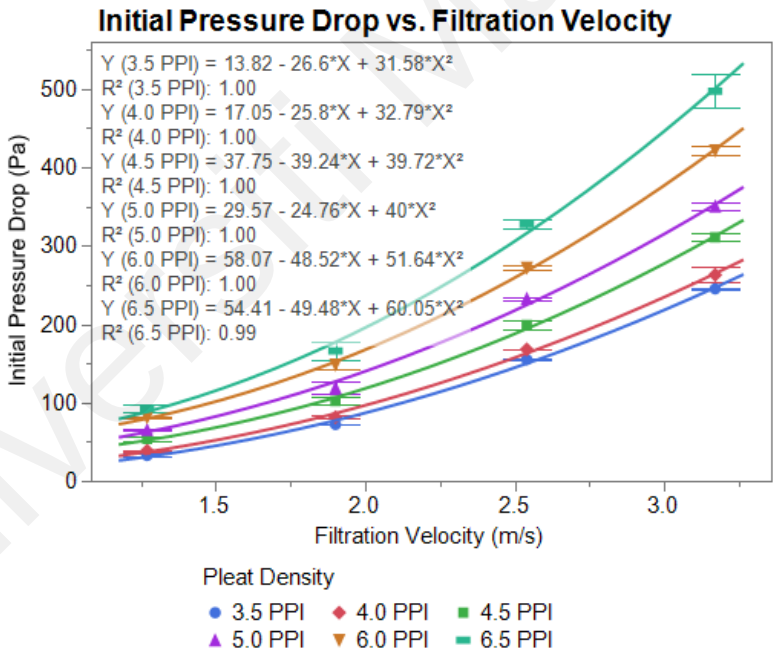

Figure 8.3: Initial Pressure Drop against Filtration Velocity based on Different Pleat Densities

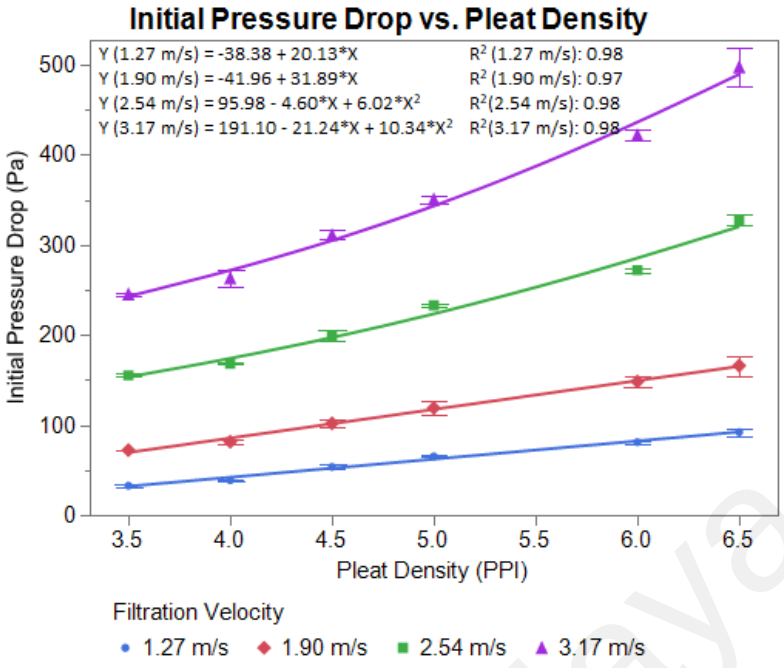

Figure 8.4: Initial Pressure Drop against Pleat Density at Different Filtration Velocity

Therefore, it can be summarized that the initial pressure drop is dependent on the pleat density, where the initial pressure drop increases with increasing pleat density. The effect of pleat density on the initial pressure drop is more pronounced, showing a quadratic increment of initial pressure drop at higher filtration velocity due to the increasingly significant inertial effect across the denser pleats.

8.2.2 Pleat Depth of Filter Media

From Figure 8.5, the relationship between the initial pressure drop and the filtration velocity exhibits a quadratic growth at different pleat depths, which is the similar trend with pleat density as shown in Figure 8.3. Figure 8.6 demonstrates a decreasing linear relationship between the initial pressure drop and pleat depth at different filtration velocities. The initial pressure drop increases when the pleat depth is smaller. This can be explained that the increasing pleat depth increases the total filtration area, which will increase the air permeability. Air can pass through the filter media easily with a larger filtration surface and hence, causing a lower resistance to airflow.

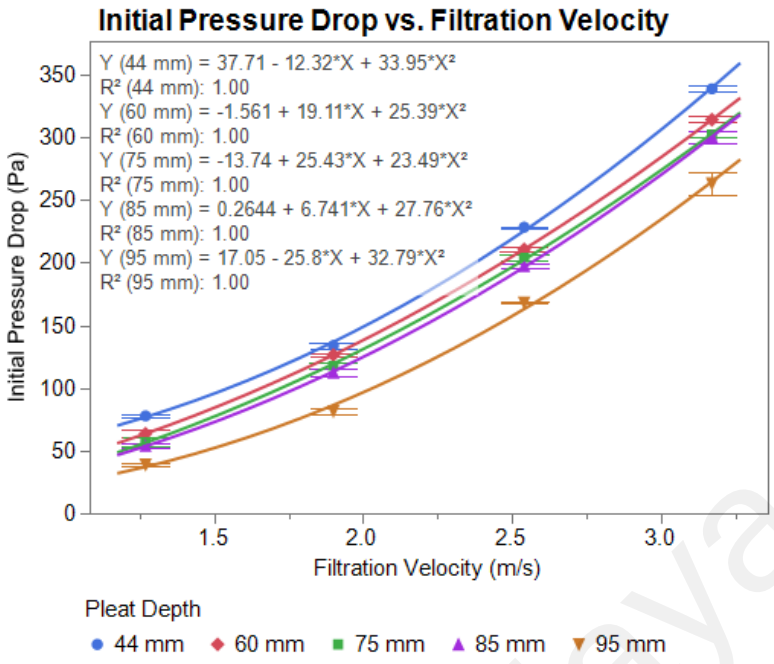

Figure 8.5: Initial Pressure Drop against Filtration Velocity based on Pleat Depth

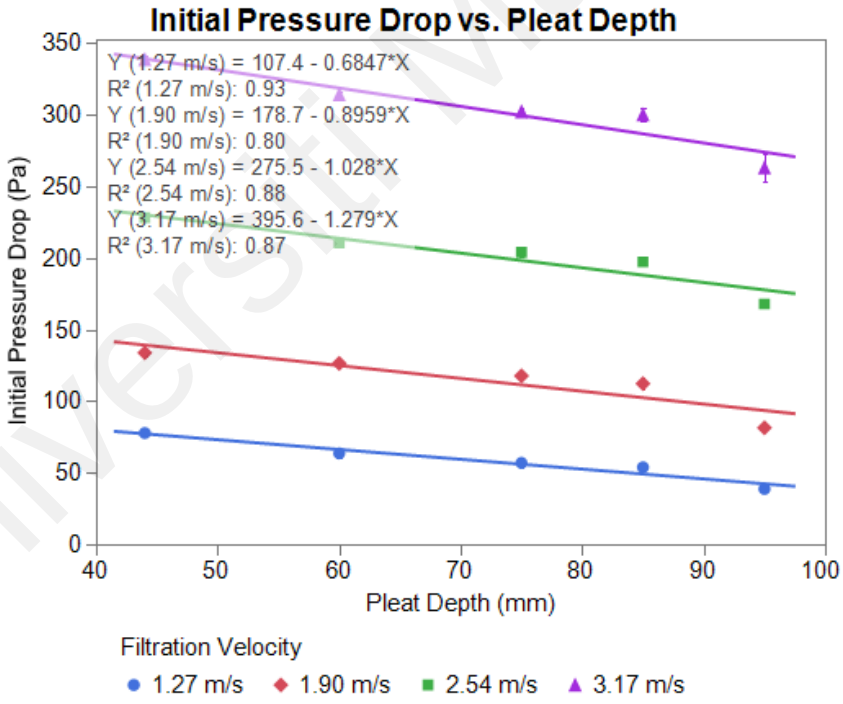

Figure 8.6: Initial Pressure Drop against Pleat Depth at Different Filtration Velocity

8.2.3 Pleat Ratio

Pleat ratio, α is a dimensionless parameter in terms of pleat density and pleat depth to represent the pleat geometry. The pleat ratio is calculated by dividing pleat depth, P_d with pleat width, P_w as shown in Equation (8.2).

$$\alpha = \frac{P_d}{P_w}, P_w = \frac{25.4}{Pleat\ density} \quad \textbf{(8.2)}$$

Figure 8.7 is plotted to reveal the relationship between the initial pressure drop and pleat ratio. It shows that the initial pressure drop shows a positive quadratic relationship with the pleat ratio, having an optimum pleat ratio to obtain the minimum initial pressure drop at different filtration velocities. This outcome is also proven by Persaud et al. (2021) that increasing the pleat depth and using an optimal pleat density can achieve an optimum filtration performance which is the initial pressure drop in current finding.

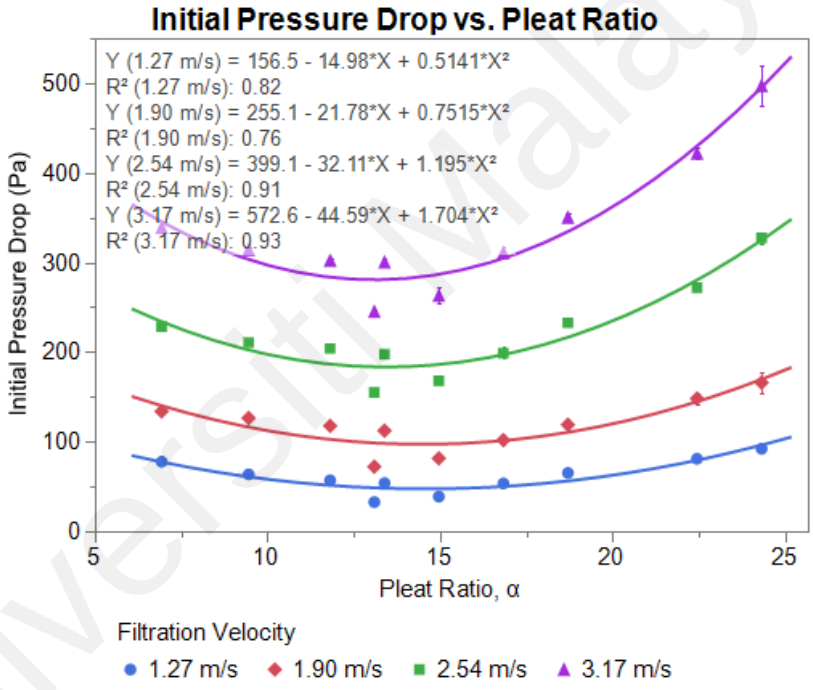

Figure 8.7: Effect of Pleat Ratio on the Initial Pressure Drop

Table 8.1 summarizes the optimum pleat ratio to achieve lowest initial resistance to air flow at different velocities. The optimum pleat ratio decreases slightly as the filtration velocity increases, and the difference between the highest and lowest optimum pleat ratio is only a decrease of 10.2 % while the lowest filtration velocity of 1.27 m/s increases by 119.69% to 2.79 m/s. It can be concluded that the effect of filtration velocity is insignificant on the pleat ratio to achieve minimum initial pressure drop.

Table 8.1: Optimum Pleat Ratio for Minimum Initial Pressure Drop

Filtration Velocity (m/s)	Optimum Pleat Ratio for Minimum Initial Pressure Drop
1.27	14.57
1.90	14.49
2.54	13.44
2.79	13.08

Therefore, the optimum pleat ratio is found to be at a range of 13.08 to 14.57 at a median value of 13.895. The pleat ratios concluded from the literature are below 1.59 (Li et al., 2019), 1.48 (Park et al., 2012) or 2.22 - 3.70 (Teng et al., 2022), which are relatively smaller than the outcome of this study. This is due to the filter tested are mini pleats or cartridge filters, which is not suitable for the HVAC application. Thus, a pleat ratio range of 13.08 to 14.57 is recommended to obtain a low initial pressure drop for the full-scaled HVAC pleated filters.

8.3 Pressure Drop across Dust Cake

8.3.1 Arrestance

Figure 8.8 shows the graphs of arrestance against mass of loaded dust at different pleat densities and pleat depths. When the arrestance starts to drop more than 2%, the dust loading process will be stopped. This indicates the filter media's failure, and the dust holding capacity is taken.

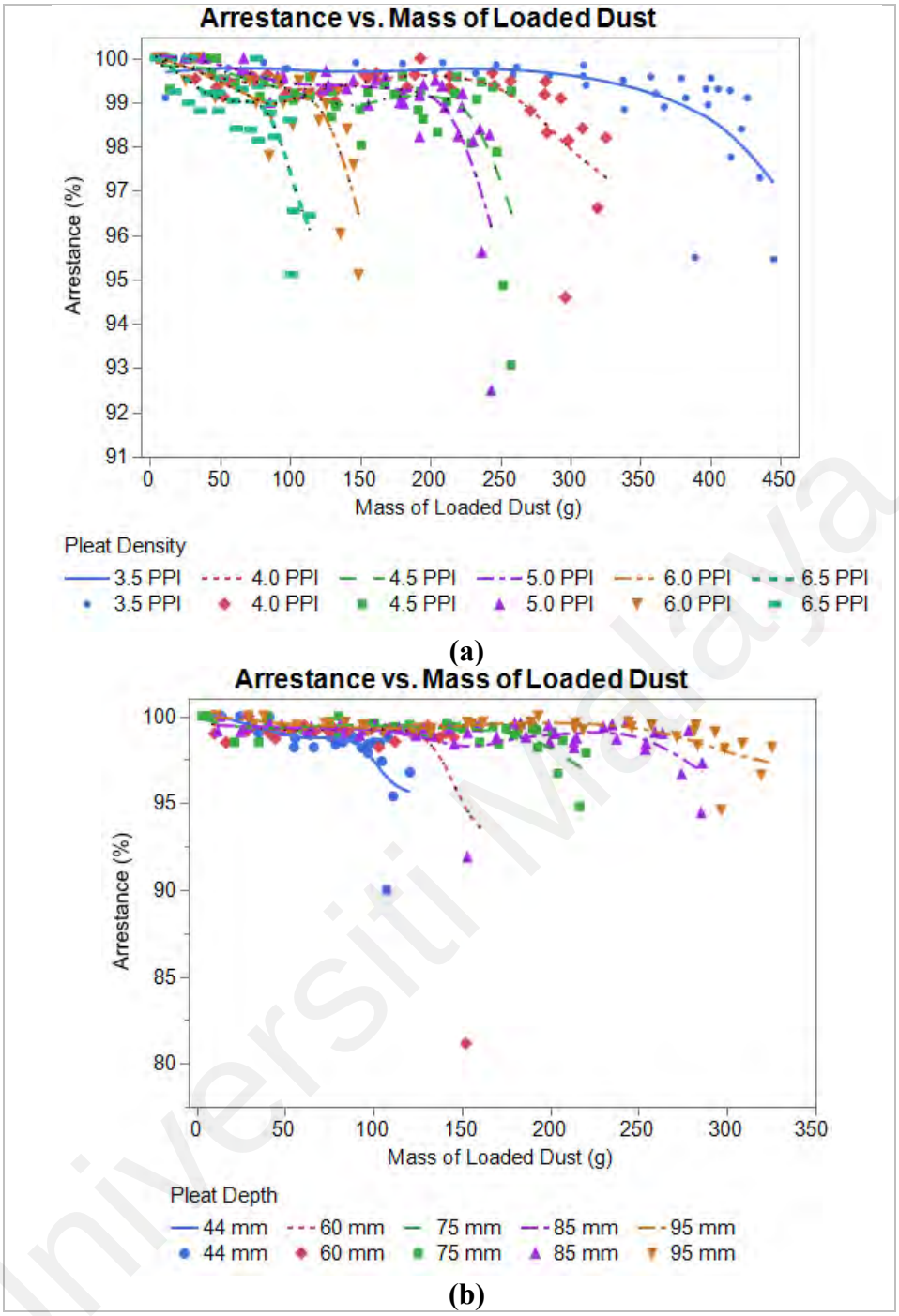

Figure 8.8: Arrestance against Mass of Loaded Dust at Different (a) Pleat Densities (b) Pleat Depths

8.3.2 Effect of Pleat Density on K_c

Figure 8.9 is the total pressure drop plotted against the mass of loaded dust to the filter for different pleat densities. The total pressure drop is the summation of initial pressure drop of the clean filter and the instantaneous pressure drop across dust cake, which has been discussed in Equation (7.3). The pressure drop across dust cake are illustrated in Figure 8.10, by subtracting the initial pressure drop from total pressure drop. It can be

observed that the pressure drop across dust cake for all pleat densities increases in three gradient zones, which are depth filtration (constant increase stage at a lower gradient), transitional filtration (accelerating increase stage), and surface filtration (constant increase stage at the steepest slope). The dust loading stages are in consistence to typical dust loading behavior, which is also similar to Section 6.3.2. In the depth filtration, the particles are collected within the fibre media, where the pressure drop increases gradually at a lower gradient. After most filter fibres are filled with dust particles, the transitional filtration begins when the dendritic structures start to form, and the pressure drop increases at a higher rate than depth filtration. The surface filtration is the regime where the dendritic structures overlay each other, forming a dust cake layer. Dust is then trapped on the dust cake surface and the pressure drop across dust cake increases rapidly.

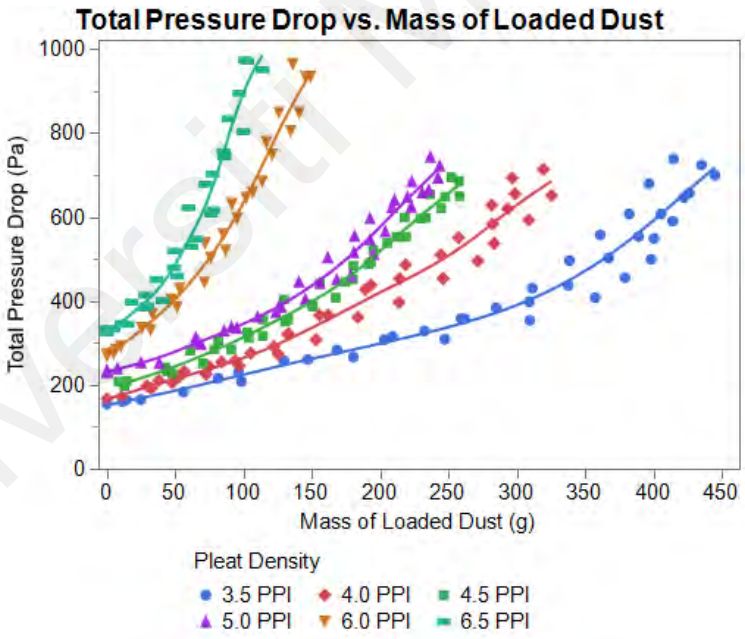

Figure 8.9: Total Pressure Drop against Mass of Loaded Dust at Different Pleat Densities

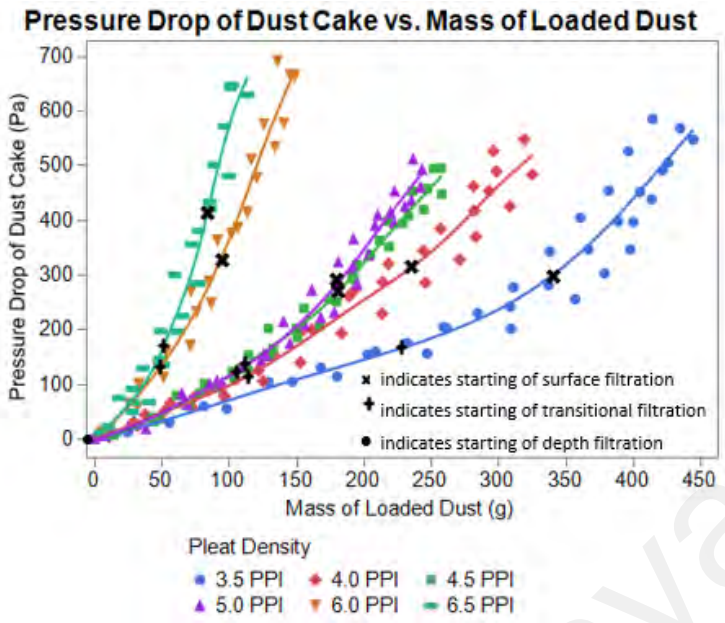

Figure 8.10: Pressure Drop across Dust Cake against Mass of Loaded Dust at Different Pleat Densities

Using Equation (7.3) $\Delta P = \Delta P_0 + \Delta P_c = \Delta P_0 + K_c \mu \frac{m V_f}{S_f}$, the graph of $\frac{\Delta P - \Delta P_0}{V_f \cdot \mu}$ against mass of loaded dust per filtration area, $\frac{m}{S_f}$ is plotted in Figure 8.11(a) where the gradient of the graphs represents the specific resistance coefficient of dust cake, K_c. The curve is transformed into a linear graph of K_c against $\frac{m}{S_f}$ to study the effect of pleat density on K_c. From Figure 8.11(b), the gradient increases with increasing pleat density. With the same mass of dust fed, it results in a higher pressure drop across the filter at higher pleat density. Figure 8.12 depicts that the K_c shows an exponential increment with increasing pleat density, P_ρ at dust concentration of 5 g/m^2, 10 g/m^2, 15 g/m^2 and 20 g/m^2. There are no K_c values for pleat density of 6.0 and 6.5 PPI at the dust concentration of 15 g/m^2 and 20 g/m^2 due to filter's failure beyond 10 g/m^2. In addition, it also shows that the K_c value increases drastically when the pleat density is bigger than 5.0 PPI. This can be explained that when the media is highly packed (at high pleat density), the pleat is very dense that they are in contact with each other and create a blockage to the air flow. This subsequently reduces the effective filtration area, even though the total media area is large at high pleat density. This result is in consistency of the findings of Al-Attar (2011) and Teng et al.

(2022) that the pleat crowding effect as a result of the excessive number of pleats will cause a loss in effective filtration area. In summary, the specific resistance coefficient of dust cake, K_c increases exponentially as the pleat density increases.

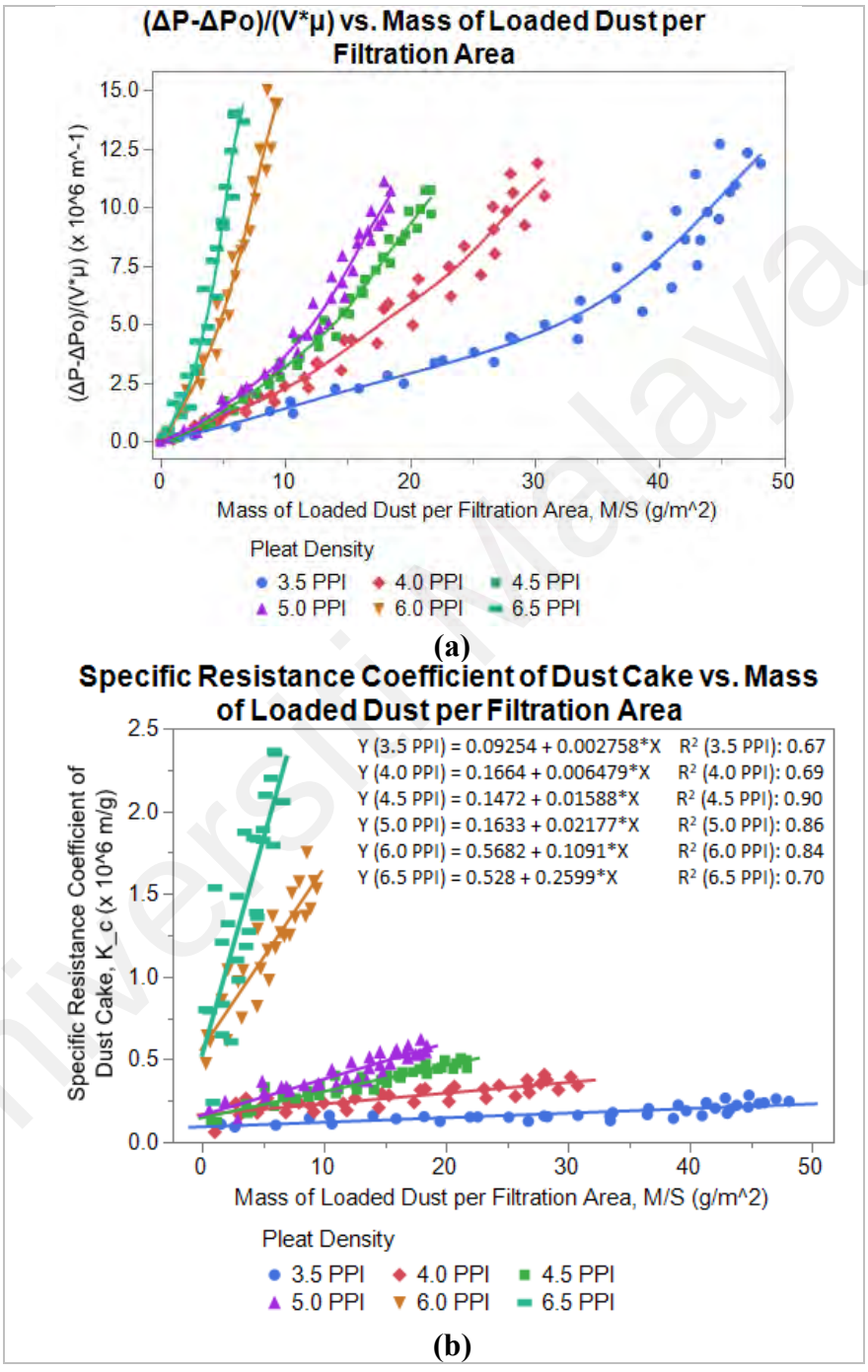

Figure 8.11: Effect of the Pleat Density on the Dust Cake Specific Resistance Coefficient, K_c (a) $\frac{\Delta P-\Delta P_0}{V_f \cdot \mu}$ against $\frac{m}{S_f}$ where gradient is K_c (b) $\frac{(\Delta P-\Delta P_0)S_f}{V_f \cdot \mu \cdot m}$ against $\frac{m}{S_f}$ where y-axis is K_c

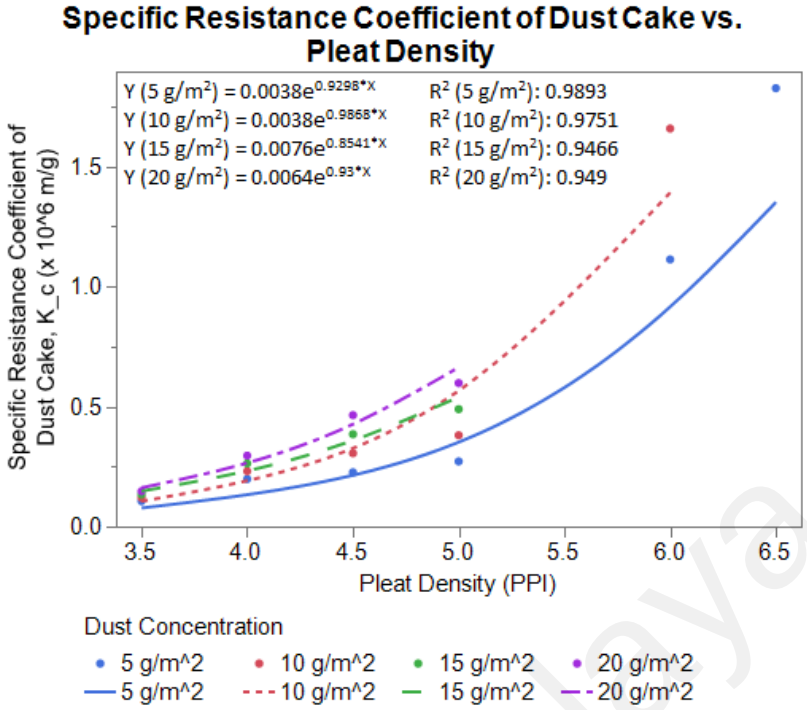

Figure 8.12: Relationship of the Pleat Density on the Dust Cake Specific Resistance Coefficient, K_c

8.3.3 Effect of Pleat Depth on K_c

Figure 8.13 and Figure 8.14 show the total pressure drop and the pressure drop across dust cake respectively for different pleat depths whereas Figure 8.14 shows that the dust loading curve follows the typical 3 different filtration regions: depth filtration, transitional filtration and surface filtration.

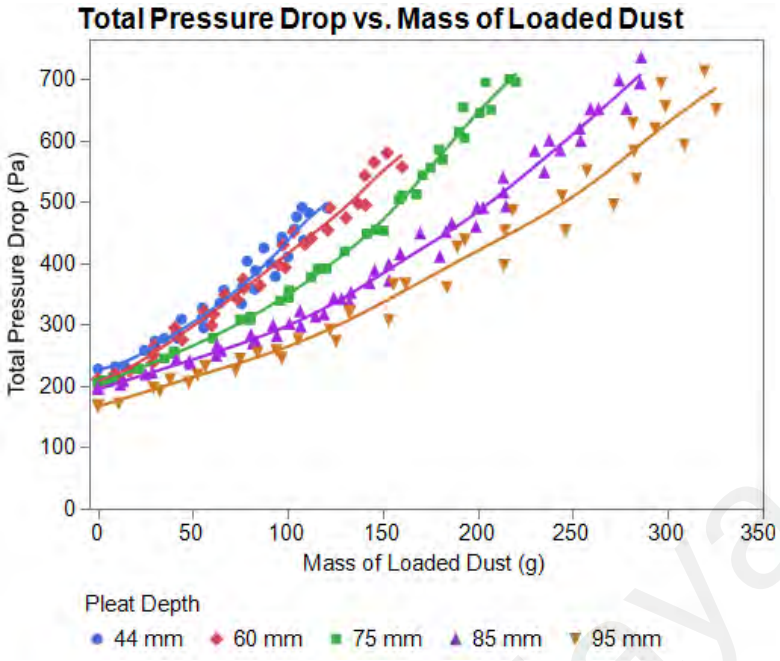

Figure 8.13: Total Pressure Drop against Mass of Loaded Dust at Different Pleat Depths

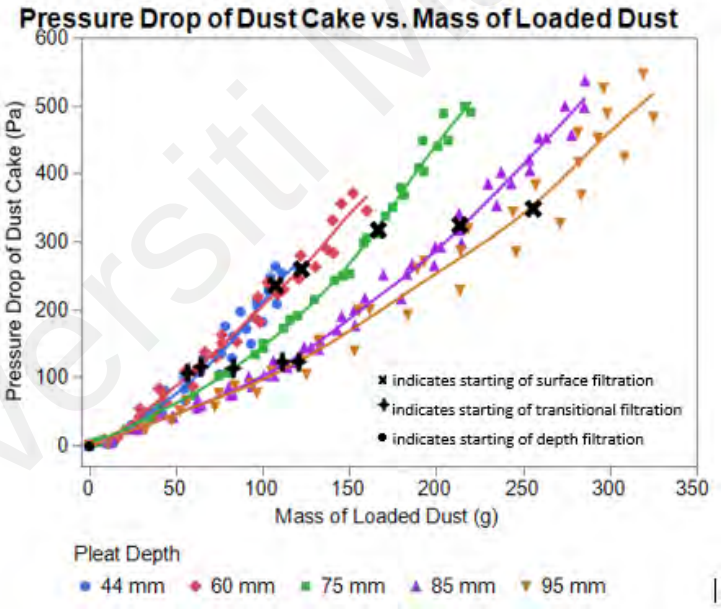

Figure 8.14: Pressure drop across Dust Cake against Mass of Loaded Dust at Different Pleat Depths

The effect of the pleat depth on the dust cake specific coefficient, K_c can be studied from Figure 8.15. It can be observed that the dust cake specific coefficient, K_c increases as the mass of loaded dust on the filter increases. Figure 8.16 shows that the K_c shows a negative parabolic curve with increasing pleat depth, P_d. At a pleat depth below 75 mm, K_c shows an increasing trend along with pleat depth. This is because as the pleat depth is

small, the effective surface area to hold dust is smaller. When the filter reaches its maximum dust holding capacity, it can no longer support the relatively high pressure drop exerted on the filter with lower pleat depth, which is physically less rigid. At a constant pleat density or pleat width, as the pleat depth is greater than 75 mm, K_c decreases along with increasing pleat depth. The filter structure is more rigid and the effective filtration area to hold dust increases with increasing depth, causing the specific resistance of dust cake to decrease.

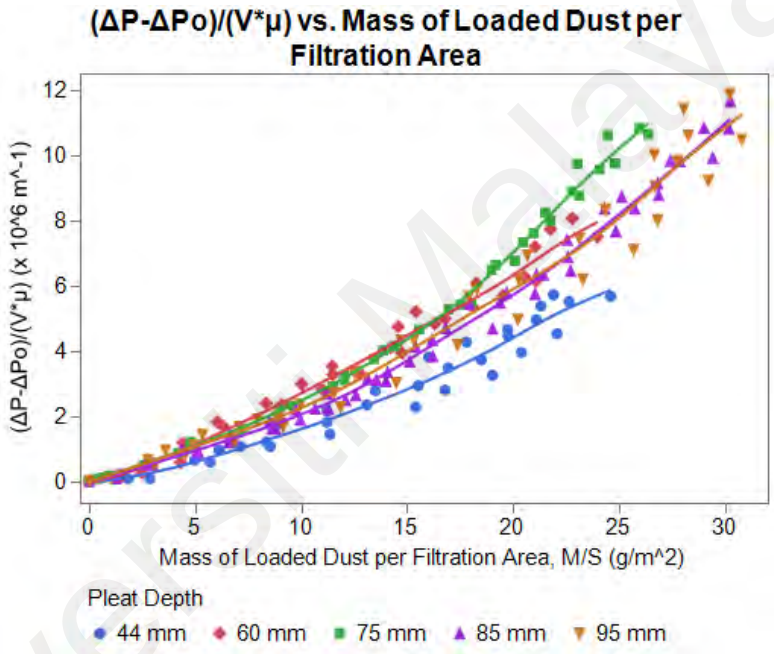

(a)

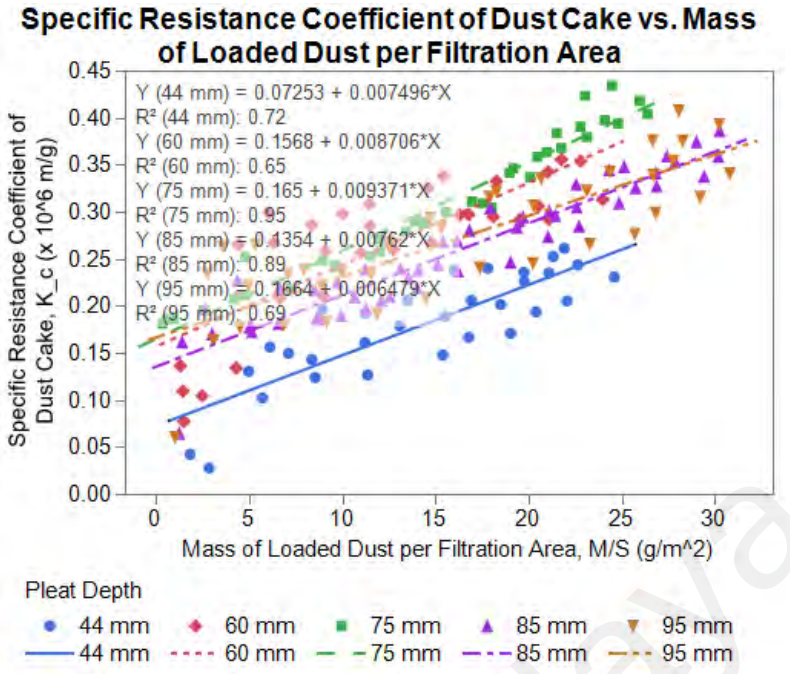

(b)

Figure 8.15: Effect of the Pleat Depth on the Dust Cake Specific Resistance Coefficient, K_c (a) $\frac{\Delta P - \Delta P_0}{V_f \cdot \mu}$ against $\frac{m}{S_f}$ where gradient is K_c (b) $\frac{(\Delta P - \Delta P_0) S_f}{V_f \cdot \mu \cdot m}$ against $\frac{m}{S_f}$ where y-axis is K_c

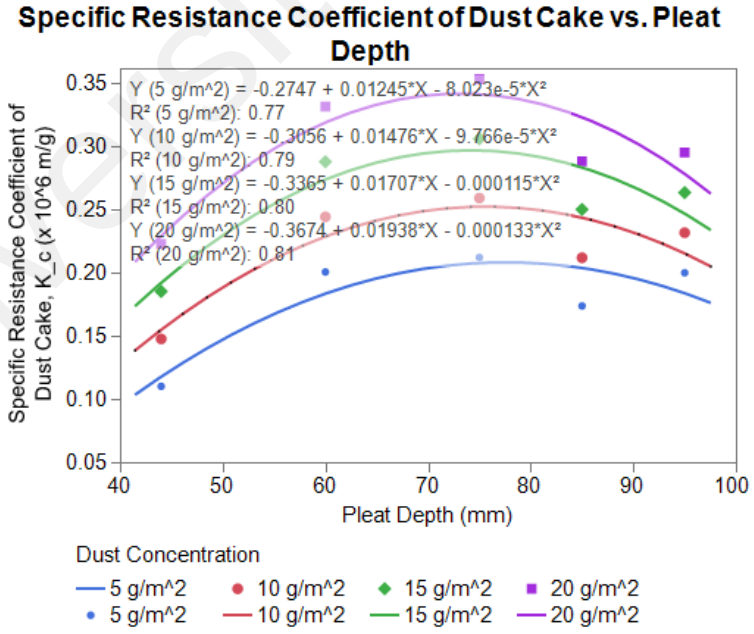

Figure 8.16: Relationship of the Pleat Depth on the Dust Cake Specific Resistance Coefficient

8.3.4 Effect of Pleat Ratio on K_c

The effect of pleat geometry on the specific resistance coefficient of dust cake, K_c can be studied using pleat ratio, α, as shown in Figure 8.17. Pleat ratio is a dimensionless parameter to represent the pleat geometry by taking into the account of pleat density and pleat depth, which is expressed as

$$\alpha = \frac{Pleat\ depth\ \times Pleat\ density}{25.4} \tag{8.3}$$

A positive parabolic relationship is found between the pleat ratio and K_c values with the optimum K_c value occurred at the pleat ratio of 11.72, 11.46, 9.96 and 10.26 respectively for dust concentration of 5 g/m^2, 10 g/m^2,15 g/m^2 and 20 g/m^2.

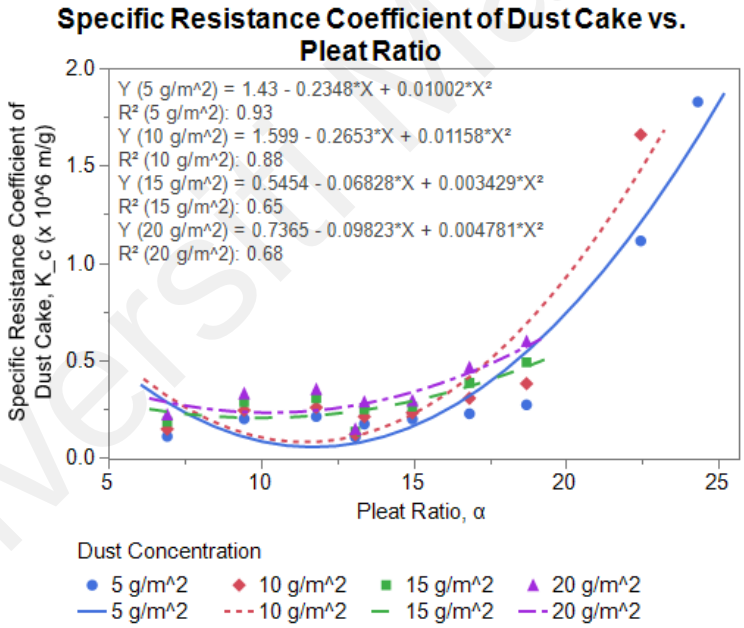

Figure 8.17: Effect of Pleat Ratio on the Specific Resistance Coefficient of Dust Cake

The K_c values are increases drastically when the pleat ratio is higher than 20, which corresponds to the pleat density above 5.5 PPI, as compared with Figure 8.12. It can be said that the pleat density is the key contribution factor to K_c as the K_c values increase significantly at higher pleat density, causing the effect of pleat density dominates in the overall effect of pleat geometry on K_c. Figure 8.18 illustrates the effect of pleat geometry

on the resistance to air flow. When the pleat density increases, the pleat channel allowing air to pass through decreases; this results the viscous effect to increase significantly compared to increasing pleat depth.

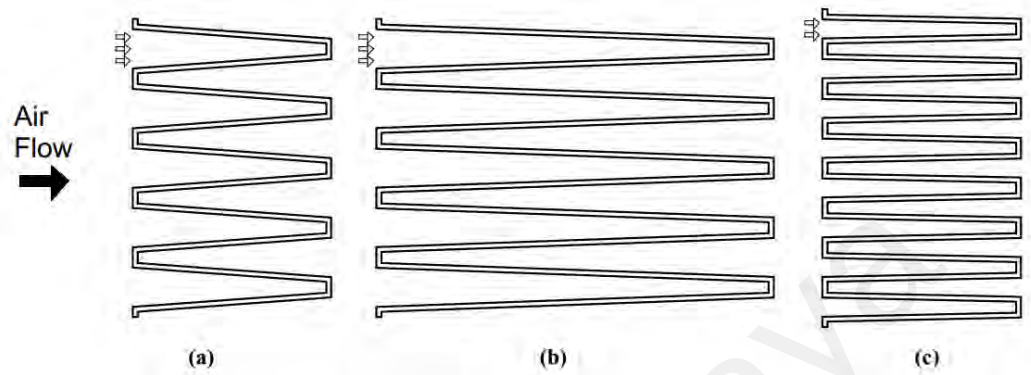

Figure 8.18: Effect of Pleat Geometry on the Resistance to Air Flow (a) Base Case (b) Greater Pleat Depth (c) Higher Pleat Density

There are two contribution factors to the effect of pressure drop, which is the inertial and the viscous effects. If there is only inertial effect which contributes to the pressure drop across dust cake, the specific resistance of dust cake can be minimized by increasing the filtration area (Rebaï et al., 2010), which can be demonstrated by the effect of pleat depth in Section 8.3.3. On the other hand, at a higher pleat density, the pleat channel is narrow for air flow to pass through, which could significantly increase the viscous drag. When the pressure drop across dust cake is contributed by the viscous and inertial effects, the specific resistance of dust cake will increase at a high gradient, as happened at pleat ratio more than 20 as shown in Figure 8.17. This explains why the effect of pleat density outweighs the effect of pleat depth, causing the overall effect of pleat ratio follows the curve trend of pleat density.

In short, it shows a positive quadratic relationship between the pleat ratio and the specific resistance coefficient of dust cake, K_c with an optimum pleat ratio of 9.96 to 11.75 for dust concentration of 5 g/m^2 to 20 g/m^2 to obtain the minimum specific coefficient of dust cake.

8.4 Pleat Ratio Overview

Figure 8.19 summarizes the effect on pleat ratio on the filtration performance, including initial pressure drop, pressure drop of dust cake, final pressure drop, specific resistance coefficient of dust cake and the dust holding capacity. The dust holding capacity reaches a maximum value at pleat ratio of 13.5 while the specific resistance coefficient of dust cake at 5 g/m^2 maintains at acceptable minimum values within pleat ratio range of 9.96 to 14.50 before increasing drastically. The initial pressure drop is at its minimum at a pleat ratio range of 13.08 to 14.57, as concluded in Section 8.2.3. Final pressure drop is the summation of the initial pressure drop of clean filter and the total pressure drop across dust cake. Both final pressure drop and pressure drop across dust cake reach at local peak at a pleat ratio of 13.50, which corresponds to the peak of the dust holding capacity. This outcome is acceptable as the dust loading is highest at this point which results a relatively higher final pressure drop. Although the filter's final pressure drop can go higher at higher pleat ratio, its respective dust holding capacity drops, which can be seen at the drastic increase in K_c value. A high pressure drop with low dust holding capacity is not ideal, as the energy consumption will be relatively high as well. Considering all filtration performance, this can be concluded that the pleat ratio range of 13.08 to 14.57 contributes to the optimum filtration performance with the highest dust holding capacity and minimum initial pressure drop and specific resistance coefficient of dust cake.

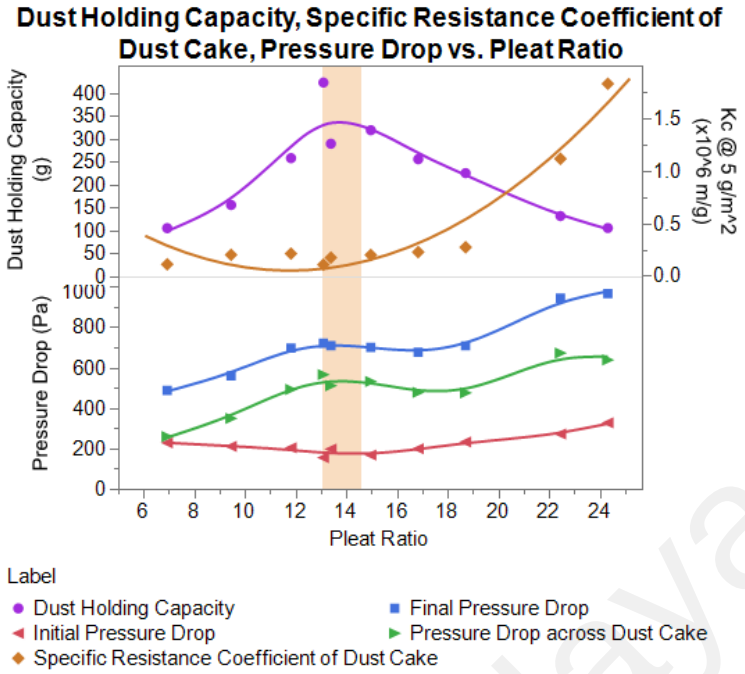

Figure 8.19: Comparison of Filter Performance at Different Pleat Ratios

Comparing with the literature findings, the pleat ratio was found to be below 1.59, (Li et al., 2019) at a range of 2.22 to 3.70 (Teng et al., 2022) and 1.48 (Park et al., 2012) to achieve good filtration effect. The pleat ratio concluded in previous works were based on small-scale pleats, mainly on cartridge filters. The pleat ratio of a HVAC filter for an optimum filtration performance were found to be much higher (13.08 - 14.57) from this study, showing that the pleat ratio are different for different filtration applications. Théron et al. (2017) studied a down-sized pleated filter and concluded that the initial pressure differential can be reduced with a pleat shape toward a flat geometry, without considering the formation of dust cake. However, the pleating feature was important as the dust holding capacity could be increased when the filtration area was higher. Taking into consideration of the dust loading effect on the pleat geometry, it was hence found that the optimum pleat ratio occurs at a range of 13.08 - 14.57, for a triangular pleat. The findings of this study could be directly applicable in the actual filter selection, as the suggested pleat ratio range was studied comprehensively using a full-scaled filter based on the filtration performance of the filter's clean and dirty states.

In short, the filter media is normally pleated to increase the filtration area of a filter within a fixed filter size, and the optimal filtration performance is greatly affected by the pleat geometry. The optimum pleat ratio in obtaining high dust holding capacity, low initial pressure drop and specific resistance coefficient of dust cake happens at a range of 13.08 to 14.57 for the full-scale fibrous filters on HVAC system applications.

8.5 Summary

It is found that the pleat geometrical parameter is a contributing factor on the filtration performance. The effect of pleat geometry on the filtration efficiency is concluded to be insignificant while the filter's initial pressure drop and the pressure drop across dust cake are dependent on the pleat geometry.

The initial pressure drop increases as the pleat density increases, while the effect of the pleat density is more pronounced on the initial pressure drop at a higher filtration velocity, depicting a quadratic increment of initial pressure drop along with pleat density with a higher inertial effect across the denser pleats. As for the influence of pleat depth, the initial pressure drop decreases with an increasing pleat depth as the air can pass through the filter at a lower air flow resistance when the total filtration area is bigger at a higher pleat depth. The overall pleat geometry, including the pleat density and pleat depth can be represented using pleat ratio. It can be summarized that the optimum pleat ratio to obtain the minimum initial pressure drop is found to be at a range of 13.08 to 14.57 for a full-sized pleated fibrous filter.

The specific resistance coefficient of dust cake, K_c increases exponentially with the increasing pleat density, due to the high blockage to air flow of the high pleat density. K_c shows a negative parabolic curve with increasing pleat depth, with maximum K_c value at pleat depth of 75 mm. Before the pleat depth of 75 mm, the filter is physically less rigid, causing the structure fails at lower dust holding. After the pleat depth of 75 mm, the filter

structure is more rigid and the effective filtration area to collect dust is greater at higher pleat depth, resulting the dust holding capacity to be higher and the overall K_c decreases. Seeing the effect of the pleat geometry in terms of pleat ratio, α to the specific resistance coefficient of dust cake, K_c, it exhibits a positive parabolic relationship between α and K_c, with an optimum pleat ratio of 9.96 to 11.75 for dust concentration of 5 g/m^2 to 20 g/m^2.

In conclusion, the optimum pleat ratio occurs at 13.08 to 14.57 to obtain an optimal filtration performance at low initial pressure drop and low specific resistance coefficient of dust cake while getting a high dust holding capacity.

CHAPTER 9: EMPIRICAL MODELLING OF FILTRATION PERFORMANCE AND FINAL RESISTANCE RELATIONSHIP

In this chapter, the formulation of final resistance in consideration of different filtration performance which are the filtration efficiency, initial pressure drop, dust holding capacity, pressure drop across the dust cake and the filter's energy consumption is discussed. Firstly, the relationship of filtration performance depending on different filter design parameters, including the media physical properties (fibre diameter, filter packing density), filtration velocity, pleat geometry (pleat depth, pleat density) is investigated. There are a total of 51 sets of experimental data used in the linear regression modelling, in which 67% is used as training set and 33% is used to validate the predicted model. The respective multiple linear regression reports are attached in Appendices D to G. Next, the estimated filter lifespan and the filter operating time with cost consideration are studied and the final resistance is finally modelled.

9.1 Empirical Models of Filtration Performance with Design Parameters

The empirical models of the filtration performance are discussed in this section. The models are valid when the design parameters are within the ranges stated in Table 9.1.

Table 9.1: Valid Ranges for Design Parameter

Design Parameters	Valid Range
Fibre Diameter	$4.57\ \mu m \leq d_f \leq 7.86\ \mu m$
Filtration Velocity	$1.27\ m/s \leq V_f \leq 2.79\ m/s$
Pleat Depth	$44\ mm \leq P_d \leq 95\ mm$
Pleat Density	$3.5\ PPI \leq P_\rho \leq 6.5\ PPI$

9.1.1 Filtration Efficiency

As discussed from Chapters 6 to 8 earlier, the filtration efficiency is concluded to be depending on the fibre diameter, d_f filter packing solidity, $\propto_f$ and filtration velocity, V_f. The experimental datasets are analysed with a multiple linear regression to determine the relationship of filtration efficiency and the dependent parameters. From Table 9.2, it can be seen that the multicollinearity occurs between fibre diameter and filter packing solidity. Therefore, the redundant variable with higher VIF, which is the filter packing solidity will be omitted from the regression model and the filtration efficiency, η_T is expressed in Equation (9.1) as a function of fibre diameter, d_f and filtration velocity, V_f. The final predictive model of filtration efficiency is expressed in Equation (9.2).

Table 9.2: VIF values for Independent Variables for Filtration Efficiency

Parameters	VIF
Fibre Diameter	18.048
Filter Packing Solidity	18.109
Filtration Velocity	1.0224

$$Filtration\ Efficiency = f(d_f, V_f) \quad \textbf{(9.1)}$$

$$Filtration\ Efficiency, \eta_T = -17.63 d_f + 14.59 V_f + 150.37 \quad \textbf{(9.2)}$$

From Equation (9.2), filtration efficiency increases with the decreasing fibre diameter and the increasing filtration velocity. As the fibre diameter decreases, the fibre network formed in denser which increases the collection probability of the dust particles, causing the filtration efficiency to increase. When the filtration velocity is high, it increases the inertial impaction between the dust particles and the fibre media. This causes the filtration efficiency to increase with an increasing filtration velocity.

9.1.2 Initial Pressure Drop

The initial pressure drop, ΔP_0 is found to be dependent on the fibre diameter, d_f filter packing solidity, $\propto_f$, square of filtration velocity, ${V_f}^2$, pleat depth, P_d and square of pleat density ${P_\rho}^2$. The relationship between the dependent variables and the initial pressure drop are justified with *p*-values. It is found that the filter packing density has no obvious relationship with the initial pressure drop as the *p*-value is greater than 0.05. Therefore, the function of initial pressure drop is expressed in Equation (9.3) and the final predictive model of initial pressure drop is expressed in Equation (9.4).

$$Initial\ Pressure\ Drop, \Delta P_0 = f(d_f, {V_f}^2, P_d, {P_\rho}^2) \quad \textbf{(9.3)}$$

$$Initial\ Pressure\ Drop, \Delta P_0 \quad \textbf{(9.4)}$$
$$= -39.78 d_f + 29.32\, {V_f}^2 - 1.23 P_d + 5.79 {P_\rho}^2 + 264.93$$

From Equation (9.4), it can be observed that the initial pressure drop increases with increasing filtration velocity and pleat density while decreases with increasing fibre diameter and pleat depth. The contributing effect of filtration velocity is the strongest with its quadratic relationship and relatively higher coefficient on the initial pressure drop. This is due to the higher inertial resistance effect incurred by high filtration velocity, which is in correspondence with Darcy Forchheimer equation (Théron et al., 2017).

9.1.3 Pressure Drop across Dust Cake

The pressure drop across the dust cake, ΔP_c is investigated in terms of specific resistance coefficient of dust cake, K_c in earlier chapters and found that the contributing factors to K_c are square of filtration velocity, ${V_f}^2$, square of pleat depth, ${P_d}^2$ and the natural exponential of pleat density, e^{P_ρ}. As ΔP_c corresponds to K_c, ΔP_c can be defined as Equation (9.5). The final predictive model of pressure drop across dust cake is expressed in Equation (9.6).

$$Pressure\ drop\ across\ dust\ cake, \Delta P_c = f(V_f{}^2, P_d{}^2, e^{P_\rho}) \quad \textbf{(9.5)}$$

$$Pressure\ Drop\ across\ Dust\ Cake, \Delta P_c \quad \textbf{(9.6)}$$

$$= 72.80\, V_f{}^2 + 0.03598 P_d{}^2 + 0.1754 e^{P_\rho} - 253.87$$

The pressure drop across dust cake increases with filtration velocity, pleat depth and pleat density. At a higher filtration velocity, the dust particles are compressed into a denser dust cake, hence causing the dust cake resistance to air flow becomes higher. Another significant contributing factor is the pleat density. At a higher pleat density, the pleat channel is narrowed for the airflow to pass through, and this leads to an increase of viscous drag, increasing the dust cake pressure drop.

9.1.4 Dust Holding Capacity

The contributing factors of dust holding capacity, DHC are found to be fibre diameter, d_f, filter packing solidity, $\propto_f$, filtration velocity, V_f, square of pleat depth, $P_d{}^2$ and square of pleat density $P_\rho{}^2$. The relationship between the dependent variables and the dust holding capacity are justified with *p*-values. It is found that the filter packing density has no obvious relationship with the dust holding capacity as the *p*-value is greater than 0.05. Therefore, the function of dust holding capacity is expressed in Equation (9.7) and the final predictive model of dust holding capacity is expressed in Equation (9.8).

$$Dust\ holding\ capacity, DHC = f(d_f, V_f, P_d{}^2, P_\rho{}^2) \quad \textbf{(9.7)}$$

$$Dust\ holding\ capacity, DHC \quad \textbf{(9.8)}$$

$$= 44.85 d_f - 57.37 V_f + 0.0340 P_d{}^2 - 9.956 P_\rho{}^2 + 51.27$$

The dust holding capacity increases with fibre diameter and pleat depth but decreases with filtration velocity and pleat density. The fibre diameter and filtration velocity contribute the most on the effect of dust holding capacity, with relatively greater regression coefficients. As the fibre diameter increases, the media fibre network is less

dense and this leads to a bigger pore size, increasing the dust holding capacity. Next, the dust holding capacity decreases with filtration velocity as a greater force exerts on the filter media at a higher velocity. This results the filter media to deform easily and fail at a lower dust holding capacity.

9.1.5 Summary of Statistical Tests for the Empirical Models

Table 9.3 and Table 9.4 summarize the statistical test results of the empirical models discussed earlier from Section 9.1.1 to 9.1.4. All empirical models of the filtration performance parameters explain a significant relationship with high R^2 values and the model is a significant predictor with low p-value from F-test ($p < 0.05$). The independent predictor variables show a significant contribution to the model with $p < 0.05$. There is no multicollinearity among the independent predictor variable as the VIF is approximate to unity.

Table 9.3: Bivariate Analysis between Design Parameters and Filtration Performance

		Fibre Diameter	Filter Packing Density	Filtration Velocity	Pleat Depth	Pleat Density
Filtration Efficiency	**Correlation**	-0.8704	0.8520	0.9676	0.2307	0.1436
	Significance Probability	0.0002	0.0004	< 0.0001	0.4082	0.5698
	Significance	Yes	Yes	Yes	No	No
Initial Pressure Drop	**Correlation**	-0.9552	0.9693	0.9796	-0.9374	0.9867
	Significance Probability	< 0.0001	< 0.0001	< 0.0001	< 0.0001	< 0.0001
	Significance	Yes	Yes	Yes	Yes	Yes
Pressure Drop across Dust Cake	**Correlation**	-0.0454	0.1444	0.9749	0.9490	0.6306
	Significance Probability	0.8885	0.6544	< 0.0001	< 0.0001	0.005
	Significance	No	No	Yes	Yes	Yes
Dust Holding Capacity	**Correlation**	0.8305	-0.7882	-0.7816	0.9809	-0.9692
	Significance Probability	0.0008	0.0023	0.0006	< 0.0001	< 0.0001
	Significance	Yes	Yes	Yes	Yes	Yes

Table 9.4: Statistical Test Results of Linear Multiple Regression

Predicted Model	R^2	Analysis of Variance (F-test)	Independent Predictor Variable		
			Parameter Estimates		VIF
Filtration Efficiency, η_T	0.6755	$F(2,31) = 32.26$ $p < 0.0001$	Fibre diameter, d_f	$\beta = -17.63$ $p < 0.0001$	1.001
			Filtration velocity, V_f	$\beta = 14.59$ $p = 0.0017$	1.001
Initial Pressure Drop, ΔP_0	0.9762	$F(4,29) = 297.64$ $p < 0.0001$	Fibre diameter, d_f	$\beta = -39.78$ $p < 0.0001$	1.008
			Square of filtration velocity, ${V_f}^2$	$\beta = 29.32$, $p < 0.0001$	1.060
			Pleat depth, P_d	$\beta = -1.23$ $p < 0.0001$	1.085
			Square of pleat density, ${P_\rho}^2$	$\beta = 5.79$ $p < 0.0001$	1.079
Pressure drop across dust cake, ΔP_c	0.8359	$F(3,30) = 50.95$ $p < 0.0001$	Square of filtration velocity, ${V_f}^2$	$\beta = 72.80$ $p < 0.0001$	1.056
			Square of pleat depth, ${P_d}^2$	$\beta = 0.03598$ $p < 0.0001$	1.078
			Natural exponential of pleat density, e^{P_ρ}	$\beta = 0.1754$ $p = 0.011$	1.068
Dust holding capacity, DHC	0.9087	$F(4,29) = 72.14$ $p < 0.0001$	Fibre diameter, d_f	$\beta = 44.85$ $p < 0.0001$	1.008
			Filtration velocity, V_f	$\beta = -57.37$ $p = 0.0040$	1.067
			Square of pleat depth, ${P_d}^2$	$\beta = 0.0340$ $p < 0.0001$	1.095
			Square of pleat density, ${P_\rho}^2$	$\beta = -9.956$ $p < 0.0001$	1.086

9.2 Validation of Predicted Models

17 out of the 51 sets of experimental data are used to validate the predicted models., It can be justified that the predicted models are acceptable as the difference between R^2 values are small, which is only less than 1.5% as shown in Table 9.5.

Table 9.5: Comparison of R^2 Values for Training and Validation Dataset

	R^2 Value of Training Sets	**R^2 Value of Validation Sets**	**Percentage of Difference (%)**
Filtration Efficiency	0.6755	0.6720	0.52%
Initial Pressure Drop	0.9762	0.9701	0.62%
Pressure Drop across Dust Cake	0.8359	0.8236	1.47%
Dust Holding Capacity	0.9087	0.9033	0.59%

9.3 Modelling of Recommended Final Resistance

When the design parameters such as fibre diameter, filtration velocity and pleat geometry are varied, the filtration performance including filtration efficiency, η_T, initial pressure drop, ΔP_i, pressure drop across dust cake, ΔP_C and dust holding capacity, DHC can be calculated using the empirical models in Section 9.1. Final resistance is the maximum operating resistance to air flow of the air filter. In this section, the modelling of the final resistance is discussed by comparing the filter's lifespan until the final pressure drop and the energy cost. In this modelling, the terms of "final pressure drop" refer to the ΔP_f calculated using Equation (9.9) while the "final resistance" is defined as the recommended maximum operating resistance for the filter replacement after considering the energy cost.

$$\begin{aligned} Final\ pressure\ drop, \Delta P_f &= Initial\ Pressure\ Drop, \Delta P_0 \\ &+ Pressure\ Drop\ across\ Dust\ Cake, \Delta P_c \end{aligned} \quad \textbf{(9.9)}$$

9.3.1 Filter Lifespan until its Final Pressure Drop

The dust loading curve of instantaneous pressure drop, $\Delta P(m)$ against mass of loaded dust, m is found to be fitted as Equation (9.10) (Montgomery et al., 2012) where a and b are the empirical constants of the dust loading curve. The constants a and b can be obtained by inserting the initial pressure drop ($m = 0$) and final pressure drop ($m = DHC$) into the equation. Equations (9.11) and (9.12) express constants a and b.

$$\Delta P(m) = ae^{bm} \quad \textbf{(9.10)}$$

$$a = \Delta P_0 \quad \textbf{(9.11)}$$

$$b = \frac{1}{DHC} \ln \frac{\Delta P_f}{\Delta P_0} \quad \textbf{(9.12)}$$

The instantaneous mass of loaded dust, m can be estimated using Equation (9.13) (Bulejko et al., 2021) where Q is the airflow rate, t is the filtration time, η_T is the filtration efficiency and C_{u_P} is the upstream dust concentration of the building.

$$m = Q\ t\ \eta_T\ C_{u_P} \quad \textbf{(9.13)}$$

At the final pressure drop, the mass of loaded dust, m is the dust holding capacity, DHC. Equation (9.13) can be rearranged to determine the filter lifespan, t_f and expressed as Equation (9.14).

$$t_f = \frac{DHC}{Q\ \eta_T\ C_{up}} \quad \textbf{(9.14)}$$

The filter lifespan at its final pressure drop, t_f is dependent on the upstream dust concentration which is related to the building's indoor and outdoor air quality. The upstream dust concentration, C_{up} can be estimated from Equation (9.15) using the ratio of fresh air and return air of the HVAC system, where $\%OA$ is the percentage of fresh air introduced by the HVAC system, $C_{outdoor}$ is the outdoor particle concentration, $\%RA$ is the percentage of return air and C_{indoor} is the indoor particle concentration.

$$C_{up} = \%OA \times C_{outdoor} + \%RA \times C_{indoor} \quad \textbf{(9.15)}$$

9.3.2 Filter Usage in Consideration of Costs

The energy consumed by the air filter, E can be estimated using Equation (9.16) where W_{avg} is the average power, t is the filter operating time, $\overline{\Delta P}$ is the average pressure drop, Q is the airflow rate and η is the system efficiency or the fan efficiency.

$$E = W_{avg}t = \frac{\overline{\Delta P}Q}{\eta}t \quad \textbf{(9.16)}$$

By operating integration on Equation (9.10), the average pressure drop of the dust loading curve, $\overline{\Delta P}$ can be obtained and is expressed as Equation (9.17).

$$\overline{\Delta P} = \frac{1}{m}\int_0^m \Delta P(m)\, dm = \frac{a}{bm}(e^{bm} - 1) \quad \textbf{(9.17)}$$

Substituting Equations (9.11), (9.12) and (9.13) into Equation (9.17), the average pressure drop can be expressed as Equation (9.18) with constant B_1 defined in Equation (9.19) (Montgomery et al., 2012).

$$\overline{\Delta P} = \frac{\Delta P_0}{B_1 t}(e^{B_1 t} - 1) \quad \textbf{(9.18)}$$

$$B_1 = \frac{Q\ \eta_T\ C_{u_P}}{DHC}\ \ln\frac{\Delta P_f}{\Delta P_0} \quad \textbf{(9.19)}$$

Therefore, the power energy consumption of the filter can be estimated using Equation (9.20) and (9.21) respectively. By substituting the estimated filter lifespan, t_f from Equation (9.14), the total power consumed throughout the filter lifespan, W_{t_f} can be estimated from Equation (9.22).

$$W = \frac{\Delta P_0 Q}{\eta B_1 t}(e^{B_1 t} - 1) \quad \textbf{(9.20)}$$

$$E = \frac{\Delta P_0 Q}{\eta B_1}(e^{B_1 t} - 1) \quad \textbf{(9.21)}$$

$$W_{t_f} = \frac{\Delta P_0 Q}{\eta B_1 t_f}(e^{B_1 t_f} - 1) \quad \textbf{(9.22)}$$

Besides, it is important to take into the consideration the filter replacement cost (filter cost, C_F + installation cost, C_I) and the energy cost, C_E. If the filter replacement cost is relatively low, it would be more cost effective to replace the filter as soon as the energy cost exceeds the replacement cost. The filter operation time in which the energy cost equals to the filter replacement cost, t_{cost} can be solved using Equations (9.23) and (9.24).

$$C_E = E \times Energy\ Unit\ Cost = C_F + C_I \quad \textbf{(9.23)}$$

$$t_{cost} = \frac{1}{B_1}\ln[\frac{(C_F + C_I)\eta B_1}{\Delta P_0 Q \times Energy\ Unit\ Cost} + 1] \quad \textbf{(9.24)}$$

9.3.3 Definition of Final Resistance Model

Therefore, in the filter design stage, the final resistance can be recommended based on the estimation of filter lifespan at its final pressure drop, t_f using Equation (9.14) or the filter operation time with cost-saving, t_{cost} using Equation (9.24), whichever is shorter. Hence, with the selected filter usage time, namely t_{FR} , the final resistance can be recommended using Equation (9.25).

$$Final\ Resistance = \Delta P_0 e^{\frac{Q\eta_T t_{FR} C_{up}}{DHC} \ln\frac{\Delta P_f}{\Delta P_i}} \quad \textbf{(9.25)}$$

where

$\eta_T = -17.63d_f + 14.59V_f + 150.37$

$\Delta P_0 = -39.78d_f + 29.32\,{V_f}^2 - 1.23P_d + 5.79{P_\rho}^2 + 264.93$

$DHC = 44.85d_f - 57.37V_f + 0.0340{P_d}^2 - 9.956{P_\rho}^2 + 51.27$

$C_{up} = \%OA \times C_{outdoor} + \%RA \times C_{indoor}$

$$\Delta P_f = \Delta P_0 + \Delta P_c \quad \textbf{(9.26)}$$

$$= -39.78 d_f + 102.12\, {V_f}^2 + 0.03598 {P_d}^2 - 1.23 P_d$$

$$+ 5.79 {P_\rho}^2 + 0.1754 e^{P_\rho} + 11.06$$

9.3.4 Comparison with Previous Works

In the current manufacturer's practice in the air filtration industry, the final resistance is given as a predefined value using the Rule of Thumbs or by setting two times the initial resistance (ASHRAE, 2017; Nassif, 2012). The predefined value might be resulting a longer lifespan of the filters, but the high energy consumption will be the trade-off for the prolonged filter usage, which is not cost-effective in actual applications. Therefore, the optimal filter replacement or final resistance recommendation should be considering the life-cycle operational cost of the filters instead of using the predefined values.

Pöyhönen et al. (2021) has developed a real-time energy calculation for the air filters by installing the calculation program on the fan monitoring system. The filter replacement can be conducted based on the real-time results which could bring to a lower life-cycle cost of the filters. However, this method only works during the filter application and might not be feasible to some consumers where the energy monitoring system is not available for their HVAC systems. The final resistance model found in the current study is useful during the filter design stage, in order to maximize the filtration performance, at the same time considering the filter operational cost.

The current final resistance model is in-line with the findings of Montgomery et al. (2012) that the filter should be replaced if the filter reaches a resistance where the operation or energy cost is higher than the initial filter cost. This can minimize the annual operational cost of the filtration system. The final resistance model in this study is aided with the filtration performance prediction using the empirical models based on various

filter design parameters, taking into consideration of filter operational cost. This could predict the optimal filter lifespan and suggest the actual final resistance of a filter.

9.4 Summary

The empirical models in determining the filtration performance in the function of design parameters (fibre diameter, filtration velocity, pleat depth and pleat density) are developed with multiple linear regression method. The discrepancy between the training data and validation data is only less than 1.5% for all empirical models, including filtration efficiency, initial pressure drop, pressure drop across dust cake and dust holding capacity. With these empirical models, the filter lifespan and the filter energy consumption are estimated. By comparing the estimated filter lifespan model and the energy cost model, the final resistance can be recommended.

CHAPTER 10: CONCLUSIONS & RECOMMENDATIONS

The development of the formulation of the final resistance model has been presented in the previous chapters from the investigation of the factors affecting the filtration performance through experimental data collection, modelling of the filtration performance parameters to the consideration of filter lifespan with energy cost.

10.1 Conclusions

The objectives of this research have been achieved and the conclusions are drawn as follows:

1. The triangular pleat shape gives the lowest initial pressure drop, followed by S-shaped, Z-shaped, rectangular, U-shaped and the box pleat, due to its least resistance against air flow at the upstream and the minimum turbulence at the downstream.
2. The quality factor increases with decreasing fibre diameter and increasing filter packing density. Dust holding capacity increases with increasing fibre diameter. Tensile strength of the media does not affect the filtration performance.

   The filtration efficiency increases with increasing filtration velocity as the inertial impaction becomes more dominating at high filtration velocity. The initial pressure drop is expressed in term of filtration velocity as $\Delta P_0 = 36.8\,{V_f}^2 - 42.69\,V_f + 28.92$. The relationship between K_c and V_f is in a linear relationship for depth filtration and the starting of transitional filtration at an empirical equation of $K_c = aV_f + b$. Since the middle of transitional filtration and the surface filtration, K_c shows a quadratic growth with increasing V_f at an empirical equation of $K_c = a{V_f}^2 + bV_f + c$ where a, b and

c are empirical constants. The dust holding capacity decreases and the final pressure drop increases with increasing filtration velocity.

The pleat ratio range of 13.08 to 14.57 contributes to the optimum filtration performance with the highest dust holding capacity and minimum initial pressure drop and specific resistance coefficient of dust cake.

3. The empirical models of filtration performance are listed as below. The models are validated that the predicted models are acceptable as the difference between predicted and validated R^2 values are less than 1.5 %.

$$\eta_T = -17.63d_f + 14.59V_f + 150.37$$

$$\Delta P_0 = -39.78d_f + 29.32\,{V_f}^2 - 1.23P_d + 5.79{P_\rho}^2 + 264.93$$

$$\Delta P_c = 72.80\,{V_f}^2 + 0.03598{P_d}^2 + 0.1754e^{P_\rho} - 253.87$$

$$DHC = 44.85d_f - 57.37V_f + 0.0340{P_d}^2 - 9.956{P_\rho}^2 + 51.27$$

where

$$4.57\ \mu m \leq d_f \leq 7.86\ \mu m$$

$$1.27\ m/s \leq V_f \leq 2.79\ m/s$$

$$44\ mm \leq P_d \leq 95\ mm$$

$$3.5\ PPI \leq P_\rho \leq 6.5\ PPI$$

4. The final resistance can be recommended using the expression as below where the selected filter operation time, t_{FR} is selected from the predicted filter lifespan, t_f and the operation time with cost breakeven, t_{cost} , whichever shorter. Both t_f and t_{cost} can be calculated using the empirical models concluded in Conclusion 5 mentioned earlier.

$$Final\ Resistance = \Delta P_0 e^{\frac{Q\eta_T t_{FR}\, C_{up}}{DHC}\ln\frac{\Delta P_f}{\Delta P_i}}$$

$$t_f = \frac{DHC}{Q\ \eta_T\ C_{up}}$$

$$t_{cost} = \frac{1}{B_1}\ln\left[\frac{(C_F+C_I)\eta B_1}{\Delta P_0 Q \times Energy\ Unit\ Cost} + 1\right], B_1 = \frac{Q\ \eta_T\ C_{u_P}}{DHC}\ \ln\frac{\Delta P_f}{\Delta P_0}$$

Based on the results summarized, it can be concluded that filtration performance is affected by various factors and should be taken into consideration for the filter design and applications. In addition to that, the recommendation of the suitable final resistance is important to maintain the good indoor air quality with the optimum energy cost and filter lifespan. The findings of this research can be applied directly in the industrial work as it gives a reference to the manufacturers during the filter design. As for the end users, a better prediction of the filter selection can be done with the proposed filtration performance models, giving a better solution in maintaining the building's IAQ and at the same time minimizing the operation cost.

10.2 Significance of Study

The proposed filtration performance models and the recommended final resistance model give significant contributions to the air filtration industry for both design and application stages. A comprehensive prediction of the filtration performance and its expected lifespan can be carried out during design stage or during selection of filter applications. The proposed models can effectively act as an important guideline to the manufacturers in recommending the final resistance with analytical method instead of using the Rule of Thumbs.

10.3 Recommendations for Future Work

The recommendations that could be carried out in the future work in the contribution of the air filtration research. The suggestions are listed as below:

1. The type of filter media can be studied using synthetic fibre or the filter model can be varied using pocket filters. The respective filtration performance models can be

developed as pocket filters are another widely adopted filter model in the HVAC filter application.

2. The filter performance could be tested in the actual HVAC system of the buildings and the result can be compared against the test filter standard results. This can study the difference between the laboratory test and the actual filtration performance based on the environmental air conditions.
3. Computational fluid dynamics could be adopted in prediction of the dust loading behaviours of the filters until its maximum pressure drop. It would be more cost-effective in filtration study.

REFERENCES

Air Filter Institute. (1960). Dust Spot Test Code. In.

Al-Attar, I. (2011). The effect of face velocity, pleat den-sity and pleat orientation on the most penetrating particle size, pressure drop and fractional efficiency of HEPA filters. *IN: Proceedings of Filtech*, 318-329.

Alderman, S. L., Parsons, M. S., Hogancamp, K. U., & Waggoner, C. A. (2008). Evaluation of the effect of media velocity on filter efficiency and most penetrating particle size of nuclear grade high-efficiency particulate air filters. *Journal of Occupational and Environmental Hygiene, 5*(11), 713-720.

ANSI/Standard 52.2-1999, Method of Testing General Ventilation Air-Cleaning Devices for Removal Efficiency by Particle Size. (1999). In. Atlanta: ASRAE.

ASHRAE. (2017). ANSI/ASHRAE Standard 52.2 - 2017 Method of testing general ventilation air - cleaning devices for removal efficiency by particle size. In. Atlanta: ASHRAE.

ASHRAE Standard. (1992). Standard 52.1-1992. *Gravimetric and Dust Spot Procedures for Testing Air Cleaning Devices Used in General Ventilation for Removing Particulate Matter*.

ASHRAE Standard. (2019). Standard 62.1-2019. *Ventilation for acceptable indoor air quality*.

Baheti, S., & Tunák, M. (2017). *Characterization of fiber diameter using image analysis.* Paper presented at the IOP Conference Series: Materials Science and Engineering.

Bajpai, P. (2018). Chapter 2 - Paper and Its Properties. In P. Bajpai (Ed.), *Biermann's Handbook of Pulp and Paper (Third Edition)* (pp. 35-63): Elsevier.

Bao, L., Seki, K., Niinuma, H., Otani, Y., Balgis, R., Ogi, T., . . . Okuyama, K. (2016). Verification of slip flow in nanofiber filter media through pressure drop measurement at low-pressure conditions. *Separation and Purification Technology, 159*, 100-107.

Ben-David, T., & Waring, M. S. (2018). Interplay of ventilation and filtration: Differential analysis of cost function combining energy use and indoor exposure to PM2. 5 and ozone. *Building and Environment, 128*, 320-335.

Betts, R. (2013). HVAC: Maintaining HVAC equipment with air intake filters. *Filtration+ Separation, 50*(4), 32-35.

Bian, Y., Wang, S., Zhang, L., & Chen, C. (2020). Influence of fiber diameter, filter thickness, and packing density on PM2. 5 removal efficiency of electrospun nanofiber air filters for indoor applications. *Building and Environment, 170*, 106628.

Billings, C. E. (1966). *Effects of particle accumulation in aerosol filtration.* California Institute of Technology, Ann Arbor. Retrieved from http://ezproxy.um.edu.my:2048/login?url=https://search.proquest.com/docview/302210373?accountid=28930 ProQuest Dissertations & Theses Global database. (6610960)

Brown, R. C. (1993). *Air filtration: an integrated approach to the theory and applications of fibrous filters*: Pergamon.

Bulejko, P., Krištof, O., & Dohnal, M. (2021). An Assessment on Average Pressure Drop and Dust-Holding Capacity of Hollow-Fiber Membranes in Air Filtration. *Membranes, 11*(7), 467.

Cai, Q. (1993). *Study of air filter flow by computational fluid dynamics.* Oklahoma State University,

Carrier. (2005). Applications: Filtration. In. Syracuse, New York: Carrier Corporation.

CEN. (2017). Energy performance of buildings - Ventilation for buildings - Part 3: For non-residential buildings – Performance requirements for ventilation and room-conditioning systems (Modules M5-1, M5-4). In. Brussels.

Chae, S. J. (2000). *Experimental Study of Air Filtration by Fibrous Filters.* University of Louisville,

Chambers, F. W., Al-Sarkhi, A., & Yao, S. (2001). Velocity distribution effects in air filter testing. *Particulate science and technology, 19*(1), 1-21.

Chen, C. Y. (1955). Filtration of aerosols by fibrous media. *Chemical Reviews, 55*(3), 595-623.

Chen, D.-R., Pui, D. Y. H., & Liu, B. Y. H. (1995). Optimization of Pleated Filter Designs Using a Finite-Element Numerical Model. *Aerosol Science and Technology, 23*(4), 579-590. doi:10.1080/02786829508965339

Chen, Z., Bao, B., Zhu, W., & Lin, Z. (2014). Effect of test dust on performance test for a pleated filter cartridge.

Cheng, Y.-H., & Tsai, C.-J. (1998). Factors Influencing Pressure Drop through a Dust Cake during Filtration. *Aerosol Science and Technology, 29*(4), 315-328. doi:10.1080/02786829808965572

Choi, J.-H., Ha, S.-J., Bak, Y.-C., & Park, Y.-O. (2002). Particle size effect on the filtration drag of fly ash from a coal power plant. *Korean Journal of Chemical Engineering, 19*(6), 1085-1090.

Choi, J.-H., Ha, S.-J., & Jang, H.-J. (2004). Compression properties of dust cake of fine fly ashes from a fluidized bed coal combustor on a ceramic filter. *Powder Technology, 140*(1-2), 106-115.

Comparing ISO 16890 and ASHRAE 52.2/MERV. Retrieved from https://www.energysmartfilters.com/comparing-iso-16890-and-ashrae-52.2-merv-air-filter-test-standards

Courtey, S. (2017). Definition of filtration performance-from EN 779 to ISO 16890. *REHVA Journal-February*, 16-19.

Dake, L. P. (1983). *Fundamentals of reservoir engineering*. Amsterdam: Elsevier.

Dales, R., Liu, L., Wheeler, A. J., & Gilbert, N. L. (2008). Quality of indoor residential air and health. *Canadian Medical Association Journal, 179*(2), 147-152. doi:10.1503/cmaj.070359

Daoud, J. I. (2017). *Multicollinearity and regression analysis.* Paper presented at the Journal of Physics: Conference Series.

Davies, C. (1953). The separation of airborne dust and particles. *Proceedings of the Institution of mechanical engineers, 167*(1b), 185-213.

Del Fabbro, L., Laborde, J., Merlin, P., & Ricciardi, L. (2002). Air flows and pressure drop modelling for different pleated industrial filters. *Filtration & Separation, 39*(1), 34-40.

Dennis, R., & JA, D. (1981). Comparison of laboratory and field derived K2 values for dust collected on fabric filters.

EN, C. (2012). EN 779-2012 Particle air filters for general ventilation-determination of filtration performance. *Brussels: CEN*.

Endo, Y., Chen, D.-R., & Pui, D. Y. H. (1998). Effects of particle polydispersity and shape factor during dust cake loading on air filters. *Powder Technology, 98*(3), 241-249. doi:https://doi.org/10.1016/S0032-5910(98)00063-1

EPA, U. (2022). What is a HEPA filter? Retrieved from https://www.epa.gov/indoor-air-quality-iaq/what-hepa-filter

Eurovent. (2014). Eurovent 4/21-2014 Energy Efficiency Classification of Air Filters for General Ventilation Purposes. In. Paris, France: Eurovent.

Eurovent. (2018). Eurovent 4/21-2018 Energy Efficiency Evaluation of air filters for general ventilation purposes. In. Paris, France: Eurovent.

Fan, J., Lominé, F., & Hellou, M. (2018). A numerical analysis of pressure drop and particle capture efficiency by rectangular fibers using LB-DE methods. *Acta Mechanica, 229*(7), 2843-2860. doi:10.1007/s00707-018-2140-4

Farr, C. (2013). ASHRAE testing for HVAC air filtration: A review of standards 52.1-1992 & 52.2-1999. *Technical Services Bulletin. Recuperado el, 2*, 2-3.

Faulkner, D. (2001). Performance and cost of particle air filtration technologies.

Feng, Z., & Cao, S.-J. (2019). A newly developed electrostatic enhanced pleated air filters towards the improvement of energy and filtration efficiency. *Sustainable Cities and Society, 49*, 101569.

Feng, Z., & Long, Z. (2016). Modeling unsteady filtration performance of pleated filter. *Aerosol Science and Technology, 50*(6), 626-637.

Feng, Z., Long, Z., & Chen, Q. (2014). Assessment of various CFD models for predicting airflow and pressure drop through pleated filter system. *Building and Environment, 75*, 132-141. doi:https://doi.org/10.1016/j.buildenv.2014.01.022

Ferziger, J. H., Perić, M., & Street, R. L. (2002). *Computational methods for fluid dynamics* (Vol. 3): Springer.

Fluent, A. (2017). Fluent 12. *Theory guide, Ansys inc*.

Fluent, I. (2006). FLUENT 6.3 user's guide. *Fluent documentation*.

Fotovati, S., Hosseini, S., Tafreshi, H. V., & Pourdeyhimi, B. (2011). Modeling instantaneous pressure drop of pleated thin filter media during dust loading. *Chemical engineering science, 66*(18), 4036-4046.

Fotovati, S., Tafreshi, H. V., & Pourdeyhimi, B. (2012). A macroscale model for simulating pressure drop and collection efficiency of pleated filters over time. *Separation and Purification Technology, 98*, 344-355. doi:https://doi.org/10.1016/j.seppur.2012.07.009

Fu, H. M., Fu, Y., & Xu, F. (2014). *Experiment and simulation on pressure drop of pleated air filters.* Paper presented at the Advanced Materials Research.

Ginestet, A. (2017). *ISO 16890: a new worldwide standard for testing of general ventilation filters.* Lublin, Poland.

Goodfellow, H. D., & Tahti, E. (2001). *Industrial Ventilation Design Guidebook*: Elsevier Science.

Guo, W., & Zhou, M. (2009, 11-14 Oct. 2009). *Technologies toward thermal comfort-based and energy-efficient HVAC systems: A review.* Paper presented at the 2009 IEEE International Conference on Systems, Man and Cybernetics.

Gustavsson, J. (1996). New developments in air filter test methods and classification. *Filtration & Separation, 33*(2), 155-154.

Handbook, A. (2005). American Society of Heating. *Refrigerating and Air Conditioning Engineers, Atlanta*.

Hassan, J., Zin, R., Majid, M. A., Balubaid, S., & Hainin, M. (2014). Building energy consumption in Malaysia: An overview. *Jurnal teknologi, 70*(7).

Hinds, W. C., & Kadrichu, N. P. (1997). The effect of dust loading on penetration and resistance of glass fiber filters. *Aerosol Science and Technology, 27*(2), 162-173.

Huurdeman, B., & Banzhaf, H. (2006). CFD Simulation of Flows in Air Cleaners with Transient Dust Loading of the Filter Element. *SAE Technical Papers*. doi:10.4271/2006-01-1316

Institute, A. F. (1954). Code for Testing Air Cleaning Devices Used in General Ventilation. In *Section 1*.

ISO. (2015). ISO 15957:2015 Test dusts for evaluating air cleaning equipment. 9.

ISO. (2016a). ISO 12103-1:2016 Road vehicles — Test contaminants for filter evaluation — Part 1: Arizona test dust. In (pp. 14). Geneva, Switzerland: ISO.

ISO. (2016b). ISO 16890-1, Air filters for general ventilation – Part 1: Technical specifications, requirements and classification system based upon particular matter efficiency (ePM).

ISO. (2016c). ISO 16890-2, Air filters for general ventilation – Part 2: Measurement of fractional efficiency and air flow resistance.

ISO. (2016d). ISO 16890-3, Air filters for general ventilation – Part 3: Determination of the gravimetric efficiency and the air flow resistance versus the mass of test dust captured.

ISO. (2016e). ISO 16890-4, Air filters for general ventilation – Part 4: Conditioning method to determine the minimum fractional test efficiency.

Jeon, W., Lee, B. H., Yun, H., Kim, J., Kang, S., & Seo, Y. (2020). Characterization of pressure drop through two-stage particulate air filters. *Science and Technology for the Built Environment*, 1-11. doi:10.1080/23744731.2020.1738870

Ji, J., Bae, G., Kang, S., & Hwang, J. (2003). Effect of particle loading on the collection performance of an electret cabin air filter for submicron aerosols. *Journal of Aerosol Science, 34*(11), 1493-1504.

Joubert, A., Laborde, J.-C., Bouilloux, L., Chazelet, S., & Thomas, D. (2011). Modelling the pressure drop across HEPA filters during cake filtration in the presence of humidity. *Chemical engineering journal, 166*(2), 616-623.

Kanaoka, C. (2019). Fine particle filtration technology using fiber as dust collection medium. *KONA Powder and Particle Journal, 36*, 88-113.

Kang, S., Bock, N., Swanson, J., & Pui, D. Y. (2020). Characterization of pleated filter media using particle image velocimetry. *Separation and Purification Technology, 237*, 116333.

Kasper, G., Schollmeier, S., Meyer, J., & Hoferer, J. (2009). The collection efficiency of a particle-loaded single filter fiber. *Journal of Aerosol Science, 40*(12), 993-1009. doi:https://doi.org/10.1016/j.jaerosci.2009.09.005

Khomenko, S., Cirach, M., Pereira-Barboza, E., Mueller, N., Barrera-Gómez, J., Rojas-Rueda, D., . . . Nieuwenhuijsen, M. (2021). Premature mortality due to air

pollution in European cities: a health impact assessment. *The Lancet Planetary Health, 5*(3), e121-e134.

Kim, H. B., Lee, W. J., Choi, S. C., Lee, K. B., & Lee, M.-H. (2021). Filter quality factors of fibrous filters with different fiber diameter. *Aerosol Science and Technology, 55*(2), 154-166.

Kim, J. S., & Lee, M.-H. (2019). Measurement of effective filtration area of pleated bag filter for pulse-jet cleaning. *Powder Technology, 343*, 662-670.

Kimberly-Clark. (2013). Filtration Products - Operating Cost Analysis Tool. Retrieved from https://www.kcprofessional.com/umbraco/Operating%20Cost%20Analysis%20Tool.html

Klenk, D. HVAC Filter Selection and MERV Ratings: What Does It All Mean? Retrieved from https://pdf4pro.com/cdn/hvac-filter-selection-and-merv-ratings-what-27a1d7.pdf

Kuwabara, S. (1959). The forces experienced by randomly distributed parallel circular cylinders or spheres in a viscous flow at small Reynolds numbers. *Journal of the physical society of Japan, 14*(4), 527-532.

Langmuir, I. (1942). US Office of Scientific Research and Development Report No. 865. *Part IV*.

Lee, K.-S., Hasolli, N., Lee, J.-R., Kim, K.-D., Kim, S.-D., Park, Y.-O., & Hwang, J. (2020). Dust loading performance of a non-electret HVAC filter module in the presence of an external electric field. *Separation and Purification Technology*, 117204.

Lee, K. W., & Gieseke, J. A. (1980). Note on the approximation of interceptional collection efficiencies. *Journal of Aerosol Science, 11*(4), 335-341. doi:https://doi.org/10.1016/0021-8502(80)90041-5

Lee, K. W., & Liu, B. Y. H. (1980). On the Minimum Efficiency and the Most Penetrating Particle Size for Fibrous Filters. *Journal of the Air Pollution Control Association, 30*(4), 377-381. doi:10.1080/00022470.1980.10464592

Legg, R. (2017). *Air conditioning system design*. Oxford: Butterworth-Heinemann.

Leung, W. W.-F., Hung, C.-H., & Yuen, P.-T. (2010). Effect of face velocity, nanofiber packing density and thickness on filtration performance of filters with nanofibers coated on a substrate. *Separation and Purification Technology, 71*(1), 30-37.

Li, S., Hu, S., Xie, B., Jin, H., Xin, J., Wang, F., & Zhou, F. (2019). Influence of pleat geometry on the filtration and cleaning characteristics of filter media. *Separation and Purification Technology, 210*, 38-47.

Liu, G., Xiao, M., Zhang, X., Gal, C., Chen, X., Liu, L., . . . Clements-Croome, D. (2017). A review of air filtration technologies for sustainable and healthy building

ventilation. *Sustainable Cities and Society, 32*, 375-396. doi:https://doi.org/10.1016/j.scs.2017.04.011

Liu, Z. G., & Wang, P. K. (1997). Pressure Drop and Interception Efficiency of Multifiber Filters. *Aerosol Science and Technology, 26*(4), 313-325. doi:10.1080/02786829708965433

Lo, L.-M., Chen, D.-R., & Pui, D. Y. (2010). Experimental study of pleated fabric cartridges in a pulse-jet cleaned dust collector. *Powder Technology, 197*(3), 141-149.

Löffler, F. (1968). On the adhesion of dust particles on fiber and particle surfaces. *Staub Reinhaltung der Luft, 11*, 456-461.

Maddineni, A. K., Das, D., & Damodaran, R. M. (2019). Numerical investigation of pressure and flow characteristics of pleated air filter system for automotive engine intake application. *Separation and Purification Technology, 212*, 126-134.

Mann-Hummel. HVAC air filters: Calculating the cost. Retrieved from https://airfiltration.mann-hummel.com/fileadmin/user_upload/news/Case_Studies/Calculating_the_costs/AA54-Calculating_the_cost_of_HVAC_filters_white_paper-EN-v3.pdf

May, J. W. (1965). *Evaluation of Air Filter Test Methods.* Paper presented at the ASME 1965 Gas Turbine Conference and Products Show.

Mayer, M., Caesar, T., & Klaus, J. (2008). Energy efficiency classification of air filters. *Proc. 10th World Filt. Cong, 3*, 313-317.

Montgomery, J. (2015). *Air filtration: predicting and improving indoor air quality and energy performance.* University of British Columbia,

Montgomery, J. F., Green, S. I., Rogak, S. N., & Bartlett, K. (2012). Predicting the energy use and operation cost of HVAC air filters. *Energy and Buildings, 47*, 643-650.

Nassif, N. (2012). *The impact of air filter pressure drop on the performance of typical air-conditioning systems.* Paper presented at the Building Simulation.

National Air Filtration Association. (1993). *NAFA Guide to Air Filtration*. Salt Lake City: National Air Filtration Association.

Noh, K.-C., & Hwang, J. (2010). The effect of ventilation rate and filter performance on indoor particle concentration and fan power consumption in a residential housing unit. *Indoor and Built Environment, 19*(4), 444-452.

Park, B. H., Lee, M.-H., Jo, Y. M., & Kim, S. B. (2012). Influence of pleat geometry on filter cleaning in PTFE/glass composite filter. *Journal of the Air & Waste Management Association, 62*(11), 1257-1263.

Park, H.-S., & Park, Y. O. (2005). Simulation of particle deposition on filter fiber in an external electric field. *Korean Journal of Chemical Engineering, 22*(2), 303-314.

Payen, J., Vroman, P., Lewandowski, M., Perwuelz, A., Calle-Chazelet, S., & Thomas, D. (2012). Influence of fiber diameter, fiber combinations and solid volume fraction on air filtration properties in nonwovens. *Textile Research Journal, 82*(19), 1948-1959.

Pérez-Lombard, L., Ortiz, J., & Pout, C. (2008). A review on buildings energy consumption information. *Energy and Buildings, 40*(3), 394-398. doi:https://doi.org/10.1016/j.enbuild.2007.03.007

Persaud, D., Smirnov, M., Fong, D., & Sanaei, P. (2021). Modeling of the Effects of Pleat Packing Density and Cartridge Geometry on the Performance of Pleated Membrane Filters. *Fluids, 6*(6), 209.

Pich, J. (1973). Theory of gravitational deposition of particles in fibrous aerosol filters. *Journal of Aerosol Science, 4*(3), 217-226. doi:https://doi.org/10.1016/0021-8502(73)90004-9

Pöyhönen, S., Ahola, J., Niemelä, M., Hammo, S., & Punnonen, P. (2021). Variable-speed-drive-based method for the cost optimization of air filter replacement timing. *Energy and Buildings, 240*, 110904.

Qian, F., Huang, N., Zhu, X., & Lu, J. (2013). Numerical study of the gas–solid flow characteristic of fibrous media based on SEM using CFD–DEM. *Powder Technology, 249*, 63-70. doi:https://doi.org/10.1016/j.powtec.2013.07.030

Ranz, W. (1951). Technical Report No. 3. *Contract AT-(30-3)-28, University of Illinois*.

Rebaï, M., Prat, M., Meireles, M., Schmitz, P., & Baclet, R. (2010). A semi-analytical model for gas flow in pleated filters. *Chemical engineering science, 65*(9), 2835-2846.

Regan, B. D., & Raynor, P. C. (2009). Single-fiber diffusion efficiency for elliptical fibers. *Aerosol Science and Technology, 43*(6), 533-543.

Roh, S., Park, K., & Kim, J. (2019). Design of Web-to-Web Spacing for the Reduced Pressure Drop and Effective Depth Filtration. *Polymers (20734360), 11*(11), 1822-1822. doi:10.3390/polym11111822

Saleem, M., & Krammer, G. (2007). Effect of filtration velocity and dust concentration on cake formation and filter operation in a pilot scale jet pulsed bag filter. *Journal of hazardous materials, 144*(3), 677-681.

Saleh, A., Fotovati, S., Tafreshi, H. V., & Pourdeyhimi, B. (2014). Modeling service life of pleated filters exposed to poly-dispersed aerosols. *Powder Technology, 266*, 79-89.

Schousboe, F. C. (2017). *Media Velocity Considerations in Pleated Air Filtration.* (Graduate thesis). University of South Florida, Florida, Tampa.

Shihang, L., Fei, W., Jie, X., Biao, X., Shuda, H., Hao, J., & Fubao, Z. (2019). Study on effects of particle size and maximum pressure drop on the filtration and pulse-jet cleaning performance of pleated cartridge filter. *Process Safety & Environmental*

Protection: Transactions of the Institution of Chemical Engineers Part B, 123(Part B), 99-104. doi:10.1016/j.psep.2019.01.002

Shin, E. H., Cho, K. S., Seo, M. H., & Kim, H. (2008). Determination of electrospun fiber diameter distributions using image analysis processing. *Macromolecular research, 16*(4), 314-319.

Shrivastava, A. (2018). Additives for plastics. *Introduction to Plastics Engineering; William Andrew (Elsevier): Oxford, UK*, 111-141.

Siegel, A. F. (2016). Chapter 15 - ANOVA: Testing for Differences Among Many Samples and Much More. In A. F. Siegel (Ed.), *Practical Business Statistics (Seventh Edition)* (pp. 469-492): Academic Press.

Stephens, B. (2018). Evaluating the Sensitivity of the Mass-Based Particle Removal Calculations for HVAC Filters in ISO 16890 to Assumptions for Aerosol Distributions. *Atmosphere, 9*(3), 85.

Sun, C., & Woodman, D. (2009). Delivering sustainability promise to HVAC air filtration--part I: classification of energy efficiency for air filters. *ASHRAE Transactions, 115*(2), 581-586.

Sutherland, K. S., & Chase, G. (2011). *Filters and filtration handbook*: Elsevier.

Syazwan Aizat, I., Juliana, J., Norhafizalina, O., Azman, Z., & Kamaruzaman, J. (2009). Indoor air quality and sick building syndrome in Malaysian buildings. *Glob J Health Sci, 1*(2), 126-136.

Tainio, M., Andersen, Z. J., Nieuwenhuijsen, M. J., Hu, L., de Nazelle, A., An, R., . . . Bull, F. (2021). Air pollution, physical activity and health: A mapping review of the evidence. *Environment international, 147*, 105954.

Teng, G., Shi, G., Zhu, J., Qi, J., & Zhao, C. (2022). Research on the influence of pleat structure on effective filtration area during dust loading. *Powder Technology, 395*, 207-217.

Théron, F., Joubert, A., & Le Coq, L. (2017). Numerical and experimental investigations of the influence of the pleat geometry on the pressure drop and velocity field of a pleated fibrous filter. *Separation and Purification Technology, 182*, 69-77. doi:https://doi.org/10.1016/j.seppur.2017.02.034

Tian, E., Mo, J., & Li, X. (2018). Electrostatically assisted metal foam coarse filter with small pressure drop for efficient removal of fine particles: Effect of filter medium. *Building and Environment, 144*, 419-426.

Vaughn, E., & Ramachandran, G. (2002). Fiberglass vs. synthetic air filtration media. *International Nonwovens Journal*(3), 1558925002OS-1501100309.

Vijayan, V. K., Paramesh, H., Salvi, S. S., & Dalal, A. A. K. (2015). Enhancing indoor air quality-The air filter advantage. *Lung India, 32*(5), 473-479. doi:10.4103/0970-2113.164174

Wang, C.-S. (2001). Electrostatic forces in fibrous filters—a review. *Powder Technology, 118*(1-2), 166-170.

Wang, K., & Zhao, H. (2015). The influence of fiber geometry and orientation angle on filtration performance. *Aerosol Science and Technology, 49*(2), 75-85.

Wang, Q., Kwan, M.-P., Zhou, K., Fan, J., Wang, Y., & Zhan, D. (2019). The impacts of urbanization on fine particulate matter (PM2.5) concentrations: Empirical evidence from 135 countries worldwide. *Environmental Pollution, 247*, 989-998. doi:https://doi.org/10.1016/j.envpol.2019.01.086

Wang, Q., Lin, X., & Chen, D.-R. (2016). Effect of dust loading rate on the loading characteristics of high efficiency filter media. *Powder Technology, 287*, 20-28.

Wiegmann, A., Rief, S., & Kehrwald, D. (2007). *Computational Study of Pressure Drop Dependence on Pleat Shape and Filter Media.* Paper presented at the Filtech 2007 International Conference for Filtration and Separation Technology.

Xia, T., Bian, Y., Zhang, L., & Chen, C. (2018). Relationship between pressure drop and face velocity for electrospun nanofiber filters. *Energy and Buildings, 158*, 987-999. doi:https://doi.org/10.1016/j.enbuild.2017.10.073

Xu, Y., Raja, S., Ferro, A. R., Jaques, P. A., Hopke, P. K., Gressani, C., & Wetzel, L. E. (2010). Effectiveness of heating, ventilation and air conditioning system with HEPA filter unit on indoor air quality and asthmatic children's health. *Building and Environment, 45*(2), 330-337.

Yang, D., Ye, C., Wang, X., Lu, D., Xu, J., & Yang, H. (2018). Global distribution and evolvement of urbanization and PM2.5 (1998–2015). *Atmospheric Environment, 182*, 171-178. doi:https://doi.org/10.1016/j.atmosenv.2018.03.053

Zaatari, M., Novoselac, A., & Siegel, J. (2014). The relationship between filter pressure drop, indoor air quality, and energy consumption in rooftop HVAC units. *Building and Environment, 73*, 151-161. doi:https://doi.org/10.1016/j.buildenv.2013.12.010

Zhai, Z. J., & Johnson, S. N. (2017). Full-Scale Laboratory Test on Energy Dependence on Pressure Drops in HVAC Systems. *Procedia Engineering, 205*, 2133-2140.

Zhang, R., Liu, C., Hsu, P.-C., Zhang, C., Liu, N., Zhang, J., . . . Chu, S. (2016). Nanofiber air filters with high-temperature stability for efficient PM2. 5 removal from the pollution sources. *Nano letters, 16*(6), 3642-3649.

Zhang, Y. (2004). *Indoor Air Quality Engineering*. Boca Raton, Florida: CRC Press.

Zhao, X., Li, Y., Hua, T., Jiang, P., Yin, X., Yu, J., & Ding, B. (2017). Cleanable air filter transferring moisture and effectively capturing PM2. 5. *Small, 13*(11), 1603306.

Zhou, B., & Shen, J. (2007). Comparison of general ventilation air filter test standards between America and Europe. *International Network for Information on Ventilation and Energy Performance*.

Zhu, C., Lin, C.-H., & Cheung, C. S. (2000). Inertial impaction-dominated fibrous filtration with rectangular or cylindrical fibers. *Powder Technology, 112*(1), 149-162. doi:https://doi.org/10.1016/S0032-5910(99)00315-0